Cosmological simulations of cosmic rays and the epoch of reionisation

Marion Farcy

THESE de DOCTORAT DE L'UNIVERSITE CLAUDE BERNARD LYON 1

Ecole Doctorale N°52
Ecole Doctorale de Physique et Astrophysique

Discipline : Physique

Soutenue publiquement le 30/09/2022, par :
Marion FARCY

Cosmological Simulations of Cosmic Rays and the Epoch of Reionisation

---

Devant le jury composé de :

SLYZ Adrianne, Professeur associée, Université d'Oxford	Rapporteure
PFROMMER Christoph, Professeur, Université de Potsdam	Rapporteur
CODIS, Sandrine, Chargée de recherche, CEA	Examinatrice
RICHARD, Johan, Astronome, CRAL	Examinateur
BLAIZOT Jérémy, Astronome, CRAL	Directeur de thèse
ROSDAHL Joakim, Chargé de recherche, CRAL	Co-directeur de thèse

Abstract

The formation and the evolution of the Universe is probably one of the most fascinating topics in science. To understand how our present-day Universe came into being, we have to look back to a few hundred million years after the Big Bang, when the first stars and galaxies start to form. The radiation they emit progressively floods the Universe, which turns from being dark, cold and neutral to warm and ionised. Approximately one billion years after the Big Bang, this last major transition of our Universe ends: this marks the limit of the Epoch of Reionisation. This is a crucial part in the history of the Universe, which involves the formation of the first stars and galaxies and the radiation from those galaxies ionising the intergalactic medium. The Epoch of Reionisation is at the frontier of our observational capabilities, and the focus of the major upcoming telescopes such as the James Webb Space Telescope. To prepare and interpret the results of future observational campaigns, a theoretical understanding of galaxy formation during this epoch is mandatory. To decipher the highly complex, non linear and multi-dimensional interactions of the processes at play in galaxy evolution, numerical simulations are our best tool.

Thanks to numerical simulations, it is now established that feedback - physical processes in galaxies that regulate their growth - is an important ingredient of the galactic ecosystem. In particular, feedback provided by the explosions of the most massive stars as supernovae is thought to regulate star formation. It is also thought to launch galactic winds, that carve low-density channels through which radiation can escape and ionise the inter-galactic medium. However, many works also suggest that supernova feedback alone is not sufficient, and that additional feedback mechanisms are important in galaxies.

In particular, one promising channel of feedback is cosmic rays. Cosmic rays are charged particles, accelerated to relativistic speed after successive passages at shock fronts, e.g. in the remnants of supernova explosions. While diffusing from dense to diffuse media along magnetic field lines, cosmic rays exert a significant pressure on the interstellar medium, carrying dense gas and affecting the galactic gas distribution. Because radiation is preferentially absorbed by dense gas, cosmic ray feedback may affect the escape of ionising photons, and hence the reionisation of the Universe. This topic, which has never been investigated before, raises a number of questions that are the main focus of my thesis: Are cosmic rays an important source of feedback in the early Universe? If so, how do they impact the observational properties of galaxies, their growth and their circum-galactic medium? Do they play a role in the reionisation of the Universe by affecting the escape of ionising radiation from galaxies?

To answer these questions, I performed and studied the first radiation-magneto-hydrodynamical simulations of galaxies combining supernova, radiation and cosmic ray feedback. For this purpose, I used the RAMSES code, which uses an adaptive refinement technique and includes state-of-the art star formation and feedback models.

The first part of my work focuses on idealised simulations of high-redshift galaxy disc analogues, that allow me to explore the effects of various physics on galaxies

of different masses. I especially investigate the sensitivity of cosmic ray feedback to the cosmic ray energy injection from supernovae and the cosmic ray diffusion coefficient, which are parameters that respectively govern cosmic ray energetics and transport. The results of this study, published in MNRAS, confirm the ability of cosmic ray feedback to regulate star formation, with a decreasing efficiency with both increasing galaxy mass and diffusion coefficient. At any galaxy mass, I measure a similar enhancement of the mass outflow rate (the mass rate of gas flowing out of galaxies) by cosmic rays, with winds cooler than those driven by supernova and radiation feedback only. This quantitatively varies with the cosmic ray diffusion coefficient: higher diffusivity globally maintains a larger cosmic ray energy, which helps to drive outflows. Conversely, if cosmic rays have enough time to impact the interstellar medium, they in turn suppress the escape of ionising photons from the interstellar medium. Hence the process of reionisation could be sensitive to the efficiency and some of the unconstrained parameters of cosmic ray feedback.

In order to study consistently the effect of cosmic ray feedback on the escape of ionising photons, cosmological simulations are required to enable a global view of the impact cosmic rays have on the process of reionisation. In the second part of my thesis, I rely on the SPHINX cosmological simulations dedicated to the study of the high-redshift Universe. These simulations are able to capture the reionisation of the Universe by resolving the escape of radiation through the interstellar medium of thousands of galaxies. However, as all numerical simulations, some compromises are made. One of them is to use a calibrated and strong supernova feedback in order to regulate galaxy growth enough to reach agreement with high-redshift observational constraints. To determine if cosmic ray feedback can mitigate this boosted and likely artificial supernova feedback, I performed a suite of SPHINX simulations in a volume of 5 cMpc in width that include cosmic rays and radiation-magneto-hydrodynamics. I also target two halos from a SPHINX simulation 64 times larger in volume, that I re-simulate with cosmic ray feedback using the zoom-in technique, in order to increase my sample of galaxies with two massive objects that cannot emerge in my SPHINX simulations. In my simulations, I relax the calibration of strong supernova feedback at the benefit of cosmic ray feedback, and investigate the effect of cosmic ray feedback on galaxy properties and ionising radiation escape fractions. When cosmic ray feedback sufficiently regulates star formation at high-redshift, it also strongly delays the reionisation of the inter-galactic medium, by suppressing ionising radiation escape fractions. In addition, the dense winds carried by cosmic ray pressure in the circum-galactic medium of the galaxies further absorb ionising radiation in the most massive halos, whose contribution to the total ionising photon budget is reduced.

The details of cosmic ray feedback hence may play a large role in this last major phase transition of the Universe that is the Epoch of Reionisation. In turn, observational constraints of reionisation, combined with numerical simulations, may therefore be used as an additional constraint on models of cosmic ray feedback.

Résumé

La formation et l'évolution de l'Univers est probablement l'un des sujets scientifiques les plus fascinants. Pour comprendre l'état actuel de l'Univers, il nous faut regarder quelques centaines de millions d'années après le Big Bang, quand les premières étoiles et galaxies commencent à se former. Le rayonnement qu'elles émettent inonde progressivement l'Univers, qui cesse d'être sombre, froid et neutre pour devenir chaud et ionisé. Environ un milliard d'années après le Big Bang, cette dernière transition majeure de notre Universe s'achève : ceci marque la fin de l'Epoque de Réionisation. Cette époque est une étape cruciale de l'histoire de l'Univers, qui implique la formation des premières étoiles et galaxies, et le rayonnement de ces galaxies ionisant le milieu inter-galactique. L'Epoque de Réionisation est à la frontière de nos capacités observationnelles, et sera prochainement la cible de nouveaux télescopes comme le James Webb Space Telescope. Pour préparer et interpréter les résultats des futures campagnes d'observation, une compréhension théorique de la formation des galaxies pendant cette époque est indispensable. Afin de déchiffrer les interactions hautement complexes, non linéaires et multi-dimensionnelles des processus en jeu dans l'évolution des galaxies, les simulations numériques sont nos meilleurs outils.

Grâce aux simulations numériques, il est maintenant établi que le feedback - la rétroaction des processus physiques au sein des galaxies régulant leur croissance - est un ingrédient important de l'écosystème galactique. En particulier, le feedback issu des explosions des étoiles les plus massives en supernovae est considéré comme pouvant réguler la formation stellaire. Il pourrait également permettre d'éjecter des vents galactiques, qui creusent des cavités de faible densité à travers lesquelles le rayonnement peut s'échapper et ioniser le milieu inter-galactique. Néanmoins, de nombreux travaux suggèrent que le feedback des supernovae seul n'est pas suffisant, et que d'autres mécanismes de feedback sont importants au sein des galaxies.

En particulier, les rayons cosmiques sont un canal de feedback prometteur. Les rayons cosmiques sont des particules chargées, accélérées à des vitesse relativistes par passages successifs au niveau des fronts d'onde de choc, par exemple dans les vestiges des explosions de supernova. Pendant qu'ils diffusent des milieux denses à diffus le long des lignes de champ magnétique, les rayons cosmiques exercent une pression significative sur le milieu interstellaire, transportant du gaz dense et affectant la distribution du gaz galactique. Parce que le rayonnement est préférentiellement absorbé par le gaz dense, le feedback des rayons cosmiques pourrait affecter l'échappement des photons ionisants des galaxies, et donc la réionisation de l'Univers. Ce sujet, qui n'a jamais été exploré avant, soulève un nombre de questions qui sont les intérêts principaux de ma thèse : Les rayons cosmiques sont-ils une source de feedback importante pendant la jeunesse de l'Univers ? Si oui, comment impactent-ils les propriétés observationnelles des galaxies, leur croissance et leur milieu cricum-galactic ? Jouent-ils un rôle dans la réoinisation de l'Univers en affectant l'échappement du rayonnement ionisant des galaxies ?

Pour répondre à ces questions, j'ai réalisé et étudié les premières simulations rayonnement-magneto-hydrodynamiques de galaxies combinant le feedback des supernovae, du rayonnement et des rayons cosmiques. J'ai pour cela utilisé le code

RAMSES, qui permet de réaliser des simulations avec un maillage adaptatif et qui inclut des modèles de formation stellaire et de feedback correspondant à l'état de l'art actuel.

La première partie de mon travail se concentre sur des simulations idéalisées de disques de galaxies analogues à des galaxies à haut-redshift, qui me permettent d'explorer l'effet de différents processus physiques dans des galaxies de différentes masses. Spécifiquement, j'examine comment le feedback des rayons cosmiques est sensible à la fraction d'énergie que les supernovae leur injectent et à leur coefficient de diffusion, qui sont des paramètres qui régissent respectivement l'aspect énergétique et le transport des rayons cosmiques. Les résultats de cette étude, publiés dans MNRAS, confirment l'habilité du feedback des rayons cosmiques à réguler la formation stellaire, avec une efficacité décroissante à la fois pour des masses de galaxie et des coefficients de diffusion croissants. Peu importe la masse de la galaxie, je mesure une augmentation du taux de masse d'outflows (les flots de gaz sortants de la galaxie) avec les rayons cosmiques, et des vents plus froids que ceux conduits par le seul feedback des supernovae et du rayonnement. Ceci varie quantitativement avec le coefficient de diffusion des rayons cosmiques: une diffusivité plus élevée permet globalement aux rayons cosmiques de conserver une plus grande énergie, ce qui aide à éjecter davantage d'outflows. Inversement, si les rayons cosmiques ont le temps d'impacter le milieu interstellaire, ceci affecte à son tour l'échappement des photons ionisants du milieu interstellaire. Ainsi, le processus de réionisation pourrait être sensible à l'efficacité du feedback des rayons cosmiques et à certains de ses paramètres incertains.

Pour étudier de manière consistante l'effet du feedback des rayons cosmiques sur l'échappement des photons ionisants, les simulations cosmologiques sont nécessaires pour permettre une vision globale de l'impact des rayons cosmiques sur le processus de la réionisation. Pour la deuxième partie de ma thèse, je me suis basée sur les simulations cosmologiques SPHINX dédiées à l'étude de l'Univers à haut redshift. Ces simulations sont capables de capturer la réionisation de l'Univers en résolvant l'échappement du rayonnement à travers le milieu interstellaire de milliers de galaxies. Cependant, comme pour toutes les simulations numériques, certaines simplifications sont faites. L'une d'entre elles est de calibrer un fort feedback des supernovae afin de réguler la croissance des galaxies en accord avec les contraintes observationnelles à haut-redshift. Pour déterminer si le feedback des rayons cosmiques peut mitiger ce feedback des supernovae boosté et probablement artificiel, j'ai réalisé une suite de simulations SPHINX d'un volume de 5 cMpc de large et qui incluent rayons cosmiques et rayonnement-magneto-hydrodynamique. Je cible également deux halos d'une simulation SPHINX d'un volume 64 fois plus grand, qui sont re-simulés avec le feedback des rayons cosmiques grâce à la technique zoom-in, afin d'augmenter mon échantillon de galaxies de deux objets massifs qui ne peuvent pas émerger dans mes simulations SPHINX. Dans mes simulations, je relaxe la calibration du fort feedback des supernovae au bénéfice de l'ajout du feedback des rayons cosmiques, et explore l'effet du feedback des rayons cosmiques sur les propriétés des galaxies et sur la fraction d'échappement du rayonnement ionisant. Quand le feedback des rayons cosmiques régule suffisamment la formation stellaire à haut-redshift, il retarde fortement la réionisation du milieu inter-galactique, en supprimant les fractions d'échappement du rayonnement ionisant. De plus, les vents

denses portés par la pression des rayons cosmiques dans le milieu circum-galactique des galaxies absorbent de nouveau le rayonnement ionisant dans les halos les plus massifs, dont la contribution au budget total de photons ionisants est réduite.

Les détails du feedback des rayons cosmiques pourraient donc jouer un rôle important dans cette dernière phase de transition majeure de l'Univers qu'est l'Epoque de Réionisation. A leur tour, les contraintes observationnelles sur la réionisation combinées aux simulations numériques pourraient donc être utilisées comme contrainte additionnelle sur les modèles de feedback des rayons cosmiques.

Acknowledgments

La langue française a beau être riche en vocabulaire, les mots manquent toujours pour exprimer toute l'étendue des émotions. Si cette page et toutes les suivantes existent, c'est d'abord grâce à Joakim Rosdahl. Mille fois merci Joki de m'avoir accompagnée et fait confiance depuis mon stage de master, et pour avoir tout simplement permis à ces trois dernières années d'avoir lieu. Un grand merci également à Jérémy Blaizot, Yohan Dubois et Sergio Martin-Alvarez pour avoir toujours pris le temps de répondre à mes questions et pour les échanges si constructifs. Tous mes remerciements à Léo Michel-Dansac, sans qui il y aurait bien peu de simulations dans cette thèse et au CRAL, à Benoît Commerçon pour avoir suivi mes avancées dans les méandres du feedback des rayons cosmiques, et à Frédéric Bournaud pour m'avoir invitée au CEA et pour les mots rassurants quand je doutais de mes chances de décrocher un post-doctorat.

En ses temps quelque peu troublés, j'ai une pensée toute particulière pour tout ceux que j'ai pu rencontrer lorsque c'était encore possible. Hassan, Viktor, Stefano, Arnaud et tous les autres doctorants à l'OHP, cette courte semaine d'école sur les rayons cosmiques restera gravée comme la plus chaleureuse, amicale et instructive que j'ai vécu. Je pense aussi à tous ceux que j'ai pu croiser au CRAL et qui ont rendu la vie au labo si agréable. A tous les Maxime, Adélaïde, Mathieu, Kieran, Alexandre, Laurence, Yucheng, Romain, Stéphane, Asiyeh, Edouard, Jenny, Floriane, Valentin, Thibault, j'espère qu'on pourra se croiser à nouveau et qu'il vous arrivera tout le meilleur. Bien évidemment, merci à Maxime (Rey) d'être le plus top de tous les co-doctorants : c'est génial d'avoir pu grandir (scientifiquement, bien entendu) et avancer ensemble, dans les simus comme dans les galères. Je remercie tous les autres membres de l'Obs pour leur gentillesse et leur convivialité, notamment Isabelle Vauglin et Emmanuel Pécontal pour leur bienveillance et leurs discussions si enrichissantes. Depuis le CRAL jusqu'aux confins du Caucase, je ne saurais jamais remercier assez Dmitri Makarov pour nos échanges scientifiques, linguistiques et culturels qui me sont infiniment précieux.

Je remercie chaleureusement Johan Richard, Sandrine Codis, Adrianne Slyz et Christoph Pfrommer (et Jeff !) d'avoir accepté de juger mes travaux en dépit de leurs emplois du temps pourtant déjà bien chargés. Merci à Dany Davesne et Sylvie Florès d'être si réactifs et disponibles auprès des doctorants, et à Anne Carré, Alycia Blanchon et Sylvie Réa de gérer les côtés administratifs avec toute leur bonne humeur et leur sympathie. Merci enfin à l'équipe du GEII de l'IUT de Lyon avec qui ça a été un challenge et un plaisir d'enseigner, et surtout à Ali Sari pour m'avoir pris sous son aile et appris les rudiments de l'électrotechnique.

Je serai à jamais reconnaissante à ma famille pour avoir cru en moi depuis mon plus jeune âge, et d'être là à chaque étape de ma vie. A mon frangin, qui m'incite à être une meilleure grande soeur, à mon papa, que j'espère rendre fier de sa fille encore longtemps, à Mélanie, qui est et restera mon modèle et à ma maman, qui

m'a toujours exhortée à atteindre mes rêves : je ne serais indubitablement pas la même personne sans vous. Je ne pourrais pas finir cette page sans mentionner à nouveau Arnaud, qui est la meilleure rencontre qu'il ne m'ait jamais été donnée de faire. Merci merci merci d'avoir changé ma vie et d'en faire partie, d'avoir été si patient dans les moments difficiles, et pour tout cet amour inestimable au quotidien.

Contents

List of Figures

List of Abbreviations

ΛCDM Lambda Cold Dark Matter

AGN Active Galactic Nucleus

AMR Adaptive Mesh Refinement

AMS Alpha Magnetic Spectrometer

BH Black Hole

CGM Circum-Galactic Medium

CIC Cloud-In-Cell

CIE Collisional Ionisation Equilibrium

CMB Cosmic Microwave Background

COBE COsmic Background Explorer

CR(s) Cosmic Ray(s)

CR-RMHD Cosmic Ray-Radiation-MagnetoHydroDynamics

CREAM Cosmic Ray Energetics And Mass

CTA Cherenkov Telescope Array

DM Dark Matter

DSA Diffusive Shock Acceleration

EoR Epoch of Reionisation

GMC Giant Molecular Cloud

HD HydroDynamics

HESS High Energy Stereoscopic System

HST Hubble Space Telescope

ICs Initial Conditions

IGM Inter-Galactic Medium

IMF Initial Mass Function

IR Infra-Red

ISM Inter-Stellar Medium

JWST James Webb Space Telescope

LF Luminosity Function

Lyα Lyman Alpha

LyC Lyman Continuum

MHD Magneto-HydroDynamics

MPI Message Passing Interface

MUSCL Monotone Upstream-centered Scheme for Conservative Laws

MZR Mass-Metallicity Relation

PDF Probability Distribution Function

PIC Particle In Cell

RHD Radiation-HydroDynamics

RMHD Radiation-MagnetoHydroDynamics

RT Radiative Transfer

SAM Semi Analytical Models

SDSS Sloan Digital Sky Survey

SED Spectral Energy Distribution

SF Star Formation

SFR Star Formation Rate

SKA Square Kilometre Array

SN(e) SuperNova(e)

SNR SuperNova Remnant

SPH Smooth Particle Hydrodynamics

UV Ultra-Violet

WMAP Wilkinson Microwave Anisotropy Probe

CHAPTER 1
Introduction

My thesis focuses on the impact of cosmic rays in galaxy evolution, in particular during the Epoch of Reionisation which marks a crucial transition in the history of the Universe, initiated by the formation of the first galaxies.

For this reason, this first chapter gives an introduction on the history of the Universe, from the formation of the first galaxies to the reionisation of the intergalactic medium, that lead to the present day Universe (**Section 1.1**). I briefly state our understanding of these processes, and explain how feedback mechanisms have a major role in regulating galaxy growth and the reionisation of the Universe (**Section 1.2**). As it is the very core of this thesis, I particularly emphasise the importance of cosmic ray (**CR**) feedback, by reviewing the astrophysics of cosmic rays (**CRs**) and results from the literature (**Section 1.3**). I finally summarise the objectives of this thesis and present the outline of the manuscript (**Section 1.4**).

1.1 Overview of the history of the Universe

1.1.1 From the Big Bang to the Cosmic Dawn

As far as we know, the history of the Universe begins about 13.7 billion years ago. This is the starting point of modern cosmological models, such as the Big Bang theory. This model, which still prevails nowadays, emerged in the beginning of the 20^{th} century and relies on two theoretical pillars (Peebles et al., 1994). The first one is the general relativity theory, developed by Albert Einstein in 1916 (Einstein, 1916). It establishes how mass and energy are distributed, both in space and in time. The second one is called the cosmological principle. It consists of the simple assumption that the Universe is the same in any direction, resulting in a homogeneous distribution of matter over the largest scales of the Universe (Brush, 1992). To trigger the events that turned the initial mix of particles into the present day Universe, one key aspect is missing: the Universe is expanding. This is what Alexander Friedmann realised in 1922 (Friedmann, 1922), before George Lemaître (Lemaître, 1927) and Edwin Hubble (Hubble, 1929) quantified it. Because the Universe expands, the speed at which an object moves away from an observer is proportional to the distance between the object and the observer. If we consider a galaxy emitting radiation at a given wavelength λ, an observer moving away from this galaxy will measure a wavelength $\lambda^{'} > \lambda$. As the radiation received is redder than the radiation emitted due to the increasing distance between the receiver and the emitter, this well-known phenomenon is called the redshift z, defined as $z = (\lambda^{'} - \lambda)/\lambda$. Because it takes time for light to travel through the Universe, increasing redshift values indicate that we are looking backward in time. Therefore, this quantity is also an indirect way to distinguish the different epochs of the Universe, whose current age corresponds to $z = 0$, by definition.

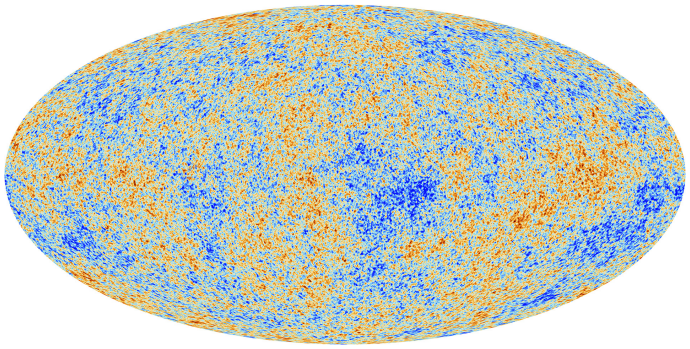

Figure 1.1: *Temperature fluctuations in the Cosmic Microwave Background from the Planck satellite. The average temperature of the CMB is around* 2.7 K*, and fluctuates from red to blue by* 10^{-5} K*. Credit: ESA (European Space Agency) and the Planck Collaboration.*

The discovery of the expansion of the Universe was crucial to go one step further in the understanding of its history. Initially, the Universe is so dense and hot that it is fully ionised, as radiation is constantly absorbed and re-emitted via the black-body process. In their famous $\alpha\beta\gamma$ paper, Alpher et al. (1948) proposed that this is the stage during which light chemical elements form through thermonuclear reactions, marking the nucleosynthesis phase of the Universe. These light elements, like lithium and beryllium, barely contribute to the total baryonic mass, which rather consists of 73% of hydrogen and 27% of helium. With time, as the Universe expands, the initial particle soup which mainly consists of protons and electrons becomes more and more diluted, causing the overall temperature to drop to around 3000 K. We are now some 380 thousand years after the Big Bang (or equivalently at $z \sim 1100$), and the Universe becomes cool enough that protons and electrons (and neutrons for elements heavier than hydrogen) can combine to form the first atoms (see e.g. Bennett et al., 2013; Hinshaw et al., 2013). This is what we call the recombination era. Photons, decoupled from the gas, can eventually propagate freely. The Universe is then transparent to its blackbody radiation, flooding us with light that we call the Cosmic Microwave Background (CMB).

This thermal cosmic radiation was first detected accidentally by Penzias and Wilson in 1965, before being studied more recently with the COsmic Background Explorer (COBE; Smoot et al., 1990, 1992), the Wilkinson Microwave Anisotropy Probe (WMAP; Bennett et al., 2003a,b; Komatsu et al., 2011) and the Planck satellite (Planck Collaboration et al., 2014). One of the most recent observations of the CMB is shown in Fig. 1.1. The CMB represents the temperature of the early Universe, and follows the density fluctuations. Independently of the direction from which it is measured, the CMB currently has a temperature of 2.7 K, and only reveals tiny fluctuations of the order of 10^{-5} (e.g. Smoot et al., 1992). The relative homogeneity of the CMB therefore gives a strong confirmation of the isotropic and homogeneous Universe predicted by the Big Bang theory[1].

[1]Other theories, such as the inflation theory, are however needed to reconcile the Big Bang cosmology with a number of issues. This is for example the case for the horizon problem, which needs to assume an extremely quick expansion of the Universe at its very beginning to explain the

The CMB encodes the primordial density anisotropies from which the current Universe has evolved. After the recombination era that allows the CMB to be emitted, the Universe is neutral. Because of the absence of collapsed structures like stars emitting radiation, this epoch is also referred to as the dark ages. With gravity, the primordial adiabatic fluctuations which are close enough to each other gather and grow, until they progressively form the very first gravitationally bound structures. This is captured in a number of cosmological models, among which the most commonly adopted is the Λ Cold Dark Matter (ΛCDM) model. Given the angular power spectrum fluctuations of the CMB, the ΛCDM model together with the Big Bang theory describe the evolution and the content of the Universe. In this context, the space and time mass-energy distribution in the Universe is characterized by the Friedmann-Lemaître-Robertson-Walker metric, where the expansion of the Universe is described by its expansion factor $a(t) = 1/(1+z)$. Different density components contribute to the total energy density of the Universe, and are parameterised by their fraction relative to the total mass in the Universe. One of these, the baryon mass fraction in the Universe Ω_b, has a current (at $z = 0$) value of $\Omega_{\mathrm{b},0} \simeq 0.04$. However, the baryonic mass alone cannot explain observations of the rotation curves of galaxies or the velocity dispersion of galaxy clusters. This suggests that an invisible and massive component dominates the gravitational potential of these objects. This missing mass, supported by gravitational lensing observations, is known as Dark Matter (DM). The DM, and especially the cold DM (which refers to the prediction that it has a non relativistic velocity), has weak or even no interactions with matter (whether it be baryons or itself) and radiation, and is hence not directly visible. Similar to the baryonic mass, one can define a DM mass fraction Ω_DM, whose current value is estimated to be $\Omega_{\mathrm{DM},0} \simeq 0.23$. With matter alone, only 27% of the Universe is described. Then, there remains one key contribution in the standard cosmology, necessary to explain the fact that the expansion of the Universe is accelerating. This acceleration has been discovered through observations of distant type Ia supernovae (Riess et al., 1998; Perlmutter et al., 1999), and implies the existence of an additional invisible pressure acting on the Universe. This is what is referred to as the cosmological constant Λ, also termed as a dark energy, with a dark energy fraction of $\Omega_\Lambda \simeq 0.73$. Finally, relativistic species such as photons and neutrinos exist but currently barely contribute to the total energy density budget. Following this formalism, the rate of cosmological expansion $H(t)$ is a function of the current expansion rate $H_0 \simeq 67.66\ \mathrm{km\,s^{-1}\,Mpc^{-1}}$ and of the different density parameters aforementioned (Planck Collaboration et al., 2020). While matter (baryons and DM) dilutes as $(z+1)^3$ with the expansion of the Universe, relativistic species dilute as $(z+1)^4$, and Λ, which is constant, does not evolve with time (Carroll, 2001). Even if the nature of dark matter and dark energy remains a mystery still under investigation, this cosmological paradigm is our best way to explain the formation of large-scale structures and galaxies, and how the Universe evolved.

In the standard ΛCDM cosmology, the initial small density fluctuations give rise to small DM halos that grow and merge into larger ones, inside of which the first stars and galaxies form: this is the hierarchical structure formation theory (White & Rees, 1978). In this framework, the ambient gas falls into the gravitational potential of forming DM halos, and consequently becomes denser and denser. Because baryonic

homogeneity of the CMB (see e.g. De Haro & Elizalde, 2022, for a recent discussion).

matter is able to cool, more compact structures form inside the halos, which can eventually collapse into molecular clouds and form stars. This epoch is called the cosmic dawn, and marks the end of the dark ages. The stars emit radiation that heats the surrounding gas, creating bubbles of ionised hydrogen around them. As more and more stars form, those bubbles progressively grow and overlap. About a billion years after the Big Bang, the Universe is once again ionised (see e.g. Barkana & Loeb, 2001; Zaroubi, 2013, for reviews about the reionisation scenario). This period, from the emission of the first stellar light to the reionisation of the Universe, is called the Epoch of Reionisation (EoR hereafter)[2]. The different epochs of the Universe mentioned in this section are illustrated in Fig. 1.2.

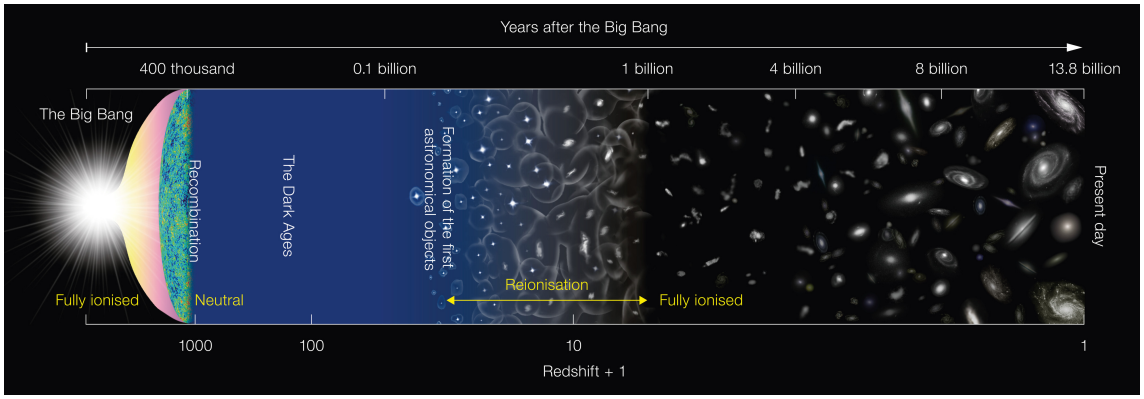

Figure 1.2: *Schematic diagram depicting the timeline of the Universe (not to scale). From left to right, time increases, the Universe expands, and galaxies form and evolve until the present day, roughly 13.7 billion years after the Big Bang. Credit: ESO (European Southern Observatory) and NAOJ (National Astronomical Observatory of Japan).*

1.1.2 The Epoch of Reionisation

The EoR is often described as the last major phase transition in the history of the Universe. As the first galaxies start to form, it changes the structure of the Universe. The Inter-Galactic Medium (IGM), initially neutral following the recombination era around $z = 1100$, is transformed by the Ultra-Violet (UV) photons emitted by the galaxies. As reionisation progresses, Lyman Continuum (LyC) photons, which have an energy > 13.6 eV, gradually ionise the neutral hydrogen. As shown in Fig. 1.2, ionisation bubbles start to appear around $z \sim 15$ until they fill the whole Universe at $z \simeq 6$ (about 1 Gyr after the Big Bang). This is a highly inhomogeneous process, causing a patchy and progressive reionisation. Two important questions, still under investigation, arise: what is the timeline of the EoR, and what are the sources responsible for the reionisation of the Universe? These questions are challenging, as it is difficult to probe the high-redshift Universe due to the limited sensitivity of our instruments. Fortunately, some indirect observations provide valuable information to constrain the process of reionisation.

[2]In all the manuscript, the EoR refers to the Epoch of hydrogen Reionisation, and not to the complete reionisation of helium that happens later.

The Gunn-Peterson effect

Radiation with an energy > 13.6 eV (or equivalently with $\lambda < 912\,\text{Å}$), ionises hydrogen, the dominant constituent of gas in the Universe. The recombination of free protons with free electrons gives rise to radiative cascades to the ground state of the hydrogen atom. This results in the emission of Lyman-α (Lyα) photons at a wavelength $\lambda_{\text{Ly}\alpha} = 1216\,\text{Å}$, corresponding to a transition from the first excited state of a hydrogen atom to its ground state. The Lyα line, which is the strongest recombination line of neutral hydrogen, historically allowed the first estimation of the end of the reionisation thanks to the Gunn-Peterson effect (Gunn & Peterson, 1965), first detected by Becker et al. (2001).

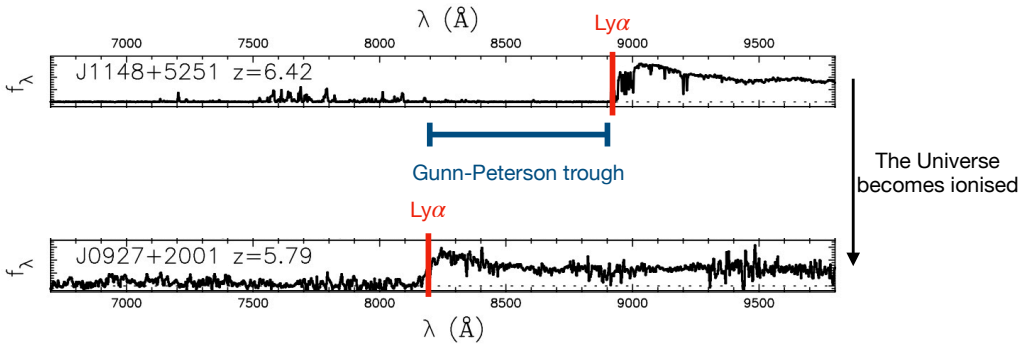

Figure 1.3: *Spectra of two distant quasars from the Sloan Digital Sky Survey (SDSS). The red vertical lines show the wavelength corresponding to the Lyα emission, redshifted depending on the quasar redshift. At $z = 6.42$ (top panel), neutral hydrogen absorbs the Lyα photons, producing the Gunn-Peterson troughs which are not visible anymore in the spectrum of the quasar located at $z = 5.79$ (bottom panel), once the Universe is reionised. Credit: quasar spectra from Fan et al. (2006).*

Let us consider a very distant quasar, so that the light it emits traces back to the EoR, when the IGM and most of the content of the Universe is still composed of neutral hydrogen. A quasar is a very luminous Active Galactic Nucleus (AGN), which emits in particular UV radiation as a result of the accretion of matter by the central supermassive black hole. Before the radiation emitted by our distant quasar can reach a present-day observer, it is continuously redshifted, while crossing a significant amount of gas transitioning from neutral to ionised through time. Along the sightline of the quasar, the photons emitted will first interact with the neutral hydrogen and be absorbed. This is especially the case for Lyα photons, which, once emitted, are immediately absorbed by the surrounding atoms of hydrogen. As a result, we measure a drop of the flux of the quasar at the wavelengths corresponding to the redshifted Lyα lines (i.e. at $\lambda_{\text{Ly}\alpha}(1 + z)$), which are called Gunn-Peterson troughs. Conversely, once there is no more neutral hydrogen, the Lyα photons can travel freely through the ionised IGM. Because the Lyα photons stop being absorbed, the Gunn-Peterson troughs disappear from the quasar spectrum. An example with two quasars is shown in Fig. 1.3. Because it traces the presence of remaining neutral gas in the IGM, the Gunn-Peterson phenomenon gives constrains

on when the reionisation of the Universe is complete, which is determined to be around $z = 6$ from a number of quasar absorption spectra observations (Fan et al., 2006; Goto et al., 2012; Becker et al., 2015; Barnett et al., 2017).

The Thomson scattering optical depth from the CMB

Another way to probe the timeline of the EoR is to rely on the CMB radiation. On their way to an observer, photons from the recombination era can interact with free electrons through Thomson scattering, which modifies the CMB radiation. When a low-energy photon meets a free non relativistic electron, the latter absorbs and then re-emits the photon. Therefore, both the photon and the electron change their propagation direction, with no energy loss: this is an elastic scattering. However, such interactions are responsible for damping the temperature anisotropies of the CMB, by a factor proportional to the Thomson optical depth. Moreover, Thomson scattering also polarises the CMB radiation, which translates into a rise of the 10^{-5} K temperature anisotropies of the CMB, not more than 10^{-6} K in amplitude. These two effects allow to measure the Thomson optical depth and consequently to infer the number of free electrons in the Universe, thus quantifying its ionisation state.

Initially, the first measurements of the Thomson optical depth from the WMAP was highly incoherent with the results from the Gunn-Peterson effect in quasar spectra, suggesting that reionisation ended much earlier, around $8 < z < 15$ (Spergel et al., 2003; Larson et al., 2011; Bennett et al., 2013; Hinshaw et al., 2013). Nowadays, the latest results from the Planck satellite estimate that the mid-point reionisation redshift is around $z = 8$ (Planck Collaboration et al., 2020; Pagano et al., 2020), showing the difficulty to have an accurate determination of the timeline of the EoR.

Other methods to constrain reionisation

Independently of the Gunn-Peterson effect, the Lyα line is a powerful probe of the EoR. When the amount of neutral hydrogen around a quasar is low enough, its spectrum does not show the Gunn-Peterson trough anymore, as the Lyα photons can travel without being immediately absorbed. However, if these photons encounter clouds of neutral hydrogen along their path in the IGM, this will produce typical absorption lines in the quasar spectrum, whose position varies with the redshift of the clouds. The fingerprint left by each of these clouds finally produces what is called the Lyα forest, shown in Fig. 1.4. Using the Lyα forest provides useful details about the density and the frequency of neutral hydrogen clouds, and indicates that reionisation is not uniform nor homogeneous but rather patchy (Becker & Bolton, 2013).

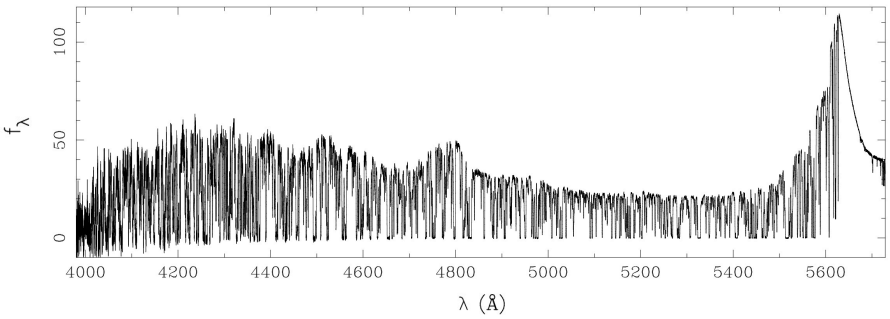

Figure 1.4: *Lyα absorption line forest, with the Lyα emission line at the right of the spectrum. The Lyα forest corresponds to the series of absorption lines due to neutral hydrogen in the sightline of the quasar, located at $z = 3.62$. Credit: quasar spectrum from Rauch (1998), using the data from Womble et al. (1996).*

Furthermore, if one of the neutral hydrogen clouds encountered by a Lyα photon has a high column density, this will translate into a damping of the Lyα line. Again, this effect has the same origin as the Gunn-Peterson trough. The presence of neutral hydrogen leads to an absorption of the redder part of the Lyα line, which is called the damping wing effect, and can be used to constrain the end of the EoR (Schroeder et al., 2013).

Finally not only quasars but also star-forming galaxies emit Lyα radiation. By using surveys of high-redshift galaxies, supposed to emit Lyα photons, one can constrain the ionisation state of the Universe depending on the fraction of Lyα emitters measured at different redshifts. Typically, the increasing amount of neutral hydrogen at $z > 6$ leads to increasingly less Lyα emitters, gives constrains on the neutral gas fraction in the Universe and hence sets a limit to the EoR (Schenker et al., 2014; Sobacchi & Mesinger, 2015; Inoue et al., 2018; Ouchi et al., 2018).

Another promising probe of the EoR is the redshifted hydrogen 21 cm line, which allows direct observations of the neutral hydrogen content of the Universe. The 21 cm signal corresponds to a hyperfine transition in which the electron of the hydrogen atom flips its spin relative to the proton, from a parallel to an anti-parallel state in the rest-frame of the hydrogen atom (Hogan & Rees, 1979; Scott & Rees, 1990; Madau et al., 1997). The 21 cm line is a forbidden line, which occurs approximately every 11 Myr, a low decay rate which is counterbalanced by a large amount of hydrogen in the Universe. Any emission or absorption of 21 cm photons implies the presence of electrons bound to their atom of hydrogen, so that the 21 cm signal is sensitive to the density of neutral hydrogen. Therefore, this line is a powerful way to map the distribution of neutral hydrogen in the IGM, thus giving precious information about the average ionisation state of the Universe with redshift. However, it remains a very challenging task to extract the 21 cm signal, and foremost to identify it correctly among the foreground emission, which can be several orders of magnitude stronger (Di Matteo et al., 2002; Jelić et al., 2008; Ali et al., 2008; Ghosh et al., 2012). For this reason, forthcoming instruments with higher sensitivity, such as the Square Kilometre Array (SKA, Koopmans et al., 2015; Mellema et al., 2015; Shaw et al., 2019), will be dedicated to go one step further in searching for

the small-scale fluctuations in the 21 cm background.

Globally, the multiple probes of the EoR mentioned in this section give us evidence of an extended and late reionisation scenario, whose end is expected at $z < 6$ (e.g. Keating et al., 2020; Nasir & D'Aloisio, 2020). According to the latest reionisation models, it is most likely that the transition from a neutral to an ionised Universe occurred at $z > 6$ (Fan et al., 2006; Pentericci et al., 2011; Mason et al., 2018), and that this patchy and non homogeneous transition continued down to $z \simeq 5$ (Becker et al., 2015; Bosman et al., 2018; Eilers et al., 2018; Kulkarni et al., 2019; Yang et al., 2020; Kusakabe et al., 2020). However, the exact process as well as the sources of reionisation are still debated.

The sources of reionisation

The two main candidates for producing the LyC photons responsible for the reionisation of the Universe are the AGN (e.g. Grazian et al., 2018) and the brightest stars, by extension mentioned as star-forming galaxies (e.g. Finkelstein et al., 2015; Eldridge et al., 2017; Shivaei et al., 2018). By means of numerical simulations, Trebitsch et al. (2022) found that AGN are likely to be responsible for less than 10% of the total ionising photon budget, with mainly a late contribution after $z = 5$. This is also confirmed by several recent observational results, such as by Madau & Haardt (2015) using data from the Planck Collaboration. This may be due to the rareness of AGN at increasing redshift, so that they cannot contribute significantly to the UV background before $z = 6$ (Kakiichi et al., 2018). While star-forming galaxies are the likeliest candidates, it is not certain whether the bulk of the ionising photon budget comes from the bright but rare galaxies or from the multitude of faint ones. We refer to the former scenario as a reionisation by the oligarchs (e.g. Naidu et al., 2020), and to the latter as a democratic reionisation (e.g. Finkelstein et al., 2019). Disentangling the two scenarios is especially difficult because of the faintness of potential sources of reionisation (Bian & Fan, 2020; Meštrić et al., 2020), and also due to the opacity of the IGM at high redshift (Inoue & Iwata, 2008; Steidel et al., 2018; Bassett et al., 2021), making it hard to provide accurate LyC emission estimates.

From an analytical consideration, the process of reionisation results from the interplay between the luminosity density of UV photons $\rho_{\rm UV}$, the efficiency of ionising photon production given the UV radiation emitted $\xi_{\rm ion}$, and the escape fraction of these hydrogen ionising photons $f_{\rm esc}$. These quantities lead to $\dot{N}_{\rm ion}$, the emission rate (in number density) of the LyC photons that participate in hydrogen reionisation[3]:

$$\dot{N}_{\rm ion} = f_{\rm esc} \left(\frac{\xi_{\rm ion}}{\rm Hz\ erg^{-1}} \right) \left(\frac{\rho_{\rm UV}}{\rm erg\ s^{-1}\ Hz^{-1}\ cm^{-3}} \right) \tag{1.1}$$

In an inhomogeneous Universe, the hydrogen stays ionised when $\dot{N}_{\rm ion}$ reaches or even exceeds a critical value[4] such as (Madau et al., 1999):

$$\dot{N}_{\rm ion} = 10^{51.2}\ {\rm s^{-1}\ Mpc^{-3}} \left(\frac{1+z}{6} \right)^3 \left(\frac{h^2 \Omega_b}{0.02} \right)^2 \left(\frac{\mathcal{C}}{30} \right) , \tag{1.2}$$

[3] When not specified, quantities are expressed in cgs units.

[4] The critical value comes from the ratio between the mean hydrogen density in an expanding IGM and the volume-averaged gas recombination time for gas at 10^4 K., see the text below.

where $\mathcal{C} = \langle n_{\rm H}^2 \rangle \,/\, \langle n_{\rm H} \rangle^2$ is the ionised hydrogen clumping factor which parameterises the inhomogeneity of the Universe, with $n_{\rm H}$ the number density of hydrogen, and where h is the Hubble constant H_0 in units of 100 km s^{-1} Mpc^{-1}.

Then, the evolution of the ionised hydrogen filling fraction $\mathcal{Q}_{\rm HII}$ can be expressed as a competition between ionisation and recombination events (Meiksin, 2009; Romanello et al., 2021):

$$\dot{\mathcal{Q}}_{\rm HII} = \frac{\dot{N}_{\rm ion}}{\langle n_{\rm H} \rangle} - \frac{\mathcal{Q}_{\rm HII}}{\langle t_{\rm rec} \rangle}\,, \tag{1.3}$$

where $\langle n_H \rangle = 1.7 \times 10^{-7}$ cm$^{-3} \times (\Omega_b h^2/0.02)$ is the mean hydrogen density of the expanding IGM, and $\langle t_{\rm rec} \rangle = 3.2$ Gyr $\times\, [(1+z)/7)]^{-3}\, \mathcal{C}^{-1}$ is the recombination timescale, when considering only case B recombinations for which electrons in the ground state of hydrogen generate ionising photons that are immediately re-absorbed by an optically thick IGM (Lapi & Danese, 2015).

Quantifying the evolution of $\mathcal{Q}_{\rm HII}$ therefore requires a precise knowledge of both the production of LyC photons and their escape fraction $f_{\rm esc}$, in order to determine the portion of ionising photons emitted that reach the IGM and actually contribute to the reionisation.

One of the most powerful observational tools to study the emission of UV radiation from galaxies is the Luminosity Function (LF) (e.g. Bouwens et al., 2015). The LF corresponds to the number density of galaxies as a function of their luminosity, in a chosen band of wavelengths. Reconstructing the UV LF at high redshift therefore provides the first step to estimate the contribution of galaxies to reionisation, which is currently possible thanks to HST (e.g. Stanway et al., 2003, among the first to study high-redshift UV LF). However, this is a difficult task, biased by the detection limit of our instruments. At the low-mass end of the LF, galaxies are so faint that they cannot be detected. To improve the completeness of our surveys, we need to correct our measurements by estimating the number of low-mass galaxies that exist but cannot be detected. Necessarily, our understanding of how galaxies contribute to the EoR is thus strongly dependent on the fraction of faint objects we assume to miss. This is particularly problematic when considering a high-redshift LF, as high-redshift galaxies tend to be fainter and less massive than current-day ones. One way to push the detection limits of our current instruments is to make use of foreground galaxy clusters as magnifying glasses, a process known as gravitational lensing (e.g. Richard et al., 2011; Atek et al., 2015). Last but not least, a fraction of the UV light produced by the young stars is absorbed by dust, before being re-emitted at Infra-Red (IR) wavelengths (Casey et al., 2014). This process especially impacts the UV LF of bright galaxies around $z \simeq 6$ (Ma et al., 2018). It is therefore necessary to account for dust obscuration in order to accurately estimate the total UV photon budget.

The production of UV photons directly encapsulates information about the star formation rate (SFR) within galaxies. To estimate which fraction of UV radiation in a galaxy consists of ionising LyC radiation, we have to rely on models that assume the stellar composition of galaxies (based on stellar population models, later described in **Section 1.2.1**) and the overall radiation emitted by these stars. Assuming a stellar population for high-redshift galaxies, this allows an estimate of $\xi_{\rm ion}$ in Equation 1.1. Until recently, it was suggested that galaxies could not produce

enough LyC photons for reionisation to be complete by $z = 6$. For example, Bolton & Haehnelt (2007) estimated that not more than 3 LyC photons are emitted per atom of hydrogen over one billion years, which implies a lack of LyC photons during the EoR. One common explanation is that the UV luminosity function lacks very faint galaxies whose contribution could solve the deficit of ionising photons (Robertson et al., 2013). Another possible explanation invokes the issue of accurately determining which fraction of the ionising photon budget participates in reionisation. In other words, this involves quantifying the $f_{\rm esc}$ of LyC photons.

Ideally, one would directly observe the LyC emission from high redshift galaxies, also described as LyC leakers. However, because of the significant presence of neutral hydrogen at $z > 6$, directly measuring hydrogen ionising radiation is barely possible. Thus, one way to estimate $f_{\rm esc}$ at high redshift is to infer its value from the local Universe. This remains challenging, with only some 10% of the objects observed leaking ionising radiation at $z = 3$ (Nestor et al., 2013). For these objects, $f_{\rm esc}$ determined from observations is not higher than a few percent, which is well below the minimum of 20% required for galaxies to contribute significantly to reionisation (Robertson et al., 2013). However, $f_{\rm esc}$ likely varies with redshift and galaxy mass, which makes it even more uncertain to rely on low-redshift measurements only (Razoumov & Sommer-Larsen, 2006; Wise et al., 2014). As we cannot have similar measurements at higher redshift due to the IGM opacity, our best chance to estimate $f_{\rm esc}$ is to rely on numerical simulations (e.g. Paardekooper et al., 2015; Rosdahl et al., 2018). Simulations of the reionisation of the Universe show that the time and mass dependency of $f_{\rm esc}$ is very much controlled by the physical processes that regulate star formation and the ejection of gas, clearing the way for radiation to propagate from galaxies to the IGM, with $f_{\rm esc}$ that can vary from 10% to 70% (Hutter et al., 2021). Additionally, they reveal that different models for $f_{\rm esc}$ change drastically the identification of the key drivers of reionisation.

Currently, our best scenario for the dominant contributors to reionisation are the faint low-mass galaxies (e.g. Wise & Cen, 2009; Robertson et al., 2013; Paardekooper et al., 2015; Bouwens et al., 2015), which are, once again, at the frontier of the detection limit of our current instruments. To circumvent this aspect and better target the astrophysical sources that drive the EoR, the James Webb Space Telescope (JWST, Gardner et al., 2006) is one of the most (if not the most) promising instrument, just launched in December 2021. With the plethora of upcoming results expected, there is hope to gain an unprecedented understanding of the contribution of the different sources of ionising radiation, as well as to better constrain the timeline and the topology of the EoR.

1.1.3 From the Epoch of Reionisation to present times

The EoR is not only interesting for being the last major transition of the Universe, but also for being the epoch at which the very first stars, galaxies and large-scale structures form, before leading to the present-day Universe we can directly observe. From the time of their formation until the present, galaxies grow via gas accretion and/or mergers, depending on their environment. In particular, galaxies are connected to the cosmic web through its dense and cold filaments of gas, which feed the halos with the necessary material to form stars, as well as affect the composition

of galaxies' Circum-Galactic Medium (CGM) before reaching them. The galaxies in turn impact these filaments through the radiation they emit, which can photo-evaporate the gaseous filaments unless they are dense enough to be self-shielded from UV radiation. This reduces the amount of gas that is accreted onto galaxies, which, coupled to a more local effect from photoionisation in the inter-stellar medium (ISM) of the galaxies, has the ability to delay or even suppress star formation, and the associated production of LyC radiation. Consequently, there is a non trivial interplay between the processes of reionisation and galaxy evolution.

Thus, questions about how the first stars and galaxies form and what type of physical processes regulate the evolution of galaxies and shape their properties are essential to understand the current Universe. In the following section, I review some of our key knowledge about galaxy evolution, as well as the physical processes thought to play an important role.

1.2 Galaxy formation and evolution

Galaxies are gravitationally bound objects that host thousands of billions of stars, and exhibit a wide diversity of properties. In particular, focusing on galaxy formation and evolution provides the perfect challenge for evaluating our knowledge of the physical processes involved at the different stages of the Universe. Incredibly large ranges of time and length scales are associated to galaxy evolution: stars form in molecular clouds tens of parsecs wide while embedded in galaxies with radius of several kpc that need hundreds of Myr to orbit only one single time. Obviously, there is no hope to make direct astrophysical experiments on Earth when such time scales are longer than all of human history, nor to track individual galaxies over their full lifetime. Our main tools are observations, but probing the high-redshift Universe and in particular high-redshift galaxies remains arduous due to technical limitations. Nonetheless, thanks to forthcoming observational campaigns dedicated to the EoR, the study of galaxy formation and evolution appears to be set for rapid progress over the coming years. In any case, observational measurements alone are not sufficient, and need to be combined with theory. Analytical models are useful to develop a theoretical framework for galaxy evolution, but are oversimplifications of the complex and highly non-linear effects arising from the multitude of physics involved at different scales. Another approach, which is the one adopted in this thesis, is to rely on simulations that numerically evolve the physical processes of interest, modelled as closely as possible. Our understanding of all astrophysical events can only develop progressively, by deciphering, interpreting and predicting data from current and upcoming surveys by means of analytic theories and simulations. Galaxy evolution therefore remains an open field of research, that needs further investigation. In the following, I will briefly state what we (think we) know and what is missing in our understanding of galaxy evolution (e.g. Mo et al., 2010, for a review).

1.2.1 What we know about galaxy formation

Dark matter halos as the sites of galaxy formation

Within the ΛCDM framework, galaxies form out of the gas accreting into DM halos (White & Rees, 1978). Therefore, at first glance, galaxy formation can be considered to be driven by DM halo growth and assembly. As any massive structures, DM halos are subject to gravitational collapse, which converts potential energy into kinetic energy. The balance between halo expansion and its collapse stops when its average kinetic energy equals half its average potential energy, in accordance with the virial theorem. When the DM halo satisfies the virial theorem, it is said to be virialized. If we consider a spherical virialized halo of radius $R_{\rm vir}$, we can define its virial mass ($M_{\rm vir}$) and its virial velocity ($v_{\rm vir}$) as:

$$M_{\rm vir} = \frac{4\pi}{3} R_{\rm vir}^3 \ \Delta \ \rho_0 \tag{1.4}$$

$$v_{\rm vir} = \sqrt{\frac{GM_{\rm vir}}{R_{\rm vir}}}, \tag{1.5}$$

where Δ is the virial over-density parameter, ρ_0 is the mean density of the Universe and G is the gravitational constant. Similarly, it is also possible to define M_{200} as the mass enclosed in a sphere of radius R_{200} whose density is 200 times the critical density of the Universe, defined as $\rho_{\rm c} = 3H^2(t)/8\pi G$. The non linear evolution of DM perturbations leads to approximately stable halos, where DM particles support halos against their own gravity. Then, when the first DM potential wells become sufficiently deep, at $z \sim 20 - 50$, gas can start to condense to form the first galaxies (Tegmark et al., 1997; Gao et al., 2007).

Gas cooling

Initially, baryons follow the distribution of DM. DM halos, which constitute the gravitationally dominant matter, accrete gas from the IGM as easily as their potential well is deep, until gas collapses at their center. When the gas accreted is colder than the virial temperature of the halo, it is accreted at supersonic speed, which creates a strong virial shock. Like other virial properties, the virial temperature $T_{\rm vir}$ is defined as the temperature within a sphere of radius $R_{\rm vir}$:

$$T_{\rm vir} = \frac{\mu m_{\rm p}}{5k_{\rm B}} \ v_{\rm vir}^2, \tag{1.6}$$

where μ is the average mass per particle in the gas, $m_{\rm p}$ is the proton mass and $k_{\rm B}$ is the Boltzmann constant. Because $T_{\rm vir}$ scales with the virial mass (through $v_{\rm vir}^2$), the most massive halos have the highest $T_{\rm vir}$. Gas falling in such halos thermalizes its kinetic energy and is heated to $T_{\rm vir}$, while remaining in hydrostatic equilibrium in the absence of any dissipative process (Birnboim & Dekel, 2003). In other words, the internal pressure of the gas and the gravitational force to which it is subject balance each other. Conversely, gas can fall ballistically towards the center of the DM halo, without forming a hot quasi-hydrostatic halo. In this case, gas flows along cold and dense filaments, resulting in the cold mode accretion of gas (Kereš et al., 2005). For both accretion modes, gas cannot fall and reach the halo center - the condition to finally form a galaxy - without losing its infall energy. The loss

of energy is equivalently associated to a reduction of thermal pressure, thanks to which the gravitational force can dominate again. This loss of energy occurs when gas cools radiatively through various processes, a condition necessary to ignite star formation and form structures more complex than DM halos. Below we summarise the cooling processes active at different gas temperatures.

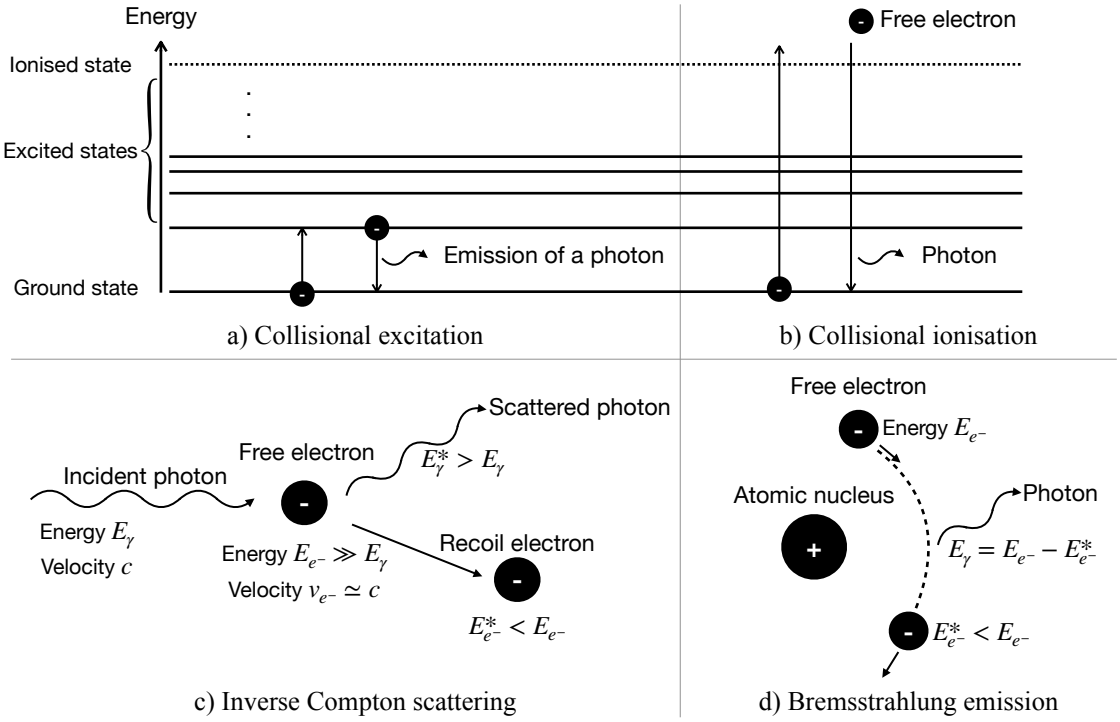

Figure 1.5: *Illustration of gas cooling processes. The basic idea behind cooling gas is to remove a part of its internal energy by the emission of a photon, which carries this energy away from the system. The different processes through which a photon may be emitted are (a) by recombination of an electron after its collisional excitation, (b) by ionisation, (c) through inverse Compton scattering and (d) via free-free bremsstrahlung emission. Starred energies in panels (c) and (d) refer to energies post-collision.*

- In halos with $T_{\rm vir} < 10^4$ K, gas is mostly neutral. At high redshift, the pristine gas is almost exclusively composed of hydrogen and helium. It is needed to wait for the first generation of stars (also designated population III stars) to enrich the gas in metals[5], heavy atoms that form out of the fusion of lighter elements in a process known as stellar nucleosynthesis. Therefore, the dominant coolant responsible for the very first population of stars is molecular hydrogen (Abel et al., 1997). In the case of molecular hydrogen cooling, photons responsible for removing the internal energy of the system come from rotational and vibrational transitions.

- As soon as gas contains metals, cooling of gas colder than 10^4 K becomes possible via fine and hyperfine structure line transitions, in addition to (hydrogen

[5]In astrophysics, metals refer to any elements other than hydrogen and helium.

and metal) molecular cooling. Similarly to the emission of 21 cm photons we described in **Section 1.1.2**, these transitions originate from the splitting of spectral levels into finer levels, defined by the state of the electron spin. Since neither hydrogen nor helium have fine levels in their ground state (they have hyperfine levels, whose contribution to gas cooling is subdominant), cooling from fine structure lines is only possible through metal species, mainly carbon and oxygen (Wolfire et al., 1995). Gas is also unable to cool via other atomic processes, because there are not enough electrons and energy available to trigger atomic transitions through excitation and ionisation.

- When the gas is sufficiently hot ($T \gtrsim 10^4$ K) for hydrogen to be collisionally ionise, the dominant cooling processes are atomic, based on collisional excitation and ionisation. The de-excitation or recombination event that follows the electron excitation or ionisation produces a photon, which removes kinetic energy from the atom that undergoes the collision. If the medium is optically thin, the photon produced propagates away from the system, carrying with it the energy removed from the change of the electron state, which cools the initial system. We illustrate such processes in panels a) and b) of Fig. 1.5. Eventually, when gas reaches temperatures between $10^5 \lesssim T \lesssim 10^7$ K, hydrogen and helium become progressively ionised and have no chance to get back their electrons without them being ripped away from them again. For this reason, metals, when present, are the dominant coolant of gas with $10^5 \lesssim T \lesssim 10^7$ K, as shown in Fig. 1.6.

- Other cooling mechanisms involving free particles exist. We already discussed the Thomson scattering of CMB photons, in **Section 1.1.2**, where there is no energy exchange between the particles. In Thomson scattering, a photon meets an electron which moves non-relativistically and is more energetic than it. When the free electron speed approaches the relativistic limit, a part of its energy is imparted to the photon during the scattering of the two particles: this is the inverse Compton process[6], shown in panel c) of Fig. 1.5. During the inverse Compton scattering, photons gain energy, which is removed from the system when the photons escape, eventually cooling the gas. Compton cooling is preferentially relevant at high redshift ($z \gtrsim 6$), when the density of CMB photons is sufficient to cool the gas from an ionised plasma inside DM halos.

- Finally, in massive halos where $T_{\rm vir} > 10^7$ K, gas is fully ionised, and cools through bremsstrahlung emission. This process, which means "braking radiation" in German, involves the deceleration of a free electron deflected by another charged particle, which emits a photon as a conversion of the electron loss of kinetic energy. This emission, illustrated in panel d) of Fig. 1.5, is also qualified as free-free, as it involves the interaction of free charged particles.

[6]Direct Compton scattering occurs when the photon energy exceeds that of the electron and when the electron is non relativistic. During the process, the electron gains a part of the photon energy.

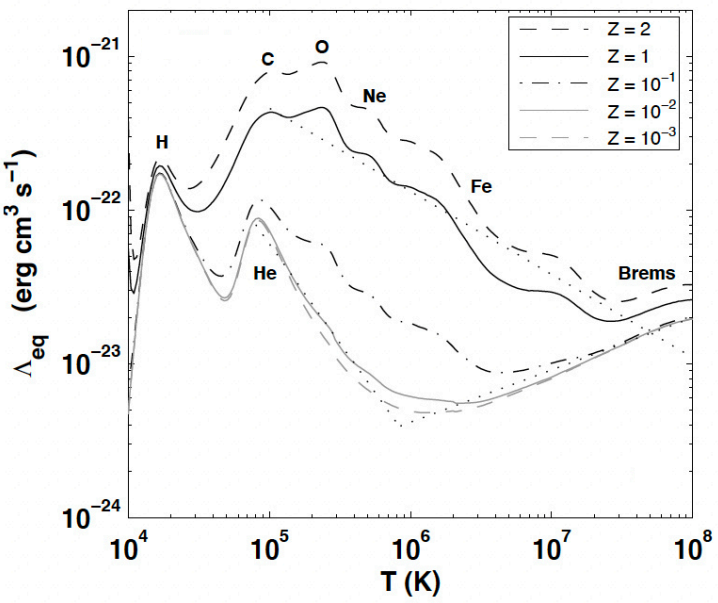

Figure 1.6: *Cooling functions at different gas metallicities Z as a function of temperature. Collisional ionisation equilibrium (CIE) is assumed, which means that gas is considered to keep the same ionisation state thanks to a balance between collisional ionisations and recombinations. Hydrogen and helium atomic cooling is important for gas at $T \simeq 10^4$ K, and dominates the cooling of gas at low metallicity ($Z \leq 10^{-2}$). For gas with $10^5 \lesssim T \lesssim 10^7$ K, metal species become more efficient at cooling the gas, with carbon then oxygen then neon kicking in with increasing temperature. For gas hotter than 10^7 K, bremsstrahlung emission becomes the dominant cooling process. Compton cooling, which depends on redshift, is not shown. Credit: reproduced from Gnat & Sternberg (2007).*

Star formation in galaxies

Stars form in giant molecular clouds (GMC), in particular if gas cooling is efficient enough to dominate over heating processes (for instance photoionisation heating). Inside a GMC, dense cloud cores collapse and fragment, until they reach the density required to initiate nuclear fusion. To first order, we can consider a spherical cloud of gas of radius R and density ρ, which starts to collapse under its own gravity. In the absence of any additional pressure forces, gas collapses at a free-fall time $t_{\rm ff}$:

$$t_{\rm ff} = \left(\frac{3\pi}{32G\rho}\right)^{1/2} \tag{1.7}$$

Inside the cloud, gas exerts a pressure to balance the gravitational collapse, sending sound waves at the characteristic sound speed $c_{\rm s}$:

$$c_{\rm s} = \left(\frac{\gamma k_{\rm B} T}{\mu m_{\rm p}}\right)^{1/2}, \tag{1.8}$$

where γ is the adiabatic index, whose value is 5/3 for a non relativistic, ideal and monoatomic gas. The typical time for the sound waves to travel through the cloud and restore the pressure balance is $t_{\rm s} = R/c_{\rm s}$, also referred to as the sound crossing

time. As soon as $t_{\rm ff}$ becomes shorter than $t_{\rm s}$, the gas cloud cannot stay in equilibrium anymore and thereafter continues its collapse (e.g. Larson, 2005). The turnover length at which such a transition occurs is the Jeans length $R_{\rm J}$:

$$R_{\rm J} = c_{\rm s} \times \sqrt{\frac{3\pi}{32G\rho}} \tag{1.9}$$

Similarly, one can define the mass enclosed in a sphere of radius $R_{\rm J}$, the Jeans mass $M_{\rm J}$, derived by equating the internal gas pressure to the gravitational force per unit area to estimate the maximum mass before a cloud of gas begins to collapse:

$$M_{\rm J} = \frac{4}{3}\pi R_{\rm J}^3 \rho \propto \frac{c_{\rm s}^3}{\sqrt{G^3\rho}}, \tag{1.10}$$

Unlike this very idealised example, there is not only gravity acting in molecular clouds. Gravitational instabilities, turbulence, rotation and magnetic fields compete together to determine the spatial and mass distribution of stars that will form out of smaller fragmenting and collapsing clumps. One can estimate the number of stars that will form as a function of the amount of gas available, the time necessary to form these stars and the rate of conversion of gas to stars. This information is combined in the star formation rate (SFR), which can be expressed as the conversion of a certain mass of gas $M_{\rm g}$ at a certain efficiency ϵ_* over a free-fall time $t_{\rm ff}$:

$$\mathrm{SFR} = \frac{dM_*}{dt} = \frac{\epsilon_* M_{\rm g}}{t_{\rm ff}} \tag{1.11}$$

Because stars form in dense cloud of gas, it is possible to construct an empirical relation between the rate of star formation per unit surface area $\Sigma_{\rm SFR}$, and the surface density of gas $\Sigma_{\rm gas}$, as expressed by the Kennicutt-Schmidt relation:

$$\Sigma_{\rm SFR} \propto \Sigma_{\rm gas}^n, \tag{1.12}$$

where n is approximately equal to 1.4 (Schmidt, 1959; Kennicutt, 1998). We additionally know that star formation occurs in the presence of molecular gas thanks to local observations of CO emission[7], so that the star formation rate is actually proportional to the density of molecular hydrogen (e.g. Kennicutt & Evans, 2012).

Eventually, it was found that the distribution of stellar masses is rather universal, and can be described by mathematical functions that define a stellar Initial Mass Function (IMF). The first determination of such a relation goes back to 1955, when the mass distribution of stars was described as $\Phi\ (m) \propto m^{-2.35}$ by Salpeter (1955), where $m > 0.4$ M$_\odot$ represents the mass of a star. According to this relation, derived from observations of stars in the Solar neighbourhood, a galaxy is expected to contain increasingly more stars towards its low mass end. However, as we show in Fig. 1.7, different IMFs exist. They vary in their estimate of the proportion of stars in a given mass range through different power law indexes (Kroupa, 2001), via log-normal distributions, or even by means of an exponential profile (Chabrier, 2003).

[7]H2 molecules do not have a dipole moment, as they are composed of the same two atoms. As a consequence, molecular hydrogen can barely be traced by emission, and other molecules such as CO, which is excited by H2 collisions, have to be used as a proxy.

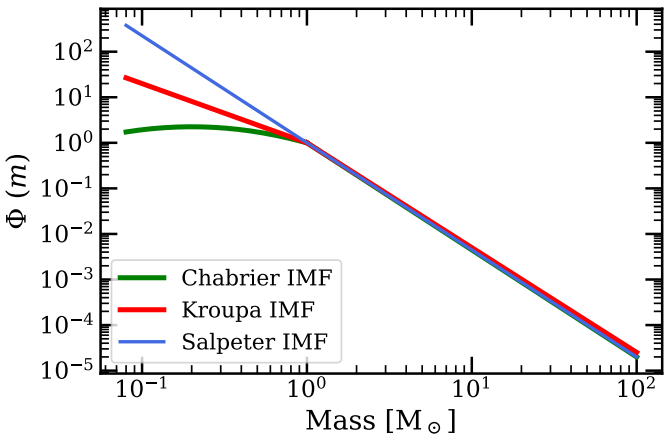

Figure 1.7: *Initial mass functions as derived by Salpeter (1955), Kroupa (2001) and Chabrier (2003). The stellar mass distribution is described piece-wise by power laws of different indexes or exponential profiles for specific intervals of masses. While the three IMFs predict a different distribution for stars less massive than* 1 $M_\odot$*, they have similar slopes towards the high mass end of their distribution.*

The properties of stars depend strongly on their initial mass, impacting in turn the photometric and chemical evolution of galaxies. While ambitious, it is crucial to determine the IMF as accurately as possible, as different IMFs can have dramatic consequences on our interpretation of observations. The initial mass and metallicity of a star define the type and the duration of the fusion processes that take place in it. Accordingly, this rules the lifetime of the star, or equivalently the time during which it belongs to the main sequence, the period during which the star consumes its material through nuclear fusion. When its internal pressure is no longer sufficient to counterbalance its gravity, the star may end up exploding as a supernova, or even collapsing into itself to form a neutron star or even a black hole, in the most extreme cases. This evolution occurs relatively quickly, leaving stars not more than a few tens of Myr on the main sequence branch. If stars are initially less massive than ~ 8 $M_\odot$, they simply end as white dwarfs, and progressively stop to emit light. As a consequence, the initial mass and the evolution of stars are tightly connected to the radiation they emit. Based on their spectral properties, stars can be classified by analysing their electromagnetic radiation, according to the MKK system (Morgan et al., 1943). Depending on their temperature, they are attributed a letter from the sequence "O, B, A, F, G, K, M" and a number, where letter "O" and number "0" correspond to hottest stars and "M" and "9" to the coldest. Finally, Roman numbers give additional information about a star's luminosity (for example, the Sun is classified as G2V). Stars with similar properties form a stellar population, and one can build empirical frameworks for stellar evolution by combining theoretical models to observations of stars whose age and metallicity are known. Combining such models together with an IMF can constrain the spectral evolution of a stellar population and lead to stellar population synthesis models. The latter consist of libraries of Spectral Energy Distributions (SEDs), that provide information about stellar luminosities of different wavelengths depending on the age and metallicity of the stellar population (Bruzual & Charlot, 2003; Maraston, 2005, among others). Thanks to the radiation they emit throughout their lifetime, stars thereby provide

our best tool to probe the visible part of galaxies, and play a major role in our understanding of their evolution.

Galaxy properties and evolution

Galaxies are the building blocks of the Universe. In order to infer their physical properties, observational studies of galaxies rely on the radiation they emit, mainly originating from their stellar component, and from the absorption of dust and gas. The spectrum of a galaxy consists of the complex convolution of its star formation history, IMF, light transmission, and dust extinction. Then, with the help of stellar population synthesis models (as previously described) examining the SED of a galaxy can teach us about some of its properties, such as its SFR.

For instance, massive stars ($M_* > 5\ M_\odot$) contribute the most to the UV luminosity of a galaxy, and have a lifetime very short compared to the age of a galaxy. Therefore, combining a spectral synthesis model with an IMF allows one to trace back the number of massive stars over relatively short timescales (of ~ 100 Myr), and hence to diagnose the star formation. The accuracy of the SFR estimate is sensitive to the details of the modelling, and in particular to the IMF. Indeed, as visible in Fig. 1.7, low mass stars likely dominate the total stellar mass of a galaxy. A realistic IMF is thus required to correctly attribute the UV luminosity measured to the fraction of high mass stars, without contaminating the SFR calculation from the UV radiation emitted by older low mass stars. In a similar way, it is also possible to use the nebular emission lines, that originate from the ionisation of the ISM by the UV continuum radiation that the young and massive stars emit. The recombination of the ionised gas produces in particular hydrogen emission lines, that can be used to probe the SFR as they are proportional to the flux of LyC photons produced. One example is the $H\alpha$ line, which comes from the recombination of an electron from the third to the second excited levels, emitting a photon at around $\lambda = 6563\ \mathring{A}$. Because part of the UV radiation from star-forming regions is absorbed by dust and re-emitted in the IR wavelengths, in a process termed dust extinction, it is also possible to infer the SFR via far IR luminosity (at $\lambda \simeq 8 - 1000\ \mu$m). Whether it be through UV or IR luminosity measurements, a consistent picture of the history of the Universe has emerged, where the peak era of cosmic star formation occurred some 3.5 Gyr after the Big Bang, around $z = 2$. At this epoch, called cosmic noon, the Universe was more active, with SFR approximately 9 times higher than measured today (Madau & Dickinson, 2014).

Not only is star formation a process varying with time but also with space. Stars can be distributed drastically differently from one galaxy to another, which impacts their visual appearance. When stars mainly rotate along with the galactic gas, they predominantly follow spiral structures in disc galaxies (e.g. Kormendy & Kennicutt, 2004). On the other hand, when the star distribution is smooth and dominated by random motions rather than the bulk rotation, galaxies appear elliptical (e.g. Binney, 1978). Initially, this led to a classification of galaxies by Hubble (Hubble, 1926), which is known as the Hubble tuning fork. This scheme distinguishes elliptical from spiral galaxies, with parameters quantifying the strength of the structures, and reports the presence of other patterns such as a bar or bulge within galaxies. This is an idealised classification model, neglecting more peculiar irregular galaxies which exist, especially at high redshift where galaxy morphology rarely resembles that of

older galaxies which had more time to acquire their shapes (Abraham, 1999). We illustrate the variety of galaxy morphologies with a selected sample of objects in Fig. 1.8.

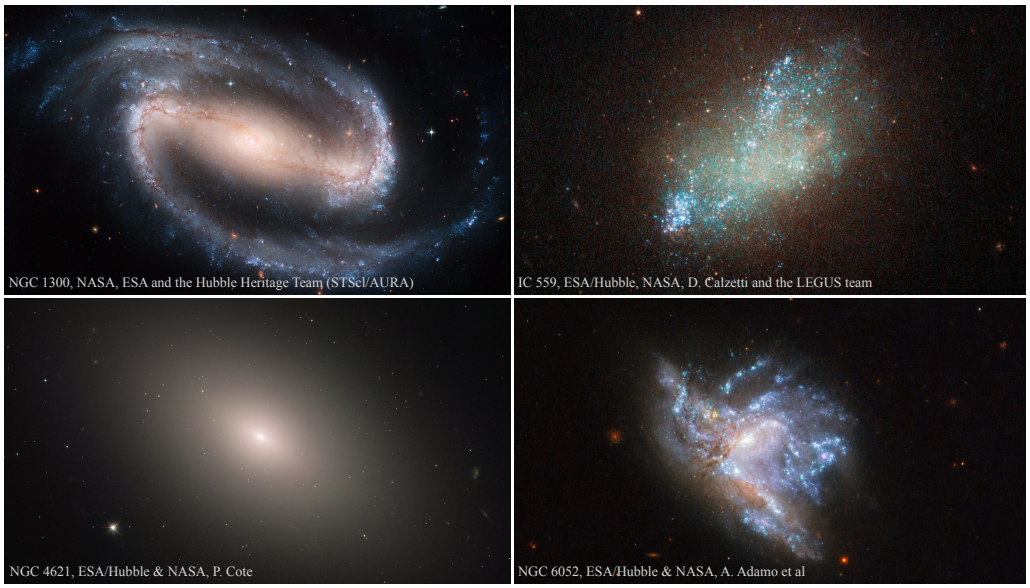

Figure 1.8: *Observations of different types of galaxies with HST. From top left to bottom right: barred spiral, irregular, elliptical and pair of colliding galaxies. Credit: ESA/Hubble & NASA (National Aeronautics and Space Administration), see each panel.*

Galaxies all have a different reservoir of gas, and obviously do not form stars at the same rate nor at the same moment. This simple fact creates several distinctions between the various galaxies observed. When a galaxy's UV luminosity is particularly strong, this is associated with a peak of star formation: the galaxy undergoes a starburst event. Conversely, a galaxy in which star formation progressively stops looks redder, and is hence categorised as being in the red or passive sequence. If no or little star formation occurs, the galaxy is quenched. Galaxies that lie in between, with a moderate UV luminosity, are said to belong to the green valley (Martin et al., 2007).

In addition, both the stellar content and the shape of a galaxy can be highly impacted by its cosmic environment. Galaxies in clusters frequently interact with each other, through collisions and mergers, and are all subject to mass loss and accretion. All of these processes cause galaxies to change their morphology and their gas content (Cooper et al., 2015; Rodriguez-Gomez et al., 2016). After successive episodes of mergers and accretion, a large amount of gas can accumulate in a small volume, and galaxies can undergo bursts of star formation. Conversely, galaxies can also become totally quenched if cut off from their fuelling material. Thus the stellar content of a galaxy can originate from the galaxy itself (in-situ formation), or from other structures that have merged during the galaxy history (ex-situ formation).

For all of these reasons, galaxy properties such as luminosity, size and stellar mass are subject to changes and evolution with time. Thanks to observational surveys, which provide a large sample of different galaxies at different epochs, it is possible to estimate the expected time evolution of such properties. Observations also reveal that some galaxy properties scale with others. This is the case of the galaxy lumi-

nosity, which scales with the SFR and the galaxy size (Kawamata et al., 2018), and the SFR density, which scales with the gas density following the Kennicutt-Scmhidt relation (Schmidt, 1959; Kennicutt, 1998). We already mentioned the galaxy luminosity function, which describes the number density of galaxies per luminosity bin. In a similar way, it is possible to build the galaxy mass function, depicting the number density of galaxies per stellar mass bin. Both the luminosity and galaxy mass functions are useful to constrain the galaxy population in the Universe.

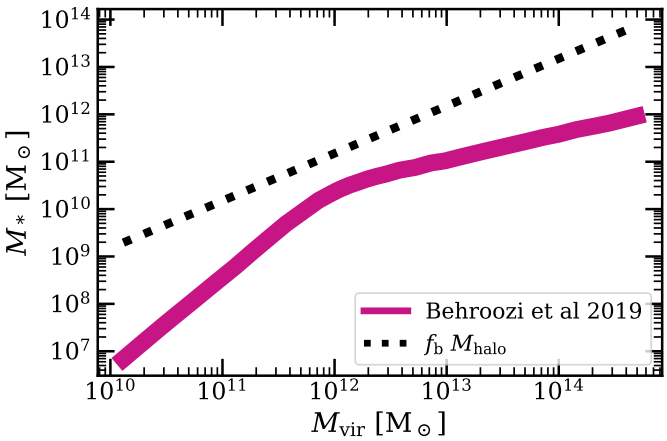

Figure 1.9: *Stellar mass to halo mass relation. The pink line corresponds to the best fit from observations at $z = 0.1$. The dotted black line shows the expected SMHM relation, if a constant fraction of baryons $f_{\rm b} = 0.15$ was hosted in each DM halo and converted into stars. While stellar masses come from measurements, the associated halo masses come from theory and statistical models (see the text). As the expected SMHM is well above the measurements, additional physical processes regulate star formation and galaxy growth at any halo mass. Credit: data from the UniverseMachine first data release, reproduced from Fig. 34 in Behroozi et al. (2019).*

Another example of a correlation largely used by the community is the relation between the halo mass and the stellar mass of galaxies: the stellar mass to halo mass relation (SMHM, see the example in Fig. 1.9). In order to connect galaxies with their DM halos, one possibility is to determine the DM mass via kinetic measurements, as the halo velocity dispersion can be related to its mass (in a similar way as in Equation 1.5). Another possibility is to use the halo abundance matching technique, so called because it is designed to match the number density of galaxies of a given mass (or equivalently of a given luminosity) to the abundance of DM halos predicted at a given virial mass. The method relies on the simple assumption that the most massive halos host the most massive galaxies. It is required to properly model the abundance of DM halos via their mass distribution, which is commonly done by means of N-body cosmological simulations (Kravtsov et al., 2004). Statistical models, such as the formalism of Press & Schechter (1974), also recover the abundance of halos as a function of their mass.

Scaling relations, combined with numerical experiments, are our best tools to infer the behaviour and the evolution of galaxies. Yet, the physical processes mentioned so far are not sufficient to explain a number of observations. For instance, when assuming that each DM halo hosts a constant fraction of baryons, which are

converted into stars at a certain constant efficiency, a major inconsistency appears between our naive model and observations. As shown in Fig. 1.9, the predicted stellar masses assigned at any halo mass are above the data actually measured. To explain this behaviour, we have to invoke a crucial ingredient in the evolution of galaxies: feedback mechanisms.

1.2.2 The importance of feedback

Scaling relations, built from the correlations of different galaxy properties such as halo mass, stellar mass, gas fraction and metallicity, play a fundamental role in constraining models of galaxy evolution. As implied by Fig. 1.9, star formation in galaxies is a very inefficient process. At any halo mass, less than 15% of the baryons hosted in halos are converted into stars, as the SMHM relation lies below the dotted line corresponding to an already small gas to star conversion rate. Actually, based on local Milky-Way and extra-galactic observations, the global star formation efficiency (see Equation 1.11) is likely to be around 2% only (Krumholz & Tan, 2007; Bigiel et al., 2008). This suggests that some processes must prevent baryons from forming stars. Environmental effects are among the causes that can drastically alter the evolution of galaxies. One example already mentioned is the merger of galaxies, and notably satellites. They consist of small galaxies, attracted by the gravitational potential of a more massive one, usually suffering tidal forces from the massive galaxy that sweep their gas. This process obviously disrupts the satellites, and also impacts the massive galaxy, which receives more material such as gas and stars to be mixed with its former content. Another important environmental effect depends on the gas available around a galaxy, as a drop in gas accretion prevents further star formation in a process named starvation (Larson et al., 1980). Quantifying the role of these different environmental effects, in particular during the whole history of a galaxy, can only be achieved by means of cosmological simulations (see **Chapter 2.1.1**). However, simulations teach us that environmental effects are not sufficient to explain the evolutionary stages of galaxies, and that internal mechanisms are needed to regulate galaxy growth. Interestingly, the astrophysical objects that compose galaxies such as stars and massive black holes are also the one that can regulate them, in the sense that the heating, momentum and pressure they provide may prevent, delay and even suppress star formation and black hole growth, respectively. This process consists of a loop, in which specific astrophysical objects regulate their own evolution, and it is hence referred to as a feedback loop. The effects of this feedback may originate from a pressure support, which for instance fights against the cooling of gas necessary to convert it into stars: this is a preventive feedback mode. If this pressure support is significant enough, another simple but yet efficient way to impact star formation is to remove gas from the ISM to prevent the formation of GMCs: this is an ejective mode, usually associated with galactic winds. Winds - also named outflows because they consist of gas flowing out of the galaxies - sweep gas away from the ISM, and thereby deplete the galaxies from the gas needed to form stars (e.g. Croton et al., 2006). Additionally, galactic winds appear to enrich the CGM with multi-phase gas, at different temperatures and metallicities, which modulates the metallicity within galaxies (Steidel et al., 2010; Werk et al., 2014). While the physical mechanisms that sustain galactic winds remain under

investigations, observations show that they are a common feature of local (Heckman et al., 2000; Roberts-Borsani et al., 2020) and high-redshift galaxies (Shapley et al., 2003; Davies et al., 2019). Like gas fountains, galactic winds can fall back to the galaxy at later times, and provide material to form stars again. In the end, different processes intrinsic to galaxies provide such pressure sources, allowing them to eject gas that escapes the ISM and to hence regulate the evolution of galaxies. We list below some of the most important of these mechanisms.

Radiation feedback

Radiation, whether it be emitted from stars or AGN, plays a major role in galaxy evolution. The "power" of photons, and their impact on gas, is the core of the feedback processes described below. We will further ellaborate on some of them afterwards, whether they are attributed to stellar or AGN feedback respectively. There are mainly three radiative feedback mechanisms: photoionisation heating, direct pressure from ionising photons, and indirect pressure from multi-scattering IR photons.

- The photoionisation process is the equivalent of collisional ionisation, depicted in Fig. 1.5. By receiving the energy of an incoming photon in the first case, or a particle in the second, an electron unbinds from its atom. Until it gets back the electron, the atom is not neutral anymore: it is an ion, hence the name of the process. Photoionisation heating is dominant when gas is neutral, with $T \lesssim 10^4$ K. At this temperature, collisions are too weak to produce ionisation or even excitation, so the cooling through collisions is essentially zero, and photoionisation dominates. One can argue: how is it that collisional ionisation cools the gas and yet we invoke photoionisation as a heating process? In the first case, a particle, which is likely an electron, collides with an atom and pulls one of its electrons off. Even if the electron removed directly recombines with the atom, the one responsible for the collision loses energy, which is not recovered. In the case of photoionisation, it is not a baryon but a photon which is involved in tearing off an electron (also termed photoelectron in this case). When the photoelectron loses its binding energy during the process, which is transmitted to the gas, it heats it.

- Photons have a specific frequency ν, or equivalently a specific wavelength λ, with associated energy $E_\gamma = h\nu = hc/\lambda$, where h is the Planck constant. Then, the momentum of a photon is $p_\gamma = E_\gamma/c$, and is especially higher for energetic photons, such as ionising UV. Here comes another source of feedback from radiation: the ionising radiation pressure, which consists of the transfer of the momentum of all the ionising photons to the particles of gas. Thanks to the interactions with gas, radiation pressure may contribute to drive galactic winds if the momentum input is significant enough (Murray et al., 2010).

- In a similar way as for ionising photons, indirect pressure may also provide a source of feedback. Indirect radiation pressure is the consequence of light acting on dust, itself imparting momentum to gas. While this process can in principle be attributed to photons from the whole electromagnetic spectrum,

it is more likely to be important when being the result of IR photons (Thompson et al., 2015). IR photons are mainly re-emitted and scattered photons originating from the absorption of UV photons by dust grains. The efficiency of indirect radiative pressure via dust from IR photons depends on the optical depth of the medium, which sets the details of the multiple scatterings that the reprocessed IR photons endure.

Another aspect, which relies on photoionisation heating, is the radiative feedback provided by the UV background, that contributes to the Reionisation of the Universe. UV background photons come from stars and AGN, and can heat the IGM to temperature of a few 10^4K. Therefore, they heat the medium in which a halo can form, exerting a radiative pressure force that can oppose the growth of a galaxy, and prevent gas accretion from cosmic filaments that provide the material to form stars (Benson et al., 2002). In particular, the growth of low-mass galaxies ($M_{\rm vir} < 10^8$ M$_\odot$) during the EoR is thought to be impacted by UV background radiation (Dawoodbhoy et al., 2018; Katz et al., 2021). There is an intricate relation between the growth of low-mass galaxies and reionisation, as the former are thought to be the dominant contributors to the latter. When interested in the formation of the first galaxies, a peculiar caution must be given to the feedback mechanisms that have an impact on the escape of ionising radiation, because it is an additional way to indirectly impact galaxy growth. This is an important point which motivates this thesis, as we will explain later in the chapter.

Stellar feedback

Stars, during their lifetime, provide two sources of feedback through radiation and stellar winds, that act in concert. The mechanisms associated to stellar radiation feedback are the same as described above. One of the best way to consistently study how and which radiation feedback plays a role in galaxy evolution is to perform radiation-hydrodynamics simulations, which model the emission, propagation and interaction of photon packets with gas. In a number of studies, as for instance Rosdahl et al. (2015), it appears that photoionisation heating is the dominant process through which star formation is impacted. Stars, and especially hot stars classified as "OB" in the MKK system (Morgan et al., 1943), emit ionising UV photons that theoretically create spherical regions of ionised gas around them, also called HII regions or Strömgren spheres (Strömgren, 1939). The cloud of gas, inside the HII region, is heated from a few tens to 10^4 K. Therefore, it is thought that the local UV radiation can lead to a suppression of star formation. A similar consequence from radiative pressure, direct or indirect, remains however more controversial, and some studies find it to have negligible effects on galaxy evolution (Rosdahl et al., 2015).

Another way for stars to impact their surrounding medium is by the launching of radiation-driven stellar winds (Puls et al., 1996; Kudritzki & Puls, 2000), especially from massive OB stars. Stellar winds can be defined as approximately spherical outflows, emitted close to the surface of a star that belongs to the main sequence. They consist of thin gaseous envelopes surrounding their star and inject mass, momentum and energy that affect the GMC and can theoretically prevent star formation. Historically, the interaction of spherical winds from "O" stars with gas clouds was studied by Weaver et al. (1977). When the winds collide with cold and

dense ambient gas, from the HII region or the molecular gas, their kinetic energy quickly thermalises[8] and the hot winds cool down. If they cool slowly, the winds expand adiabatically, driven by thermal pressure. Conversely, if the cooling is fast, winds behave isothermally, driven by ram pressure[9] (Capriotti & Kozminski, 2001). In both cases, stellar winds affect stellar atmospheres and create low density bubbles around the stars, which increases the impact of the supernova (SN) explosions (the fate of the most massive stars that we describe below). Typically, stellar winds can reach a total energy between 10^{47} and 10^{51} erg, so they remain globally less energetic than SN feedback. Nevertheless, the momentum they provide is thought to contribute to reduce star formation (Dale & Bonnell, 2008), even if the effects of stellar winds and radiation remain uncertain (Dale et al., 2013, 2014). Observationnally, stellar winds can be diagnosed through emission or absorption lines, that arise from the interactions between the winds and the surrounding gas.

Supernova feedback

Stars, and more specifically the most massive ones, are probably more efficient at impacting galaxy growth when they explode as supernovae (SN). This explosion occurs at the end of the lifetime of some stars, and blows huge quantities of gas through the ISM. These very disruptive events are thought to impact the growth of low-mass galaxies with $M_{\rm vir} \lesssim 10^{12}$ M$_\odot$, also named dwarf galaxies. Indeed, because they have a weak gravitational potential, they are more sensitive to gas removal than more massive galaxies that can more easily counteract large-scales ejection of gas. First pointed out by Dekel & Silk (1986), SN feedback is even thought to be the dominant source of feedback in dwarf galaxies, and we will explain how this works.

Two main kinds of SNe exist, and have different progenitors (Branch et al., 1991). They are named Type I and Type II SN, and the latter can be distinguished from the former by the presence of hydrogen lines in its spectra. Type I SNe are separated into three sub-classes: Type Ia has significant Si^+ absorption in its spectrum in contrast to Type Ib and Type Ic, this last one containing particularly poor traces of helium. Regardless of their spectra, the supernova explosions can be categorised as "thermonuclear" (Type Ia only) or "core collapse" (mainly Type II SN). Type Ia supernovae occur for stars with an initial mass $\lesssim 8$ M$_\odot$. After hundreds of Myr of evolution, the progenitor star evolves into a white dwarf, mainly composed of carbon and oxygen. If the white dwarf is part of a binary system, it accretes gas from its companion when the latter becomes a giant star. If the mass of the progenitor star becomes higher than the Chandrasekhar mass of ~ 1.4 M$_\odot$, the limit beyond which a white dwarf becomes unstable to its own gravity, carbon is ignited at the center of its degenerate core (Woosley, 1990). This ignition converts most of the carbon and the oxygen into heavier elements up to iron in about one second, producing a carbon deflagration resulting in the so-called Type Ia SN. This is the single degenerate scenario, first theorised by Whelan & Iben (1973). The thermonuclear explosion can also be the result of two white dwarfs merging together (Pakmor et al., 2010, 2012): this is the double degenerate scenario (Iben & Tutukov, 1984; Webbink,

[8]Thermalisation refers to the process through which a system reaches thermal equilibrium.

[9]Ram pressure is a pressure originating from the relative bulk motion of a fluid, contrary to thermal pressure caused by random thermal motion.

1984), favoured by recent observations (e.g. Sai et al., 2022).

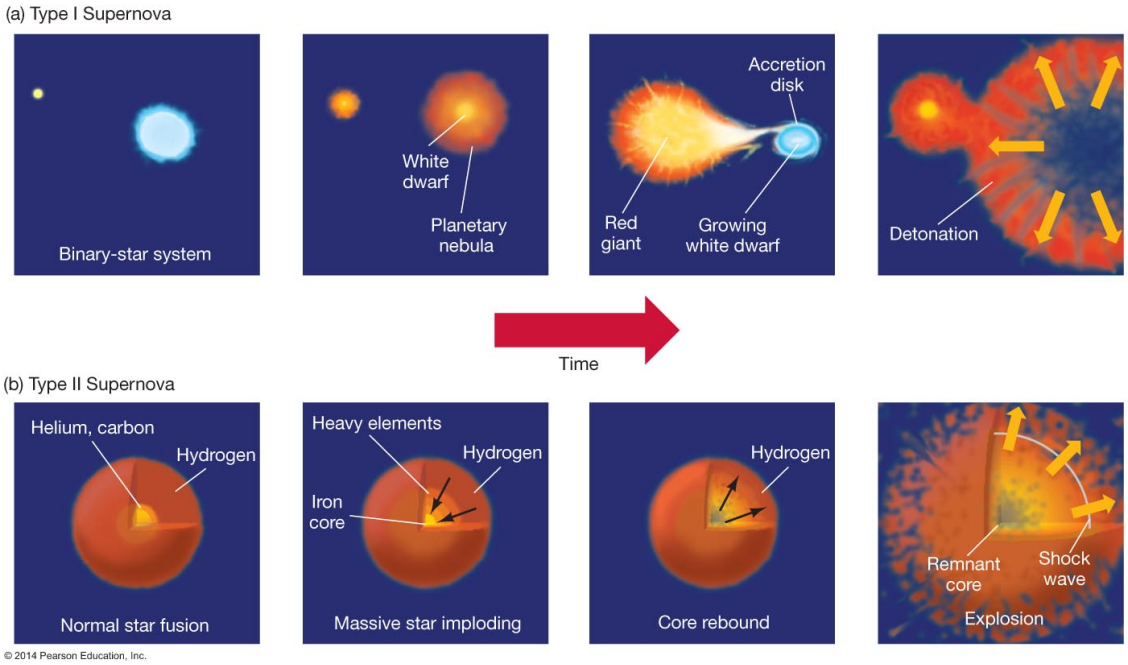

Figure 1.10: *Schematic of the evolution of Type Ia (top panels) and Type II SNe (botttom panels) with time from left to right. In the case of Type Ia SNe, a white dwarf accretes material from a companion star, such as a red giant. When the mass of the star eventually exceeds the Chandrasekhar limit, it ignites carbon on very short timescales, producing the detonation at the origin of the SN (this is the single degenerate scenario, see the text for the case of double degenerate progenitor systems). In contrast, a Type II SN originates from a star that has fused all its gas until its core is made of iron. When the internal pressure of the star becomes insufficient to counteract its gravity, it collapses into itself, leading to a shock wave that expands and blows the star's external layers into a SN remnant. Credit: Pearson Education Inc, image reproduced from the lecture notes developed for Astronomy 122 by Professor James Brau.*

Conversely, Type II SNe presumably originate from stars initially more massive than 8 $M_\odot$, and occur relatively shortly after the birth of these stars which have only a few Myr to live before they explode (as shown for the first time by Baade & Zwicky, 1934). These stars are massive enough to have the pressure and temperature conditions necessary for fusion to occur for all elements lighter than iron[10]. When the stellar core made of iron becomes massive enough, it collapses as a consequence of its own weight. Right after this event, the external layers of the star's atmosphere also collapse down to the core, which is now made of neutrons, and bounce. The core collapse explosion thus consists in the last evolutionary stage of the star, and ejects matter at a velocity so fast that a shock forms. Before fading away, the SN blast expands and sweeps up material that interacts with the ISM: this is called the SN remnant (SNR) (Chevalier, 1977). We illustrate the evolution of Type Ia and Type II SN in Fig. 1.10.

[10]More energy is needed to ignite iron than the reaction would release, so iron is the last element that can result from fusion.

After a supernova explosion, the evolutionary stages of a SNR can be described by four phases, that highly contribute to regulating galaxy growth. We examine them below and in Fig. 1.11.

- During the first few hundreds of years after the explosion (for a typical ISM density of $1\,\mathrm{H\,cm^{-3}}$), the mass of ISM swept up by the shock is much lower than the ejecta. Because the pressure of the ISM is therefore lower than the pressure of the expanding ejecta, this first phase is called a free phase of expansion. During this period of time, the velocity of the blast wave is roughly constant, and its size evolves linearly with time. The ISM gas swept up and shocked by the expanding SNR accumulates behind the blast wave, separated from it by a contact discontinuity. When the mass of yet non shocked ISM gas becomes higher than the swept component, the SNR slows down, initiating a backward blast wave which heats the ejecta on its way (McKee, 1974). The dynamics of the SNR then changes and starts its second phase of evolution.

- The second phase of the SNR consists of an adiabatic expansion, during which gas cools only due to its expansion. Radiative losses are negligible, and the total energy remains constant. This stage is usually termed the Sedov-Taylor phase, because the evolution of the SNR corresponds to the solution of a spherically symmetric explosion in a uniform medium, as described by Sedov (1959) and Taylor (1950). For a typical ISM density of $1\,\mathrm{H\,cm^{-3}}$, this phase lasts a couple of tens of Myr, during which the velocity of the blast wave drastically decreases while its size grows as $t^{2/5}$, t being time since the explosion.

- When the radiative losses inside the blast wave become significant, the SNR starts its third stage of evolution: the radiative phase (Woltjer, 1972). A dense shell of gas encloses a volume of hot gas where radiative losses remain negligible. However, in the dense shell, emission lines cool the gas whose temperature drops sharply. Once the temperature of the shocked material is $< 10^5$ K, the radiative losses become important because the cooling time becomes shorter than the dynamical time.

- Right after this phase of radiative losses, the energy of the SNR is not constant anymore, Conversely, the momentum of the blast wave is conserved, and the expansion is momentum-driven. The ambient medium swept progressively increases the mass of the dense shell in a "snowplough" process, so that the phase is also called the momentum-driven snowplough phase (while the previous stage of the SNR is also termed the adiabatic pressure-driven snowplough phase). The velocity of the shock continues to gradually decrease, during a period that typically lasts ~ 50 Myr.

- Finally, once the internal pressure of the SNR is comparable to that of the ambient medium, the SNR merges with the ISM: this is the merging phase. Now, the shock speed is approximately the same as the sound speed, and the shock slowly disappears. While this stage marks the end of the SNR, the hot plasma left behind still remains, and emits X-rays whose observation gives information about the shocked ISM.

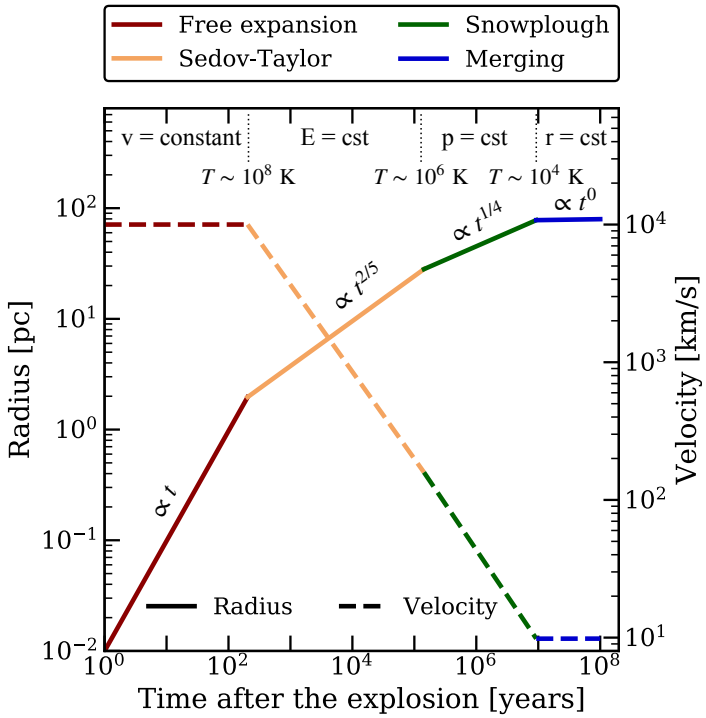

Figure 1.11: *Time evolution of the remnant from a SN explosion. The left axis is associated to solid lines corresponding to the radius of the SNR, while the right axis represents the velocity of the blast wave shown in dashed lines. The size of the SNR increases with time while the blast wave velocity decreases, at a rate depending on the phase of the SNR. The density of the ISM around the SN is assumed to be constant with* $\rho_{\rm ISM} \simeq 10^{-24}$ g cm^{-3}. *Credit: image adapted from Micelotta et al. (2018).*

Through its different phases of evolution, the SNR injects energy, mass and momentum into the ISM, and therefore provides both ejective and preventive modes of feedback. This is responsible for altering the physical properties of the galaxy, on different scales. At galactic scales, the SNR drives significant winds, which can delay the gas to star conversion (Bigiel et al., 2008). At ISM scales, molecular gas undergoes the shock compression from the expanding SNR, which can alter the gas dynamics by increasing its local density and turbulence. Modelling the different phases of the SNR, and most particularly the Sedov-Taylor phase, is thus crucial to correctly investigate the effect of SN momentum injection. In any case, SN events of all kinds release an energy $E_{\rm SN} \simeq 10^{51}$ erg, theoretically sufficient to heat and blow away consequent amounts of gas from a galaxy. In particular, the SNe help to distribute metals throughout the galaxy, impacting its chemical evolution. This has important consequences, notably for gas cooling, as shown in Fig. 1.6. Metals are the most efficient coolants beyond a few 10^4 K, so mixing metals in the ISM or removing them through SN-driven outflows may have drastic effects on star formation. Both types of SN (differently) contribute to enrich galaxies with heavy elements, but Type II SNe represent between 70 and 90% of the SN explosions (Tsujimoto et al., 1995). Therefore, core collapse SNe are more frequent, and have faster and more direct effect on their host galaxies than Type I SNe that occur on much longer timescales. For this reason, we exclusively focus on Type II SNe in the following.

AGN feedback

While supernova feedback is invoked to regulate star formation in low-mass galaxies ($M_{\rm vir} < 10^{12}$ M$_\odot$), a more energetic feedback is needed to produce a similar effect in massive halos, and is provided by active galactic nuclei (Silk & Rees, 1998; King & Pounds, 2015). AGN are supermassive black holes located at the centers of galaxies, which grow by accreting the surrounding matter thanks to their deep potential wells. This process releases large amounts of energy, which is the reason why AGN are bright.

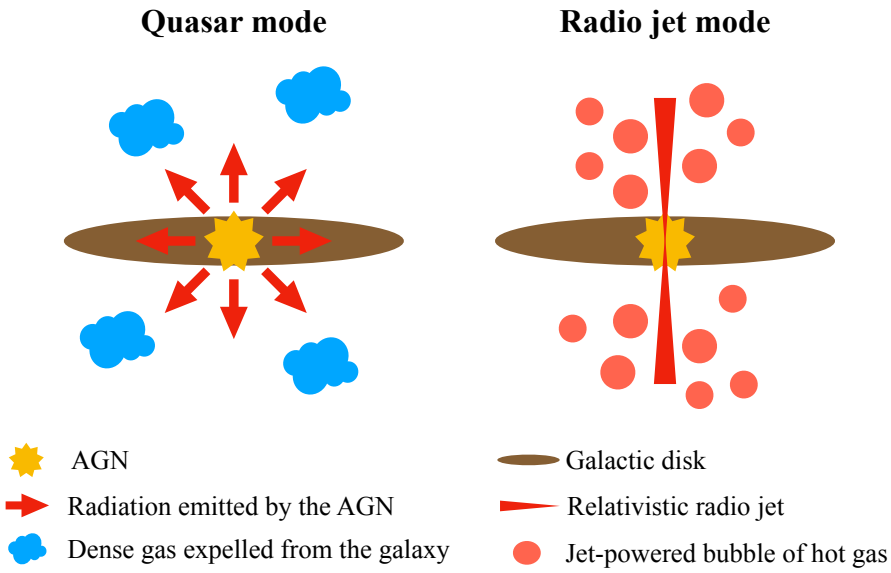

Figure 1.12: *Schematic of the AGN feedback quasar and radio jet modes, which dominate in the high and low accretion rate regimes of the black hole respectively. The quasar mode occurs when AGN radiate efficiently, and the radiation heats the gas through photoionisation and ejects outflows via radiative pressure. The radio jet mode involves the injection of kinetic energy powering radio jets, themselves inflating hot bubbles of gas. Maintaining and heating these bubbles outside of the galaxy prevents gas from cooling and collapsing.*

The feedback provided by AGN comes from the interaction between the galactic gas and the radiation (and energy) generated by the accretion process. AGN feedback consequently depends on mass accretion, which is associated to two different modes having distinct effects illustrated in Fig. 1.12.

- When the mass accretion rate is close to the Eddington limit, AGN radiate energy efficiently. In this case, the main way through which an AGN interacts with its surrounding is through direct radiation, also known as the quasar mode (Gabor & Bournaud, 2014). In the first instance, AGN generate high energy UV and X-ray photons, that can ionise and heat the gas through photoionisation. Additionally, if the gas is ionised but remains colder than the average temperature of the radiation field, Compton scattering delivers a part of the photon energy to the gas, thereby also heating it (Ciotti & Ostriker, 2001). In both cases, this heating fights against the gas cooling necessary to form stars. Moreover, photons exert radiative pressure, which transfers momentum to the gas. If radiation pressure overcomes the gravitational pull of

the galaxy, gas even flows out of the galaxy (Murray et al., 2005), forming momentum driven outflows that deplete the galaxy from a part of its material. For this reason, the quasar mode is classified into the category of ejective feedback.

- When the mass accretion rate of the supermassive black hole becomes low, mechanical feedback becomes more efficient than the radiative quasar mode. This second regime of accretion cooresponds to the emission of radio jets and lobes: this is hence the radio jet mode. Among the gas flows that the accretion luminosity can drive, jets originate from gas collisions and take the form of collimated flows in the close vicinity of the AGN, potentially changing their direction over time (Fabian, 2012). These jets are believed to inflate X-ray cavities filled with relativistic gas, bubbles of hot gas powered by the kinetic energy injected. Being hot and at low density, these jet-powered bubbles barely suffer from radiative losses, and can expand supersonically. Therefore, gas is heated and prevented from cooling: the radio jet mode is thus a preventive feedback mechanism which maintains gas in the CGM (Zinger et al., 2020).

To summarise, from a theoretical point of view, AGN can induce both a negative and a positive feedback, mainly through the launching of energetic outflowing gas (Zinger et al., 2020). AGN driven winds can suppress star formation, by removing fuelling material from the ISM and preventing gas clumps from cooling and collapsing (Costa et al., 2018), but can also favour gas compression and lead to local star formation events (Mukherjee et al., 2018). Furthermore, winds driven on large scales can affect the properties of gas not only in the ISM but also beyond, in the CGM (Cicone et al., 2015). These outflows may be driven by radiation pressure or radio jets. However, from the observational side, it is not straightforward to distinguish the impact of the AGN on their host galaxy and on star formation from other physical processes. Nevertheless, some observational signatures confirm some of the aspects just depicted, such as massive ($M_{\rm out} > 10^8$ $\rm M_\odot$) fast ($v_{\rm out} > 1000$ km/s) winds (Venturi et al., 2021), probably ejected from the cold ISM, and hot bubbles of gas, generated by the radio jets heating the hot gaseous halo (see Fabian, 2012, for a recent review). We show in Fig. 1.13 an example of this signature with AGN driven radio jets.

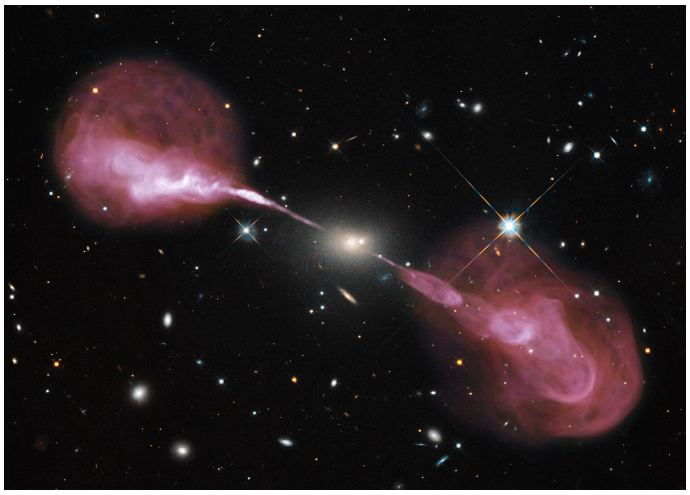

Figure 1.13: *Optical-radio composite image of the elliptical galaxy Hercules A (in yellow colours) hosting a supermassive black hole in its center. The AGN power 460 kpc wide radio jets (in pink-red colours), emerging from the central galaxy. Credit: NASA, ESA, S. Baum and C. O'Dea (RIT), R. Perley and W. Cotton (NRAO/AUI/NSF), and the Hubble Heritage Team (STScI/AURA).*

In the end, AGN feedback is thought to be able to delay star formation, and even may be responsible for quenching the host galaxy (e.g. Dubois et al., 2016). However, AGN are also thought to have a negligible contribution in low mass galaxies, even if this remains highly debated (Dashyan et al., 2018). One reason is that SN feedback is already so efficient at emptying the galaxy from its fuelling material that it prevents BHs from growing, and therefore prevents AGN feedback from having any significant and additional effect on star formation and galaxy evolution. Because AGN are generally thought to have a negligible impact both on reionisation and on the evolution of low-mass galaxies, dominant during the EoR, AGN feedback is not studied in this thesis.

Caveats and remaining challenges

Flows of baryons within galaxies influence their evolution, and are regulated by stellar[11] and AGN activity for dwarf and massive galaxies respectively (e.g. Somerville & Davé, 2015; Naab & Ostriker, 2017, for reviews). These two dominant sources of feedback play a major role in driving star formation, galactic winds, and setting galaxy properties such as gas temperature and metallicity within their ISM and CGM. Thanks to numerical simulations of galaxy evolution, we know that they are mandatory ingredients, without which galaxy masses are over-predicted (Hopkins et al., 2012b). Yet, it is a major theoretical challenge to understand and correctly model the details involved in stellar and AGN feedback. Initially, and even if it is still the case nowadays to a lesser extent, galaxy simulations had very coarse resolution. Their inability to capture the smallest scales of the ISM, whether it be the regions around AGN or the different phases of SN remnants, leads to a quick dissipation of the energy injected by SNe and AGN (e.g. Cen & Ostriker, 1992; Katz, 1992). In

[11] We mainly refer to supernova feedback here. As SN explosions are the last evolutionary stage of massive stars, SN feedback can also be denoted as a type of stellar feedback.

the case of SN feedback for instance, simulations must reach resolutions down to ~ 20 pc (Kim & Ostriker, 2015), the size of the shell during the Sedov-Taylor phase of the SNR. This is the necessary condition to capture the processes that happen during this stage of the SNR, and to avoid the significant radiative losses that dissipate the thermal energy injected by the SN explosion and that occur during its next phase. This numerical issue is also known as the overcooling problem (Katz et al., 1996). One solution is to implement feedback models via sub-grid prescriptions, so-called because they mimic the behaviour of gas below the scales resolved by a simulation. However, the new generation of simulations that make use of such sub-grid feedback models reveal that stellar feedback alone is likely to be insufficient to produce realistic galaxies, and that additional ISM physics play a role (Hopkins et al., 2014; Emerick et al., 2018; Kannan et al., 2019; Smith et al., 2019b). Despite the recent progress and increased capabilities in computer performances, the nature and the details of such physics remain however highly debated. In order to reach agreement with observations, feedback models are usually calibrated following empirical relations, sometimes in an artificial fashion. Some methods consist of manually disabling radiative cooling for a certain time (delayed cooling model, Stinson et al., 2006; Teyssier et al., 2013), or of injecting it stochastically around a SN (Dalla Vecchia & Schaye, 2012), among others (see Chaikin et al., 2022 who summarise how SN feedback can be modelled in their introduction). Another simple way to proceed is to allow more SN explosions to happen, by boosting the number of such events (Rosdahl et al., 2018; Semenov et al., 2018). Now that simulations can afford higher resolutions, efforts aim at probing the underlying physics behind galaxy evolution, and determining if they are correctly accounted for.

Overall, by means of sub-grid models which combine different feedback mechanisms, simulated galaxies finally capture the basic characteristics of their real counterparts. While simulations are usually calibrated to reproduce observed galaxy luminosity functions or the stellar mass to halo mass relation, some discrepancies survive. One such discrepancy comes from the ΛCDM paradigm, in which low-mass halos are predicted by DM only simulations (Bullock & Boylan-Kolchin, 2017) to have steep inner density profiles (a "cuspy" profile), while observations suggest the presence of low density cores instead (Moore, 1994; Walker & Peñarrubia, 2011). Again, feedback mechanisms and baryon physics are invoked to explain this so-called cusp/core problem (Flores & Primack, 1994) which could be related to the strength of feedback. However, no consensus has emerged yet, with some simulations reproducing only cuspy profiles (e.g. Vogelsberger et al., 2014) while others generate different levels of cores (e.g. Di Cintio et al., 2014). Another important discrepancy is directly related to the baryonic content of galaxies through measurements of their metallicity, leading to scaling relations such as the Mass-Metallicity Relation (MZR, because the letter Z denotes gas metallicity). Most simulations exhibit trends similar to the observed MZR relation, but with incorrect metallicities in the low-mass galaxy regime, where it is also difficult to match the stellar mass function (Torrey et al., 2014; Furlong et al., 2015; Sotillo-Ramos et al., 2021). This shows that the processes involved in the CGM enrichment are not fully understood yet. In particular, the content of the CGM is highly related to star formation and feedback processes, as its content results from species produced by stars and ejected by feedback-driven winds, and provides feeding material for galaxies to grow. How-

ever, the vast majority of galaxy simulations fail in reproducing the ionic column densities that come from emission and absorption spectroscopy measurements (Werk et al., 2016), with values that can differ from observations by orders of magnitude (Tumlinson et al., 2017).

All in all, the community is still struggling to make feedback regulate the baryon content in galaxies with realistic models. Inconsistencies with measurement data definitely points towards the fact that we are missing other fundamental ingredients. We intentionally omitted one feedback mechanism, which relies on providing an additional and non thermal pressure to the gas : feedback from cosmic rays (CRs). The study of the effects of CRs on galaxy evolution, and in particular during the EoR, is the aim of this thesis. As we explain in the next section, CRs can potentially solve a number of tensions between observations and simulations, and bring us one step forward in filling the gap in our understanding of galaxy evolution.

1.3 Cosmic rays

The first milestone in cosmic ray astrophysics is the discovery of their existence by Victor Hess, in 1912 (Hess, 1912). At this time, the presence of an electric charge in an object was measured with an electroscope, an instrument that reacts to an electric voltage. After being charged, an electroscope is naturally expected to discharge through the photo-electric effect if subject to an ionising radiation. Because electroscopes still discharged even when protected from any light, the common thought was that the ionising radiation causing this phenomenon is produced on Earth from radioactive matter, and that the discharge rate would naturally decrease with altitude. To check this theory, Hess went on board of a balloon, equipped with electroscopes, and compared their discharge rate at different distances from the ground. Contrary to what was expected, the discharge rate of the electroscopes increased with altitude: Hess' measurements revealed that some ionising radiation of extra-terrestrial origin discharged his electroscopes. The cause of these measurements was first hypothesised to be photons (Millikan, 1925), and referred to as **cosmic rays**. It took a few years until the realisation was made that the rays are actually charged particles, thanks to observations of variations in the cosmic ray flux with latitude, as a consequence of their deflection by the geomagnetic field (Clay et al., 1934). Because photons have no electric charge, cosmic rays would not have been deflected by the geomagnetic field if they were really "rays". Thenceforth, the discovery of cosmic rays opened the door for a plethora of questions, some of them still open, such as: what are they, where do they come from, how do they propagate, and what effect do they have at different scales? We review the current answers to these questions below.

1.3.1 Origin and composition

Cosmic rays are energetic charged particles that permeate the galaxy (see e.g. the review by Grenier et al., 2015). They cover a broad range of energies, from $\sim 10^6$ eV to 10^{21} eV, and span not less than 32 orders of magnitude in flux, measured both directly and indirectly from ground-based and space instruments (as explained later in the section). The CR energy spectrum, shown in Fig. 1.14, corresponds to a

power law with different slopes. The spectrum can be seen as a leg with two points of inflexion: the knee around 10^{16} eV and the ankle at 10^{18} eV. The non thermal spectral distribution peaks at energies of a few GeV, where most of the CR energy density resides. At these energies, the composition of CRs resembles that of the Universe: 90% of the hadronic component are protons, and the vast majority of the rest are helium nuclei with a small fraction of heavier nuclei (Blasi & Amato, 2012; Gaisser et al., 2013). The ratio of CR electrons to CR protons is about 1/100 (Schlickeiser, 2002), which is not due to a more efficient acceleration of CR protons, but to the fact that electrons, being much lighter, suffer from major energy losses. Energy losses are also the reason why the flux of CRs vanishes beyond energies of 10^{21} eV. The highest energy CR protons can interact with CMB radiation, which makes them lose energy. On their way to our detectors, such CRs that travel through the Universe over long distances continuously lose a part of their energy. This provides a theoretical upper limit on the energy that can be reached by CRs that originate from distant galaxies, which is also named the GZK cut-off from the name of its authors (Greisen, 1966; Zatsepin & Kuz'min, 1966). In the end, the bulk of CRs consist of particles with an energy of a few GeV, among which protons are the most abundant.

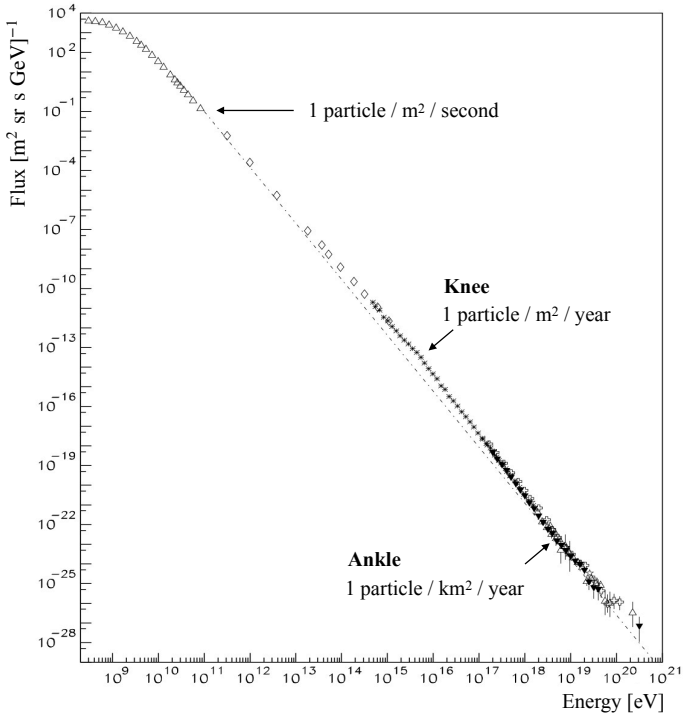

Figure 1.14: *Energy spectrum of cosmic rays, from direct and indirect measurements with ground-based and space instruments. The knee and the ankle correspond to specific energies around* 10^{16} eV *and* 10^{18} eV *at which the slopes of the spectrum change. Fewer particles are detected towards high energies. Credit: Reproduced from Swordy (2001).*

As we already mentioned, CRs are deflected by the magnetic field because of their electric charge (e.g. Zweibel, 2013). As a result, their motion is not straightforward, and it is impossible to directly trace back their origin. Nonetheless, theoretical considerations give some constraints. In a uniform magnetic field, the trajectories

of CRs respond to the Lorentz equation, according to which they gyrate around magnetic field lines. By equating the Lorentz force to the centripetal force, one can derive the radius of gyration, also called Larmor radius, which depends on the particle momentum p, its charge Ze and the strength of the magnetic field B:

$$r_{\mathrm{L}} = \frac{p}{ZeB} \tag{1.13}$$

This equation can be used to roughly determine the origin of CRs of a given energy range: this is the Hillas criterion (Hillas, 1984). For a given magnetic field strength, there is a minimum size of the accelerator site, corresponding to the Larmor radius, necessary to reach a specific energy. In our galaxy, the typical magnetic field is a couple of μG (Han & Qiao, 1994). Therefore, particles with an energy $> 10^{19}$ eV have a gyration radius of $\sim 10^4$ pc, which is roughly the radius of the Milky-Way. This means that particles with such high energies necessarily originate from other galaxies, as those produced in the Milky-Way are no longer confined there. While it is not clear if CRs with energies between the knee and the ankle are of Galactic or extra-galactic origin, the bulk of CRs measured near Earth likely comes from the Milky-Way (Blümer et al., 2009). Coming back to the CR spectrum, we note that the low-energy end ($< 10^9$ eV) does not follow a power law. This is due to Solar winds, that modulate the propagation of charged particles with energies below 10^9 eV when they enter the magnetised heliosphere, a process known as Solar modulation (Parker, 1965; Potgieter, 2013). Solar flares can also accelerate CRs (Yan et al., 2008), but mainly contribute to particles with energies ≤ 100 MeV.

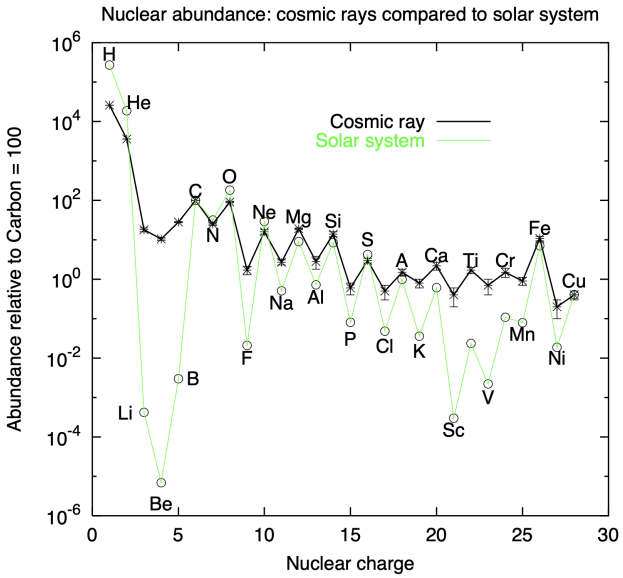

Figure 1.15: *Relative chemical abundance of Galactic CRs measured on Earth (in black) compared with Solar abundances (in green), both normalised to carbon. To get rid of any Solar modulation, the abundance of extrasolar CRs is shown at 1 TeV. Credit: Reproduced from Gaisser & Stanev (2006).*

An interesting feature arises from the comparison of Solar abundance to extrasolar CRs. As visible in Fig. 1.15, which shows the relative abundance of Galactic and Solar CRs, there is a significant excess of light elements (especially Li, Be and B) in

the flux of Galactic CRs compared with the Solar abundances. Lithium, beryllium and boron first appeared in the Universe during the primordial nucleosynthesis but are not produced by stars, which explains why they are rare in the Solar system. These light elements are actually fragmentation products, resulting from collisions between heavy CRs (in particular carbon and oxygen) and the gas they crossed all along their propagation, until they are detected. This process is known as spallation, the initial CR particles are called primary CRs, and the resulting lighter elements produced during their travel through the Galaxy are termed secondary CRs.

To recover the excess of light elements, GeV CRs have to cross a mean quantity of matter with surface density of 5 g cm^{-2} (this is known as the grammage). For an average ISM density of 10^{-24} g cm^{-3}, this means that CRs must propagate over distances of ~ 1 Mpc, which is much larger than the size of the Milky-Way, strong evidence that CRs do not travel in a straight line. For relativistic CRs (typically protons having an energy higher than $\sim 100\,\mathrm{MeV}$), the time needed to escape the Milky-Way can then be estimated to several million years (Ginzburg & Syrovatskii, 1964; Strong et al., 2007). The ratio of secondary-to-primary CRs therefore gives us important information about the residence time of CRs in galaxies, and is one of our best tools to constrain CR propagation. We come back to this aspect later.

But first, now that we have discussed the origin and composition of CRs, let us focus on the sources and processes that can accelerate and energise them. Historically, the first mechanism invoked in order to explain the acceleration of Galactic particles was proposed by Fermi (1949). He suggested that charged particles are accelerated by interacting with a moving magnetised cloud. When a charged particle encounters a cloud of ionised gas which has a stronger magnetic field than the ISM, its trajectory is altered by the Lorentz force caused by the stronger magnetic field. Once it escapes the magnetised cloud, the particle has deviated from its initial propagation direction. In the case of a relativistic CR and a cloud moving at a velocity v_{cloud}, the particle gains an energy proportional to the product of its initial energy and v_{cloud}^2/c^2. Because the energy gain varies with the velocity squared, this process is also known as second order Fermi acceleration. A number of astrophysical sources can accelerate CRs (in particular electrons) with the 2$^{\mathrm{nd}}$ order Fermi acceleration, such as black hole X-ray binary systems[12] (Zhang et al., 2018), Solar flares (Yan et al., 2008) or the ISM itself (Cho & Lazarian, 2003). While this mechanism is able to reproduce the power law of the CR spectrum, it is too inefficient to explain CR acceleration. For this purpose, faster magnetised clouds are required ($v_{\mathrm{cloud}}/c \simeq 10^{-4}$ is already very small, so squared is even worse). In addition, it is necessary for them to be closer to each other so that the acceleration of CRs does not last tens of Myr, and particles must be initially energetic enough to avoid any Coulomb losses, caused by the electric field generated by the atoms of the ISM. Absent these criteria, this process remains subdominant, and another mechanism is needed to explain the CR spectrum.

Three decades later, the diffusive shock acceleration (DSA) theory explained how shock waves may be responsible for efficient CR acceleration (Axford et al., 1977; Krymskii, 1977; Bell, 1978; Blandford & Ostriker, 1978). The DSA theory provides a modern version of the stochastic Fermi acceleration. Based on the same prin-

[12] A X-ray binary refers to a binary system of a star orbiting around a black hole or a neutron star.

ciple, charged particles interact with a magnetic field, and are especially sensitive to magnetic field inhomogeneities. The magnetic irregularities can either be of an external origin, or be generated from the oscillation of ions around the plasma magnetic field, which produces so-called Alfvén waves (Alfvén, 1942). If the magnetic perturbations are of the same order as the Larmor radius, the charged particles do not gyrate anymore. Instead, they are diffused by the magnetic irregularity with a certain pitch angle, in such a way that they go back and forth from the propagating shock wave front. Therefore, the shock waves accelerate the charged particles via successive passages, with an energy gain proportional to $v_{\rm shock}/c$, where $v_{\rm shock}$ is the shock velocity: this is why this mechanism is also termed first order Fermi acceleration. As shocks have supersonic speeds, this acceleration process is much faster than the one first proposed by Fermi, so even particles with an initially low energy gain more energy with this process than they lose through Coulomb interactions. To summarise, Fig. 1.16 proposes a schematic view of the two Fermi acceleration processes just discussed.

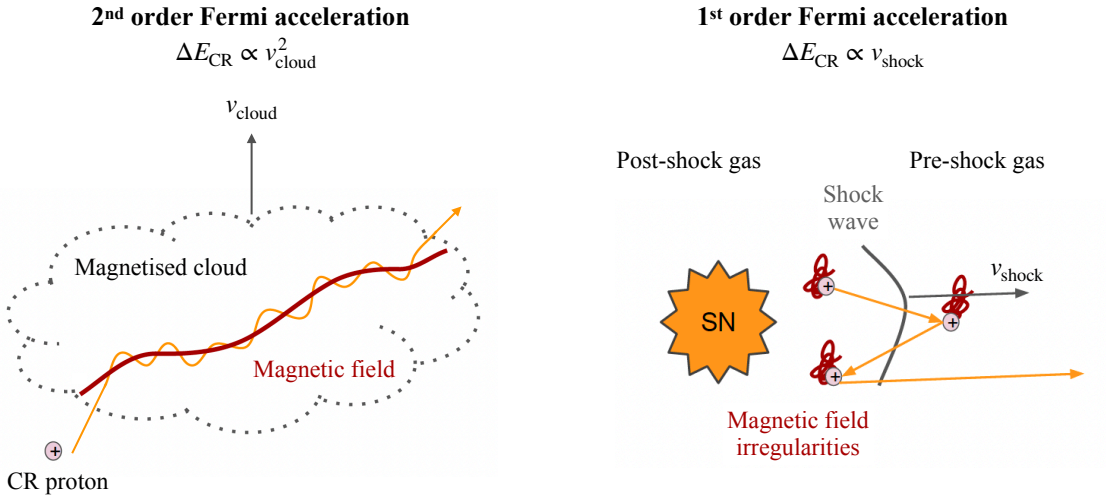

Figure 1.16: *Illustration of the second (left) and first (right) order Fermi acceleration mechanisms. We represent a CR as a positively charged particle with a pink circle, to illustrate how a charged particle is accelerated and becomes a cosmic ray. The trajectory of the CR is shown in orange, and the magnetic field is shown with red lines. The 2^{nd} order acceleration relies on a magnetised moving cloud, thanks to which CRs gain an energy proportional the square of the cloud velocity. With 1^{st} order Fermi acceleration, CRs gain energy more efficiently, in proportional to the velocity of the shock wave originating, for instance, from a supernova explosion. The charged particle repeatedly crosses the shock front, diffused by magnetic field inhomogeneities.*

Concerning the more efficient $1^{\rm st}$ order Fermi acceleration, the best candidates to accelerate CRs and in particular provide the bulk of GeV cosmic ray protons are SNRs, as first suggested by Baade & Zwicky (1934). The SNR paradigm, through which CRs are accelerated at SNR shocks, remains to date the prevailing scenario to explain the origin of Galactic CRs (Hillas, 2005; Helder et al., 2012). As stated earlier, the averaged kinetic energy released by a SN explosion is 10^{51} erg. Because aluminium is only produced by massive stars that end up exploding as SN (Diehl et al., 2006), measurements of gamma-rays produced by the decay of aluminium

atoms tell us that approximately 3 type II SNe happen per century in our galaxy (Strong et al., 2007; Morlino & Caprioli, 2012). The total power injected by SNe in the galaxy is hence $10^{42}\,\mathrm{erg\,s^{-1}}$. Furthermore, we measure a roughly constant CR energy density of 1 $\mathrm{eV\,cm^{-3}}$ (Boulares & Cox, 1990), and we know that CRs must be confined in our galaxy on timescales of ~ 10 Myr to explain observations of primary-to-secondary CR ratios. This implies that the Milky-Way is additionally subject to a CR energy injection rate of 10^{41} $\mathrm{erg\,s^{-1}}$ (e.g. Grenier et al., 2015). Therefore, the density of Galactic CRs can be explained if $\sim 10\%$ of the SN energy produced is used for CR acceleration. For this reason, the common way to model CR acceleration is via the injection of 10% of the SN energy, as done in the simulations presented in this thesis.

1.3.2 Propagation and observational signatures

Before we turn our attention to CR feedback, we examine how CRs interact with the media they come from and propagate in. Because CRs are charged particles, their propagation and interaction with the gas is mediated by the magnetic field, so that they are tightly coupled to plasma processes (e.g. Zweibel, 2013). To first order, CRs are transported along the magnetic field, and consequently follow the bulk motion of the surrounding gas to which magnetic fields are frozen (e.g. Thomas et al., 2020). Through this process, CRs are dragged with the gas flow at the gas velocity: this is called advection. Just like the thermal component, CRs can gain or lose energy from adiabatic compression or expansion respectively. The gain or loss of energy is directly linked to the adiabatic index γ following the Laplace law, according to which $PV^{\gamma} = \text{constant}$ (where P stands for pressure and V for volume). There is a significant difference between the adiabatic indices for CRs and the gas: $\gamma = 5/3$ for the ISM gas considered as monoatomic, while $\gamma = 4/3$ for relativistic species such as CRs. This means that upon adiabatic expansion, CR pressure is less diluted than thermal pressure.

Additionally, perturbations in the magnetic field cause CRs to scatter along and across magnetic field lines. This is another important process that rules their propagation, referred to as diffusion. As explained earlier, CRs themselves can be at the origin of such magnetic perturbations by resonantly exciting Alfvén waves, through a mechanism known as a streaming instability (Kulsrud & Pearce, 1969). This occurs when CRs have a velocity higher than the Alfvén velocity, defined as $v_{\mathrm{A}} = B/\sqrt{4\pi\rho}$, where B is the strength of the magnetic field, and ρ the density of the medium. The excitation of the Alfvén waves draines CR energy, so that a part of the CR energy is transferred to gas which is consequently heated (Ruszkowski et al., 2017). In addition, the self-excited Alfvén waves are subject to damping, whether it be because of the collisions between CRs and neutral particles (ion-neutral collisional damping, Armillotta et al., 2021), because of the transfer of energy between the Alfvén waves and CRs that propagate slower than the waves (non-linear Landau damping, Kulsrud, 2005) or because of background turbulence (turbulent damping, Lazarian, 2016). If the damping of the Aflvén waves is strong enough, diffusion via streaming instabilities effectively takes place. If not, CRs rather drift (stream) along the lines of magnetic field, in a transport process referred to as streaming. Similarly, the exchange of energy between CRs and gas mediated by the Alfvén

waves and mentioned above is called streaming heating. In the case of CR streaming, the self-generated Alfvén waves confine CRs to travel along the magnetic field and down their own pressure gradient (Kulsrud & Pearce, 1969). When the propagation of CRs is regulated by streaming instabilities, this is classified as self-confinement CR transport. However, diffusion can also be driven by other mechanisms such as external turbulence, and is then referred to as the extrinsic turbulence transport mode (Zweibel, 2013). We provide more details about CR propagation models in **Chapter 2**.

Diffusion tends to homogenise the distribution of CRs and leads them to eventually escape the confinement volume in which they are injected. This process can be parametrised with a diffusion coefficient, κ, that expresses the ratio of CR energy density flux to the local gradient of CR energy density, in units of area per time. In other words, this can be interpreted as the surface crossed by a given amount of CRs in a given amount of time. Just as charged particles of different energies do not have the same gyration radius around magnetic field lines, they also do not diffuse at the same speed. CRs of the highest energies can escape faster from their injection sites, and therefore have a higher diffusion coefficient (Blasi & Amato, 2012). As a result, while particles with high energies provide a greater pressure support, low energy CRs have more difficulty escaping dense environments, and have more time to interact with the ISM. This is precisely the interplay between escape and confinement of CRs of different energies which can explain the observational signatures of CRs we measure.

Among the various direct and indirect observations of CRs, we already mentioned the CR chemical abundance, as a means to distinguish between primary and secondary species. The abundance of secondary CRs such as Li, Be and B arises from spallation processes, which occur as frequently as CRs interact with gas. In other words, CRs that remain confined for longer in a galaxy suffer more collisions with galactic gas and therefore produce a larger amount of spallation products. In particular the ratio of boron to carbon is the most common secondary-to-primary CR ratio used to infer the confinement time of Galactic CRs, and can also be used to constrain the CR diffusion coefficient (by means of numerical simulations to compare observations with models, as explained in **Chapter 2**). Up to energies of several tens of TeV, the spectrum of individual species within the Milky-Way can be directly observed, for instance with the Alpha Magnetic Spectrometer (AMS) on board the International Space Station (Kounine, 2012), or with the balloon Cosmic Ray Energetics And Mass (CREAM) experiment (Ahn et al., 2008). Such low-energy CRs are absorbed by the Earth's atmosphere, and can only be directly probed with space and balloon-borne experiments. Conversely, CRs with energies beyond 10^{13} eV can only be probed with large ground-based instruments, because their flux is too low to be detected with our small space instruments (e.g. Castellina, 2017). In this case, the composition of the high-energy end of the Galactic CR spectrum and of the extragalactic CRs is indirectly reconstructed from atmospheric air showers initiated by the CRs when they interact with the atmosphere, as first discovered by Auger et al. (1939). The composition of the CRs at the origin of the atmospheric showers can be deduced from the nature of the particles that compose the showers, or using the fluorescent UV light these secondary particles emit, which is called the Cherenkov light (Čerenkov, 1937). The Pierre Auger Observatory (Abraham et al., 2004) and

the KASCADE and KASCADE-GRANDE experiments (Antoni et al., 2003) are examples of ground-based instruments that rely on these mechanisms (see e.g. Gaisser et al., 2013, for a more complete description and list of air shower detectors).

CRs can also be tracked thanks to the radiation produced when they interact with ISM gas. Even if they are subdominant in number, electrons provide important observational evidence of the CR population. Electrons can for instance transfer their energy to CMB photons through inverse Compton scattering, as explained earlier with Fig. 1.5. They are also responsible for X-ray and gamma-ray emission through the bremsstrahlung process. A similar braking radiation can be emitted from the deceleration of relativistic electrons in presence of a magnetic field, known as synchrotron radiation. In addition to emitting the X-ray and gamma-ray photons, synchrotron emission can also be responsible for emission at radio wavelengths (Reynoso & Walsh, 2015). These three processes are mainly relevant for leptons (electrons and positrons), and are negligible for more massive CRs. Instead, protons and other nuclei with energies of a few GeV and beyond suffer from significant hadronic losses (also sometimes referred to as catastrophic losses). When these CRs interact with protons (more generally with nuclei) from the ISM, they lose a part of their energy and produce three types of pions with similar probabilities: neutral π^0, positively charged π^+ and negatively charged π^-. The charged pions catastrophically decay into neutrinos and muons, themselves decaying into electron/positron pairs that eventually lose their energy through the leptonic processes aforementioned. On timescales ten times faster, the decay of the neutral pions leads to the production of two gamma-ray photons (via the decay of the mesons generated by the interaction of CRs with the background gas, Dermer, 1986). These photons can be directly observed in space, with the Fermi Large Array Telescope (Fermi-LAT, Atwood et al., 2009; Ackermann et al., 2013). As they also produce particle air showers when they enter the Earth's atmosphere, distinct from that initiated by hadrons, the gamma-ray photons can also be detected thanks to their Cherenkov radiation with instruments such as the High Energy Stereoscopic System (HESS, e.g. Aharonian et al., 2006) and soon the Cherenkov Telescope Array (CTA, Cherenkov Telescope Array Consortium et al., 2019). Gamma-ray photons produced by CRs are particularly interesting, because their straightforward propagation tells us about their provenance, and thus about the source that accelerated the CRs. Additionally, comparing models of CR transport to gamma-ray observations can strongly constrain the time during which CRs remained confined close to their injection source, and, similar to the other spallation products, constrain the CR diffusion coefficient (as done by e.g. Chan et al., 2019, in numerical galaxy simulations). In the end, all of these observational signatures[13] can help us to correctly understand the transport of CRs, which is of crucial interest to determine to what extent CRs interact with galactic gas, and to subsequently quantify their effects on galaxy evolution.

[13]See `https://doi.org/10.5281/zenodo.1468852` from Carmelo Evoli for a decomposition of the CR spectrum into its different components, as observed with multiple experiments.

1.3.3 Cosmic rays as a source of feedback

Due to their very nature, cosmic rays have a number of advantages that make them an important agent of galaxy evolution on different scales. One of the most common arguments invoked is the fact that the typical CR energy density measured in the ISM of our galaxy is of the order of ~ 1 eV cm^{-3}, meaning that CRs are at rough equipartition with magnetic, turbulent and gravitational energies (Boulares & Cox, 1990; Grenier et al., 2015). The CR energy density arises from the balance between the production of CRs[14], their escape, and their energy losses. Because these three processes depend on the momentum of cosmic rays[15], the dynamical impact they have on galaxies depends on their energy range. We note that the most energetic CRs ($E \gtrsim$ PeV) are so rare and escape their host galaxy so fast that they are not expected to have a dynamical impact on the galactic gas. Nonetheless, the exceptional interactions they have with gas produce very energetic gamma-ray photons via the hadronic process described previously. When detected, these photons can still provide constraints on CR transport.

We first focus on low-energy CRs, defined as particles with an energy $E \lesssim$ GeV (see Padovani et al., 2020; Gabici, 2022, for complete reviews about low energy CRs). These particles pervade the galactic ISM, and are confined close to the regions where they are injected due to their slow diffusivity (e.g. Jacobs et al., 2021), for timescales longer than their more energetic counterparts. There, they can penetrate dense clouds of gas where collisions occur frequently, making them lose their energy mostly through Coulomb interactions. This process is even more efficient as low energy particles have relatively large cross sections with atoms and molecules. In particular, the energy loss of low-energy CRs translates into the emission of photons from a few eV to several keV that may play a role in star formation. The interaction between low-energy CRs and the ambient gas enables for instance molecular hydrogen dissociation (the energy needed to dissociate H_2 is $E \simeq 5$ eV) and ionisation, which raises the gas temperature and can prevent or at least delay the collapse of gas leading to star formation. While UV photons from massive stars usually provide the dominant ionisation agents, their radiation is significantly self-shielded at high gas densities, unlike CRs that can easily permeate gas with surface densities $> 10^2$ g cm^{-2} (Padovani et al., 2018). Therefore, low-energy CRs can significantly contribute to alter the ISM, that they can heat and even ionise at rates ranging from 10^{-16} to 10^{-13} s^{-1} (from measurements in our galaxy as well as from NGC4418, Arp220, Mrk231, NGC253, M82 and NGC4945, González-Alfonso et al., 2013, 2018; Van der Tak et al., 2016; Holdship et al., 2022). Astrochemical models also suggest that low-energy CRs acting in protostellar clusters can dissociate CO and NH_3 molecules and promote the formation of C^+ and HCO^+, among others (Gaches et al., 2019a,b). However, it is important to note that the aforementioned processes are not accounted for in current galaxy simulations, because they are relevant at scales that are usually unresolved, and because they would demand the modelling and tracking of too many interactions between CRs and the various metal species, therefore adding computational expense, memory, and complexity.

[14] By production of CRs, we mean the acceleration of existing charged particles up to (or close to) relativistic speeds, which precisely defines CRs.

[15] The momentum of a cosmic ray $p = E/c$ is another way to quantify its energy E.

Beyond their effect on gas chemistry, CRs are thought to affect the ISM dynamics. We are now referring to CRs with relatively high energies $E \gtrsim$ GeV, which are the most abundant and mostly interact with gas through collisionless processes. The back reaction from such GeV CRs in galaxies, or equivalently CR feedback, has been studied in a number of numerical simulations, most of them modelling CRs as one CR group following a kind of Grey approximation (with the exception of Hopkins et al., 2021c; Girichidis et al., 2022). Initially, CR feedback was implemented in idealised simulations, which are controlled experiments with a single isolated galaxy (e.g. Hanasz et al., 2013; Booth et al., 2013). More recently, simulations account for CR feedback in a cosmological context, which better reproduces the evolution of the Universe, but they target a single halo to limit the numerical cost (e.g. Salem et al., 2016; Chan et al., 2019; Buck et al., 2020). Before we come back to the different types of simulations in **Chapter 2**, we expand on some of the galaxy simulations that include CR feedback, to state the effects CRs are thought to have on galaxy evolution (see also **Appendix A** for a list of studies and reviews about CRs and their main conclusions).

In the ISM, the CR pressure gradient helps to prevent self-gravitating gas fragmenting and collapsing. In addition to gas heating and momentum deposition provided by lower-energy CRs, this additional vertical support can reduce star formation. This is what is measured in a number of simulations, from idealised to cosmological. Jubelgas et al. (2008) are probably among the first to report a reduction of star formation due to CRs, with an increasing efficiency for low-mass galaxies. Globally, the same trend has been found in more recent studies, for instance Booth et al. (2013); Pfrommer et al. (2017); Wiener et al. (2017); Jacob et al. (2018). It is important to note that the ability of CRs to suppress star formation is very much related to their confinement in the densest regions of galaxies. CRs that would only be advected with gas, without suffering from any diffusion process, would be trapped close to their injection sites. There, they would interact with gas, mainly through hadronic interactions, which would significantly help to prevent star formation. This has been observed in the idealised galaxies of Wiener et al. (2017) and Dashyan & Dubois (2020). For the same reason, simulations that model CR diffusion with a low diffusion coefficient[16] measure a greater impact of CRs on star formation than ones with higher values, as slowly diffusing CRs are confined in the ISM for longer (Salem & Bryan, 2014; Dashyan & Dubois, 2020; Chan et al., 2019). However, considering a slow CR diffusivity can be ruled out by observations of gamma-ray emission, that arises from the hadronic interactions between CRs and the galactic gas. Salem et al. (2016), Chan et al. (2019) and Buck et al. (2020) all reach the same conclusions in their different cosmological simulations: low diffusion coefficients of the order of 10^{27} cm^2 s^{-1} overestimate the gamma-ray luminosity. Nonetheless, the exact diffusion coefficient value and the CR transport processes that enable a better match with observations differ from one simulation to another. To alleviate this issue, efforts have been put towards a more realistic CR propagation modelling. This is for example the case of Farber et al. (2018), who decouple CRs from gas in cold neutral media, Semenov et al. (2021), who suppress CR diffusivity in star-forming regions, or recently Girichidis et al. (2022) who spectrally resolve the CR distribu-

[16] Usually, the CR diffusion coefficient is expected to be $\kappa = 1 - 3 \times 10^{28}$ cm^2 s^{-1}. Values around 10^{27} cm^2 s^{-1} and 10^{29} cm^2 s^{-1} will be referred to as low and high respectively.

tion. As they cannot be directly inferred, the conclusions about the effect of CR feedback on star formation remain debated, and likely vary with galaxy mass and CR propagation. Moreover, numerical limitations such as the physics included and the resolution reached in galaxy simulations may also impact our understanding of CR feedback.

One of the key roles of CRs, and barely mentioned yet, is their ability to drive galactic-scales outflows. This idea was first developed analytically by Ipavich (1975), and details on this topic can be found in the recent reviews by Zweibel (2017) and Recchia (2021). Each time a star explodes as a SN, a plethora of GeV CRs are injected into the ISM, where their pressure gradient builds up and acts on the surrounding gas. Because they cool[17] less efficiently than the thermal component (Enßlin et al., 2007), in particular in dense regions, their dynamical impact on these small scales is expected to last longer than the thermal energy injected by the SN explosion. In addition to the kinetic energy released by the SNe, CRs help to generate outflows. When the winds finally reach the CGM, CRs can further maintain them, thanks to their softer equation of state that makes their pressure drop less quickly than thermal pressure upon adiabatic expansion. For these reasons, CRs are naturally thought to increase the amount and rate of outflowing gas. Qualitatively, most if not all galaxy simulations including CR feedback agree and report increased mass outflow rates (e.g. Hanasz et al., 2013; Booth et al., 2013; Salem & Bryan, 2014; Pakmor et al., 2016; Wiener et al., 2017; Jacob et al., 2018; Dashyan & Dubois, 2020; Jana et al., 2020; Girichidis et al., 2022 in idealised galaxies, Farber et al., 2018; Girichidis et al., 2018 in stratified boxes of ISM and Buck et al., 2020; Hopkins et al., 2020b; Ji et al., 2020; Butsky et al., 2021 in cosmological simulations). Determining whether it is diffusion from external turbulence or streaming from self-generated Alfvén waves that contributes the most in driving winds however remains an open question (Wiener et al., 2017; Butsky & Quinn, 2018; Armillotta et al., 2021; Hopkins et al., 2021c; Armillotta et al., 2022; Hopkins et al., 2021a; Thomas et al., 2022).

Not only do CRs participate in the launching of galactic outflows, but they are also often found to affect the temperature-metallicity phase of the feedback-driven winds and, as a result, the composition of the CGM. CR losses in intermediately dense and diffuse media occur on timescales greater than their propagation outside their injection sites. Unlike hot gas driven by thermal pressure and radiating its energy quickly, CRs thereby provide an additional energy component available to accelerate the cold ISM (Krumholz & Federrath, 2019). As a consequence, CR-driven winds are denser, accordingly slower as there is more material to push, and most importantly colder than outflows powered only by SN or by any other relevant physical process that has yet been identified (such as AGN, stellar winds, and radiation). This is found in galaxy simulations, that produce hot outflows with barely any gas colder than $\sim 10^5$ K without CRs, as noticed by Salem et al. (2016); Butsky & Quinn (2018); Girichidis et al. (2018); Buck et al. (2020); Hopkins et al. (2020b); Ji et al. (2020); Hopkins et al. (2021b); Butsky et al. (2021). This has huge implications, notably in terms of the content of CGM metals, that can be probed via absorption line measurements. One example is the data from the COS-Halos survey (Cosmic Origins Spectrograph, installed on the HST, Froning & Green, 2009; Green et al., 2012), presented by Werk et al. (2014, 2016) and which can be com-

[17] CR cooling refers to CR energy losses, by analogy with gas cooling.

pared to synthetic spectral lines from simulated galaxies. Using this method, Salem et al. (2016), Butsky & Quinn (2018), Ji et al. (2020) and Butsky et al. (2021) revealed that including CR feedback leads to a more realistic metal-enriched CGM. CR pressure helps to drive more winds in the CGM, which contributes to its metal-enrichment, and additionally affects the thermal state of these metals, so that they are visible in certain absorption lines. The CGM from simulations with CRs typically shows a better match with observations of species like HI and MgII for gas with a temperature $T \lesssim 10^4\,\mathrm{K}$, SiIV and CIII for warm gas at $T \lesssim 10^5\,\mathrm{K}$ and OVI and OVII for hotter gas (Tumlinson et al., 2017), which means that the CGM has both enough metals and a realistic temperature thanks to CRs.

1.3.4 Cosmic rays and the epoch of reionisation

CR feedback impacts both the ISM and the CGM of the galaxies. This is the reason why CRs are considered an important ingredient in galaxy evolution. Most specifically, one could be curious of the role of CRs during the initial stages of galaxy formation, at high redshift, as these primordial times eventually shape the current Universe. Thanks to simulations, we already find that gas ejected from galaxies is denser when supported by CR pressure and that CRs tend to puff up galaxies, increasing the thickness of the gaseous disc (Jubelgas et al., 2008; Girichidis et al., 2018; Hopkins et al., 2020b). As photons are more easily absorbed in dense media, we can expect propagation of radiation to be impacted, and especially the propagation of hydrogen ionising (Lyman Continuum, LyC) radiation. In dense clouds of young stars, a large fraction of the UV photons emitted is thought to be absorbed in the close neighbourhood of the stars (Kimm & Cen, 2014; Paardekooper et al., 2015; Trebitsch et al., 2017). However, when the most massive stars explode as SNe, the energy they release disrupts the star-forming clouds, and clears the way for radiation to escape. By changing the structure of the ISM in the vicinity of the stars, stellar feedback is therefore expected to strongly regulate the escape fraction of LyC photons and its fluctuations with time (Wise & Cen, 2009; Kimm & Cen, 2014; Wise et al., 2014; Ma et al., 2015; Trebitsch et al., 2017; Kimm et al., 2017). The column density of neutral hydrogen has to be low enough to give the LyC radiation a chance to reach the IGM, but CRs are predicted to make the ISM and the CGM smoother, which may naively increase gas column densities and make them more similar along different lines of sight. This leads one to question whether CRs play a non negligible role in the escape of the radiation that reionised the Universe. While CRs contribute to suppress galaxy growth, do they reduce the escape fraction of ionising photons from galaxies? There is a non trivial interplay between the regulation of star formation, the production of LyC photons, and the reionisation of the IGM. This is especially the case for low-mass galaxies, thought to be the dominant contributor to the reionisation of the Universe, and yet the most affected by feedback processes such as those provided by CRs. All in all, the interplay between radiation and CRs, never studied so far, can dramatically challenge our models of reionisation, which hardly converge with observations (e.g. Ma et al., 2015; Rosdahl et al., 2018). In addition, focusing on the effects of CRs during the EoR would also provide interesting constraints on CR feedback, if simulations manage to produce realistic galaxy evolution and reionisation histories. The purpose

of this thesis is to investigate the potential role of CRs on and during the EoR, using high-redshift cosmological simulations as a key laboratory to test the effects of CRs on galaxy growth and reionisation. The goals are to study if CRs, combined with SN and stellar radiation feedback, provide enough feedback during the EoR to match observational constraints, and how CR feedback then affects the escape of radiation from galaxies and, hence, reionisation.

1.4 Goals and structure of the thesis

The processes regulating galaxy growth remain under deep investigation. To this end, numerical simulations of galaxies are our best tool to decipher and interpret results from observational surveys. Efforts in the last decades have significantly helped to identify the mechanisms playing a role in galaxy evolution. However, discrepancies between numerical simulations and observations persist, as the result of our partial understanding of galaxy evolution. Concretely, this is the consequence of missing ingredients and/or calibrated models for star formation and feedback, that are mandatory to regulate galaxy evolution. Ideally, one would prefer to use the least calibration possible, and perform simulations from first principles[18] instead of phenomenological models. This involves the coupling of various physical processes, introducing multiple sets of equations at the cost of memory and computational resources. This is probably the reason why radiation, magnetohydrodynamics, supernova and cosmic ray feedback had never been consistently coupled all together in galaxy-scales simulations. In this thesis, I present the results from the first Cosmic-Ray Radiation-MagnetoHydroDynamics (CR-RMHD) simulations of galaxy evolution. By going beyond the usual modelling of galaxy formation, the aim is to investigate the role of cosmic ray feedback on galaxy growth, and focusing on the Epoch of Reionisation. This epoch is of a particular interest, because the reionisation history provides a unique constraint on the effect of feedback, and may give precious insight into the role of CR feedback. In addition, the EoR corresponds to the first billion years of the Universe, which is cheaper and more affordable to simulate than the full history of the Universe. This more complex description of galaxy evolution will help to determine: a) if and how cosmic rays contribute to the galactic ecosystem, b) the interplay between cosmic ray feedback and the other physical mechanisms, and especially with the escape of ionising photons in order to eventually c) infer the potential role of CRs on the process of reionisation.

The structure of the thesis is as follows:

- **Chapter 2** describes the numerical tools used in the thesis. The chapter includes a brief overview of the different codes and flavours of simulations dedicated to astrophysics. I introduce the SPHINX suite of cosmological simulations devoted to the study of the EoR, which serve in later chapters. The rest of the chapter is dedicated to the RAMSES code, used to perform the simulations studied throughout the thesis. I provide details about the different physical modules and the equations to be solved in order to account for MHD, radiative transfer, star formation, SN and CR feedback.

[18] First principles simulations refer to the fact they are not directly calibrated from observations nor any empirical relations.

- In **Chapter 3**, I investigate the effects of CR feedback and its interplay with various physics by means of idealised simulations of isolated disc galaxies. I provide a sample of three galaxies spanning 2 orders of magnitude in mass, to show how CR feedback varies with galaxy mass. I also take advantage of the relatively low cost of such simulations to perform various runs, in order to distinguish the effect of radiation, magnetic field, resolution, star formation and SN feedback. In particular, I compare my results to those obtained when using the same setup as the SPHINX simulations, which have been found to reproduce a number of observable at high redshift. Doing so provides a first estimate of the ability of CRs to contribute to galaxy evolution. I also test the sensitivity of CR feedback to the diffusion coefficient, to the CR injection efficiency by SNe, and to the coupling of CRs with an already strong SN feedback. This study provides a comprehensive framework on the effect of CRs in an idealised context, before studying CR feedback in a cosmological context. A part of the results presented in this chapter led to the publication of a paper, enclosed in the chapter.

- In **Chapter 4**, I include CRs in the state-of-the art SPHINX simulations, with the aim of determining how including them compares to the calibrated and artificially strong SN feedback model originally adopted. Therefore, I probe if CRs efficiently regulate galaxy growth across cosmic time, and if and how they alter the process of reionisation through their interplay with the escape of ionising radiation. For this purpose, I perform the first cosmological simulations with CR-RMHD. I first focus on two rather massive galaxies, and show how a standard SN feedback and CR feedback differently regulate galaxy evolution in a cosmological context, compared to the strong SN feedback adopted in the fiducial SPHINX simulations. In a second part, I perform several SPHINX simulations in which hundreds of galaxies are resolved in a volume of 5 cMpc in width. By means of observational estimates, I investigate how CR feedback leads to realistic regulation of star formation and reionisation history, in order to shed light on the role of CRs during the EoR.

- Eventually, **Chapter 5** summarises the results presented and states future lines of work that will provide follow-up to this thesis.

CHAPTER 2
Galaxy evolution with numerical methods

This second chapter aims to describe the numerical tools commonly used to study galaxy evolution. I present the different kinds of simulations and the diversity of codes dedicated to galaxy evolution in **Section 2.1**. I give more details about the RAMSES code and the physical modules implemented, as it is the code I used to run all my simulations (**Section 2.2**). The aim of this thesis is to focus on the role of CRs on galaxy evolution. For this reason, I give an overview of the numerical astrophysics of CRs, from the equations that trace their transport as charged particles to the methods adopted to include them as a source of feedback in galaxy simulations, and most specifically in RAMSES (**Section 2.3**). Finally, I introduce the SPHINX simulations, which are used in a part of this thesis (**Section 2.4**).

2.1 Numerical simulations of galaxies

The huge amount of observational data, collected over decades, comprises the base material to build theories about the evolution of the Universe. However, consistent frameworks of structure and galaxy formation require a precise knowledge of the plethora of physical processes involved at different scales, as galaxy formation is non-linear, multi-physics, multi-dimensional and multi-scale, and cannot be studied in laboratories. To better interpret the observations, refine our theoretical models, and predict the results from future experimental surveys, numerical simulations are a powerful tool, which continuously evolve and improve thanks to increasing numerical capabilities and improved methods.

Dark matter is one of the main components that drives the formation and evolution of structures in the Universe, as DM and gravity rule the cosmological web and collapse into haloes. A basic kind of numerical simulation consists of the N-body technique, so called because it considers DM as individual collisionless particles whose mass contributes only to the gravitational force (e.g. Kravtsov et al., 1997). N-body simulations track the evolution of dark matter fluctuations down to the formation of structures, from the cosmic web to the halos in which galaxies are hosted, and can efficiently cover a wide range of scales from hundreds or thousands of Mpc down to kpcs. However, even though ordinary matter (also termed as baryonic matter) only represents about 5% of the total Universe energy budget, it is another essential component of the Universe. Baryons are the primary components of gas and stars, which themselves compose galaxies. Their evolution can be modeled with analytical schemes, that rely on equations built from our understanding of galaxy growth. It is possible to combine N-body simulations, evolving DM structures only, to analytical models, that predict the evolution of the baryonic matter from the cooling of gas and the formation of stars, to the energy and momentum injected by BH and SN explosions. This approach is known as semi-analytical modelling

(SAMs, see e.g. De Lucia & Blaizot, 2007, Knebe et al., 2015 and Gabrielpillai et al., 2021). By means of empirical or phenomenological recipes, SAMs basically consist of evolving equations that model the effects of physical processes such as gas to star conversion, gas cooling and stellar feedback. However, they do not explicitly solve the equations of e.g. gravity and (magneto)hydrodynamics. While SAMs are a useful tool to provide a theoretical framework for galaxy evolution, they lack the predictive power of numerical simulations that couple DM and baryons to track their non-linear and spatial distribution and kinematics. The processes involved in galaxy evolution have a complex and highly non linear interplay, and simulations are our most powerful (and only!) theoretical instrument to disentangle their distinct effects. For this reason, I will focus exclusively on numerical simulations in what follows.

2.1.1 Idealised and cosmological simulations

Different approaches exist to model galaxy evolution. The starting point of any simulation is a set of initial conditions, to be evolved in space and in time following the physics modelled in the code. The nature and the number of the objects considered, the size of the simulation box as well as the resolution targeted are important factors that depend on numerical capabilities. Therefore, it is necessary to make compromises between running a large simulated box, designed for statistical studies, versus reaching a resolution high enough to capture the physics in the ISM of galaxies. Depending on the goals of the numerical experiment one wants to perform, different kinds of simulations have to be considered. We describe them and state their main advantages and limitations.

Idealised simulations

In the context of galaxy evolution, idealised simulations generally correspond to an isolated galaxy, placed in the middle of a box, and designed for controlled experiments. In such simulations, an initial distribution of DM, stars and gas is set up, and consists of the reservoir material used by the galaxy to form stars, grow and develop during several hundreds of Myr (e.g. Springel et al., 2005; Dalla Vecchia & Schaye, 2008; Dubois & Teyssier, 2008; Hopkins et al., 2011; Rosdahl et al., 2015). Idealised simulations can also be restricted to a portion of a galaxy, such as its ISM, whose properties are reproduced in stratified boxes, such as those studied by Farber et al. (2018) and Girichidis et al. (2018).

These idealised set-ups get rid of any complex large-scale effects, such as gas infall or galaxy mergers (unless it is the aim of the simulation, as in Fensch et al., 2017). Doing so, they are nice test-beds to investigate the impact of different physics. For example, they are useful for testing the implementation and effects of star formation or feedback models. This is precisely what I do in **Chapter 3**, where I specifically use idealised simulations of isolated disc galaxies to study the role of CR feedback on star formation and outflows.

Idealised simulations are usually the most affordable numerical simulations, with a moderate computational cost in terms of resources, memory and computing time. One considerable benefit is that it is possible to reach good resolution of the order of $\sim$ pc, and to reconcile this with galactic kpc scales. However, they suffer from

two major caveats due to their very nature: they omit any interactions between the galaxy and its cosmological environment, and cannot follow the growth of galaxies through cosmic time. In order to predict the long term consequences of various physical processes, cosmological simulations are required.

Cosmological simulations

Cosmological simulations are designed to reproduce virtual universes, with volume widths between a few and several hundreds of Mpc (see Vogelsberger et al., 2020, for a review). Among some of the most famous cosmological simulations, we mention the DM only MILLENNIUM simulations (Springel, 2005), whose maximum box size reaches 4110 Mpc (Angulo et al., 2012), and ILLUSTRIS (Vogelsberger et al., 2014), HORIZON (Dubois et al., 2014) or EAGLE (Schaye et al., 2015) with smaller box sizes of around ~ 100 Mpc but with baryonic physics included.

Unlike idealised simulations, a cosmological setup involves initial gas velocity and density fields, together with DM velocity and position generated from a cosmological framework, which is usually chosen to be a ΛCDM Universe model. To get these initial distributions, the idea is to start from a generated linear matter power spectrum, randomly sampled by a Gaussian function, and to let it evolve, which is done in initial conditions (ICs) generation codes like MUSIC (Hahn & Abel, 2011) and GRAFIC (Bertschinger, 2001). Structures then emerge with decreasing redshift, and the simulated (part of the) Universe evolves as an expanding box to mimic its expansion.

Cosmological simulations are not expected to reproduce exactly our Universe, but instead provide a statistical sample of structures that enables a helpful comparison with observational surveys. Thus, they are our best tool for a number of astrophysical concerns. By modelling cosmic evolution on large scales, they can be used to study the wide variety of galaxy morphologies, the progress of galaxy growth, or the evolution of cosmological processes such as the reionisation of the Universe. In **Chapter 4**, I use cosmological simulations to study the influence of CRs during the EoR.

To be as reliable as possible, cosmological simulations should both cover a large volume and reach high resolution, which considerably increases their numerical cost. To circumvent this aspect, an intermediate approach has become popular: cosmological zoom simulations.

Zoom simulations

Large cosmological volumes with high resolution would be, in principle, feasible, if they were not so greedy in terms of memory and computational time. For this reason, zoom simulations have emerged as a good compromise, as they allow for big but mostly unresolved volumes, focusing on small resolved targeted areas instead.

While large volume simulations model large samples of galaxies, a zoom simulation preferentially targets one or a small sample of galaxies. Instead of sampling uniformly large volumes, the zoom initial conditions set a high resolution region of interest surrounded by a low resolution background, as the full box is needed but does not need to be highly resolved to account for the large-scale gravitational effects on the targeted region. This allows physical processes to be resolved in more

detail in a targeted region, with the advantage of it being embedded in a cosmological context accounting for environmental effects, such as cosmic accretion and mergers. Depending on the size of the volume which is zoomed-in, these simulations still follow the merger history of a halo, with enough resolution to study the star formation within it. Just to name a few, NIHAO (Wang et al., 2015), FIRE (Wetzel et al., 2016; Hopkins et al., 2018) and AURIGA (Grand et al., 2017) are all zoom simulations that can reach a resolution between hundreds and a few pc.

In order to investigate the long-term effects of feedback driven outflows, we analyse two cosmological zoom simulations that include CRs in the beginning of **Chapter 4**, which provides a continuity to the study of CR feedback in idealised galaxies (**Chapter 3**).

2.1.2 Grid and particle codes

In order to decipher the physics of galaxy formation, simulations have to solve the fundamental equations of gravity, (magneto)hydrodynamics (MHD) and radiative transfer (RT). The starting point to deal with gas dynamics is to solve the Euler equations, treating the astrophysical gases as ideal. These partial differential equations, further discussed in the rest of this chapter (see **Section 2.2.3**), trace the time variations and the conservation of gas mass, momentum and energy. To numerically discretize the Euler equations, different approaches exist, and give rise to particle and grid-based codes.

SPH codes

One of the technique to discretize the Euler equations is to decompose gas as particles and to follow their trajectories with Lagrangian smoothed particle hydrodynamics (SPH), as introduced by Gingold & Monaghan (1977) and Lucy (1977) (see also Springel, 2010a, for a review). Among the major SPH codes used for galaxy formation, we mention GADGET (Springel, 2005), SWIFT (Gonnet et al., 2013), CHANGA (Menon et al., 2015) and GASOLINE (Wadsley et al., 2017). SPH codes are mesh-free methods, where gas is sampled by a set of particles, and for which hydrodynamics rely on the interactions of each particle with its neighbours. For example, the gas density associated with a particle is determined by summing the masses of its neighbouring particles, in a given spherical volume set by a smoothing length. The sum is weighted by the use of a kernel function, which smoothes the particle distribution depending on the smoothing length, usually chosen to enclose a similar number of particles both in dense and diffuse media (the smoothing length is therefore small in dense environments and large in diffuse ones). This smoothing length is equivalent to a physical resolution, and explains the name of this category of particle code. With this Lagrangian prescription, SPH codes have varying local resolution, and the gas density is determined by the local number of particles with resolution naturally refining on regions with the highest densities. The advantage of SPH codes is that they automatically follow the gas flow. Conversely, a fundamental issue of SPH codes is that the solutions for the Euler equations, which are set in a Lagrangian form, are only valid far from discontinuities (Agertz et al., 2007). Indeed, shocks are not directly tracked by the fluid particles. As a result, they are poorly

resolved, which affect the accuracy of discontinuous solutions, which are common in gas dynamics and in astrophysics[1].

Grid codes

Numerically and theoretically, it is more convenient to consider the Euler equations in their conservative Eulerian form to reach a better accuracy in the treatment of discontinuities. The counter approach to SPH codes is to consider gas as a fluid which is arranged and evolved on a grid. The simulated volume is decomposed into grid cells, each of them encapsulating gas properties that are advected with time. Unlike the Lagragian approach where the solutions of the Euler equations are derived in the fluid frame, the basic idea of the Eulerian approach is to formulate these solutions in the fixed frame of the grid, meaning that while the gas flows from cell to cell, the grid does not move. To better follow the large density contrasts in astrophysical problems, the grid can be inhomogeneously refined, following the Eulerian adaptive mesh refinement (AMR) numerical technique (see e.g. Berger & Oliger, 1984, and Teyssier, 2015 for a review). Popular AMR codes are ART (Kravtsov et al., 1997), FLASH (Fryxell et al., 2000), PLUTO (Mignone et al., 2012), ENZO (Bryan et al., 2014) and RAMSES (Teyssier, 2002), the latter being the one used in this thesis. The AMR technique allows for variable resolution, depending on chosen refinement criteria, so that the mesh is adaptively refined. Then, cells can be the smallest where gas is the densest, where discontinuities take place, and can also be sized to track the radiation ionisation front in low density or void regions. This makes AMR more adaptable than SPH codes for shocks and radiative transfer studies.

Other codes

An intermediate method, which mixes the two former approaches, uses the grid-based techniques and adds deformable Lagrangian meshes. A recent popular code employing this technique is the AREPO code (Springel, 2010b), which employs the so called moving mesh method. As for grid-based codes, the mesh is decomposed into cells, which are however not squares anymore but consist of polyhedra (in three dimensions). The mesh then continuously deforms and changes its topology due to its Lagrangian nature, in order to follow the fluid in such way that particles belong to one polyhedral cell (this is the principle of the Voronoi tessellation). Consequently, the moving-mesh approach inherits the flexibility of SPH codes and the accurate treatment of shocks and discontinuities of AMR codes, at the cost of a highly complex mesh structure. We should also mention the GIZMO code (Hopkins, 2015), which adopts a hybrid format between mesh-free particle and finite volume methods.

The large number of astrophysical codes offers good opportunities to test our understanding of galaxy evolution. With the aim of disentangling the effects from one numerical technique to another, the AGORA project investigates results from simulations as similar as possible while performed with different codes (Kim et al.,

[1]To fix this issue, SPH methods introduce numerical artefacts, such as artificial viscosity in order to reproduce the dissipation of energy that occurs at shock fronts.

2014). Although systematic differences between grid and particle codes exist, it seems that the greatest discrepancies between simulations performed with one code or another arise from their sub-grid prescriptions for star formation and feedback modelling rather than from the different hydrodynamical techniques (see also Kim et al., 2016; Roca-Fàbrega et al., 2021; Braspenning et al., 2022).

2.2 Numerical methods in RAMSES

The RAMSES code belongs to the category of grid codes and was initially designed for cosmological gravito-hydrodynamical simulations (Teyssier, 2002). It is among the most actively developed astrophysical codes, and includes a wide variety of physics (gravity, MHD, RT, evolution of DM, gas and stars...) together with state-of-the art star formation and feedback models (AGN, SN, CRs...). RAMSES is a public code[2], and the modules that are not publicly released are available upon request. RAMSES can be used to run both idealised and cosmological simulations, and can focus on the physics of various objects and environments thanks to the adaptive refinement strategy. For all of these reasons, it is the code I used extensively to perform all the simulations that are studied in this thesis. Like any code user, I had to understand its different components and manage to properly combine them. In this section, I therefore describe the most relevant aspects of the RAMSES code that allow one to perform Radiation-MagnetoHydroDynamics (RMHD) simulations of galaxy evolution. The propagation and feedback of CRs in RAMSES is discussed in **Section 2.3**.

2.2.1 Basics of the RAMSES code

RAMSES is a code written in FORTRAN 90, which can be used on massively parallel architectures thanks to the MPI library (MPI stands for Message Passing Interface). Due to its AMR strategy, RAMSES is well-suited to study galaxy evolution. Thanks to the varying size of the cells, it is possible to trace both the ISM, where gas at densities up to a few $100\,\mathrm{cm}^{-3}$ resides, and the diffuse CGM, where gas density drops down to $\sim 10^{-5}\,\mathrm{cm}^{-3}$. In order to capture both scales, the most straightforward refinement criterion is to refine cells whose mass or density exceeds a chosen threshold. In the context of star formation, one may be particularly interested in the turnover length scales at which gas collapses under its own gravity. This is the definition of the Jeans length, introduced in Equation 1.9 from **Section 1.2.1**. Therefore, another refinement strategy commonly adopted (and which can be combined with others) is to refine cells whose size exceeds a multiple of the Jeans length. In any case, the cells identified for refinement, called parent cells, can only divide into 2^n children cells at a time, where n is the number of dimensions of the simulation. In 3D ($n = 3$), this means that a parent cell splits into 8: this is referred to as an oct. Then, each parent cell of level ℓ points towards 8 cells of level $\ell + 1$. Cells that are not refined are called leaf cells. Both the coarsest ℓ_{min} and the finest ℓ_{max} levels are set by the user, and define the minimum and maximum resolution of the simulation, respectively. While the full simulation box of size L_{box} can be considered as a cell

[2] https://bitbucket.org/rteyssie/ramses/wiki/Home

at level $\ell = 0$, the width of a cell at level ℓ corresponds to $\Delta x_\ell = L_{\rm box}/2^\ell$, as going from one refinement level to another implies that the width of a cell is divided by two. The grid is progressively refined in space, so that a cell at level ℓ can only have neighbours at level $\ell - 1$, ℓ and $\ell + 1$. We illustrate this in Fig. 2.1, which shows the refinement levels for one of the idealised galaxies studied in **Chapter 3**.

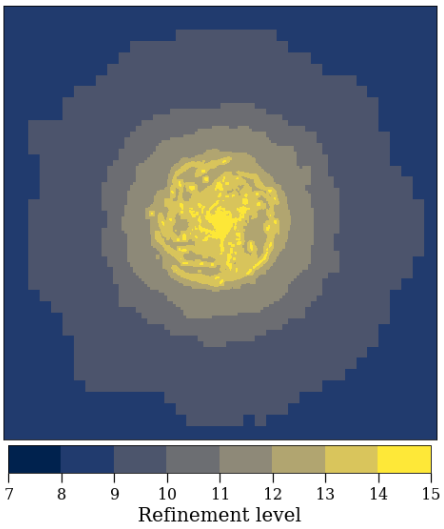

Figure 2.1: *Map of the refinement levels for the G9 galaxy studied in* ***Chapter 3****. The highest refinement levels correspond to the smallest cells in yellow. The transition between cells is done progressively from one level to the next.*

Each cell stores a number of properties, such as gas density, momentum, pressure, metallicity. To evolve these quantities, time is discretised into time-steps which are also adaptive. In the single time-step scheme, the equations relevant for galaxy evolution are integrated from t to $t + \Delta t$, where Δt is the same for all levels. Conversely with the sub-cycling time-step scheme, levels are evolved with their own Δt (whose value at each level is set by the Courant condition described in **Section 2.2.3**). In the sub-cycling scheme, the grid is synchronised: cells of level ℓ have to execute two time-steps before cells of level $\ell - 1$ execute one. To keep track of the galaxy evolution, the whole set of cells and particles are written in binary files, which store the outputs that correspond to specific snapshots of the simulation.

Cells may also contain dark matter and stars, modelled as collisionless DM and stellar particles. Modelling DM as particles allows the calculation of the time-independent contribution of DM to the gravitational potential. For this purpose, the mass of the DM particles may range from $10^3 - 10^9\,{\rm M}_\odot$, depending on the size of the volume and the amount of computational resources. The same particle methodology is used to model stars. Moreover, stars are too low-mass and numerous to be directly tracked as individual objects in simulations of galaxy evolution, already spanning a huge range of scales. Stars are represented as stellar populations instead, whose properties are encapsulated within a stellar particle of a given mass, age and metallicity. We come back to this aspect later (see **Section 2.2.6**).

2.2.2 Gravity

One of the main aspects impacting galaxy evolution is gravity, due to the contribution of baryons (gas and stars) and DM. Stellar and DM particles behave as a collisionless N-body system, and their trajectories only depend on the gravitational potential Φ:

$$\frac{d^2\boldsymbol{x}}{dt^2} = -\nabla\Phi \ , \tag{2.1}$$

where $\boldsymbol{x}$ represents the position of a particle. Φ is a solution the Poisson equation, which depends on the total mass density $\rho_{\rm tot}$ and the gravitational constant G:

$$\nabla^2\Phi = 4\pi \mathrm{G}\rho_{\rm tot} \tag{2.2}$$

Therefore, solving or the gravitational potential Φ requires knowing the total mass density field distribution, thereby coupling the N-body system to hydrodynamics (i.e. when the gas is included in $\rho_{\rm tot}$). While gas density is one of the quantities tracked and stored in grid cells in RAMSES, the code uses a Cloud-In-Cell (CIC) interpolation scheme (Hockney & Eastwood, 1981) in order to infer the stellar and DM mass densities in each cell. For this purpose, the DM and stellar particles are considered as cubic clouds whose centre corresponds to the position of the particle. Then, each cell is attributed a portion of the particle mass depending on the fraction of the "cloud" that overlaps with it. If the cloud entirely overlaps with one single cell, all its mass is attributed to this cell. After this step, the gravitational potential Φ is computed on the mesh for the coarse levels using fast Fourier transform technique. For fine levels, the Poisson equation is then solved by using a conjugate gradient method, which iteratively solves for the gravitational potential starting from a first guess. Differentiating Φ allows to find back the gravitational acceleration $\boldsymbol{g} = -\nabla\Phi$, and thus to update in turn the velocity and position of each particle.

2.2.3 Hydrodynamics

Gas is an important component of galaxies. In RAMSES, gas is treated as an ideal fluid, whose evolution is governed by the Euler equations (for a review, see Teyssier, 2015). These equations express mass, momentum and energy conservation, and are written in their conservative form as follows:

$$\frac{\partial\rho}{\partial t} + \nabla\cdot(\rho\boldsymbol{u}) = 0 \tag{2.3a}$$

$$\frac{\partial\rho\boldsymbol{u}}{\partial t} + \nabla\cdot(\rho\boldsymbol{u}\otimes\boldsymbol{u}) + \nabla\cdot P\boldsymbol{I} = -\rho\nabla\Phi \tag{2.3b}$$

$$\frac{\partial\rho\epsilon}{\partial t} + \nabla\cdot(\rho\epsilon + P)\,\boldsymbol{u} = -\rho\boldsymbol{u}\cdot\nabla\Phi \tag{2.3c}$$

Here, ρ corresponds to gas mass density, $\boldsymbol{u}$ to the velocity of the fluid, ϵ to the total specific energy (in units of energy per mass), P to gas pressure and $\boldsymbol{I}$ to the identity tensor. For hydrodynamic (HD) simulations, the total energy volume density $e = \rho\epsilon$ (in units of energy per volume) is the sum of the kinetic energy density $\rho u^2/2$ and

the thermal energy density $e_{\rm th} = \rho\epsilon_{\rm th}$. In more complex simulations, including magnetohydrodynamics (MHD) and CRs, magnetic and CR energy densities are added to the total energy budget, as we will explain afterwards.

The three Euler equations describe the evolution of four quantities (density, velocity, energy and pressure). In order to close the system of equations, a fourth equation is needed. For this purpose, an equation of state links gas pressure to gas specific internal energy $\epsilon_{\rm th}$:

$$P = (\gamma - 1)\,\rho\epsilon_{\rm th}\ , \tag{2.4}$$

where γ is the adiabatic index, whose value is 5/3 for a monoatomic ideal gas. For an ideal gas, we can also define gas temperature T through the relation $P = \frac{\rho {\rm k_B} T}{\mu m_{\rm H}}$, where $\rm k_B$ is the Boltzmann constant, μ is the mean molecular mass of the gas, and $m_{\rm H}$ the mass of an atom of hydrogen.

In order to solve the Euler equations, RAMSES adopts an Eulerian approach in which gas properties are discretised both in space and in time. At time t_n and for a cell i, a vector $\boldsymbol{U}_i^n$ gathers the averaged gas properties $(\rho, \rho\boldsymbol{u}, \rho\epsilon)$ to be evolved. The cell is subject to gravity, accounted for in a source term $\boldsymbol{S(U)} = (0, \rho\nabla\Phi, -\rho\boldsymbol{u}\nabla\Phi)$. Eventually, gas flows through the mesh, which translates into a flux function vector $\boldsymbol{F(U)} = (\rho\boldsymbol{u}, \rho\boldsymbol{u}\otimes\boldsymbol{u} + P\boldsymbol{I}, (\rho\epsilon + P)\boldsymbol{u})$. Using a time-centered approach for $\boldsymbol{F}$ and $\boldsymbol{S}$, the numerical discretised Euler equations are written:

$$\frac{\boldsymbol{U}_i^{n+1} - \boldsymbol{U}_i^n}{\Delta t} + \frac{\boldsymbol{F}_{i+1/2}^{n+1/2} - \boldsymbol{F}_{i-1/2}^{n+1/2}}{\Delta x} = \boldsymbol{S}_i^{n+1/2} \tag{2.5}$$

where the subscript i denotes the cell position and the superscript n corresponds to time t_n. The time-centered approach adopted comes from splitting Equation 2.5 according to an operator splitting approach. The equation is first solved without any source term, evolving the system to an intermediate state $n+1/2$. This intermediate state is then updated in a second step during which the source terms are eventually taken into account.

Until now, we only considered self-gravitating gas, but cooling and heating processes also impact gas dynamics. The contribution from these processes, detailed in **Section 1.2.1**, can be described with a cooling function $\Lambda(\rho, T, Z)$. This additional term contributes to the right-hand side of Equation 2.3c, and consequently to the source term $\boldsymbol{S(U)}$. In RAMSES, the values of $\Lambda(\rho, T, Z)$ are tabulated for gas density, temperature and metallicity, and are inferred from the ionisation state of the gas when using RAMSES-RT, presented in **Section 2.2.5**.

To determine the state of the system $\boldsymbol{U}_i^{n+1}$ when $t_{n+1} = t_n + \Delta t$, RAMSES uses a Godunov method. This numerical scheme solves partial differential equations, such as the Euler equations, and consists of evaluating fluxes at the surfaces of the cells. As fluxes are conserved, the Godunov method is a conservative scheme. In order to determine $\boldsymbol{U}_i^{n+1}$, it is necessary to calculate the mean gas flux at the interfaces of cell i between t_n and t_{n+1}, which is analoguous to a Riemann problem: a problem composed of partial differential conservation equations, with piecewise initial data on each side of a discontinuity. In our case, the discontinuity corresponds to the interface of a left-hand and a right-hand cell, for which $\boldsymbol{U}_{\rm left}^n$ and $\boldsymbol{U}_{\rm right}^n$ are known and $\boldsymbol{U}_{\rm left}^{n+1}$ and $\boldsymbol{U}_{\rm right}^{n+1}$ are to be determined. Different Riemann solvers exist, as described by e.g. Toro (1997). To find the solutions of a Riemann problem, it is

needed to determine the left and right states close to the discontinuity. For this, first order Godunov methods suppose that the average gas properties within a cell are constant, which implies that the state of the gas at the cell interfaces and at its center are identical. Instead of adopting this piecewise constant approach, piecewise linear methods interpolate the state of the gas from the center to the edges of the cell, such as what is done by the second order MUSCL (Monotone Upstream-centered Scheme for Conservative Laws) scheme implemented in RAMSES (Teyssier et al., 2006).

In order for the scheme to be stable, the timestep Δt must be sufficiently short so that no information can travel more than one cell of length Δx. In the simple case where gas is advected at a maximum velocity $u_{\max}$, this stability criterion reads:

$$\frac{u_{\max}\Delta t}{\Delta x} \leq C \tag{2.6}$$

where C is a parameter between 0 and 1 known as the Courant factor. This criterion is referred to as the CFL condition, after Courant, Friedrichs and Lewy, and applies at any level of the simulation grid in RAMSES, i.e. the timestep length is uniform for all cells on a given level.

2.2.4 Magnetohydrodynamics

Magnetic fields are ubiquitous in galaxies, and require a proper treatment in addition to gas dynamics, known as magnetohydrodynamics. The time evolution of a magnetic field, usually denoted $\boldsymbol{B}$ for the vector and B for its norm, follows the induction equation (derived from Maxwell and Faraday's equation and Ohm's law) which is:

$$\frac{\partial \boldsymbol{B}}{\partial t} = \nabla \times (\boldsymbol{u} \times \boldsymbol{B}) + \eta \nabla^2 \boldsymbol{B} \tag{2.7}$$

where η is the magnetic diffusivity, and $\boldsymbol{u}$ the plasma velocity. A plasma is an electrically conductive fluid, but we will indistinctly refer to plasma as "fluid" or "gas", under the assumption that they are magnetised. When there is a non perfect coupling between magnetic field lines and gas, non-ideal MHD processes arise. These processes consist of magnetic diffusion, whose nature varies with the state of coupling between charged and neutral species depending on gas density. However, non-ideal processes happen at very high gas densities ($\gtrsim 10^7\,\mathrm{cm}^{-3}$) and small scales ($\ll$ pc) typically not resolved in galaxy simulations. Therefore, magnetic diffusivity is negligible for galaxy and intergalactic medium scales. For this reason, we will only consider ideal MHD, where magnetic field lines are frozen to the gas and magnetic diffusivity vanishes ($\eta = 0$). Another important aspect regarding the magnetic field is the fact that it satisfies the divergence-free constraint according to the Maxwell-Thompson equation, i.e. $\nabla \cdot \boldsymbol{B} = 0$.

The ideal MHD equations are similar to the Euler equations previously written in the hydrodynamic case. While the mass conservation equation remains unchanged, the momentum and energy mass conservation equations include the contribution from the magnetic field and magnetic pressure $P_{\mathrm{mag}} = B^2/8\pi$ (in cgs units):

$$\frac{\partial \rho \boldsymbol{u}}{\partial t} + \nabla \cdot \left(\rho \boldsymbol{u} \otimes \boldsymbol{u} + P_{\rm tot} \boldsymbol{I} - \frac{\boldsymbol{B} \otimes \boldsymbol{B}}{4\pi} \right) = -\rho \nabla \Phi \tag{2.8a}$$

$$\frac{\partial \rho \epsilon}{\partial t} + \nabla \cdot \left((\rho \epsilon + P_{\rm tot}) \boldsymbol{u} - \frac{\boldsymbol{B}(\boldsymbol{B} \cdot \boldsymbol{u})}{4\pi} \right) = -\rho \boldsymbol{u} \cdot \nabla \Phi \tag{2.8b}$$

Both the total pressure $P_{\rm tot}$ and the total energy density ρe includes the magnetic component in addition to the kinetic and the thermal ones. We note that solving the Euler equations via the Godunov method described for HD simulations works similarly in an ideal MHD context. In addition to the classic HD sound wave, other types of propagating waves emerge: the so-called Alfvén waves whose speed is $u_A = B/\sqrt{4\pi\rho}$, and the fast and slow magnetosonic waves. Because the Alfvén waves are generally slower than the gas flow, the CFL condition mainly depends on gas velocity.

The presence of MHD waves requires the use of more sophisticated Riemann solvers than in the pure HD case, in order to solve the induction equation. To do this, one approach is to define the magnetic field as a volume average quantity, just as is done for the other HD variables. However, this does not ensure that $\nabla \cdot \boldsymbol{B} = 0$, and divergence cleaning techniques must be used in order to suppress the non-null divergence of the magnetic field (Brackbill & Barnes, 1980). Instead of defining the magnetic field like the HD quantities, another method consists of using a staggered mesh, where the magnetic field components (six in number in 3D simulations) are defined at the centers of the cell faces and represent the surface average over each of the cell faces. This alternative approach corresponds to the constrained transport (CT) method (Evans & Hawley, 1988), and is the one adopted in RAMSES (Teyssier et al., 2006). By construction, the CT technique satisfies the divergence-free condition, to machine precision provided that the initial magnetic field also does. Combined with the Godunov methodology, the CT algorithm solves the full set of ideal MHD equations, as explained by Fromang et al. (2006).

2.2.5 Radiation-hydrodynamics with RAMSES-RT

As stated in **Chapter 1**, radiation plays an important role on the thermal state of the gas, acts as a feedback source, and is responsible for the reionisation of the Universe. There is a non linear interplay between the emission of UV photons by young stars, the reionisation of the IGM via the escape of these energetic photons and the regulation of galaxy growth. All of these aspects involve complex interactions between radiation and gas, whose treatment requires coupling radiative transfer and hydrodynamics into radiation-hydrodynamics (RHD). For this purpose, RAMSES-RT is a RHD version of the RAMSES code, developed by Rosdahl et al. (2013) and Rosdahl & Teyssier (2015). We briefly summarise it below.

The basis of radiative transfer consists of describing how light is emitted and absorbed, and how it propagates. For photons of a frequency ν, at location x and time t, this can be quantified through the specific intensity I_ν, which is such that the total energy radiated through an elementary surface dA, in a solid angle $d\Omega$ along a direction $\boldsymbol{n}$ and during a time dt, is given by $I_\nu \, d\nu \, dA \, d\Omega \, dt$. The equation of radiative transfer (Mihalas & Mihalas, 1984) then describes the time evolution of I_ν for photons in a given frequency range $d\nu$ around ν, as:

$$\frac{1}{c}\frac{\partial I_\nu}{\partial t} + \boldsymbol{n}\cdot\nabla I_\nu = -\kappa_\nu I_\nu + \eta_\nu \ , \tag{2.9}$$

where κ_ν corresponds to an absorption coefficient and η_ν to a source term, both functions of x, t and $\boldsymbol{n}$, where c is the speed of light. To solve this equation, radiative transfer codes usually follow one of two approaches: either radiation is traced as rays, giving rise to ray-tracing scheme, or it is modelled as a radiation field instead of a ray, giving rise to moment-based method. The computational cost of the former increases with the number of radiative sources, which is an indisputable disadvantage in large cosmological simulations. Instead, the latter models photons as a fluid flowing at the speed of light, making it easier to couple RT to the Euler equations, but losing any information about the direction in which radiation propagates or the source it comes from.

Moment-based RT is precisely what is adopted in RAMSES-RT. It is so-called because it uses the angular moments of the RT equation 2.9, from which the radiative energy density E_ν, the radiative flux $\boldsymbol{f_\nu}$ and the radiative pressure tensor $\mathbb{P}_\nu$ are defined:

$$E_\nu = \frac{1}{c}\oint I_\nu \, d\Omega \tag{2.10a}$$

$$\boldsymbol{f_\nu} = \oint \boldsymbol{n} I_\nu \, d\Omega \tag{2.10b}$$

$$\mathbb{P}_\nu = \frac{1}{c}\oint \boldsymbol{n}\otimes\boldsymbol{n}\, I_\nu \, d\Omega \tag{2.10c}$$

Within RAMSES-RT, E_ν, $\boldsymbol{f_\nu}$ and $\mathbb{P}_\nu$ are actually divided by the photon energy $h\nu$ (where h is the Planck constant) in order to respectively evolve the number density of photons N_ν, the number density of flux $\boldsymbol{F_\nu}$ and the photon pressure tensor $\boldsymbol{\mathcal{P}_\nu}$, which ensures the conservation of the photon number instead of energy. Additionally, radiation in RAMSES-RT propagates over a continuum, which means that photons belong to a given interval of frequency instead of a narrow frequency range, as done in line transfer codes. Therefore, N_ν, $\boldsymbol{F_\nu}$ and $\boldsymbol{\mathcal{P}_\nu}$ can be written N_i, $\boldsymbol{F_i}$ and $\boldsymbol{\mathcal{P}_i}$, where i denotes a photon group, a package of photons that belongs to a fixed frequency interval, thereby discretising the light frequency distribution. Throughout the thesis, three groups of photons are considered: hydrogen ionising photons ($h\nu \in [13.6; 24.59]\,\mathrm{eV}$) and radiation that leads to singly ($h\nu \in [24.59; 54.42]\,\mathrm{eV}$) and doubly ($h\nu > 54.42\,\mathrm{eV}$) ionised helium.

By taking the zeroth and first angular moments[3] of Equation 2.9 and replacing the moments of the specific intensity by N_i, $\boldsymbol{F_i}$ and $\boldsymbol{\mathcal{P}_i}$, we end up with one equation describing the conservation of the radiative energy (or equivalently here the photon number density, Equation 2.11a) and three equations (in 3D) for the conservation of the radiative flux (Equation 2.11b), for each photon package:

$$\frac{\partial N_i}{\partial t} + \nabla\cdot\boldsymbol{F_i} = -\kappa_i c N_i + S_i \tag{2.11a}$$

$$\frac{\partial \boldsymbol{F_i}}{\partial t} + c^2\nabla\cdot\boldsymbol{\mathcal{P}_i} = -\kappa_i c \boldsymbol{F_i} \tag{2.11b}$$

[3]The nth moment of a function $f(x)$ is the integral over dx of $x^n f(x)$.

S_i corresponds to an isotropic source term, including the (stellar) injection rate of photons $\dot{N}_i^{\rm inj}$ and radiation coming from the recombination of electrons with the ionised gas $\dot{N}_i^{\rm rec}$. κ_i represents the weighted average absorption coefficient for the photon group i, where absorption mainly comes from the ionisation of hydrogen and helium. As this absorption term is the sum of the interaction between photons from the group i and n_j atoms or ions of species j, it directly depends on the cross section $\overline{\sigma}_{ij}$ of a photon i interacting with an atom or ion j. We can therefore write $\kappa_i = \Sigma_j n_j \overline{\sigma}_{ij}$.

In 3D, these four RT equations describe the state of 13 variables (one for the energy, 3 for the flux, and 3x3 for the pressure tensor). Therefore, just as for the Euler equations, a closure relation is needed to close the system of equations. For this purpose, RAMSES-RT adopts the M1 closure relation (Levermore, 1984), which consists of making the link between the pressure tensor and the radiative energy thanks to the Eddington tensor $\boldsymbol{D_\nu}$. With our frequency-discretised approach, this reads $\boldsymbol{\mathcal{P}_i} = \boldsymbol{D_i} N_i$, and the Eddington tensor for photons of group i is:

$$\boldsymbol{D_i} = \frac{1-\chi_i}{2}\boldsymbol{I} + \frac{3\chi_i - 1}{2}\boldsymbol{n_i} \otimes \boldsymbol{n_i} \ , \tag{2.12}$$

where $\chi_i = \frac{3+4f_i^2}{5+2\sqrt{4-3f_i^2}}$ with $f_i = |\boldsymbol{F_i}|/cN_i$. Once the Eddington tensor is computed, the two moment equations can be solved with the Godunov methodology, just as for HD and MHD equations.

The first step in a RAMSES-RT computation is to propagate radiation by omitting any interaction with the surrounding gas. This corresponds to solving Equation 2.11a and Equation 2.11b without their right-hand side, which is analoguous to the Euler equations: radiative fluxes have to be evaluated at cell interfaces, which is done by means of the Godunov method, using a Riemann solver.

The next step is to determine the injection rate of photons for each group, which contributes to S_i in Equation 2.11a. The photons are injected from radiative sources, which are stars in our simulations. As previously stated, stars in RAMSES are stellar particles that represent stellar populations. Depending on their age and their metallicity, the stellar particles have a specific energy spectrum, described by a spectral energy distribution (SED). The injection of ionising photons in RAMSES-RT therefore relies on integrating the spectra of all the stellar particles from the simulation. This gives information about the luminosity (or energy) emitted by the "stars" for a given range of frequency, converted into a number density of photons dN_i which is addded to the previous number density of photons in cell i at time t N_i^t to get $N_i^{t+\Delta t} = N_i^t + dN_i$.

The last step consists of coupling radiation and hydrodynamics to evolve gas thermochemistry. Gas that absorbs photons is heated and ionised, while photons emitted from recombinations cool the gas, impacting both gas temperature and the ionisation state of hydrogen and helium. Equations 2.11a and 2.11b have to be finally solved with their right-hand side, using the updated values for the photon densities and fluxes, and finally taking into account the absorption and recombination rates. Within this step, the fractions of ionised hydrogen and helium are updated depending on collisional ionisations, photoionisations (adding the potential contribution of a homogeneous UV background) and recombinations. Once determined, the ionisation state of the gas is used to update the photoheating and radiative cooling

rates that contribute to the Euler energy conservation equation (Equation 2.3c for HD and Equation 2.8b for MHD). The cooling function may also include the tabulated contribution from atomic metal cooling for gas hotter than 10^4 K (Ferland et al., 1998) and from fine-structure line cooling for gas colder than 10^4 K (using the fitting function from Rosen & Bregman, 1995). All the detailed equations are described by Rosdahl et al. (2013). In the end, solving the RT equation combined to the (M)HD equations change the gas internal energy, which translates into changes in gas temperature.

It has to be noted that radiation transport, injection and the thermochemistry steps impose a new constraint on the minimum time-step required for the stability of the RT numerical scheme. Globally, light propagates at a speed of $3 \times 10^5\,\mathrm{km\,s^{-1}}$, which is at least a few hundred times faster than gas. Following the CFL condition, the time-steps have to be accordingly a hundred times smaller for the RT calculation as opposed to only the gas dynamics calculation. To reduce the computing time cost associated to radiation propagation, one way to proceed is to decrease the speed of light, as initially described by Gnedin & Abel (2001). Instead of using the same reduced values for all the grid, one may also vary the speed of light according to the refinement level of the cells, going from a reduced to a variable speed of light approximation (Katz et al., 2017). In many regimes, Rosdahl et al. (2013) showed that reducing the speed of light by a few orders of magnitude is valid as long as the propagation of the fastest radiation front remains slower than the reduced speed of light. Provided there is a careful choice of the reduced speed of light, reducing the hydro time-step down to the RT one then leads to accurate solutions, at a moderate computing time cost.

After the RT steps and for each cell, RAMSES-RT stores and saves the three components of the photon flux and the ionisation state of each photon group. In our RMHD simulations, we combine RAMSES-RT to the MHD solver from Fromang et al. (2006) described in the previous section, which adds 21 variables to the 6 already stored in purely hydro runs (density, 3 velocity components, thermal pressure and metallicity for HD, 3 variables for HI, HeI and HeII ionisation fractions, 12 RT variables for the photon density N and the 3D flux $\boldsymbol{F}$ of the three photon groups, and 6 variables for the 3D left and right states of the magnetic field).

2.2.6 Star formation sub-grid models

Even though simulations of galaxy evolution span orders of magnitude in length and time-scales, they cannot capture all the relevant scales involved in star formation, and do not directly model how single stars emerge from the collapse and the fragmentation of dense molecular clouds. Instead, sub-grid models are used to encapsulate the processes happening at scales that are unresolved. With these prescriptions, stars are represented as stellar particles of from hundreds to several thousands of solar masses that correspond to stellar populations, as previously stated in this chapter. The aim of this section is now to explain how gas is converted into stellar particles in RAMSES.

The star formation model in RAMSES was initially implemented by Rasera & Teyssier (2006). When gas density ρ within a cell exceeds a certain threshold ρ_{thres}, star particles form at a rate $\dot{\rho}_*$, converting gas during a free fall time t_{ff} with an

efficiency ϵ_*:

$$\dot{\rho}_* = \frac{\epsilon_* \rho}{t_{\rm ff}} \tag{2.13}$$

Then, cells that are flagged as star-forming stochastically generate N particles of mass m_0 with a probability $P(N)$, following a Poisson distribution of mean value λ:

$$P(N) = \frac{\lambda^N}{N!} e^{\lambda} \tag{2.14}$$

For a time-step Δt and a cell width Δx, the Poisson parameter λ is:

$$\lambda = \frac{\rho \Delta x^3}{m_0} \frac{\Delta t}{t_{\rm ff}} \tag{2.15}$$

The particles generated in the cell are gathered into one stellar particle of mass $m_* = N \times m_0$, and the corresponding mass of gas needed to form this stellar particle is removed from the cell. Therefore, with this method, the conversion rate described in Equation 2.13 holds on average.

For some of the simulations studied in the thesis, star formation depends on a constant star formation efficiency $\epsilon_* = 0.02$, and is allowed when $\rho > \rho_{\rm thres} = 100$ H cm^{-3}. Throughout the thesis, we refer to this star formation (SF) model as the density SF model. Recently, a more physically motivated model has been implemented in RAMSES by Julien Devriendt, as described by Kimm et al. (2017) and Trebitsch et al. (2017). This model, that we will refer to as the turbulent SF model, is the fiducial model adopted in the simulations I performed. It relies on the fact that turbulent support adds to thermal pressure to act against gas compression at star formation scales. Under this prescription and in addition to the $\rho > \rho_{\rm thres}$ criterion, cells are flagged as star forming only if gas is gravitationally unstable. This means that the turbulent Jeans length $\lambda_{\rm J,turb}$ has to be unresolved, or equivalently that the cells at the highest level of refinement have a width Δx larger than $\lambda_{\rm J,turb}$, defined as:

$$\lambda_{\rm J,turb} = \frac{\pi \sigma_{\rm gas}^2 + \sqrt{36\pi c_s^2 G \Delta x^2 \rho + \pi^2 \sigma_{\rm gas}^4}}{6 G \rho \Delta x}, \tag{2.16}$$

where $\sigma_{\rm gas}$ is the gas velocity dispersion, computed using the velocity gradients in neighbouring cells, and c_s is the local sound speed. In the turbulent SF model, while stars still form following Equation 2.13, ϵ_* is not a constant globally defined value anymore, but it is a local star formation efficiency that varies with gas properties. The definition of this local ϵ_* is based on the work of Padoan & Nordlund (2011) and Federrath & Klessen (2012), and its implementation in RAMSES is detailed by Kimm et al. (2017). With this recipe, ϵ_* directly depends on the ratio between the gas velocity dispersion and the local sound speed, better accounting for the fact that turbulence may prevent or encourage gas compression. As a result, stars form less homogeneously with the turbulent SF model than with the density one, and in a more bursty way, which has some consequences on galaxy evolution that are studied in **Chapter 3**.

2.2.7 Supernova feedback sub-grid models

Stars more massive than $8\,M_\odot$ explode as SNe, releasing an energy E_{SN} of the order of 10^{51} erg. During the process, energy and momentum blow away mass and metals that enrich the ISM, and that can even reach the CGM when carried by winds generated by the explosion. As described in **Section 1.2.2**, this dramatically impacts galaxies, by regulating in particular star formation: this process is SN feedback. Because individual stars are not modelled in RAMSES, SN feedback takes the form of single or multiple, instantaneous or delayed injections of SN energy per stellar particle. Following a specific IMF (which describes the number of stars formed per Solar mass bin), we can infer the expected number of SN produced per Solar mass of stars formed ζ_{SN}. For instance, integrating a Kroupa IMF from 8 to 100 $M_\odot$ leads to $\zeta_{SN} \simeq 0.01\,M_\odot^{-1}$, which means that one SN explosion happens each time 100 $M_\odot$ are formed. In the context of RAMSES, this means that a stellar particle exploding as SN releases $\sim 10^{49}\,\mathrm{erg}\,M_\odot^{-1}$, and the most basic way to inject such energy is to instantaneously put it in the cell hosting the stellar particle and its neighbouring cells. To be more realistic, one can ask to wait a few Myr after the birth of the stellar particles, to better mimic the fact that massive stars explode after between 3 and 50 Myr. However, this does not take into account the fact that the stellar particles represent a stellar population, encapsulating stars of different masses that are unlikely to explode at the same moment. To overcome this aspect, Kimm et al. (2015) implemented a model to follow stellar particles undergoing N_{SN} SN explosions, each of them occurring after a time delay determined stochastically from sampling the lifetime of massive stars. The number of explosions is $N_{SN} = m_* \eta_{SN} / M_{SN}$, where m_* is the mass of the stellar particle, η_{SN} is the mass fraction of the stellar population exploding as Type II SNe (0.2 for a Kroupa IMF) and M_{SN} is the average mass of the exploding stars (20 $M_\odot$ for a Kroupa IMF). This multiple SN explosion prescription is the fiducial model adopted in my galaxy simulations, as it is the one used in SPHINX (see **Section 2.4**). In the latter, the SN feedback is boosted to allow four times more SN explosions per stellar particle, in order to sufficiently regulate star formation at high-redshift.

Now that we have explained how SN explosions are modelled in RAMSES, we have to describe how the SN energy is injected and propagates in the ISM. Whether it be through single or multiple explosions, the most basic way to model SN feedback is to inject the energy, mass and metals blown by the explosion in the cell hosting the SN, and remove the corresponding mass from the stellar particle. As the temperature of the cell rises, this SN feedback prescription is also known as the thermal dump model. With this simple model, one major issue arises. If the resolution of the simulation is not high enough ($\lesssim 3$ pc for a SN explosion releasing 10^{51} erg in a medium at a density of $100\,\mathrm{cm}^{-3}$, see Kim & Ostriker, 2015), the Sedov-Taylor phase of the SNR is not resolved. The SN energy then directly suffers from dramatic radiative losses, completely diluting any effect from SN feedback (see also **Section 1.2.2**). To overcome this so-called overcooling problem (Katz et al., 1996), different sub-grid models exist and are implemented in RAMSES, and have been notably studied by Rosdahl et al. (2017). Among the first of them, Dubois & Teyssier (2010) implemented a kinetic SN feedback model, in which kinetic (instead of thermal) energy is distributed in cells that belong to a given region around the SN host cell. The portion of energy deposited in the cells increases with distance from

the SN host to mimic the increasing velocity of the SNR from the ideal Sedov-Taylor solution (see also Fig. 1.11), which avoids the spurious energy losses that occur close to the unresolved SNR. Another method, developed by Teyssier et al. (2013), keeps injecting thermal energy in the host cell but turns off any radiative cooling for a certain time, while the local turbulence is significant, and is hence referred to as the delayed cooling thermal feedback. However, one would ideally circumvent the overcooling problem without artificially removing energy losses, which are a physical feature of the evolution of a SNR, but rather by injecting the correct energy budget regardless of the phase of the remnant. To this end, Kimm & Cen (2014) implemented in RAMSES a mechanical feedback model, in which momentum (instead of energy) is injected in the close neighbourhood of the SN host cell (for details, see also Kimm et al., 2015; Rosdahl et al., 2017). With this method, the radial momentum deposited in each cell depends on the local resolution, in order to determine if the momentum has to be that of the Sedov-Taylor or the snowplough phase, respectively defined by the SN energy conservation and by gas density and metallicity (as cooling depends on density and metallicity, see Blondin et al., 1998; Thornton et al., 1998). Doing so, this model limits the numerical radiative losses due to a lack of resolution. This is the most physically-motivated SN sub-grid model implemented in RAMSES, and it is consequently the prescription adopted in SPHINX and in the simulations performed within the framework of this thesis. It is worth mentioning also that the mechanical feedback model, especially when combined with individual SN explosions, is the best converged with resolution of all models in RAMSES (Maxime Rey, private communication).

2.3 Simulations of cosmic rays

The key physical ingredient investigated throughoutthis thesis is feedback from CRs. However, there is a huge difference between simulations of CRs and simulations of CR feedback in galaxy simulations. In this section, I propose to first review the different equations and approaches that allow modelling of the transport of CRs, mainly relying on the comprehensive reviews from Marcowith et al. (2020) and Hanasz et al. (2021). This will provide the motivation and foundation to then focus more specifically on how CRs are implemented in galaxy simulation codes, and to state what is in place in RAMSES and used in this thesis.

2.3.1 How to model cosmic rays

Modelling billions of billions of particles as small as protons and almost as fast as photons is a real challenge. In the context of galaxy formation, it becomes impossible to numerically combine cosmic rays with ISM and CGM scales. Depending on what aspect of CRs is studied, a choice must be made between adopting a microscopic or a macroscopic perspective. When interested in the trajectory of CRs, microscopic models that follow the transport of particles are best. On the other hand, if the parameter of interest is the energy of CRs and their back-reaction, CRs have to be coupled to their environment, through their interplay with magnetic, thermal and kinetic energies. In this case, the most affordable and efficient method is to rely on macroscopic prescriptions, gathering CR properties into macroscopic tracer

particles, or treating collisionless CRs as a fluid. Additionally, adopting a kinetic particle approach or a fluid prescription depends on the energy, the number and the type of particles considered. Very high-energy CRs, such as those having a gyration radius that exceeds the size of our Galaxy (CR energy above 10^{19} eV, see Fig. 1.14), are very rare and barely interact with gas. Because the scattering of high energy CRs is inefficient, it is more appropriate to regard them as particles moving ballistically, and to favour kinetic models. Conversely, lower energy CRs may be confined in the Galactic disk and interact with the ISM gas, so that their dynamical impact becomes of a particular interest, and fluid models are preferred. This mainly holds for CR hadrons, while CR electrons do not have a dynamical impact on galaxies. For this reason, they can either be treated as passive tracer particles or a passive fluid. We now detail some of the particularities of the different approaches mentioned, in order to explain how microscopic kinetic CR models distinguish themselves from fluid macroscopic models of CR feedback such as the one used in this thesis.

Kinetic models

In microscopic kinetic models, CRs are considered as individual particles, and tracked at small spatial scales. This approach is preferentially used in plasma studies, in order to investigate how charged particles are accelerated and propagate. For this purpose, it is necessary to disentangle the interplay between the particle distribution function and the electromagnetic field. The electric and the magnetic fields $\boldsymbol{E}$ and $\boldsymbol{B}$ satisfy Maxwell's equations, and impact the trajectory of CRs via the Lorentz force:

$$\boldsymbol{F}_{\rm Lorentz} = \frac{d\boldsymbol{p}}{dt} = q\left(\boldsymbol{E} + \frac{\boldsymbol{v}}{c} \times \boldsymbol{B}\right) \tag{2.17}$$

where $\boldsymbol{p}$ is the particle momentum, q its charge, and $\boldsymbol{v}$ its velocity. In the absence of any dissipative process, the energy of CRs is conserved, and so is the number of particles. If we define $f(t, \boldsymbol{x}, \boldsymbol{p})$ as the distribution function of CRs at a time t, located at space $\boldsymbol{x}$ with momentum $\boldsymbol{p}$, $df/dt = 0$, following Liouville's theorem. This time-independence assumption, valid in an unperturbed electromagnetic field, is at the basis of the so-called quasi-linear theory (Jokipii, 1966), which is the main theory used for CR transport studies. Following Liouville's theorem, the evolution of the CR distribution function satisfies the Vlasov equation, which, for a collisonless plasma, is:

$$\frac{df}{dt} = \frac{\partial f}{\partial t} + \frac{d\boldsymbol{x}}{dt} \cdot \nabla_{\boldsymbol{x}} f + \boldsymbol{F}_{\rm Lorentz} \cdot \nabla_{\boldsymbol{p}} f = 0 \tag{2.18}$$

where $\nabla_{\boldsymbol{x}} = \nabla = (\partial/\partial x, \partial/\partial y, \partial/\partial z)$ and $\nabla_{\boldsymbol{p}} = (\partial/\partial p_x, \partial/\partial p_y, \partial/\partial p_z)$. Therefore, solving the microscopic CR transport in kinetic models relies on solving the Maxwell and Vlasov equations. To solve this system of equations, the numerical procedure is as follows (see e.g. Marcowith et al., 2020). At the initialisation stage, an initial particle distribution function $f(t = 0, \boldsymbol{x}, \boldsymbol{p})$ is defined for each CR species, and the electric and magnetic fields emerge out of any external or non-zero fields, satisfying respectively Maxwell-Gauss equation ($\nabla \cdot \boldsymbol{E} = 4\pi\rho$, where ρ is the charge density) and the divergence-free requirement ($\nabla \cdot \boldsymbol{B} = 0$). Both the CR distribution and the electromagnetic field are discretised onto a grid. At each time-step, the idea is to 1)

evolve the CR distribution functions, 2) update the charge and current densities and 3) update the electric and magnetic fields. For the latter step, this is achieved by means of Maxwell-Ampère and Maxwell-Faraday equations. But before the charge and current densities and the electromagnetic field can be updated, the main step consists in evolving the distribution functions for all the CR species considered. For this purpose, two methods exist. On the one hand, so-called Vlasov codes rely on directly integrating the Vlasov equation on the grid. To reduce the high numerical complexity of this integration, another category of code instead considers CRs as discrete macro-particles that belong to specific cells of the simulation, and is naturally termed as "particle in cell" (PIC). For each CR species, the distribution function becomes the sum of a fixed number of macro-particles. The Lorentz force is first computed to determine the momentum of each macro-particle, before its position can be updated: this is therefore a simplified analogue of resolving the Vlasov equation (see also Feix & Bertrand, 2005, for details and comparison between Vlasov and PIC codes).

From kinetic to fluid models

In the Vlasov equation, the interactions that the charged particles may have with each other are modelled through their long-range contribution to the electromagnetic field, which impacts their trajectory. From another point of view, one may consider how a particle at a time t is deflected, regardless of its previous positions. By definition, this corresponds to a Markov process, where the state of a system at a given time does not depend on its history. For CRs, this translates into a diffusive behaviour: when the irregularities of the magnetic field are comparable in size to the gyration radius of a charged particle (see Equation 1.13), the latter is scattered with a pitch angle $\theta = \arccos(\mu)$. While this is a random walk at discrete times, the ensemble of stochastic random displacements corresponds, on average, to a diffusive propagation, characterised by the surface crossed by a particle in a certain time. Mathematically, we describe the diffusive propagation of the CR particles by the Fokker-Planck equation:

$$\frac{\partial F}{\partial t} + \frac{d\boldsymbol{x}}{dt} \cdot \nabla_{\boldsymbol{x}} F = \frac{\partial}{\partial \mu} \left(D_{\mu\mu} \frac{\partial F}{\partial \mu} \right) \tag{2.19}$$

where F corresponds to the CR distribution function $f(t, \boldsymbol{x}, \boldsymbol{p})$ averaged over the phase-space, and $D_{\mu\mu}$ to the diffusion coefficient, in units of area per time. Usually, one gets rid of the information about μ in order to write Equation 2.19 as a function of time, space and momentum only. When we write the CR distribution function as a function of space (instead of the pitch angle cosine μ) and include CR adiabatic processes and losses to couple them with the ambient gas, this leads to the canonical equation of CR propagation:

$$\begin{aligned} \frac{\partial F}{\partial t} = & - \boldsymbol{u} \cdot \nabla F + \nabla \cdot (\boldsymbol{D}_{\boldsymbol{xx}} \cdot \nabla F) + \frac{1}{3} (\nabla \cdot \boldsymbol{u}) \, p \frac{\partial F}{\partial p} \\ & + \frac{1}{p^2} \frac{\partial}{\partial p} \left[p^2 \left(Q_{\text{loss}} F + D_{pp} \frac{\partial F}{\partial p} \right) \right] + Q_{\text{CR}} \end{aligned} \tag{2.20}$$

Here, u is the velocity at which CRs are advected, corresponding to the sum of gas velocity and CR streaming velocity, and $\boldsymbol{D_{xx}}$ is the spatial diffusion tensor. The third term on the right-hand side of the equation corresponds to adiabatic processes. For the sake of completeness, the diffusion coefficient in momentum space D_{pp} is also added, in order to model CR (re)acceleration via second order Fermi processes (see **Section 1.3**). Eventually, $Q_{\rm loss}$ encapsulates CR losses, via Coulomb and hadronic interactions, and $Q_{\rm CR}$ denotes CR sources.

Equation 2.20 is the basis of modern CR propagation codes. In most cases, it is useful to know the evolution of the CR number density $n_{\rm CR}$ or the CR energy density $e_{\rm CR}$. For this purpose, the transport of particles with the same momentum p is computed, enabling a decomposition of the CR spectrum, either in terms of number density $n(p)dp = 4\pi p^2 F(p)$ or energy density $e(p)dp = 4\pi p^2 T(p) F(p)$, where $T(p)$ corresponds to the CR kinetic energy. This approach is especially used by phenomenological codes, such as GALPROP (Strong & Moskalenko, 1998), DRAGON (Gaggero et al., 2014; Evoli & Yan, 2014), USINE (Putze et al., 2011; Maurin, 2020) and PICARD (Kissmann, 2014). Their main idea is to model CR transport in our Milky-Way, focusing on the different CR species, and to compare the results from CR propagation with observations in terms of secondary-to-primary ratios and gamma-ray emission. For this purpose, a version of Equation 2.20 describing the density of CRs per unit of total particle momentum is solved on a spatial grid, whose boundaries correspond to our Galaxy disk. The different parameters governing CR transport can be defined by the user, relying for instance on turbulence models to approximate the values of the diffusion coefficients.

Because of their physical and computational complexity, phenomenological codes usually do not account for any dynamical coupling between CRs and the thermal plasma. To consistently study the effects of CRs on galaxies, so-called self-consistent models are necessary, such as the ones I used for the simulations presented in **Chapter 1.3** (see also **Appendix A**). CR species are no longer considered: instead, the CR spectrum is decomposed into bins of energy, and each of them is modelled as a non-thermal fluid. The CR propagation equation may also be simplified, by assuming constant injection of CR energy and a constant diffusion coefficient, that phenomenological codes can constrain. The fluid approximation is valid for collisionless particles, such as in the GeV regime where most CR energy density resides (Strong et al., 2007; Trotta et al., 2011). These CRs are frequently scattered by the magnetic field, as their energy confines them relatively close to the magnetic field lines and for a relatively long time in galaxies. Therefore, as long as CRs are described as a hydrodynamical fluid on scales larger than their mean free path, coupling the CR advection-diffusion propagation equation to the MHD equations is particularly well suited to study CR feedback at galaxy scales.

Cosmic ray feedback with fluid models

Usually in galaxy simulations, the CRs considered are the particles with energies around a few GeV, and are modelled as a relativistic fluid. Under this so-called grey approximation, the CR pressure $P_{\rm CR}$ is related to the CR energy density $e_{\rm CR}$ in a similar way as the thermal component, that is to say $P_{\rm CR} = (\gamma_{\rm CR} - 1) e_{\rm CR}$, where $\gamma_{\rm CR} = 4/3$ for a relativistic fluid. Following the theoretical work by Drury & Voelk (1981) and Axford et al. (1982), the first step for self-consistent methods

is to integrate the CR transport equation (Equation 2.20) in momentum space in order to evolve the CR energy density in a single momentum bin (for a complete derivation of the CR macroscopic fluid description from the kinetic prescription, see e.g. Zweibel, 2017.):

$$\begin{aligned}\frac{\partial e_{\rm CR}}{\partial t} =& -\nabla\cdot(e_{\rm CR}\boldsymbol{u}+(e_{\rm CR}+P_{\rm CR})\boldsymbol{u_{st}})\\ &-P_{\rm CR}\nabla\cdot\boldsymbol{u}-\nabla\cdot\boldsymbol{F_{CR}}-\Lambda_{\rm st}-\Lambda_{\rm CR}+Q_{\rm CR}\end{aligned} \tag{2.21}$$

Here, $\boldsymbol{u}$ corresponds to the gas velocity and $\boldsymbol{u_{st}}$ to the streaming velocity. Therefore, the first term on the right-hand side corresponds to CR advection with gas and advection-diffusion from streaming instabilities. The streaming velocity is $\boldsymbol{u_{st}} = -f_{\rm b}\boldsymbol{u_A}\frac{\boldsymbol{B}\cdot\nabla e_{\rm CR}}{|\boldsymbol{B}\cdot\nabla e_{\rm CR}|}$, where $\boldsymbol{u_A}$ is the Alfvén velocity and $f_{\rm b}$ corresponds to a boost factor, to take into account Alfvén wave damping processes that increase the streaming velocity by a factor of a few compared to $\boldsymbol{u_A}$. We remind the reader that the Alfvén velocity is $\boldsymbol{u_A} = \boldsymbol{B}/\sqrt{4\pi\rho}$, where ρ is the gas density. The second term on the right-hand side of the equation corresponds to pressure work, through which CR energy increases or decreases upon adiabatic contraction or expansion, respectively. The next term encapsulates CR diffusion via the CR diffusion flux $\boldsymbol{F_{CR}}$. For anisotropic diffusion parametrised by a diffusion coefficient D, the instantaneous flux may be written $\boldsymbol{F_{CR}} = -D\boldsymbol{b}(\boldsymbol{b}\cdot\nabla e_{\rm CR})$, where $\boldsymbol{b} = \boldsymbol{B}/|\boldsymbol{B}|$ is the magnetic field unit vector. The diffusion coefficient D varies with local MHD quantities such as the turbulence and with the CR momentum. In most cases, it is however taken as a constant effective value κ varying between $10^{27}\,{\rm cm^2\,s^{-1}}$ and a few times $10^{29}\,{\rm cm^2\,s^{-1}}$. $\Lambda_{\rm st}$ corresponds to a heating term due to streaming, as CRs scattering off of Alfvén waves lead to work transferred to the thermal component, which heats the gas. Therefore, we can write $\Lambda_{\rm st} = \frac{\boldsymbol{B}\cdot\nabla e_{\rm CR}}{|\boldsymbol{B}\cdot\nabla e_{\rm CR}|}\boldsymbol{u_A}\cdot\nabla P_{\rm CR}$. $\Lambda_{\rm CR}$ refers to radiative losses from CRs, which also partly heat the gas. We do not distinguish between catastrophic losses, due to hadronic interactions with gas depending on the CR cross section, and continuous losses arising from Coulomb collisions, synchrotron, inverse Compton or bremsstrahlung processes. Finally, $Q_{\rm CR}$ represents the energy source term of CRs, usually coming from SN explosions that give them a part of the kinetic energy they release. Depending on the code, the numerical treatment of Equation 2.21 differs, and other terms such as the CR diffusion coefficient in momentum space neglected here can be added.

Coupling Equation 2.21 with the MHD equations allows one to both propagate CR energy and to account for its effect on gas, and therefore on galaxy dynamics. Because this method solves the evolution of a non thermal fluid (CRs) and a thermal one (gas), it is also referred to as the two-fluid diffusion-advection model. One limitation of the fluid description of CRs explained so far is the grey approximation, which assumes that the whole CR population behaves similarly regardless of its energy. To better study CR feedback, more complex models have been developed. Instead of integrating the CR properties over a full momentum range as the two-fluid approach does, they solve the transport and interactions of CRs by discretising spatial and momentum spaces (Hopkins et al., 2021c; Girichidis et al., 2022). These models rely on the fact that the CR spectrum can be approximated by power-laws, in order to solve the Fokker-Planck equation with an ensemble of

piecewise power laws (Miniati, 2001; Jones & Kang, 2005), similar to what the phenomenological codes do. The transport equation is then solved either for the $n_{\rm CR}$ or $e_{\rm CR}$ moments of the CR distribution function (one moment method) or both of them (two moment methods), sampling the CR population into bins of different energies with their distinct behaviours (adiabatic index, momentum dependent diffusion coefficient, energy losses). While spectrally resolved CR models may thus provide a more accurate treatment of CR feedback, their computational and memory cost are significant. In this thesis, we focus on the simpler two-fluid advection-diffusion model implemented in RAMSES, that we describe in the next section.

2.3.2 Cosmic ray magnetohydrodynamics in RAMSES

The prescription adopted in RAMSES to compute CR feedback with MHD relies on Equation 2.21 previously described. CRs from the GeV regime are modelled as a relativistic fluid with $\gamma = 4/3$, adding an extra variable corresponding to the CR non-thermal pressure to the 27 variables tracked and stored in RMHD simulations. CR transport is described by one equation which evolves the CR energy density with time, and the total energy equation includes their contribution to account for their dynamical effect on gas. The transport of CRs consists of advection with gas, diffusion along magnetic field lines at a constant diffusion coefficient κ, and streaming proportional to the Alfvén speed. The streaming advection term $\nabla\cdot((e_{\rm CR}+P_{\rm CR})\boldsymbol{u_{\rm st}})$ is recast into a diffusion term $\nabla\cdot\boldsymbol{F_{\rm CR,st}}$ using the definition of $\boldsymbol{u_{\rm st}}$, which gives:

$$\begin{aligned}\nabla\cdot\boldsymbol{F_{\rm CR,st}} &= \nabla\cdot(-D_{\rm st}\boldsymbol{b}(\boldsymbol{b}\cdot\nabla e_{\rm CR}))\\ &= \nabla\cdot\left(-\frac{(e_{\rm CR}+P_{\rm CR})|\boldsymbol{B}|}{\sqrt{4\pi\rho}}\boldsymbol{b}\frac{\boldsymbol{b}\cdot\nabla e_{\rm CR}}{|\boldsymbol{b}\cdot\nabla e_{\rm CR}|}\right)\end{aligned} \tag{2.22}$$

where $D_{\rm st} = \frac{(e_{\rm CR}+P_{\rm CR})|\boldsymbol{B}|}{\sqrt{4\pi\rho}|\boldsymbol{b}\cdot\nabla e_{\rm CR}|}$ (omitting the damping of the Alfvén waves with $f_{\rm b}=1$). By combining $\boldsymbol{F_{\rm CR}}$ and $\boldsymbol{F_{\rm CR,st}}$, we end up with a diffusive flux given by $\boldsymbol{F_{\rm CR,d+st}} = -D_{\rm CR}\boldsymbol{b}(\boldsymbol{b}\cdot\nabla e_{\rm CR})$ where $D_{\rm CR} = D + D_{\rm st}$. In RAMSES, $D=\kappa$ is constant[4], and is a parameter defined by the user. Therefore, CRs both diffuse and stream along magnetic field lines, and streaming additionally follows the CR pressure gradient.

Defining the total and thermal energy densities $e=\rho\epsilon$ and $e_{\rm th}=\rho\epsilon_{\rm th}$ respectively, and $e_{\rm CR}$ the CR energy density, the two CR-MHD equations coupling CRs and gas dynamics are[5]:

$$\frac{\partial e}{\partial t} + \nabla\cdot\left((e+P_{\rm tot})\boldsymbol{u} - \frac{\boldsymbol{B}(\boldsymbol{B}\cdot\boldsymbol{u})}{4\pi}\right) = \rho\boldsymbol{u}\cdot\nabla\Phi + Q_{\rm CR} + Q_{\rm th} - \Lambda_{\rm rad} - \Lambda_{\rm CR} - \nabla\cdot\boldsymbol{F_{\rm CR,d+st}} \tag{2.23a}$$

$$\frac{\partial e_{\rm CR}}{\partial t} + \nabla\cdot(e_{\rm CR}\boldsymbol{u}) = -P_{\rm CR}\nabla\cdot\boldsymbol{u} + Q_{\rm CR} - \Lambda_{\rm CR} - \Lambda_{\rm st} - \nabla\cdot\boldsymbol{F_{\rm CR,d+st}} \tag{2.23b}$$

[4] We use D as the CR diffusion coefficient in general, and κ as the specific case D is constant.

[5] The other equations are the same as for the pure (M)HD case described in **Section 2.2.3** and **Section 2.2.4**)

The total energy density is $e = \frac{\rho \boldsymbol{u}^2}{2} + e_{\rm th} + \frac{\boldsymbol{B}^2}{8\pi} + e_{\rm CR}$, including kinetic, thermal, magnetic and CR energy densities. Similarly, the total pressure includes the contribution of the thermal, CR and magnetic components: $P_{\rm tot} = P_{\rm th} + P_{\rm CR} + P_{\rm mag}$. We now expand on the remaining terms and explain how the CR-MHD equations are solved numerically.

Thermal and cosmic ray injection

$Q_{\rm th}$ and $Q_{\rm CR}$ respectively correspond to thermal and CR energy source terms. In particular $Q_{\rm th}$ includes heating from the UV background and collisional CR heating, being a fraction of $\Lambda_{\rm CR}$ as described below. In RAMSES, the injection of CR energy via $Q_{\rm CR}$ corresponds to a fraction $f_{\rm ecr}$ of the energy released by SN explosions. From observations of local SNR (Hillas, 2005; Strong et al., 2010; Morlino & Caprioli, 2012; Dermer & Powale, 2013; H. E. S. S. Collaboration et al., 2018), the canonical value usually adopted in galaxy simulations is $f_{\rm ecr} = 0.1$. Regardless of the SN feedback model adopted, each SN explosion therefore releases an energy $(1 - f_{\rm ecr}) \times E_{\rm SN}$ and a CR energy $f_{\rm ecr} E_{\rm SN}$, with usually $\mathrm{E_{SN}} = 10^{51}$ erg. With the mechanical SN feedback used in all the simulations presented in this thesis, the CR energy is directly injected into the cell hosting the SN, before being propagated in the neighbouring cells.

Cosmic ray energy losses

$\Lambda_{\rm th}$ and $\Lambda_{\rm CR}$ respectively correspond to radiative cooling of thermal and CR components. Both of them are computed after each MHD timestep, and contribute to the evolution of the total energy budget. If we consider CRs as GeV protons, two main loss processes are responsible for CR cooling. On the one hand, CRs transfer a part of their energy to the ambient gas via Coulomb collisions. Following (Guo & Oh, 2008), the Coulomb loss rate of CRs $\Lambda_{\rm C}$ is:

$$\Lambda_{\rm C} = 1.65 \times 10^{-16} \left(\frac{n_e}{\mathrm{cm^{-3}}}\right) \left(\frac{e_{\rm CR}}{\mathrm{erg\,cm^{-3}}}\right) \mathrm{erg\,s^{-1}\,cm^{-3}} \tag{2.24}$$

where n_e is the electron number density. On the other hand, CR protons also interact with gas through hadronic collisions at a loss rate $\Lambda_{\rm h}$:

$$\Lambda_{\rm h} = 5.86 \times 10^{-16} \left(\frac{n_e}{\mathrm{cm^{-3}}}\right) \left(\frac{e_{\rm CR}}{\mathrm{erg\,cm^{-3}}}\right) \mathrm{erg\,s^{-1}\,cm^{-3}} \tag{2.25}$$

Then, the total CR energy loss rate due to Coulomb and hadronic collisions is $\Lambda_{\rm CR} = \Lambda_{\rm C} + \Lambda_{\rm h}$. Additionally, the CR hadronic interactions do not only result in the production of pions: 1/6th of the inelastic energy from the interactions between CRs and gas eventually leads to secondary electrons that lose most of their energy through thermalisation, additionally heating the gas. For this reason, both the CR energy losses from Coulomb interactions and 1/6th of the hadronic CR losses are directly injected into the thermal component via $Q_{\rm th}$, and gas is consequently heated by CRs. We note that these CR energy loss rates are derived assuming a steady-state CR spectrum, and neglect the influence of CR transport and energy losses due to self-generated Alfvén waves.

Numerical resolution of the cosmic ray equations

We finally summarise in a nutshell how the CR equations are solved. During the MHD step, CR advection and pressure work are computed. If streaming heating is enabled (both streaming diffusion and heating can be independently turned on and off), this additional energy exchange between CR and thermal energies is accounted for. Eventually, at the end of the MHD step, CR diffusion must be solved to update the CR energy. Removing all the terms previously treated during the MHD timestep, this diffusion step is simply given by $\frac{\partial e_{\rm CR}}{\partial t} = \nabla \cdot \boldsymbol{F_{CR,d+st}}$. Numerically discretised for a timestep Δt, evolving the CR energy density in cell i from t_n to t_{n+1} reads (in one dimension):

$$\frac{e_i^{n+1} - e_i^n}{\Delta t} = -\frac{F_{i+1/2}^n - F_{i-1/2}^n}{\Delta x} \tag{2.26}$$

For clarity, we wrote $e_i = e_{{\rm CR},i}$ and $F_i = F_{CR,d+st,i}$. As explained for Equation 2.5, solving this equation consists of computing the flux at cell interfaces, and the algorithm used to compute CR diffusion includes an adaptive treatment both in space and in time. For CR diffusion to be stable, it has to happen on timescales shorter than the time needed for CRs to cross one cell of length Δx when diffusing at a velocity $v_{\rm diff}$. For CR diffusion parametrised by a diffusion coefficient D, the diffusion velocity is $v_{\rm diff} = D/\Delta x$, which means that the CR diffusion timestep which corresponds to the CFL condition is:

$$\Delta t_{\rm diff} \leq \frac{\Delta x^2}{2D} \tag{2.27}$$

While the CFL condition for gas imposes the hydrodynamical timestep to scale with the minimum length of the cells Δx, the CFL condition for diffusion is more stringent as it scales with Δx^2, which increases the time cost of the simulations (see also **Appendix B**). With streaming diffusion, this is even worst: streaming additionally follows the gradient of CR energy density, so that the CFL condition scales with Δx^3 (see also Sharma et al., 2009). In RAMSES, instead of evolving $e_{\rm CR}$ forward in time explicitly as done in Equation 2.26, an implicit solver is used to model CR streaming, as described by Dubois & Commerçon (2016) and Dubois et al. (2019). To summarise, the CR energy density is evolved following Equation 2.28:

$$\frac{e_i^{n+1} - e_i^n}{\Delta t} = -\frac{F_{i+1/2}^{n+1} - F_{i-1/2}^{n+1}}{\Delta x} \tag{2.28}$$

Unlike explicit methods, implicit schemes put the future state of the system at time $n+1$ on the right-hand side, which results in a system of algebraic equation which are very expensive to solve. They are not limited by the CFL condition anymore, but acquire a numerical cost due to the demand of a robust converged solution. Globally, solving Equation 2.28 consists of solving a system $\boldsymbol{Ax} = \boldsymbol{b}$, where $\boldsymbol{x}$ is the 3D vector of e_{n+1} values to be determined and $\boldsymbol{b}$ the vector of values e_n from the previous known state of the system. $\boldsymbol{A}$ is a matrix encoding the diffusion and magnetic field properties at time t_n, as, e.g., $F_{i+1/2}^{n+1} = -D_{i+1/2}^n(e_{i+1}^{n+1} - e_i^{n+1})$ (see Equation 2.22). This system of equations is the result of N linear equations for each of the N cells of the grid, and is solved using the conjugate gradients method. A residual vector $\boldsymbol{r}$ is defined as $\boldsymbol{r} = \boldsymbol{b} - \boldsymbol{Ax}$, and initialised with a first estimate of $\boldsymbol{x}$.

After several iterations (less than N), the residual becomes sufficiently small, and the vector $\boldsymbol{x}$ is returned as the result. This method, used by Dubois & Commerçon (2016) and Dubois et al. (2019), is initially described by Commerçon et al. (2011) for radiation-hydrodynamics. It only holds for a square, symmetric, and positive-definite matrix $\boldsymbol{A}$, and does not ensure the monotonicity of the CR flux, which means that the CR energy density can be nonphysically found to be negative. In addition to the implementation of CR diffusion in RAMSES, a slope limiter has been included, which is an algorithm that further constrains the equations to preserve the positivity of their solutions, as proposed by Sharma & Hammett (2007). With the slope limiter, the matrix $\boldsymbol{A}$ is changed in order to ensure that $\boldsymbol{x}$ will be positive, and is consequently not symmetric anymore. To solve this system of linear equations, the biconjugate gradient stabilized method is used instead of the simpler conjugate gradient method (Van der Vorst, 1992), which is a similar algorithm that additionally defines a second residual, using the conjugate transform of $\boldsymbol{A}$, $\boldsymbol{b}$ and $\boldsymbol{x}$. Because the system of equations is solved twice (once for $\boldsymbol{A}$, $\boldsymbol{b}$ and $\boldsymbol{x}$ and a second time for their conjugate transform), and because determining the flux of CRs implies knowing the CR energy in the neighbouring cells at the cost of MPI communications, the implicit method for CR diffusion is not necessarily quicker than the explicit one, especally if the diffusion timestep from Equation 2.27 is not too small.

In the simulations studied throughout the thesis, streaming is generally not included (unless mentioned). To optimise the computing time, a switch is used to compute CR diffusion either implicitly or explicitly, depending on the ratio of $\Delta t_{\rm diff}$ to $\Delta t_{\rm hydro} \propto \Delta x/u$. In refinement levels for which $\Delta t_{\rm diff}$ is greater than $\Delta t_{\rm hydro}/100$, the explicit solver is used, and the implicit method otherwise[6].

2.4 The SPHINX suite of cosmological simulations

In **Chapter 1**, we described how the study of the high-redshift Universe, from the formation and the evolution of the first galaxies to the reionisation of the Universe, is one of the main current scientific challenges, and the focus of this thesis. We now describe the SPHINX simulations, used in this thesis as a reference and a starting point for the study of the impact of CRs during the EoR.

Ideally, the theoretical study of the EoR requires large cosmological simulations, so that the patchiness of the reionisation process can be recovered, and so that the mean reionisation history can converge regardless of the simulation initial conditions. To achieve this, Iliev et al. (2014) showed that simulation boxes of size $\gtrsim 100$ Mpc are needed to overcome cosmic variance, and that the abundance and sizes of ionisation patches are underestimated otherwise. However, studying the high-redshift Universe also requires capturing the small scales processes that drive reionisation, i.e. the production and propagation of LyC radiation through the ISM of high redshift galaxies. This demands simulations that allow the study of the ISM, in order to investigate which galaxies provide the bulk of ionising photons, how feedback-driven outflows regulate the amount of gas available to form stars and which fraction of ionising photons can actually reach the IGM and contribute to reionisation. Last

[6]While this is not shown in the thesis, I checked that using either the explicit or the implicit solver does not change the effect of CR feedback on idealised galaxy simulations.

but not least, consistently predicting the stellar UV photon production, propagation, and interplay with gas that impacts both galaxy evolution and the reionisation of the Universe requires radiation-hydrodynamics (RHD) simulations.

The reconciliation of large and small scales is accomplished in the SPHINX suite of RHD simulations[7], which reach resolution better than 10 pc at $z = 6$, at the cost of moderately small volumes of 5^3, 10^3 and 20^3 cMpc^3 [8](in the following, they are named SPHINX5, SPHINX10 and SPHINX20 respectively). The SPHINX volumes are far too small to capture the cosmological homogeneity scale, so their fiducial initial conditions have been selected among a set of 60 in order to minimise as much as possible the effects of cosmic variance. Nonetheless, they have a sample of several thousands of galaxies, in halos resolved down to the atomic cooling limit (which means halo masses of $\simeq 3 \times 10^7\,\mathrm{M}_\odot$). They are RHD simulations, so they can track the propagation of LyC photons, in order to capture the reionisation process, and to measure the escape fraction of ionising radiation for which a statistical average can be measured thanks to the large sample of halos. The inclusion of RHD also allows us to account for radiation feedback within galaxies. Therefore, the regulation of galaxy growth across time can be investigated, in particular through the effects of radiation, as done by Katz et al. (2020).

There are a number of papers that rely on SPHINX simulations. The first of the series focused on the impact of binary stars on reionisation, using a moderate-size box of 10 cMpc in width (Rosdahl et al., 2018). With 8 times smaller volumes, and as mentioned above, Katz et al. (2020) studied how reionisation affects star formation in dwarf galaxies. Garel et al. (2021) investigated the link between the suppression of Lyα line with redshift and the neutral gas fraction of the IGM. On a different topic, the evolution and the role of the inter-galactic magnetic field have been explored in a series of SPHINX5 runs in Attia et al. (2021) and Katz et al. (2021). Recently, a SPHINX20 simulation has been performed, to extend the results from Rosdahl et al. (2018) with more numerous and more massive galaxies, so that the main drivers of reionisation can better be investigated (Rosdahl et al., 2022). Finally, the last SPHINX paper to date from Katz et al. (2022) focuses on measuring the ratio of metal emission lines as a constraint of the LyC escape fraction and ISM properties of high redshift galaxies.

As in most simulation work, the sub-grid models used in SPHINX include some tuning, mainly involving the calibration of supernova feedback. In order to reproduce stellar masses, star formation rates, and luminosity functions at high redshift, the SN rate in the SPHINX simulations is boosted, such that there are 4 SN explosions per 100 $\mathrm{M}_\odot$ (see e.g. Figure C1 from Rosdahl et al., 2018), which is four times higher than predicted with a Kroupa IMF. In the rest of the manuscript, we refer without distinction to this specific SPHINX calibrated SN feedback model as "strong" or "boosted" SN feedback. With this feedback recipe, the SPHINX simulations can reproduce observational constraints on the early Universe. As shown in Rosdahl et al. (2018), the galaxy UV (1500 Å) luminosity function is similar to that derived from high-redshift observations (Bouwens et al., 2017; Livermore et al., 2017), the SFR versus halo mass matches the observational estimates at $z = 6$ from Harikane

[7] https://sphinx.univ-lyon1.fr

[8] The letter "c" before the units denotes comoving units, which are equivalent to physical units divided by the expansion factor.

et al. (2018), and the stellar mass to halo mass relation (SMHM) is in fair agreement with constraints from the abundance matching technique (Behroozi et al., 2013) and local $z = 0$ dwarf galaxy observations (Read et al., 2017). The fact that both the amount of stars formed and the luminosity they emit agree with observations ensures that the production of LyC photons roughly corresponds to the real emission of ionising photons, which makes the SPHINX simulations appropriate to study the process and the epoch of reionisation, in particular though the study of the escape fraction $f_{\rm esc}$. However, the necessity of the calibration of the rate of SN explosions may be the consequence of complementary feedback channels missing in the fiducial simulations. We investigate if CRs can replace this boosted feedback model by regulating galaxy growth in a similar way with a new set of SPHINX simulations that include CR feedback in **Chapter 4**.

Finally, it should be noted that the SPHINX simulations are performed with the RAMSES-RT code (Rosdahl et al., 2013; Rosdahl & Teyssier, 2015), using the mechanical SN feedback model from multiple SN explosions sampled between 3 and 50 Myr of the stellar particle lifetime (Kimm & Cen, 2014; Kimm et al., 2015), and where stars form following the turbulent SF prescription (Kimm et al., 2017) described previously in the chapter.

CHAPTER 3
Cosmic ray feedback in idealised galaxies

The work presented in this chapter probes the effects of cosmic ray feedback in idealised, isolated disc galaxies. I first state the motivations behind such a study (**Section 3.1**), which led to the publication of a paper enclosed in **Section 3.2**. In the rest of the chapter, I provide the analysis of additional material, tangential to the results published. I first distinguish the effects on galaxy evolution from radiation feedback, magnetic field and stellar particle mass resolution in **Section 3.3**. I compare the impact of CR feedback in a Milky-Way mass galaxy with different gas fractions in **Section 3.4**. Then, I investigate the effects of CRs when combined to an already strong SN feedback and when the SN energy injection into CRs is increased in **Section 3.5**. Finally, I analyse the role of cosmic ray streaming transport and heating in **Section 3.6**.

3.1 Motivations

Before investigating the effects of CRs in cosmological simulations, the first step of my thesis has been to ensure the compatibility of the different physics required within the RAMSES code. As explained in **Section 2.1.1**, idealised simulations are the perfect numerical experiment for fast and affordable tests, and are in particular useful to assess the viability of the implementation of a physical module. Therefore, the starting point of the work described in this chapter is the set of three idealised galaxies initially described by Rosdahl et al. (2015): G8, G9 and G10. The number associated to each galaxy corresponds to the order of magnitude of the baryonic mass they host, and they are respectively embedded in DM halos of 10^{10}, 10^{11} and 10^{12} $M_\odot$. A complete description of their initial conditions can be found in Rosdahl et al. (2015), and is restated in Farcy et al. (2022), which is appended to this manuscript in the next section.

Initially, the galaxies from Rosdahl et al. (2015) were designed to study the impact of radiation feedback, by means of RHD simulations. For this reason, they were called the "galaxies that shine". Two years later, the same objects were used to test and compare different sub-grid models for SN feedback, focusing on G9 and G10 (Rosdahl et al., 2017). Because it has a high gas fraction, G9 has been studied as an analogue of high-redshift galaxies by Yoo et al. (2020) who investigated the origin of the low escape fractions of LyC measured. Eventually, Dashyan & Dubois (2020) analysed the effects of cosmic ray feedback on G8 and G9 with MHD simulations in which the galaxies are evolved for 250 Myr with different CR physics. Therefore, the galaxies that shine are perfectly suited for both RHD and MHD simulations, and are amenable to different star formation and feedback prescriptions. The final objective of this thesis is to understand the role of CRs on galaxy evolution using more realistic cosmological simulations. As already mentioned, I most specifically rely on the SPHINX simulations, presented in **Section 2.4**. To enable closer comparisons,

the idea is to perform simulations that have the same turbulent star formation prescription and SN mechanical feedback as in SPHINX, described in **Section 2.2.6** and **Section 2.2.7**.

In the end, the genesis of the work presented in the following comes from:

1. starting by reproducing the results from Dashyan & Dubois (2020), with a simple prescription for star formation and SN feedback and no radiative transfer,
2. include the state-of-the art physics merged into the home-made version of the RAMSES code used for SPHINX,
3. in order to perform the first CR-RMHD simulations of galaxy evolution, over time-scales of 500 Myr.

This chapter is dedicated to presenting the results from these simulations, which are listed in **Appendix B** (in tables that summarise the physics included as well as the computing time cost of the runs). Unless otherwise mentioned, I will use the same color code throughout the thesis. Simulations with CRs, a fiducial energy injection of 10% and a fiducial diffusion coefficient $\kappa = 10^{28}$ cm^2/s are shown in purple. Counterparts without CRs are depicted in orange. We sometimes write the cosmic ray diffusion coefficient κ_{28}, which corresponds to κ in units of 10^{28} cm^2 s^{-1}.

3.2 Towards more realistic galaxy simulations

The galaxies that shine have initial conditions and gas content that allow them to form stars during several hundreds of Myr. As a consequence, SN explosions occur throughout the lifetime of the galaxies, and CR energy is injected in each of these events. Therefore, they are a great tool to probe the effects of CRs at different galaxy masses and on different aspects of galaxy evolution, from star formation regulation, temperature properties of feedback driven outflows, and escape fraction of ionising radiation. This is exactly the purpose of the work published during my PhD (Farcy et al., 2022), that I will call the **CosmicShine** paper in the following[1]. The galaxies studied in the **CosmicShine** paper use the same models for star formation and SN feedback (boosted or not) as in SPHINX. This enables a close comparison to the SPHINX galaxies in spite of an idealised setup. We can especially compare CR feedback to the boosted SN feedback, and predict CR feedbacl's consequences on galaxy growth and reionisation before studying this aspect more consistently in **Chapter 4**. The robustness of our conclusions to the cosmic ray diffusion coefficient is also discussed by showing the sensitivity of the results on this crucial parameter. We note that the methods used in the other sections of this chapter, to determine for instance outflowing gas, clumps of stars, and escape fractions, are the same as described in the **CosmicShine** paper.

[1] As a shortening for "cosmic rays in the galaxies that shine".

MNRAS **000**, 1–20 (2022) Preprint 24 May 2022 Compiled using MNRAS LATEX style file v3.0

Radiation-MagnetoHydrodynamics simulations of cosmic ray feedback in disc galaxies

Marion Farcy,[1]★ Joakim Rosdahl,[1] Yohan Dubois,[2] Jérémy Blaizot,[1] Sergio Martin-Alvarez[3]
[1]*Centre de Recherche Astrophysique de Lyon, CNRS UMR 5574, Univ. Lyon, Ens de Lyon, 9 avenue Charles André, F-69230 Saint-Genis-Laval, France*
[2]*Institut d'Astrophysique de Paris, CNRS UMR 7095, UPMC Univ. Paris VI, 98 bis boulevard Arago, 75014 Paris, France*
[3]*Institute of Astronomy and Kavli Institute for Cosmology, University of Cambridge, Madingley Road, Cambridge CB3 0HA, UK*

Accepted 2022 April 27. Received 2022 March 30; in original form 2022 February 2

ABSTRACT

Cosmic rays (CRs) are thought to play an important role in galaxy evolution. We study their effect when coupled to other important sources of feedback, namely supernovae and stellar radiation, by including CR anisotropic diffusion and radiative losses but neglecting CR streaming. Using the RAMSES-RT code, we perform the first radiation-magnetohydrodynamics simulations of isolated disc galaxies with and without CRs. We study galaxies embedded in dark matter haloes of 10^{10}, 10^{11} and 10^{12} $M_\odot$ with a maximum resolution of 9 pc. We find that CRs reduce star formation rate in our two dwarf galaxies by a factor 2, with decreasing efficiency with increasing galaxy mass. They increase significantly the outflow mass loading factor in all our galaxies and make the outflows colder. We study the impact of the CR diffusion coefficient, exploring values from $\kappa = 10^{27}$ to 3×10^{29} cm^2 s^{-1}. With lower κ, CRs remain confined for longer on small scales and are consequently efficient in suppressing star formation, whereas a higher diffusion coefficient reduces the effect on star formation and increases the generation of cold outflows. Finally, we compare CR feedback to a calibrated 'strong' supernova feedback model known to sufficiently regulate star formation in high-redshift cosmological simulations. We find that CR feedback is not sufficiently strong to replace this strong supernova feedback. As they tend to smooth out the ISM and fill it with denser gas, CRs also lower the escape fraction of Lyman continuum photons from galaxies.

Key words: cosmic rays – galaxies: evolution – galaxies: star formation – methods: numerical

1 INTRODUCTION

The study of galaxy evolution is strongly related to the baryon cycle, which describes how gas collapses to form stars, and how stellar feedback then suppresses star formation and drives fountains of galactic outflows. Therefore, one of the key challenges of galaxy evolution is to understand the nature of the feedback processes that regulate star formation (SF) and gas expulsion, which in the end shape the galactic gas distribution at inter-stellar medium (ISM) and circum-galactic medium (CGM) scales.

It is commonly established that supernova (SN) feedback provides an important contribution in suppressing star formation and driving galactic winds, especially in low-mass galaxies (e.g. Dekel & Silk 1986; Navarro & White 1993; Gelli et al. 2020). In the past, the ISM of galaxies could not be resolved in cosmological simulations, and it was beyond reach to model star formation and feedback from first principles. Instead, these processes were modelled with sub-grid recipes where SN feedback could be calibrated in various ways in order to reproduce a range of observations, such as the galaxy mass function and Kennicutt-Schmidt relation (e.g. Oppenheimer et al. 2010; Vogelsberger et al. 2014; Schaye et al. 2015). In the last decade, however, it has become more and more feasible to resolve the ISM in simulations of galaxy evolution, opening the way for feedback (and star formation) models that are increasingly physically motivated and have less freedom for calibration (see Vogelsberger et al. 2020, for a recent review).

Several recent studies of galaxy evolution have applied this first principles approach to SN feedback (e.g. Smith et al. 2019; Peters et al. 2017; Hu 2019; Fujimoto et al. 2019). While SN feedback is found to have a strong impact on low-mass galaxies, they generally draw into question the assumption that this feedback process alone sufficiently suppresses star formation (Hopkins et al. 2014; Grudić et al. 2018; Smith et al. 2019, and references hereafter). Therefore, complementary feedback processes such as radiation feedback and cosmic rays are likely important, if sub-dominant.

Stellar radiation interacts with ISM gas, through photoionization heating of gas and radiation pressure (e.g. Hopkins et al. 2014; Peters et al. 2017; Emerick et al. 2018). However, self-consistent radiation hydrodynamics simulation studies such as those from Rosdahl et al. (2015) and Kannan et al. (2019) find that photoionization heating has a non-negligible but insufficient effect in regulating star formation, and that radiation pressure only has a marginal effect.

Cosmic rays (CRs) have been proposed by many as an additional important source of feedback. When supernovae explode, the shock waves generated accelerate charged particles up to relativistic velocities through diffusive shock acceleration (Axford et al. 1977; Krymskii 1977; Bell 1978; Blandford & Ostriker 1978). By nature, CRs have a number of advantages for being an efficient feedback

★ E-mail: marion.farcy@univ-lyon1.fr

source. Being at equipartition with magnetic, turbulent and gravitational energies (Boulares & Cox 1990, from measurements of the Milky Way), they provide a significant non-thermal pressure that can drive the gas dynamics, on scales ranging from their injection sites to the CGM. They have a softer equation of state than the thermal energy, so their pressure drops less quickly upon adiabatic expansion. They cool less efficiently than non-relativistic gas (Enßlin et al. 2007), so their energy is maintained longer than the thermal energy of the gas. Additionally, a part of the CR energy lost through collisions and Coulomb interactions is delivered to the gas which is heated. These properties of CRs have been shown to suppress star formation (e.g. Jubelgas et al. 2008; Pfrommer et al. 2017; Chan et al. 2019; Semenov et al. 2021, in idealised galaxies) and drive dense and cold winds in a number of studies (e.g. Booth et al. 2013; Salem & Bryan 2014; Pakmor et al. 2016; Wiener et al. 2017; Jacob et al. 2018; Dashyan & Dubois 2020; Jana et al. 2020; Girichidis et al. 2022 in idealised galaxies, Farber et al. 2018; Girichidis et al. 2018 in stratified boxes of ISM and Buck et al. 2020; Hopkins et al. 2020; Ji et al. 2020; Butsky et al. 2021 in cosmological zoom-in simulations).

Therefore, CRs appear a promising complementary feedback mechanism to limit the growth of galaxies in the Universe. However, radiation, SN, and CR feedback have never been considered before in combination. Recently, Dashyan & Dubois (2020, DD20 hereafter) studied CR feedback in two isolated disk galaxies spanning an order of magnitude in mass. However they did not consider radiation feedback and they used a fairly simple and locally inefficient model for star formation which does not represent the state-of-the-art used in recent cosmological simulations. We therefore expand on the work of DD20 with the first Radiation-MagnetoHydroDynamics (RMHD) simulations of galaxy evolution combining ideal magneto-hydrodynamics (MHD), SN feedback, radiative transfer and CRs to study the combined effect of these processes. Using the RAMSES-RT code (Teyssier 2002; Teyssier et al. 2006; Rosdahl et al. 2013), we investigate how CR feedback shapes galaxy growth, studying the effects of CRs in regulating star formation and the ISM and CGM gas of three idealised galaxies spanning two orders of magnitude in mass and with resolution down to 9 pc.

CR transport is a complex process that includes advection with gas, anisotropic diffusion and streaming down the CR pressure gradient. Depending on whether the sources of CR scattering are external magnetic field inhomogeneities or waves excited by CRs themselves, the importance of each of these processes can vary significantly and impact the diffusion coefficient, through which CR propagation is parameterized (see e.g. Zweibel 2017). While this parameter is poorly constrained, we know from other studies (e.g. Salem & Bryan 2014; Farber et al. 2018; Jacob et al. 2018; Chan et al. 2019; Dashyan & Dubois 2020; Hopkins et al. 2020; Jana et al. 2020; Girichidis et al. 2022; Semenov et al. 2021) that conclusions on the role of CRs as a feedback source can differ quite dramatically depending on its value. We therefore test the variability of CR feedback using five values of diffusion coefficient, pursuing the study initiated by DD20, with an increased sample of galaxies and with our physically motivated setup.

Our eventual goal is to determine if cosmic rays, combined with SN and stellar radiation, constitute a feedback model sufficient to regulate the growth of low-mass galaxies in the Universe. To circumvent the limited predictive power of our non-cosmological galaxy disk simulations, a preliminary way of answering this question is to compare this combined feedback with the artificially boosted SN feedback model previously used in the SPHINX cosmological simulations (Rosdahl et al. 2018), which is shown to sufficiently regulate star formation at high redshift to reproduce the observed galaxy luminosity function.

The structure of this paper is as follows. Section 2 introduces the code, methods and setup used to perform our isolated disc simulations. Section 3 first focuses on the qualitative effects of CRs on our galaxies. In Section 3.1, we investigate the efficiency of cosmic ray feedback in regulating star formation, before studying its effects on the mass loading factor and the temperature phases of the outflowing gas in Section 3.2. In Section 3.3, we further explore the variability of our results when changing the cosmic ray diffusion coefficient, a key parameter governing their propagation and their role as a feedback source. We analyse to what extent CRs can shape galaxy evolution compared to a calibrated stronger SN feedback in Section 3.4. We consider the consequences of those two feedback models on the escape of Lyman Continuum radiation in Section 3.5. We finally give an overview of the main results of this paper in the context of other studies in Section 4 and conclude in Section 5.

2 SIMULATIONS AND METHODS

To perform Radiation-MagnetoHydroDynamics simulations of isolated galaxies, we use the RAMSES-RT adaptive mesh refinement (AMR) code (Rosdahl et al. 2013; Rosdahl & Teyssier 2015), a radiation-hydrodynamics (RHD) extension of the RAMSES code (Teyssier 2002). The solver described by Fromang et al. (2006) is employed to compute the full set of ideal MHD equations. The fluxes are solved with the Harten-Lax-van Leer Discontinuities (HLLD) Riemann solver (Miyoshi & Kusano 2005) and the minmod total variation diminishing slope limiter (Van Leer 1979). The magnetic field evolves following the induction equation, which is implemented using a constrained transport method, which ensures a null magnetic divergence by construction, and employs the second order Godunov scheme MUSCL (Teyssier et al. 2006). The radiative transfer equations are solved with a two-moment method and the M1 closure for the Eddington tensor. The code tracks the non-equilibrium ionization states of hydrogen and helium in each gas cell, and includes the effects of radiation pressure, photoheating and radiative cooling. Finally, we combine RAMSES-RT with the method developed by Dubois & Commerçon (2016) to solve the anisotropic diffusion of CRs. We further add the minmod slope limiter on the transverse component of the flux that preserves the monotonicity of the solution in the asymmetric method of Sharma & Hammett (2007), as described in DD20.

We simulate galaxy discs of baryonic mass 3.5×10^8, 3.5×10^9 and 3.5×10^{10} $M_\odot$ embedded in 10^{10}, 10^{11} and 10^{12} $M_\odot$ dark matter haloes respectively. We refer to them as G8, G9 and G10, where the numbers stand for the order of magnitude of the galaxy baryonic mass.

2.1 Galaxy disc setup

The initial conditions for all our simulations are generated using the MAKEDISC code (Springel et al. 2005). A more complete description can be found in Rosdahl et al. (2015), and some of the main properties of the discs are summarised in Table 1. Each of our three discs is hosted in a dark matter (DM) halo which follows a NFW density profile (Navarro et al. 1997), with a concentration parameter $c = 10$ and a spin parameter $\lambda = 0.04$. The DM is modelled by collisionless particles all of the same mass, 10^5 particles for G8 and 10^6 of them for G9 and G10, leading to a DM particles mass of 10^5 $M_\odot$ for G8 and G9 and 10^6 $M_\odot$ for G10. The discs also have an initial distribution

Table 1. Main parameters of the three disc galaxies. From left to right: galaxy name (number connected to the disc mass), $M_{\rm disc}$: baryonic disc mass (gas + stars), $M_{\rm halo}$: dark matter halo mass, $R_{\rm vir}$: halo virial radius, $L_{\rm box}$: length of the simulated box, $\Delta x_{\rm max}$: maximum cell size, $\Delta x_{\rm min}$: minimum cell size, m_*: stellar particle mass, $f_{\rm gas}$: gas disc fraction, $Z_{\rm disc}$: disc metallicity, $t_{\rm end}$: time reached at the end of the run, for the last snapshot.

Galaxy name	$M_{\rm disc}$ [$M_\odot$]	$M_{\rm halo}$ [$M_\odot$]	$R_{\rm vir}$ [kpc]	$L_{\rm box}$ [kpc]	$\Delta x_{\rm max}$ [kpc]	$\Delta x_{\rm min}$ [pc]	m_* [$M_\odot$]	$f_{\rm gas}$	$Z_{\rm disc}$ [$Z_\odot$]	$t_{\rm end}$ [Myr]
G8	3.5×10^8	10^{10}	41	150	2.34	9	2500	0.5	0.1	500
G9	3.5×10^9	10^{11}	89	300	2.34	9	2500	0.5	0.1	500
G10	3.5×10^{10}	10^{12}	192	600	4.68	18	20000	0.3	1	500

of gas and stellar particles, both following an exponential density profile in radius (with a scale radius of 0.7, 1.5 and 3.2 kpc by increasing order of galaxy mass) and a Gaussian in height (with the scale height being one tenth of the scale radius). Initially, the disc gas has a uniform temperature of $T = 10^4$ K while the rest of the box is filled with a diffuse circum-galactic gas at 10^6 K, and a hydrogen density $n_{\rm H} = 10^{-6}$ cm^{-3}. The metallicity of the gas disc is set to 0.1 $Z_\odot$[1] for both G8 and G9 and to 1 $Z_\odot$ for G10, and the CGM metallicity is set to zero. This setup describes an idealised CGM, initially almost empty from gas, and which is not designed to be realistic. We note that this description of the CGM is very simplified and does not represent very well, especially not initially, the CGM found in cosmological simulations, populated with a multi-phase mix of inflowing and outflowing gas. The initial stellar particles do not explode as SN, nor provide any other feedback to the surrounding gas. They account for 50% of the total initial baryonic mass of the discs for G8 and G9 galaxies and 70% for G10. 10% of the stellar particles are distributed in a stellar bulge and the remainder throughout the disc according to the gas profile described above, so that the bulge to total (disc plus bulge) stellar mass ratio is 0.1.

2.2 Adaptive refinement

The RAMSES code uses an adaptive refinement scheme, where each cell can be divided into 8 children cells of width half that of the parent. Equivalently, this means that the size of a cell refined at a level ℓ, Δx_ℓ, is twice smaller than the size of the next coarser cell of level $\ell - 1$, so that $\Delta x_\ell = L_{\rm box} \,/\, 2^\ell$, with $L_{\rm box}$ being the full size of the simulation box. We flag a cell to be refined if its total mass (dark matter and baryons) is higher than the mass of 8 dark matter particles (which corresponds to 8×10^5 $M_\odot$ for G8 and G9 and 8×10^6 $M_\odot$ for G10), or if its width is larger than a quarter of the local Jeans length. In this study, the three disc galaxies G8, G9 and G10 are located at the centres of boxes of 150, 300 and 600 kpc in width respectively. We adopt a maximum cell resolution of $\Delta x_{\rm max} = 9$ pc for G8 and G9, but 18 pc for G10. The minimum cell resolution is $\Delta x_{\rm min} = 2.34$ kpc for G8 and G9, and 4.68 kpc for G10. We briefly discuss resolution convergence in Section 4.

2.3 Radiative transfer

The radiative transfer equations in RAMSES-RT are solved with a first-order moment method, using the M1 closure relation for the Eddington tensor, and the Global Lax–Friedrichs (GLF) intercell flux function for the advection of the photon fluids (see Rosdahl et al. 2013). To reduce the computational cost of light propagation, we use a reduced speed of light of $c/100$. We solve the non-equilibrium chemistry and radiative cooling of neutral and ionized hydrogen and helium, for which we follow the ionization fractions. For the three photon groups (HI, HeI and HeII ionizing photons), we adopt a dust absorption opacity of 10^3 cm^2 g^{-1} ($Z/Z_\odot$). As listed in Table 2, each photon group is defined by a frequency interval, for which we track photon density and flux in each cell. Stars emit photons at a rate derived from version 2.2.1 of the Binary Population And Spectral Synthesis model (BPASS; Stanway et al. 2016; Stanway & Eldridge 2018). We assume an initial mass function close to Kroupa (2001) with slopes of -1.3 from 0.1 to 0.5 $M_\odot$ and -2.35 from 0.5 to 100 $M_\odot$. Atomic metal cooling for gas with temperature $T > 10^4$ K is computed using cooling rates tabulated from CLOUDY (Ferland et al. 1998), and fine-structure line cooling is enabled for gas with $T < 10^4$ K, using the fitting function from Rosen & Bregman (1995). We also include gas heating from an external redshift zero uniform UV background, following Haardt & Madau (2012), with self-shielding for $n_{\rm H} > 10^{-2}$ H cm^{-3}.

[1] We assume in this work a Solar metal mass fraction of $Z_\odot = 0.02$

Table 2. Properties of the three photon groups used in this study. From left to right: photon group name, ϵ_0 and ϵ_1: minimum and maximum photon energy range, $\overline{\epsilon}$: mean photon energy ±10%.

Photon group	ϵ_0 [eV]	ϵ_1 [eV]	$\overline{\epsilon}$ [eV]
$UV_{\rm HI}$	13.60	24.59	18
$UV_{\rm HeI}$	24.59	54.42	33.4
$UV_{\rm HeII}$	54.42	∞	60

2.4 Star formation

We turn gas into star particles only if cells at the highest level of refinement are gravitationally unstable, i.e. if they have a width larger than the turbulence Jeans length defined as:

$$\lambda_{\rm J,turb} = \frac{\pi\sigma_{\rm gas}^2 + \sqrt{36\pi c_s^2 G\Delta x^2\rho + \pi^2\sigma_{\rm gas}^4}}{6G\rho\Delta x}\,, \quad (1)$$

where G is the gravitational constant, $\sigma_{\rm gas}$ is the gas velocity dispersion computed using the velocity gradients with neighbour cells, c_s is the local sound speed and ρ is the gas density. We note that neither the magnetic nor the cosmic ray pressure contribute to the sound speed in the calculation of the Jeans length.

Gas is converted into stars at a rate:

$$\dot\rho_* = \epsilon\rho/t_{\rm ff}\,, \quad (2)$$

where ϵ is the star formation efficiency and $t_{\rm ff} = (3\pi/(32G\rho))^{1/2}$ is the gas free-fall time. Stellar populations are represented by collisionless stellar particles with an initial mass which is an integer multiple of m_*, whose value varies with galaxy mass and is listed in Table 1. The conversion from gas to stars is done by stochastically sampling a Poisson mass-probability distribution, as detailed

by Rasera & Teyssier (2006), so that the conversion rate described in Eq. 2 holds only on average.

We do not use a global constant star formation efficiency but rather a local ϵ depending on the gravo-turbulent properties of the gas, based on the work of Federrath & Klessen (2012) (for details, see Kimm et al. 2017 or Trebitsch et al. 2017). We show in Appendix A that the highly varying local star formation efficiency tends to create a bursty and clumpy star formation compared to the more widely used constant and small ϵ. Consequently, we expect stronger and more localised feedback events compared to what is found by DD20 who form stars with a constant 2% efficiency if the hydrogen density in the cell is $n_{\rm H} \geq 10^2\,{\rm H\,cm^{-3}}$.

2.5 Stellar feedback

We include stellar feedback in the form of type II supernova explosions, photoionization, photoheating and radiation pressure. We use the mechanical feedback prescription of Kimm & Cen (2014) and Kimm et al. (2015) to deposit momentum in the cells neighbouring SN explosions. Considering the local simulation resolution and the gas density and metallicity, this method adapts the radial momentum depending on how well the Sedov-Taylor phase is resolved. Doing so, we limit the numerical radiative losses due to a lack of resolution.

Following this prescription, each stellar particle explodes in multiple events between 3 and 50 Myr after its birth, each explosion releasing an energy $E_{\rm SN} = 10^{51}$ ergs. This is another difference between our setup and that of DD20, in which a stellar particle explodes in one single cumulative event 5 Myr after its formation. The number of explosions $N_{\rm SN}$ per particle is defined as:

$$N_{\rm SN} = \frac{m_* \eta_{\rm SN}}{M_{\rm SN}} \tag{3}$$

where m_* is the stellar particle mass, $\eta_{\rm SN}$ is the mass fraction of the stellar population exploding as type II SNe, and $M_{\rm SN}$ is the average mass of those exploding stars. We assume a Kroupa Initial Mass Function (IMF), following which we adopt $\eta_{\rm SN} = 0.2$ and $M_{\rm SN} = 19.1\,{\rm M_\odot}$.

For our runs including CR feedback, we take 10% of the energy otherwise released with each SN explosion and instead release it into the host cell in the form of CR energy[2]. The 10% value is commonly used in simulations of CR feedback and is suggested by observations of local supernova remnants (Hillas 2005; Strong et al. 2010; Morlino & Caprioli 2012; Dermer & Powale 2013). We provide more details on the equations at stake in those energy exchanges in Section 2.6.

2.6 Magnetic field and cosmic ray propagation

Following DD20, we initialise our simulations with a toroidal magnetic field permeating the disc of our galaxies, reproducing the large-scale field observed in galaxies (Beck 2015). To ensure that the divergence of the magnetic field $\boldsymbol{B}$ cancels we initialise this toroidal magnetic field as the curl of a vector potential $\boldsymbol{A}$ set to:

$$\boldsymbol{A} = \frac{3}{2} B_0 r_0 \left(\frac{\rho}{\rho_0}\right)^{\frac{2}{3}} \boldsymbol{e_z}\,, \tag{4}$$

[2] The cosmic ray energy injection does not contribute to the thermal momentum injection because, unlike the thermal pressure, the CR pressure does not substantially cool down over one time step at any of the gas densities sampled in our simulations, and the build up of momentum by CR pressure is always resolved (but see also Diesing & Caprioli 2018; Rodríguez Montero et al. 2022).

where ρ corresponds to the gas density profile, ρ_0 its normalisation of $\sim 15\ {\rm cm^{-3}}$ (for G8, G9 and G10) and r_0 its scale radius of 3.2 kpc for G10, 1.5 kpc for G9 and 0.7 kpc for G8. $\boldsymbol{e_z}$ is the z-axis unit vector in a Cartesian coordinate system. The initial magnetic field strength B_0 is set to 1μG.

CRs are advected by the bulk motion of the gas and diffused along the magnetic field, following the advection-diffusion approximation described by Dubois & Commerçon (2016) and Dubois et al. (2019). Physically, CRs are highly energetic charged particles whose motion is thus strongly restricted to the surrounding magnetic field. In RAMSES, we consider CRs as a relativistic fluid with an adiabatic index $\gamma_{\rm CR} = 4/3$ and tracked through a non-thermal pressure term. CRs diffuse along magnetic field lines with a fiducial diffusion coefficient $\kappa = 10^{28}\ {\rm cm^2\,s^{-1}}$, as determined to correspond to collisionless particles of a few GeV where most of CR energy density resides (Strong et al. 2007; Trotta et al. 2011). Including the CR contribution, the total energy of the fluid is:

$$e = \frac{\rho u^2}{2} + e_{\rm th} + e_{\rm CR} + \frac{B^2}{8\pi}\,, \tag{5}$$

where $e_{\rm th}$ and $e_{\rm CR}$ are respectively the thermal and CR energy per unit of volume contained in one cell, and u is the gas velocity. The evolution of the different energy and the magnetic field are described by the following MHD equations, in the framework of ideal MHD:

$$\frac{\partial \boldsymbol{B}}{\partial t} = \boldsymbol{\nabla} \times (\boldsymbol{u} \times \boldsymbol{B}) \tag{6}$$

$$\frac{\partial \rho}{\partial t} + \boldsymbol{\nabla} \cdot (\rho \boldsymbol{u}) = 0 \tag{7}$$

$$\frac{\partial \rho \boldsymbol{u}}{\partial t} + \boldsymbol{\nabla} \cdot \left(\rho \boldsymbol{u}\boldsymbol{u} + P_{\rm tot} - \frac{\boldsymbol{B}\boldsymbol{B}}{4\pi}\right) = \rho \boldsymbol{g} \tag{8}$$

$$\frac{\partial e}{\partial t} + \boldsymbol{\nabla} \cdot \left((e + P_{\rm tot})\boldsymbol{u} - \frac{\boldsymbol{B}(\boldsymbol{B}\cdot\boldsymbol{u})}{4\pi}\right) = \rho \boldsymbol{u} \cdot \boldsymbol{g} + Q_{\rm CR} + Q_{\rm th} - \Lambda_{\rm rad} - \Lambda_{\rm CR} - \boldsymbol{\nabla} \cdot \boldsymbol{F_{\rm CR}} \tag{9}$$

$$\frac{\partial e_{\rm CR}}{\partial t} + \boldsymbol{\nabla} \cdot (e_{\rm CR} \boldsymbol{u}) = -P_{\rm CR} \boldsymbol{\nabla} \cdot \boldsymbol{u} + Q_{\rm CR} - \Lambda_{\rm CR} - \boldsymbol{\nabla} \cdot \boldsymbol{F_{\rm CR}} \tag{10}$$

In these equations, the total pressure $P_{\rm tot} = P_{\rm th} + P_{\rm CR} + P_{\rm mag}$ where the magnetic pressure $P_{\rm mag} = B^2/(8\pi)$, the CR pressure $P_{\rm CR} = e_{\rm CR}(\gamma_{\rm CR} - 1)$, and the thermal pressure $P_{\rm th} = e_{\rm th}(\gamma - 1)$, with $\gamma_{\rm CR}$ and γ the adiabatic indices for CRs and gas. We assume a purely monoatomic gas with $\gamma = 5/3$. Among the other quantities, $\boldsymbol{g}$ is the gravitational field, and $Q_{\rm th}$ and $Q_{\rm CR}$ are respectively thermal and CR energy source terms and contribute to the gas heating, with the former including heating from the UV background and CR collisional heating. $\Lambda_{\rm rad}$ and $\Lambda_{\rm CR}$ are cooling terms representing radiative and CR energy losses respectively. We note that the $\Lambda_{\rm CR}$ component is due to Coulomb and hadronic collisions from which a reinjection to the thermal component is already taken into account in the $Q_{\rm th}$ term (Guo & Oh 2008). The anisotropic diffusion flux term is $\boldsymbol{F_{\rm CR}} = -\kappa \boldsymbol{b}\,(\boldsymbol{b} \cdot \boldsymbol{\nabla} e_{\rm CR})$ with $\boldsymbol{b} = \boldsymbol{B}/||\boldsymbol{B}||$ the magnetic field unit vector. The streaming terms, which introduce a transfer of energy from CR pressure to thermal pressure, and an advection term at about the Alfvén velocity, are neglected in this work, as they have high computational cost and were found by DD20, with a very similar setup, to have secondary effects on the gas dynamics. Since we have similar resolution and ISM structure in our simulations as DD20, we disregard CR streaming.

3 RESULTS

Throughout this section, we denote simulations with and without CRs as 'CR' and 'noCR'. We first provide a qualitative comparison of the discs with and without CR feedback.

Fig. 1 shows face-on and edge-on maps of the hydrogen column density for the three discs, comparing runs without (left) and with (right) CR feedback. In the face-on maps, one can see clumps of dense gas, which are sites of star formation.

Comparing the left and right panels, we see that the CR feedback tends to smooth out the ISM[3] in all our simulated galaxies, producing a more extended and diffuse gas distribution. By the end of our runs, the gas disc is thicker at any galaxy mass when CRs are included, as seen in the edge-on hydrogen density maps, in agreement with e.g. Salem et al. (2016) and Buck et al. (2020).

The CR feedback produces not only denser but also colder gas in the vicinity of the ISM. This is visible in Fig. 2 showing edge-on temperature maps[4]. With the exception of a few expanding bubbles of very hot gas originating from SN explosions close to the mid-plane, the three discs are dominated by gas at temperature around or below 10^5 K when CR transport is included. We come back to the temperature phase of CR-driven outflows in Section 3.2.

3.1 Regulation of star formation

Figure 3 shows the effect of CR feedback on star formation for our three galaxies. The upper panel shows the star formation rates (SFR, averaged over 10 Myr) and reveals a bursty star formation, particularly for the two lower mass galaxies (see also Faucher-Giguère 2018). CR feedback regulates the SFR for G8 and G9 after the initial collapse taking place during the first 100 Myr or so. In G10, however, the star formation is barely impacted by the CR feedback.

Globally, CRs have a significant effect on the amount of stars formed. As we can see in the lower panel of Fig. 3, they suppress the total star formation over the modelled 500 Myr by around a factor 2 in the lower-mass galaxies, with a decreasing efficiency with increasing mass. The same factor 2 in star formation reduction for our two dwarf galaxies is found by DD20. This is despite our different setups, where we also account for radiation feedback, non-equilibrium chemistry and a more bursty and physically motivated star formation model. This implies that the efficiency of CRs in regulating star formation does not depend strongly on the inclusion of radiative feedback or the star formation model (see also Appendix A for a comparison of star formation history with the two star formation models). A broader discussion of our results compared to other works is provided in Section 4.

The addition of SN feedback to the no feedback case (not shown) reduces star formation by 85, 45 and 40% in G8, G9 and G10, respectively. In our simulations with both cosmic rays and SN feedback, we find a further suppression with respect to the SN feedback case of 50% for the dwarf galaxies (G8 and G9), and 14% for our most massive mass galaxy (G10). Therefore, the star formation suppression efficiency decreases with increasing galaxy mass for both SN and CR feedback.

In Fig. 4, we show face-on maps of the SFR surface density 350

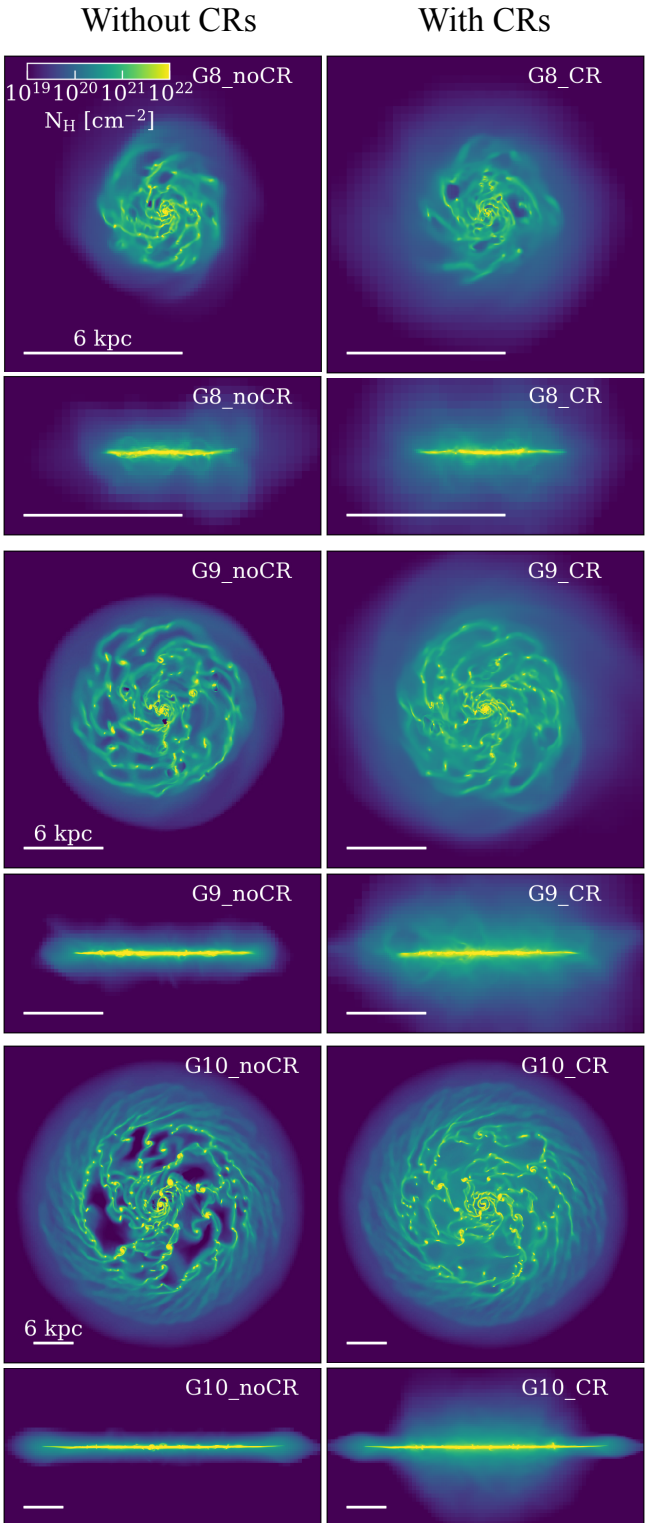

Figure 1. Maps of the three discs at 500 Myr in order of increasing mass from top to bottom. Respectively for each galaxy, 12, 24 and 48 kpc maps of face-on and edge-on hydrogen column density are shown, for the noCR discs in the left column and with CRs added on the right. The name of each run is written in the upper right corner of the maps, and a 6 kpc width scale bar is plotted in the lower left corner of each panel. The three discs tend to be thicker and with a smoother gas distribution when CRs are included.

[3] For this qualitative analysis, we somewhat arbitrary define the ISM as being gas within 1 kpc from the disc plane.

[4] Note that the temperature maps in Fig. 2 are more zoomed out for the lower-mass galaxies than in Fig. 1, and that they all have the same physical scale, in order to give a better impression of the difference in size between the different mass galaxies.

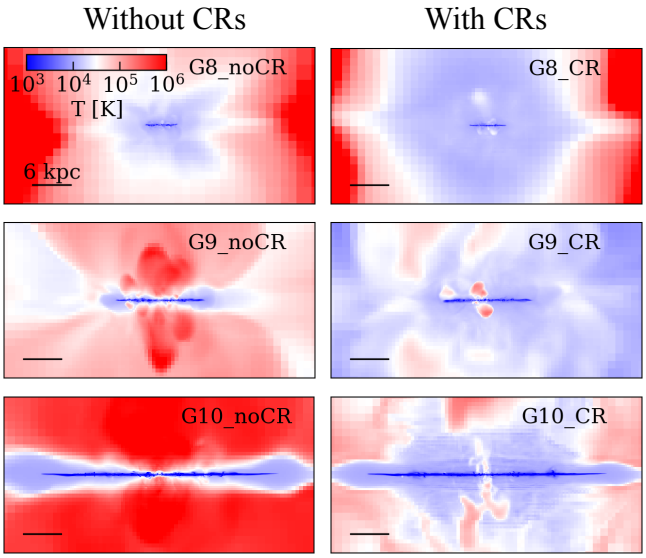

Figure 2. Mass-weighted 48 kpc-wide slices of the three discs at 500 Myr in order of increasing mass from top to bottom. For each galaxy, edge-on temperature maps are plotted for the noCR case in the left column and with CRs added on the right. The circum-galactic medium of the galaxies becomes much colder with CRs included.

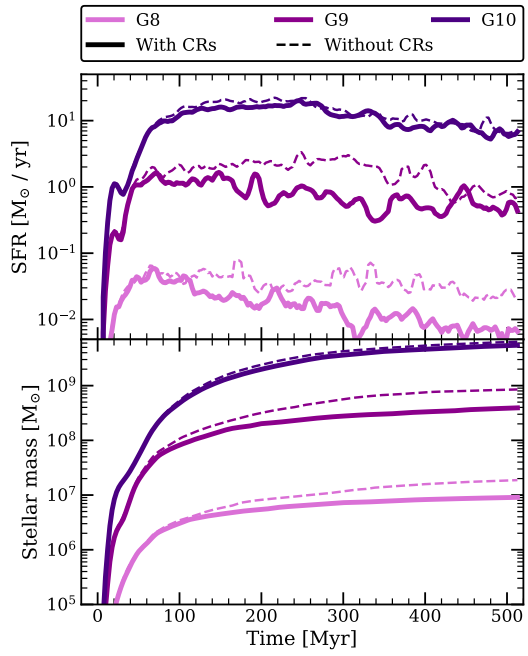

Figure 3. Star formation rate (upper panel) and stellar mass (lower panel) versus time for G8 (light purple), G9 (purple) and G10 (dark purple). We show the runs including CRs in solid line and the runs without CRs in dashed line. We exclude the initial stellar particles seeded in the initial conditions of the discs, to show only the stellar mass formed since the start of the run. We note a reduction of the total stellar mass by a rough factor 2 for the two dwarf galaxies when we include CRs, while the star formation history of G10 does not seem affected much.

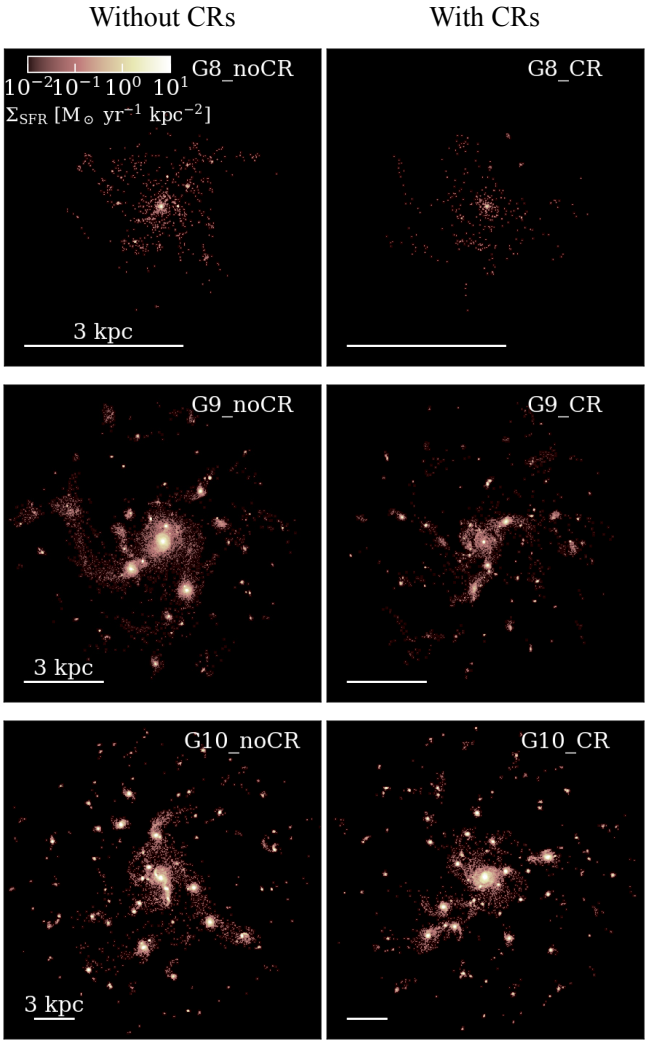

Figure 4. Face-on maps of SFR surface density at t = 350 Myr, in order of increasing galaxy mass from the top to the bottom. Left and right columns show the simulations without and with cosmic ray feedback, respectively. The star formation rate values are derived from the last 100 Myr. The maps are decomposed in 1024x1024 squared pixels, with values smoothed by a Gaussian filter of one pixel width, for a better visibility. It is especially clear for the dwarf galaxies that adding CRs leads to less numerous and massive stellar clumps.

Myr after the start of the simulations, with the SFR averaged over 100 Myr. The maps reveal the ability of CRs to reduce the number and mass of stellar clumps. This is a consequence of CR feedback smoothing out the inner gas distribution of the ISM, as shown in Fig. 1. This effect is especially visible for the lower mass galaxies, where CR feedback significantly regulates the total SFR. However there is also a somewhat reduced "clumpiness" in the case of G10 where the total star formation is not diminished.

We quantify the clumpiness at ISM scales in Fig. 5. For our three galaxies with (purple) and without (orange) CRs, we show the mass distribution of stellar clumps. The number of clumps in each mass bin is averaged by stacking data from 200 to 500 Myr, a time interval for which the SFR is roughly constant. To identify the clumps, we use the ADAPTAHOP algorithm in the most massive substructure mode (Aubert et al. 2004; Tweed et al. 2009). Following the notation used in Aubert et al. (2004, in Appendix B), we adopt N_{SPH} = 16,

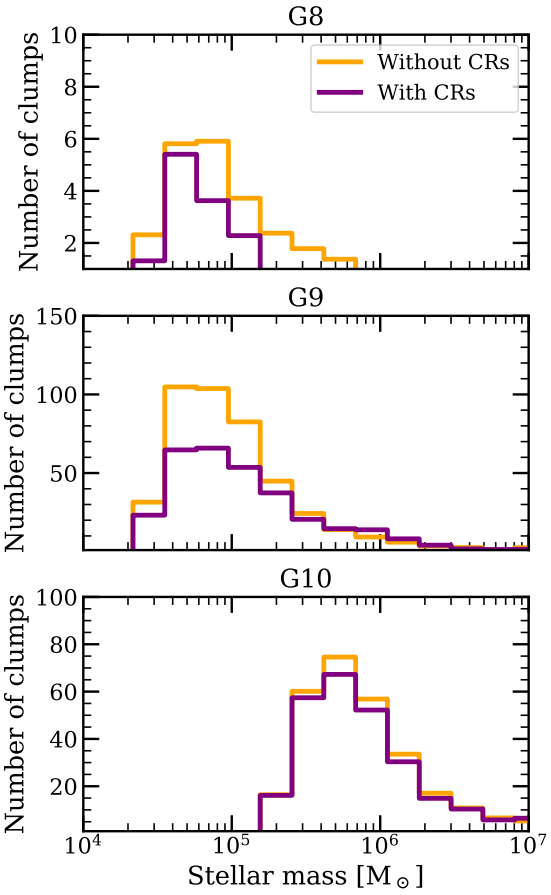

Figure 5. Number of stellar clumps as a function of their mass, with 15 logarithmic bins between 10^4 and 10^7 $M_\odot$. The panels represent increasing galaxy mass from top to bottom. Orange and purple colours correspond respectively to galaxies without and with CRs, and we show the average number of clumps in each mass-bin for outputs stacked between 200 and 500 Myr. CRs reduce the number and the mass of the stellar clumps in all our galaxies, but less efficiently with increasing galaxy mass.

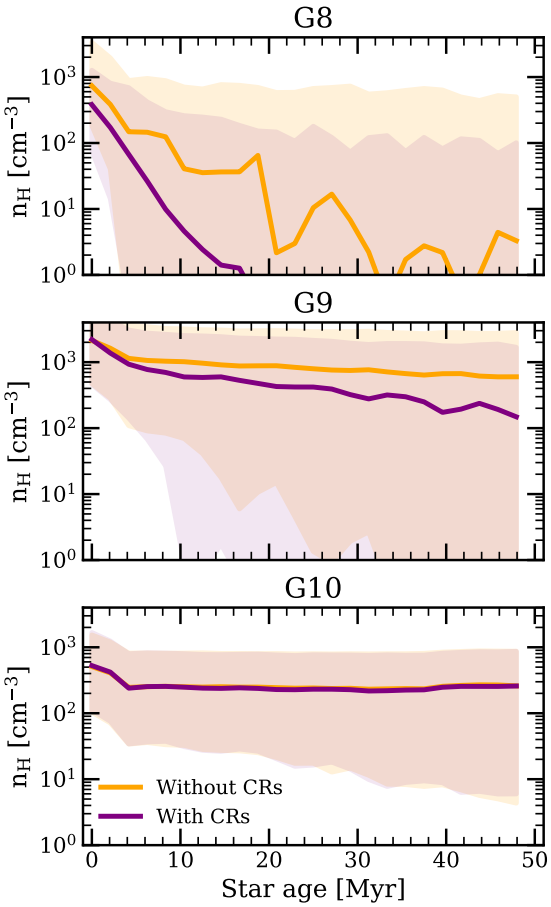

Figure 6. Densities of cells hosting stellar particles as a function of the particle age, binned every 2 Myr. The panels represent increasing galaxy mass from top to bottom. Solid lines show the median density in each age-bin for outputs stacked between 200 and 500 Myr. The shaded areas give the 10th and 90th percentiles in each stellar age bin. Orange and purple colours correspond respectively to galaxies without and with CRs. With increasing galaxy mass, CRs become less efficient in dispersing gas around the sites of star formation.

$N_{\rm HOP} = 8$, $\rho_{\rm TH} = 80$ and $f_{\rm Poisson} = 2$. Then, we define a clump as the closest stellar particles (at least 10) to a common local maximum, corresponding to the centre of the clump.

When CR feedback is included, the number of stellar clumps is strongly suppressed in the two lower-mass galaxies, as also visible in Fig. 4. However, CRs only marginally reduce the number of clumps in G10. We additionally note that there are fewer clumps at low masses in G10, compared to what is measured for G8 and G9. This is due to the coarser resolution in G10, which has stellar particles at least 8 times more massive than our dwarf galaxies (see Table 1). Because of the lower limit in the number of particles per clump set when using the ADAPTAHOP algorithm, the lower mass of a stellar clump in G10 is higher than that in our two dwarf galaxies.

In order to explain the reduction of stellar clumps with CRs, Fig. 6 explores the efficiency of CR feedback in dispersing gas locally at the sites of star formation. For each galaxy, the histograms show the median density of the cells in which the stellar particles are located as a function of their age, binned every 2 Myr. To avoid any transient effect, the density of each bin is averaged from stacking the outputs between 200 and 500 Myr in steps of 10 Myr. We show results from the runs with (without) CRs in purple (orange).

Each stellar particle undergoes several SN explosions between 3 and 50 Myr, which disperse gas locally and reduce the local density as the particles age. When CRs are injected from these SN explosions, they further disperse local densities around young stars in our dwarf galaxies. Because G8 has a shallow gravitational potential, the gas dispersal caused by the CR pressure has more visible consequences than for our two other galaxies. After 20 Myr, only half of its stellar particles are surrounded by gas more diffuse than a few atoms per cm^3 when CRs are included. Not only are stellar clumps rapidly dispersed, but star formation also occurs at slightly lower densities with CRs added, which is not the case for the two other galaxies. Nonetheless, the density of gas in star-forming regions decreases for both G8 and G9 after the first SN explosions, especially when CRs are injected, which leads to the reduced number and masses of stellar clumps shown in Figures 4 and 5. In G10 however, CRs do not act strongly enough to disperse gas, and the density of gas in star-forming regions remains the same with and without CRs. Similarly, photoionization heating from young stars has been shown to have a similar effect on local gas densities at G8 and G9 galaxy masses, but also to have negligible effect in G10 (Rosdahl et al. 2015). We additionally note that stars form at lower densities in G10 than in G9 due to the coarser resolution in G10, which does not affect the strength of CR feedback (see Section 4).

We summarise the effects of CRs on star formation as follows. In low-mass galaxies, they disperse gas in the vicinity of the SNe away from star-forming clumps, which smooths the ISM. CRs therefore delay gas in reaching the density needed to form stars, which suppresses star formation, as less numerous and/or less massive clumps can form.

3.2 Outflows

One of our main goals is to assess the role of CR feedback in launching gas from galaxy discs, and especially its ability to push away cold material. To quantify the efficiency of feedback in generating galactic winds, we focus on the mass loading factor, defined as the mass outflow rate normalised by the star formation rate. By outflowing gas, we mean all gas which is flowing away from the disc in the vertical direction. In order to avoid spurious oscillations in the mass loading factor due to the bursty star formation and the delay between starbursts and an increase in outflows kiloparsecs away from the disc, we use star formation rates averaged over the last 50 Myr. To measure the outflow rate, we define planes parallel to the disc at a given distance from it. For each cell, the rate of outflowing gas mass $\dot{m}_{\rm cell}$ is defined as the product of the gas density ($\rho_{\rm cell}$) with its vertical velocity ($u_{z,\rm cell}$) and the surface of the cell ($\Sigma_{\rm cell}$), i.e.: $\dot{m}_{\rm cell} = \rho_{\rm cell} u_{z,\rm cell} \Sigma_{\rm cell}$. The total mass outflow rate is then derived by summing the values of all the cells intersected by the selected planes.

To better study the impact of CRs on the outflowing gas phase, we distinguish three temperature regimes, namely cold for gas with $T < 10^4$ K, warm for $10^4 \leq T < 10^5$ K and hot for gas at temperature $\geq 10^5$ K. These temperature ranges are chosen to trace observational lines. What we call cold mainly corresponds to neutral gas, the warm phase can be traced through MgII, CIII or SiIV absorption lines, and the hot gas can be detected with X-ray emission, CIV or OVI absorption lines (as has been done in the COS-haloes survey data from Werk et al. 2013, 2016).

Fig. 7 shows profiles of the mass loading factor as a function of distance from the disc plane. In order to reduce the noise due to transient effects and bursty star formation, we stack 32 outputs between 200 and 500 Myr. Each panel contains what we define to be cold, warm or hot gas both for the galaxies without (in dashed lines) and with (in solid lines) CR feedback.

Focusing first on the black solid and dashed lines, adding CR feedback leads to a net increase in the loading factor at all masses. The same behaviour was qualitatively found by DD20, but with an even stronger effect from CRs on driving winds. We detail the reasons for this difference in Section 4.

Without CRs, the outflow is dominated by the hot phase in all three galaxies, with only a small amount of warm component and a tiny fraction of cold gas ejected. In contrast, with CRs, the outflows become preferentially warm, and cold outflowing gas can be found at any distance from the disc, even if in a smaller proportion for the two more massive galaxies. Measurements of MgII absorption in quasar sightlines around galaxies appear to disfavour the complete lack of warm gas produced in our non-CR simulations (Bordoloi et al. 2011; Bouché et al. 2012). We will study more quantitatively the effect of CR feedback on the MgII content around galaxies and compare to observations in upcoming work.

We note that the less massive the galaxy, the higher the mass loading factor, independently of the feedback (in agreement with observations, e.g. Heckman et al. 2015). Because dwarf galaxies have a shallower potential well, we can expect that stellar feedback can expel gas more efficiently (Dubois & Teyssier 2008). We also find a trend of decreasing outflow rate with distance, most particularly for G10 when CRs are added. For the latter, the amount of cold gas in the outflows suddenly drops, especially above 7.5 kpc.

3.3 Sensitivity to the cosmic ray diffusion coefficient

The impact of CRs, both at ISM and CGM scales, is predominantly determined by the force they apply on gas. This force directly depends on the CR pressure gradient, which evolves due to CR diffusion and dissipation, and is therefore largely ruled by their diffusion coefficient, which is a key parameter governing their propagation. We now investigate how the diffusion coefficient affects CR feedback.

Observationally or theoretically, there are not yet strong constraints on the diffusion coefficient. Empirically, and from fitting models of CR propagation (with codes like GALPROP, Strong & Moskalenko 1998), we expect a diffusion coefficient of a few 10^{28} cm^2 s^{-1}. In addition, the diffusion coefficient is not homogeneous but rather depends on the energy of the CR particles (Zweibel 2013), as well as on the local gas properties, such as the level of turbulence and the ionisation fraction (e.g. Bustard & Zweibel 2021). For simplicity and computational efficiency, simulations that include CRs generally adopt a constant diffusion coefficient, with values typically varying from 10^{27} to a few 10^{29} cm^2 s^{-1} from one work to another (see for instance Salem et al. 2016; Pakmor et al. 2016; Girichidis et al. 2018; Farber et al. 2018; Buck et al. 2020; Dashyan & Dubois 2020; Ji et al. 2020; Hopkins et al. 2020, but also Farber et al. 2018; Hopkins et al. 2021; Girichidis et al. 2022; Semenov et al. 2021 for a diffusion coefficient varying with gas properties or CR energy). We therefore test the variability of CR feedback by performing additional simulations with the following values: $\kappa_{28} = \{0.1, 1, 3, 10, 30\}$ where κ_{28} is the diffusion coefficient in units of 10^{28} cm^2 s^{-1}. As DD20 did a similar revision for the two lower mass discs G8 and G9, we also comment on how the results are affected by our additional physics, namely the inclusion of radiative transfer as well as more physically motivated models for star formation and SN feedback.

In order to appreciate the impact of CRs in our simulations, it is useful to compare time and length scales over which different competing factors operate. Being charged particles, CRs diffuse along magnetic field lines by scattering off magnetic field inhomogeneities. The characteristic time for CRs to diffuse over a length-scale L with a diffusion coefficient κ is $t_{\rm diff} = L^2/\kappa$. Because the thermal and CR components are tightly coupled to the magnetic field, CRs are also advected with the gas at the gas velocity u. The density of CRs thus evolves on a timescale related to a crossing time $t_{\rm cross} = L/u$. CRs can also be transported by streaming, which occurs along magnetic field lines and down the CR pressure gradient at about the Alfvén speed $u_{\rm A}$[5]. Streaming has been shown e.g. by DD20 to be a subdominant process compared to advection and diffusion. Therefore, we do not expect that streaming affects our results, and we do not include it in our simulations. Finally, CRs dissipate energy at a rate which scales with the gas density $n_{\rm gas}$. For Coulomb and hadronic collisions, CRs lose energy at a rate $\Gamma_{\rm CR} = \xi_{\rm coll} \times (n_{\rm gas}/{\rm cm}^{-3}) \times (e_{\rm CR}/{\rm erg\ cm}^{-3})$ erg s^{-1} cm^{-3}, where $e_{\rm CR}$ is the CR energy density and $\xi_{\rm coll} = 7.51 \times 10^{-16}$ cm^3 s^{-1} is the rate of collisional CR energy loss (Guo & Oh 2008, and as implemented in the RAMSES code used in this study. See also equations 9 and 10). The corresponding CR energy loss time-scale is therefore $t_{\rm loss} = (\xi_{\rm coll} \times n_{\rm gas})^{-1}$.

[5] The exact speed depends on the major damping process of the CR-excited Alfvén waves

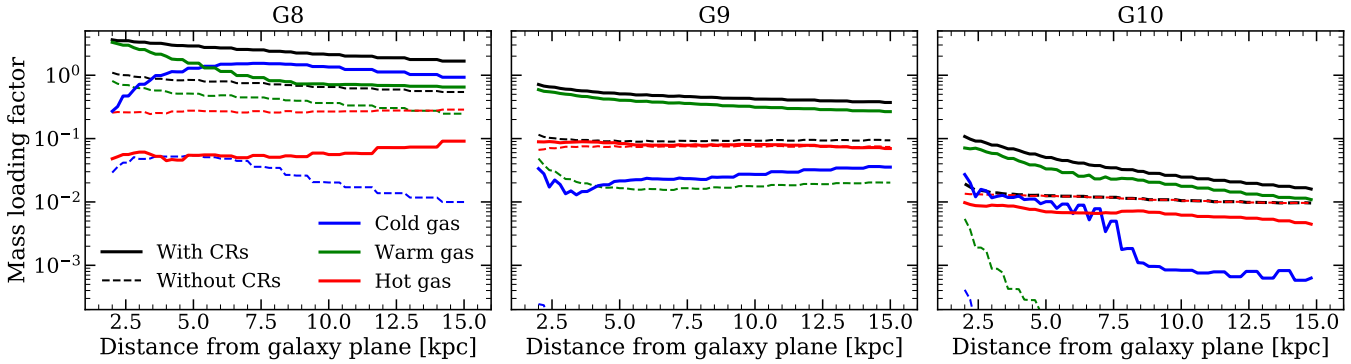

Figure 7. Mass loading factors (ratio of outflow rate to star formation rate) of gas crossing slabs at different distances from the galaxy midplane for G8 (left), G9 (middle) and G10 (right), with data stacked from 200 to 500 Myr. The blue, green and red lines respectively stand for cold ($T < 10^4$ K), warm (10^4 K $\leq T < 10^5$ K) and hot ($T \geq 10^5$ K) gas. We show the mass loading factors for the total gas without any temperature distinction in black. The dashed lines are for the runs without CRs, where no (or almost no) cold gas is outflowing at any time and no matter the galaxy mass, and the solid lines are for the runs with CRs added, with more outflowing gas in total, dominated by a warmer phase and with more cold gas than the noCR run counterparts.

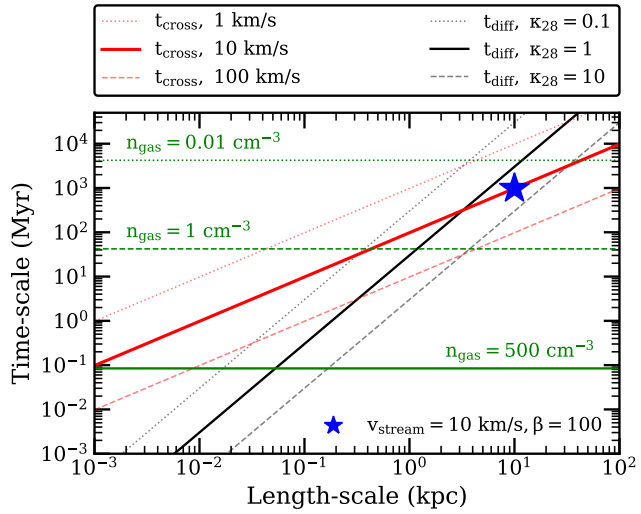

Figure 8. Time-scale against length-scale for the crossing time (in red), CR diffusion time (in black) and CR energy dissipation time (in green) for different gas velocities, diffusion coefficients, and gas densities, as indicated in the legend. At small scales ($L \leq 1$ kpc), CR diffusion is the dominant transport process. However, the lower the diffusion coefficient, the slower the diffusion, so the more significant the CR energy losses before they are propagated to disc scales. At CGM scales ($L \sim 10$ kpc), considering a gas velocity of $\sim 100\,\mathrm{km\,s^{-1}}$, CRs are mostly advected with gas, as CR diffusion is slower for any diffusion coefficient. At CGM gas densities ($n_\mathrm{H} < 0.01\,\mathrm{cm^{-3}}$), CR energy losses become negligible, and the time associated to streaming (represented by a blue star) becomes comparable to or somewhat shorter than diffusion, but remains longer than advection.

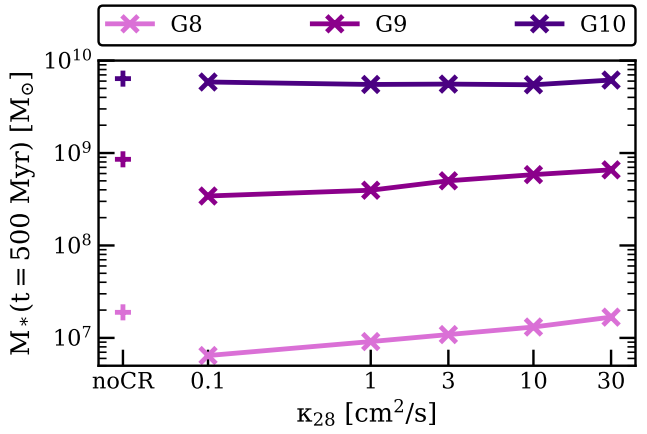

Figure 9. Stellar mass formed by the end of the 500 Myr runtime for G8, G9 and G10 with increasing diffusion coefficient from left to right. The leftmost data point for each galaxy represents the stellar mass formed without CR feedback. Star formation is most efficiently regulated with the lowest diffusion coefficient considered. In the most massive galaxy, star formation is insensitive to CR feedback at any κ (nor in fact is it sensitive to any feedback we include).

We illustrate these scaling behaviours for parameter values of interest on Figure 8, which shows transport time-scales in Myr against transport length-scales in kpc. The time-scales associated to CR diffusion are shown with black lines. The crossing time associated to CR advection is plotted with red lines. Green horizontal lines indicate the CR energy dissipation time-scales at the corresponding gas density. We use Fig. 8 in the two following subsections to analyse why different diffusion coefficients lead to different consequences on star formation and launching of winds.

3.3.1 Cosmic rays in star-forming clouds

We first focus on molecular cloud scales of around 50 pc, as this is where CRs are injected when SNe explode. At these scales, the typical gas velocity is $1 - 10\,\mathrm{km\,s^{-1}}$, corresponding to the dotted and solid red lines in Fig 8. If we compare them to the black solid line, which corresponds to $\kappa_{28} = 1$, we see that the diffusion time is shorter than the crossing time. This is the case at any diffusion coefficient in the range of values we show in the plot, meaning that typically the diffusion of CRs is much faster than their advection with gas at small scales. The escape of CRs from star-forming regions is therefore ruled by diffusion, and thus by the diffusion coefficient. With lower diffusion coefficient, CRs are stuck for longer in the ISM, so they have more time to disrupt star forming clouds. Consequently, we expect CRs to be more efficient at suppressing star formation with a low diffusion coefficient.

Figure 9 compares the stellar mass formed during the 500 Myr runtime for our three discs, with increasing diffusion coefficient. For

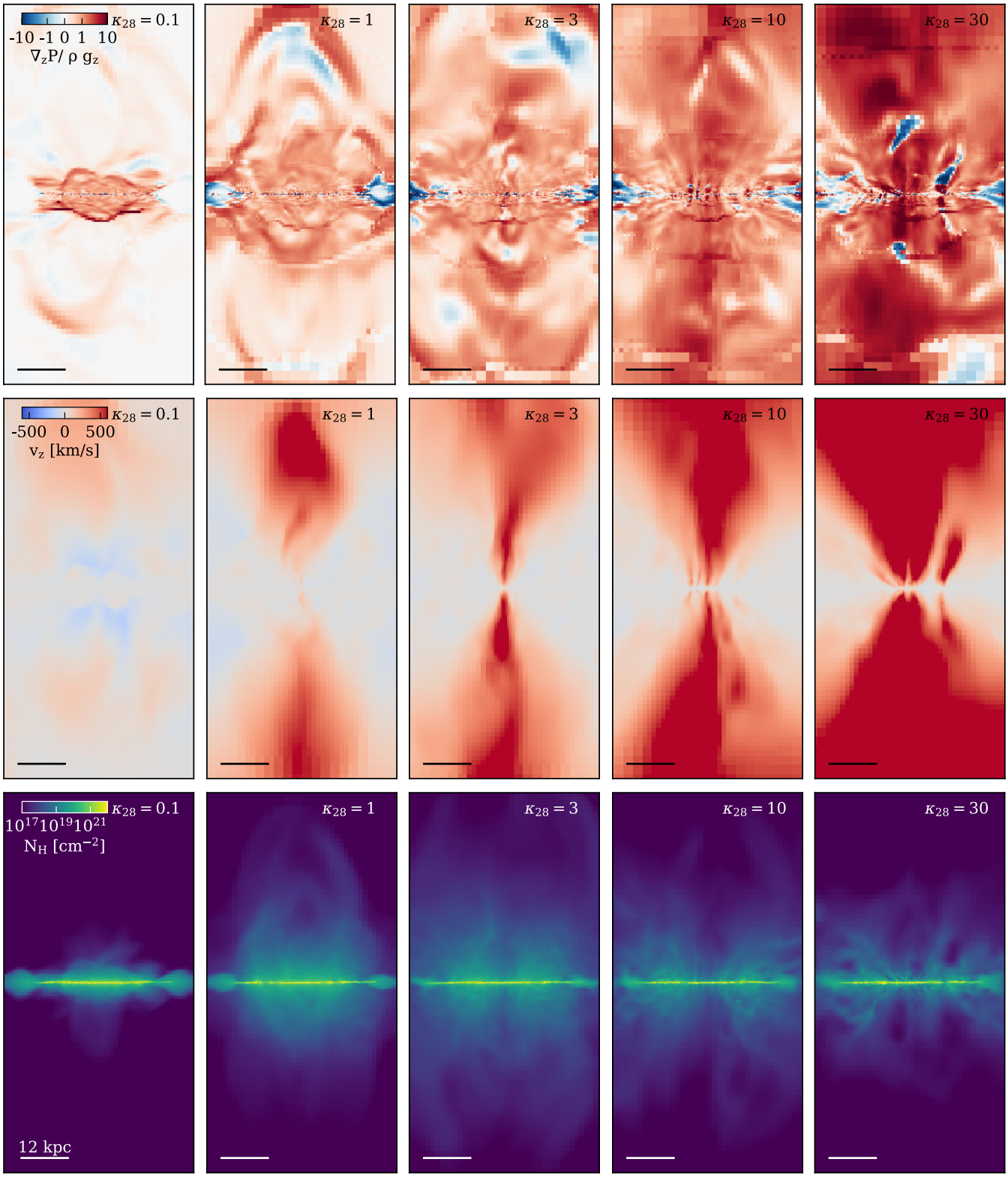

Figure 10. 6 kpc-deep projections centered on G10 at 500 Myr in order of increasing κ from left to right. For each run, we show edge-on maps of the CR pressure gradient over the vertical gravitational force (top row), vertical velocity (middle row) and hydrogen gas column density (bottom row). With increasing diffusion coefficient, the CR pressure overcomes gravity more easily. As winds are pushed faster and to larger distances, the gas distribution around the galaxy becomes increasingly extended but also more diffuse.

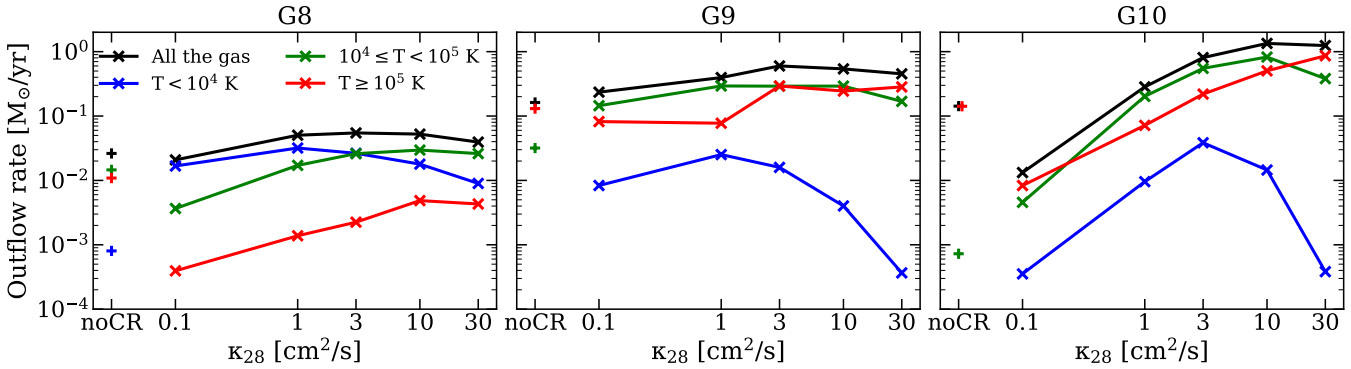

Figure 11. Mass outflow rate of gas crossing slabs at 10 kpc from the galaxy midplane as a function of the diffusion coefficient, in order of increasing galaxy mass from left to right. For each galaxy, data are stacked between 200 and 500 Myr. We show the total amount of outflowing gas in black, the cold component ($T < 10^4$ K) in blue, the warm ($10^4 \leq T < 10^5$ K) in green and the hot ($T \geq 10^5$ K) in red. The leftmost points are for runs without CRs. The total amount of outflowing gas and especially its hot component are globally enhanced with higher values of κ. However, the rate of cool outflows stops increasing and even drops beyond a diffusion coefficient limit, which increases with galaxy mass.

the two dwarf galaxies (G8 and G9), we find the largest regulation of star formation when the diffusion coefficient is the lowest, as found by Salem & Bryan (2014), Chan et al. (2019) and DD20, and as expected from our length versus time-scale analysis from Figure 8. As lower diffusion coefficient leads to a slower CR diffusion, it also leads to a stronger direct effect of CRs on the star-forming regions and, hence, on star formation. For G10 however, the effect of CRs on star formation remains weak at any κ, as do the other forms of (SN and radiation) feedback modeled here (see Rosdahl et al. 2015).

Another important process in dense star-forming clouds is the dissipation of CR energy. If embedded in a 500 cm^{-3} density gas, CRs lose their energy over time-scale of about 0.04 Myr, as shown by the solid green line in Fig 8. This energy dissipation time is shorter that the diffusion time-scales for $\kappa_{28} \leq 1$. As a result, CRs with low κ lose a large amount of their energy before they can reach less dense gas on larger scales, and we expect a lower impact from CRs at large scales in this case. We now assess whether this is indeed the case.

3.3.2 Cosmic rays in the CGM

Before assessing the effects of changing the CR diffusion coefficient on CGM gas, we first come back to our length versus time-scale analysis from Figure 8. At nearby CGM scales, the crossing time corresponds to a gas velocity of 100 $\mathrm{km\,s}^{-1}$, typical for both the sound speed and outflow velocities in the CGM. As it becomes smaller than the diffusion time, this shows that CRs are mainly advected with gas rather than via diffusion. In this medium, the gas has densities lower than 0.01 cm^{-3}, for which the loss of CR energy occurs on time-scales of several Gyr and hence is completely subdominant. The CR energy is thus conserved and propagates through the CGM.

It is only at CGM scales that CR streaming is faster than diffusion. For this reason, we show with a blue star the time associated to streaming at a scale of 10 kpc, where the plasma β (ratio of thermal to magnetic pressure) is around 100. As $v_\mathrm{A} \propto c_\mathrm{s}/\sqrt{\beta}$, at 10 kpc where the sound speed $c_\mathrm{s} \simeq 100\,\mathrm{km\,s}^{-1}$, $v_\mathrm{stream} \simeq 10\,\mathrm{km\,s}^{-1}$. Comparing the blue star to the red dashed line, we can see that the streaming time-scale is around 10^3 Myr, which is ten times longer than the advection. Even at CGM scales, streaming is subdominant compared to the transport of CRs via gas advection. To show a significant contribution, the streaming velocity has to be boosted by damping effects, such as ion-neutral damping or turbulence as in Ruszkowski et al. (2017) and Hopkins et al. (2021). Even so, these two studies have opposite conclusions on the importance of the role of CR streaming, which remains a topic of extensive investigation.

To summarize, Figure 8 shows that diffusion is the dominant process in the CR injection sites, meaning that the diffusion coefficient directly impacts the confinement of CRs in dense regions of the galaxy, where most of their radiative energy losses occur. The competition of diffusion and CR energy losses in dense gas regulates the amount of CR energy escaping into the more diffuse ISM and hence, potentially, their impact on larger scales. We will now assess whether varying the diffusion coefficient in our simulations has the effects predicted by these scale-comparisons.

Varying the diffusion coefficient has a strong effect on gas morphologies and outflows in all our galaxies. Figure 10 qualitatively illustrates the effect of the diffusion coefficient on G10, with increasing κ from left to right. The top row shows the ratio of the CR pressure gradient (i.e. the force from the CR pressure) to the vertical gravitational force of the disc, where red (blue) cells have an outward (inward) net force. Red colours thus show cells where the force exerted by CRs can overcome the gravitational potential of the galaxy. The middle row shows the vertical velocity of the gas, with red (blue) colours for outflowing (inflowing) gas. The bottom row finally shows the hydrogen column density.

The force exerted by CRs strongly affects the gas distribution around the disc. The $\kappa = 10^{27}$ $\mathrm{cm}^2\,\mathrm{s}^{-1}$ case merely produces a closely confined outflow fountain, as the CR gradient vanishes beyond a few kpc, which leads to a thick disc surrounded by dense gas. When we increase the diffusion coefficient, we find larger CR pressure gradients at larger distances, producing strong bipolar winds. The gas is expelled farther away from the ISM and at higher speed, and is more broadly distributed around the disc, becoming very diffuse for the highest values. Qualitatively, the same holds for our lower mass galaxies (not shown).

Figure 11 shows the effect of κ on the mass outflow rate for the different galaxies, in terms of total outflowing gas and its cold ($T < 10^4$ K), warm ($10^4 \leq T < 10^5$ K) and hot ($T \geq 10^5$ K) components measured at 10 kpc from the discs. For each simulation we take the average from 31 snapshots (with 10 Myr intervals) between 200 and 500 Myr. The leftmost symbols in each plot represent runs without CR feedback.

For all three galaxies, increasing the diffusion coefficient leads to stronger and eventually hotter outflows, with total outflow rates that increase, top out and finally stagnate. Our time-scale analysis at ISM

and CGM scales from Figure 8 indicates that increasing the diffusion coefficient leads to more efficient escape of CRs from dense regions in the galactic disc, meaning less radiative losses and so more energy available to push and maintain outflows at high velocities (see also Fig. 10). This explains the increasing outflow rates with increasing κ. This also explains why the maximum of the outflow rate with κ does not correspond to the maximum star formation regulation. For efficient regulation of star formation, CRs have to be trapped in clouds to build a strong CR pressure gradient (Commerçon et al. 2019), whereas launching winds requires CRs to escape these dense regions, which is an opposite condition to the regulation of SF by CRs.

On long enough time-scales, the galactic winds may lead to gas-depletion in the disc, which in turn would lead to a regulation of star formation. However such timescales are beyond our simulation runtimes. We estimate depletion timescales of approximately 1.7 (G8), 1.7 (G9), and 17 Gyr (G10), where we have assumed constant outflow rates of 0.1, 1, and 1 $M_\odot$/yr, respectively. For G10 in particular, this outflow depletion timescale is significantly longer than the star formation depletion time. Therefore, outflows are not expected to have a significant effect on star formation. For our lower mass galaxies, the relevance of such sustained outflows remains unclear, and we will review this with cosmological simulations in upcoming work.

In agreement with our results, DD20 found for their G8 and G9 counterparts that the higher the diffusion coefficient, the stronger the outflows (see also Section 4 for more details). However, we additionally report that the outflow rate does not increase steadily with κ. Furthermore, the warm and cold outflow rates peak and then drops beyond a certain κ, which depends on the galaxy mass.

This trend is especially strong for the cold outflowing gas. For the two dwarf galaxies (G8 and G9), the fraction of cold outflows peaks for $\kappa = 10^{28}$ cm^2 s^{-1}, but it peaks at $\kappa = 3 \times 10^{28}$ cm^2 s^{-1} for G10. This hints towards the existence of a diffusion coefficient value beyond which the effect of CRs gradually vanishes, dependent on galaxy mass, or alternatively its size. The more massive the galaxy, the thicker the galactic disc CRs have to cross before propagating to the CGM. For more massive galaxies, with larger length scales, a higher diffusion coefficient is then needed for CRs to escape dense regions (as shown in Fig. 8) and drive winds. This explains why the ability of CRs to drive winds starts vanishing at a diffusion coefficient higher for larger galaxies.

When the diffusion coefficient is high enough for CRs to quickly escape from the disc (1 – 10 Myr, see Fig. 8), the CR pressure starts acting at larger distance from the midplane, where gas is more diffuse, and CRs do not impact the densest and coolest gas of the galaxy anymore. Because the CR pressure gradient builds up farther away with increasing κ, the density of cold and warm outflows decreases drastically, explaining why we measure less outflowing gas at temperature below 10^5 K.

It is also interesting to note the $\kappa = 10^{27}$ cm^2 s^{-1} case for G10, which has smaller outflow rates at 10 kpc than its counterpart run without CRs. This is the consequence of CRs acting locally and puffing up the galactic disc, carrying with them high density gas but at velocities too low to escape the gravitational potential of the galaxy. There are slightly stronger outflows with $\kappa = 10^{27}$ cm^2 s^{-1} than without CRs in G10 at 2 kpc (see Fig. B1), but the dense outflowing material quickly falls back to the galaxy and the outflows are not maintained at large distances. When the diffusion coefficient is very small, CRs become irrelevant in driving significant outflows, and can actually become counter-productive in driving galactic winds on large scales.

3.4 Do cosmic rays provide the needed feedback in high-redshift galaxies?

The objects we are focusing on in this study have a fairly low mass and a high fraction of gas (see Table 1), which is typical for high-redshift galaxies (Daddi et al. 2010; Tacconi et al. 2010, 2013; Genzel et al. 2015). SNe are usually assumed to be the most efficient feedback process to regulate star formation in low-mass galaxies (see e.g. Dekel & Silk 1986; Hopkins et al. 2011; Gelli et al. 2020). However, they appear insufficient to explain a number of observed properties. Among others, we know from Hu et al. (2017), Emerick et al. (2018) or Fujimoto et al. (2019) that coupling SN and radiation feedback reduces tensions between galaxy simulations and observations. All of these studies also point to the weakness of these combined feedback mechanisms to efficiently regulate star formation. To compensate the lack of efficiency of SN (and radiation) feedback in driving sufficient regulation of star formation in high-resolution simulations of galaxy evolution, various forms of sub-grid models are used, and sometimes the energy injection from supernova explosions is simply artificially boosted to reach the desired agreement with observations. This is what is done in the SPHINX suite of cosmological simulations (Rosdahl et al. 2018), where the number of SN explosions per Solar mass formed is amplified by a factor four in order to roughly reproduce the stellar-to-halo mass relation and the UV luminosity function at $z = 6$[6]. Using here the same star formation, SN and radiation feedback implementations as in the SPHINX simulations, we want to assess whether CRs could be a real and physical substitute for the amplified SN feedback. In other words, we want to assess whether they provide a similar regulation of star formation when combined with un-amplified SN feedback and, if so, if their impact on the star formation operates differently, e.g. with higher or lower outflow rates or producing very different morphologies in the ISM or CGM. Thus, we perform additional isolated disc runs, labelled 'Strong SNe', where we increase the number of SN explosions per unit Solar mass by a factor four, which corresponds to SNe releasing an energy of 28.8×10^{48} erg $M_\odot^{-1}$ instead of the 7.2×10^{48} erg $M_\odot^{-1}$ derived from a canonical Kroupa IMF. We then investigate how the CR feedback (with $\kappa = 10^{28}$ cm^2 s^{-1}) compares to the calibrated boosted SN feedback adopted by Rosdahl et al. (2018) in terms of star formation regulation efficiency, outflows, and escape of LyC photons.

Figure 12 shows the differences in star formation and outflows between our galaxies with and without CRs in purple and orange, respectively, and with the strong SN feedback (and no CRs) in red. From top to bottom, we plot as a function of time the stellar mass, the SFR, the mass outflow rate measured at 10 kpc, and the fraction of mass outflow with temperature below 10^5 K (which we term here 'cool' outflows).

Generally the strong SN feedback is more efficient than CRs, both in regulating star formation and in launching winds. Compared to strong SN feedback, CRs have a similar efficiency in suppressing star formation in our most massive galaxy, but lead to twice higher stellar masses in G8 and G9. Therefore, the inclusion of cosmic rays appears not quite sufficient to replace the effects of amplified SN feedback. Nonetheless, they provide a reasonable match for the star formation and even outflows for the lower-mass galaxies.

CRs and strong SN feedback produce very different outflow tem-

[6] Nonetheless, at lower redshift ($z \sim 3$), Mitchell et al. (2018) show that such an over-injection of SN energy fails and that galaxies still have too high stellar masses, indicating that complementary physics are lacking, and that even this four-fold amplification of SN feedback is not enough.

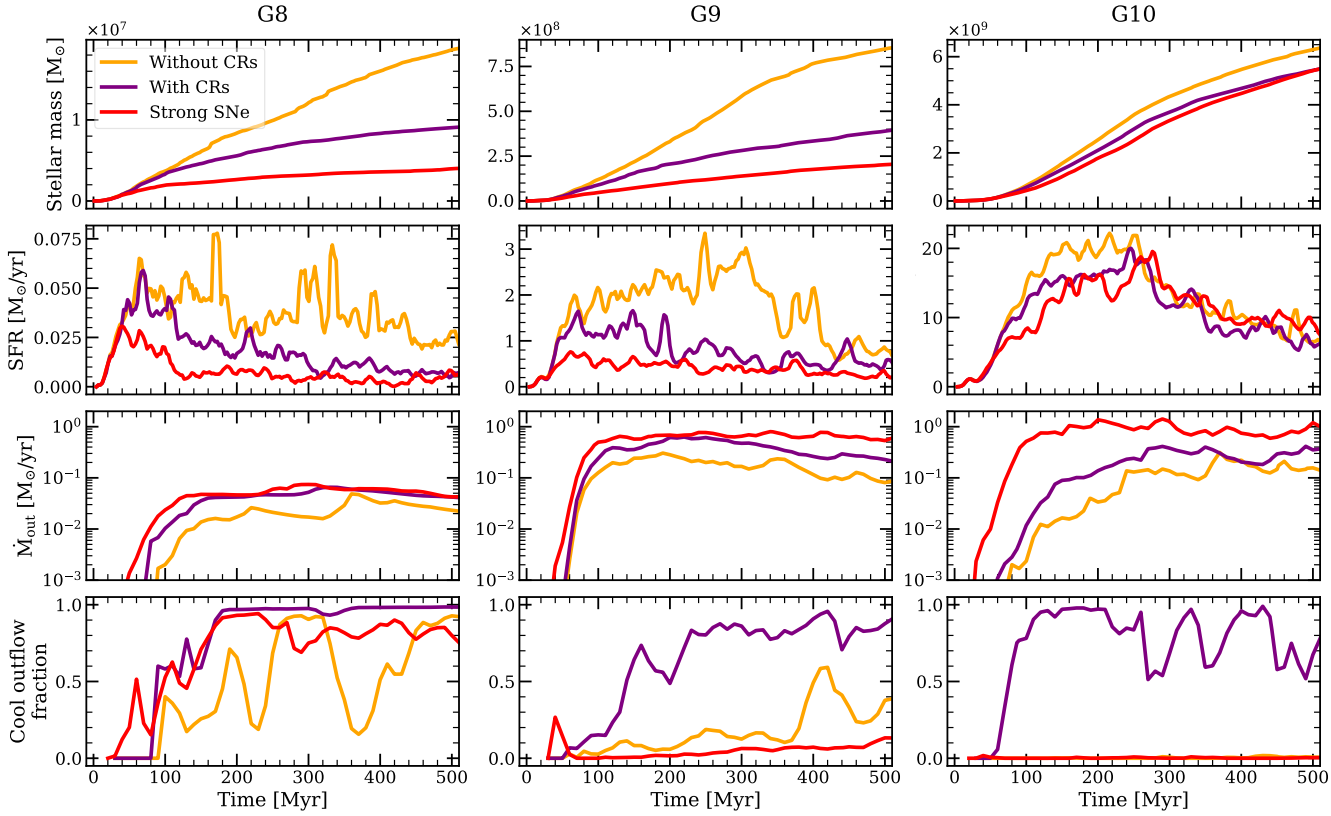

Figure 12. From top to bottom: Evolution with time of the stellar mass, star formation rate, mass outflow rate measured at 10 kpc, and fraction of outflowing gas with temperature below 10^5 K. The orange, purple and red curves correspond to runs without CRs, with CRs ($\kappa = 10^{28}\,\mathrm{cm^2\,s^{-1}}$) and with the strong SN feedback respectively. The strong SN feedback is somewhat more efficient than CRs in regulating star formation. It also drives stronger winds, albeit hotter than with CRs.

peratures. Without CRs, the fraction of outflowing gas colder than 10^5 K decreases drastically with galaxy mass, and the outflows are composed of hot gas only in the G10 case. While amplifying SN feedback can regulate star formation more efficiently than CRs, it affects other galaxy properties such as the CGM gas, which is almost exclusively fed by winds hotter than 10^5 K for our two most massive galaxies (G9 and G10). Conversely, galaxies with CRs all have a significant fraction of cool outflows. These contribute to enrich the CGM with metals that trace temperatures below 10^5 K, lacking in simulations with a strong SN feedback. For instance, by comparing HI, SiIII, SiIV and CIII CGM abundances from the COS-haloes survey (Werk et al. 2013, 2016), Salem et al. (2016) and Butsky et al. (2021) found that CR-driven winds can better reproduce the observed metal-enriched outflows. Based on these results, the outflowing CGM potentially provides a strong constraint on CR feedback, which we intend to investigate in future work.

3.5 Lyman continuum escape fraction

Several recent simulation works find that feedback regulates the escape of ionizing radiation from galaxies (Ma et al. 2016; Kimm et al. 2017; Trebitsch et al. 2017; Rosdahl et al. 2018). Therefore, it is of a particular interest to capture the physical processes that shape galaxy evolution to understand their consequences at high-redshift, where they can play an important role in the reionization of the Universe. Cosmic ray feedback tends to smooth out density fluctuations in the ISM and generate fairly dense and cold galactic outflows. How this affects the propagation and the escape of radiation through and out of galaxies however remains unexplored. The SPHINX cosmological simulations (Rosdahl et al. 2018) produce a reionization history which is in reasonable agreement with observations, implying that this strong feedback model produces an approximately correct mean escape fraction ($f_{\rm esc}$) of LyC radiation from galaxies. Therefore, in this section, we assess how replacing this strong SN feedback by CRs affects the escape fraction of LyC radiation from galaxies and, potentially, reionization.

For this purpose, we estimate the LyC escape fraction in our three galaxies as follows. The escape fraction $f_{\rm esc}$ is the ratio of the photon flux measured, divided by the intrinsic luminosity emitted by the stars. For each galaxy, we estimate the total flux of all radiation groups that crosses a spherical shell of 500 pc in width, located at the viral radius R = 41, 89 and 192 kpc for G8, G9 and G10 respectively. To avoid any spurious estimation of the photon flux due to the irregular structure of the grid, we randomly sample photon fluxes from a million points inside the shell (using the `Pymses`[7] code), from which we derive an average photon flux in the shell $F_{\rm meas}$. Without any absorption, the flux would be the total intrinsic luminosity emitted by the stars L divided by the area of the shell where the flux is measured. Because we use a reduced speed of light $c_{\rm red} = c/100$, it takes some time for the light to reach the shell. To correct for this delay, we compare the photon flux at a time t and at a distance R to the luminosity emitted a light-crossing time ago,

[7] https://irfu.cea.fr/Projets/PYMSES

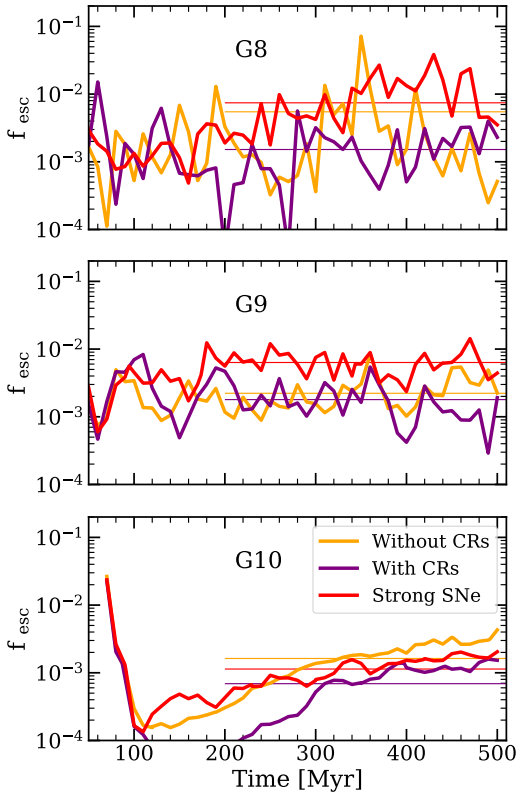

Figure 13. Escape fractions of LyC photons as a function of time. From top to bottom, panels show results for G8, G9 and G10, with (without) CRs ($\kappa = 10^{28}$ cm^2 s^{-1}) in purple (orange), and with the strong SN feedback in red. The thin lines correspond to the luminosity-weighted escape fractions averaged over the last 300 Myr. CR feedback consistently brings down the escape fraction by a factor of a few in our galaxies compared to the strong feedback model in SPHINX.

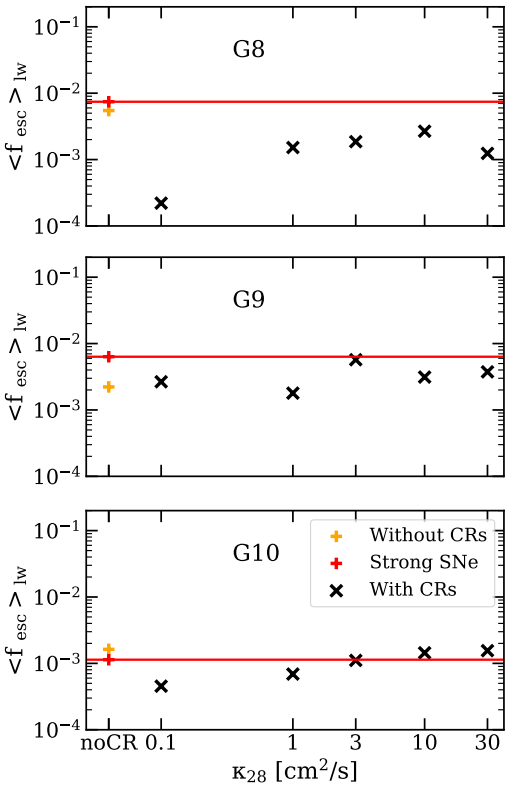

Figure 14. Luminosity-weighted escape fractions averaged over the last 300 Myr as a function of the diffusion coefficient, for increasing galaxy mass from top to bottom. The two leftmost data points show the escape fractions without CRs but with the standard and strong SN feedback in orange and red, respectively. We emphasise the escape fractions with the strong SN feedback with horizontal red lines, which we consider as the reference. Smaller diffusion coefficients suppress escape fractions, with this effect decreasing as κ increases.

i.e at $t - R/c_{\rm red}$. Therefore, the photon flux emitted by the stars is $F_* = L(t - R/c_{\rm red})/(4\pi R^2)$.

The escape fraction then provides an estimate of how much radiation has escaped from the galaxy to a given distance R from its centre, such as:

$$f_{\rm esc}(R,t) = \frac{F_{\rm meas}}{F_*} = \frac{< c_{\rm red} N(R,t) >}{L\left(t - \frac{R}{c_{\rm red}}\right)} 4\pi R^2 \,, \qquad (11)$$

where $N(R,t)$ is the photon number density measured at a distance R and at a time t.

Figure 13 shows the escape fraction of LyC photons as a function of time for our three discs, without and with CRs in orange and purple, and with the strong SN feedback in red. The escape fraction fluctuates considerably, which is a consequence of the bursty nature of star formation and feedback, as shown by e.g., Ma et al. (2016) and Trebitsch et al. (2017).

To provide a clearer picture, we show as thin horizontal lines luminosity-weighted average escape fraction over the last 300 Myr, in each simulation. In order of increasing disc mass, we find that the luminosity-weighted escape fractions are reduced by a factor 4.9, 3.5 and 1.6 when CRs are included compared to the case with strong SN feedback.

In the work of Rosdahl et al. (2018), the escape fraction of LyC photons in a galaxy with a mass similar to G8 using the strong SN feedback model peaks several times at values of ~ 0.2 during the 1 Gyr runtime, and even reaches a maximum of 0.8. Globally, and even when using the same enhanced SN feedback, the escape fractions are much smaller in our disc galaxies. This is a limitation of idealized runs that do not reproduce the bursty and irregular galaxy growth expected at high redshift.

Regardless of their low values, we note that the escape fractions are significantly reduced with CRs. This reveals that the effects of CR feedback on thickening the galaxy discs and smoothing the ISM may have important consequences on the escape of ionizing radiation, which could spell a problem in reionization models, which already tend to struggle to produce high enough escape fractions to reionize the Universe (e.g. Ma et al. 2015, 2016).

As the effects from CR feedback differ with the diffusion coefficient, Figure 14 shows the luminosity-weighted escape fraction averaged over the last 300 Myr (similar as what is plotted in thin lines in Figure 13) with increasing diffusion coefficient from left to right, and without CRs but with a standard (in orange) and strong (in red) SN feedback for the two leftmost data points. Because the strong SN feedback is found to produce high enough escape fractions to reionize the Universe before $z = 6$ in the SPHINX cosmological simulations (Rosdahl et al. 2018), we emphasise with red lines the escape fraction with the strong feedback in our disc galaxies. The escape fractions values measured in G8 with CRs are well below the strong SN feedback case, for any diffusion coefficient. However from our two higher mass galaxies, taking $\kappa_{28} = 3$ or higher produces simi-

lar escape fractions as the strong SN feedback. We stress that these results need to be confirmed with more realistic high-z galaxies in cosmological simulations, which tend to have much higher escape fractions than these idealised and rather structured galaxies. This will be the topic of our upcoming work.

4 DISCUSSION

We now compare our results with those of other studies. We first focus on the effect of CRs in regulating star formation and altering the ISM, and then review their efficiency in driving winds and the dependency of this efficiency with the CR diffusion coefficient.

4.1 CR feedback at ISM scales

From star forming clouds to the CGM, CRs significantly affect the gas component. At ISM scales, the pressure they exert pushes the gas, which tends to smooth the overall galaxy inner gas distribution (as shown in Fig. 1). We find that the efficiency of CR feedback in directly regulating star formation weakens with increasing galaxy mass. For dwarf galaxies, we find 50% lower SFR compared to runs without CR feedback (Fig. 3).

A similar reduction in star formation was found by DD20. This suggests that the effect of CRs on SF is not sensitive to the additional or different physics we include, namely more physically motivated models for star formation and SN explosions as well as the addition of radiation feedback.

The efficiency of CRs in disrupting high density regions has already been reported in other studies. The higher CR efficiency in regulating star formation in low mass galaxies has been found by e.g. Jubelgas et al. (2008), Booth et al. (2013), Pfrommer et al. (2017) and Wiener et al. (2017). However, there is divergence concerning the CR feedback efficiency in galaxies as massive as G10. While our results are consistent with those of Pfrommer et al. (2017) and Buck et al. (2020), who report very little effect of CRs on the SFR in a Milky Way mass object, they differ from those by the FIRE-2 cosmological zoom-in simulations (Chan et al. 2019).

Chan et al. (2019) found a star formation suppression up to a factor of 1.5 from CR feedback with $\kappa = 3 \times 10^{28}$ cm^2 s^{-1} in their most massive star-forming discs, whose masses are in-between those of our G9 and G10. It is unclear why CRs can still impact star formation in massive galaxies in their case and not in ours. Among the differences between our runs (in addition to the fact that they perform cosmological simulations while we study idealized galaxies), we have a local star formation efficiency with values dependent on the local gas properties, while this efficiency is set to 100% in the FIRE simulations. This is likely to have consequences on galaxy evolution, as it directly affects the spatial and temporal distribution of star formation. Nonetheless, in agreement with the FIRE simulations, we find the same reduced CR feedback efficiency in regulating star formation with increasingly high diffusion coefficient.

Another point to be noted in the FIRE-2 simulations is that they use a significantly higher fiducial $\kappa = 3 \times 10^{29}$ cm^2 s^{-1} to avoid CR energy losses and attain consistency with gamma-ray observations. This value yields much stronger winds and up to an order of magnitude higher mass loading factor than when CRs are excluded. In a cosmological context, as it is the case for the zoom-in simulations of Hopkins et al. (2021), galaxies are evolved for long enough that the greater amount of outflows ends up altering significantly the gas content of a galaxy and, hence, its star formation. In our G10 galaxy, mass loading factors are not sufficiently increased to have an impact on star formation. Considering the low 0.01 to 0.1 mass loading factors in G10, much more gas is converted into stars than pushed away in the form of outflows. We can roughly estimate that a 10 times larger timescale would be needed for the outflows expelled from G10 to start impacting the SFR. By that time, most of the gas would be converted into stars. Most long-term effects due to CR driven winds extracted from our isolated simulations are somewhat speculative and require further revision using cosmological simulations, which will be the subject of future work.

4.2 The efficiency of CRs in driving winds

While the effects of CR feedback on star formation vary with galaxy mass, it consistently helps driving more and colder outflows, which affects the gas morphology in both the galaxy and its CGM. The non-thermal CR pressure support increases the mass loading factor by 1 dex, for all our explored galaxy masses close to the disc and at least a factor two 15 kpc away from it (Fig. 7).

The efficiency of CRs in launching winds has been measured in a number of previous studies, e.g. Girichidis et al. (2018) in a stratified ISM, Pakmor et al. (2016) in an idealized disc, and Hopkins et al. (2021) in MW-luminosity zoom galaxies from cosmological simulations. There is broad agreement that the inclusion of CR feedback leads to colder and denser winds.

However, it is difficult to quantitatively compare the effects of CRs from one simulation to another because of the different feedback models used. We noted in Section 3.2 that we measure a smaller enhancement of the outflow rate when adding CRs compared to DD20. This can be explained by the fact that they measure one order of magnitude lower outflow rates in their G9 without CRs than we do. This last aspect is not due to the inclusion of radiative transfer, as Rosdahl et al. (2015) showed that radiation pressure and photo-heating have a negligible impact on wind launching (and we have confirmed this in our simulations). To determine the reason for the higher mass loading factor in our G9 compared to DD20, Figure 15 shows the outflowing gas versus time, measured at 10 kpc from G9_noCR, comparing our feedback and star formation models against those of DD20. We show the star formation model using a density threshold and a small constant star formation efficiency used by DD20 in dashed lines (that we label 'density model') and we show the turbulent model we adopt in solid lines. We also show in orange the multiple SN explosions per particle model we use compared to the single per particle model used by DD20 in green.

With the density SF model (dashed), switching from one (in green) to multiple explosions per stellar particle (in orange) increases the outflow rate by up to one order of magnitude. This difference corresponds to that noted between the outflows measured by DD20 and measured in this paper. At first glance, it may appear that the SN model is the factor governing the outflow rate. However, if we focus on the turbulent SF model (in solid lines), switching from one to multiple SN explosions leads to the opposite trend, with slightly stronger outflows in the former case. With the density SF model, stars are more broadly distributed as the gas to stars conversion can only occur if the gas density exceeds a certain threshold. If a stellar particle explodes only once, the gas is disrupted locally, but this single event is not enough to launch significant winds. A subsequent disruptive event is needed to take advantage of the previous one and make it easier to drive gas out of the disc. This is exactly what happens when switching from single to multiple SN explosions with the density star formation model. Conversely, the turbulent model leads to more bursty and clumpy star formation. Because stars form in more localised clumps, they also explode in very rapid succession, even if

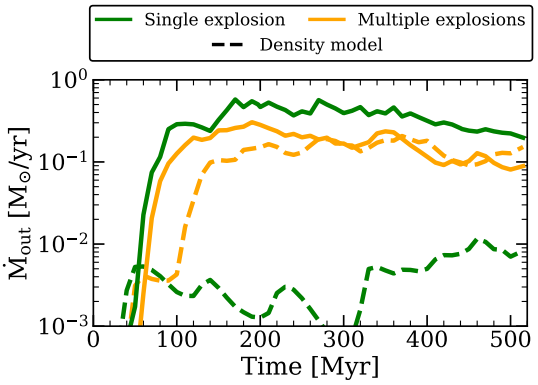

Figure 15. Mass outflow rate versus time measured at 10 kpc from the G9 galaxy. Orange (green) curves show runs with multiple (single) SN explosions. Solid lines correspond to runs with our turbulent star formation model, while dashed correspond to the model based on the gas density used by DD20. Therefore, the dashed green curve is our closest equivalent to the setup adopted by DD20. Only switching to both the turbulent SF model and multiple explosions can explain the higher outflow rate we measure for the same galaxy.

each particle explodes only once, so multiple explosions do not offer the same advantage as in the density model where star formation is more scattered in time.

All in all, the effects of varying the locality and burstiness of star formation and subsequent SN explosions is somewhat unpredictable and non-linear, as has previously been reported in e.g. Keller & Kruijssen (2022); Andersson et al. (2020); Smith et al. (2021). Consequently, the large difference in outflow rate measured by DD20 and in this paper can only be explained by the non-linear interplay of the combination of a more bursty and clumpy SF model with multiple individual 10^{51} erg SN explosions for each stellar particle. With our setup, the star formation sites tend to be destroyed by the first SNe, letting later SN explosions take place in a more diffuse medium, where more momentum can be generated. As a consequence, our SN feedback is more efficient in driving outflows, and the added effect of CRs becomes smaller. Besides, we show in Appendix A that changing from the density to the turbulent SF model with the same setup otherwise leads to different outflow rates exclusively for G8, indicating that there are additional factors that play a role, such as particle and cell resolution.

4.3 Outflow rates and the diffusion coefficient

The ejection of gas can significantly differ depending on the CR transport mechanism. For this reason, we investigate the role of the diffusion coefficient, one of the key parameters controlling CR feedback efficiency. As DD20 with G8 and G9, we find that the higher the diffusion coefficient, the higher the outflow rate (with the exception of our largest diffusion coefficient value for which the outflow rate stagnates or even slightly decreases). This is due to a more efficient escape of CRs from the disc, and hence more energy in the CGM to drive outflows. In agreement with most works(see e.g. Salem & Bryan 2014; Jubelgas et al. 2008; Farber et al. 2018; Chan et al. 2019), we find that a faster diffusion leads to more star formation. However, Salem & Bryan (2014), Jacob et al. (2018), Girichidis et al. (2018), and Quataert et al. (2022) all find higher mass loading factors with a lower diffusion coefficient, while we measure the opposite trend. We discuss below the reason behind this discrepancy.

Figure 8 suggests that CRs are more efficient to drive winds if they quickly escape the ISM where CR energy losses are dominant, or equivalently if more CR energy remains to push winds away from the galaxies with a high diffusion coefficient. In simulations without CR energy losses, a low diffusion coefficient allows CRs to escape from the disc slowly enough to drive more outflows, without losing the energy needed to accomplish this during the time they are confined in the galaxy. This is the case for the 10^{12} $M_\odot$ halo from Salem & Bryan (2014), where CR radiative losses are not included. In our case, we clearly see from Figure 10 that the CR pressure gradient cannot build up to large distances around G10 when $\kappa = 10^{27}$ cm^2 s^{-1}. For this value, CRs remain trapped close to the disc, where they lose all their energy. Furthermore, as the aforementioned studies find, we start to see a hint that with the extremely high $\kappa = 3 \times 10^{29}$ cm^2 s^{-1}, increasing the diffusion coefficient towards very high values make CRs escape so quickly that their effect starts to vanish.

While reaching a similar resolution as we have and including CR energy losses, Girichidis et al. (2018) found slightly stronger outflows with decreasing coefficient values in their stratified box of ISM. However, they measure outflows at 1 and 2 kpc. At these closer distances to the mid-plane, it is difficult to distinguish between CGM outflows and ISM fountains. In Appendix B, we show that we do measure higher outflow rates with higher κ at 2 kpc from the galaxies, but the differences with varying diffusion coefficient become much smaller than at 10 kpc.

Interestingly, Jacob et al. (2018) found in agreement with our results that the diffusion coefficient for which the maximum of outflows is reached varies with galaxy mass. This is consistent with a critical diffusion coefficient value below which the wind properties change, such as its velocity as found by Quataert et al. (2022) and its temperature as we show in Figure 11. All of this implies that the exact behaviour of outflows with changing diffusion coefficient depends on multiple parameters, from the initial conditions of the galaxy (e.g. its size) to the star formation and feedback sub-grid models.

Finally, we remark that CR propagation does not really occur under a constant diffusion coefficient. This motivates our study of the effects of CR feedback under different κ values. Ideally, one would couple the dependency of the diffusion coefficient with CR particle energy and with the gas ionization state (as CRs are charged particles that are more tightly coupled with a fully ionized gas), as well as accounting for CR streaming. The energy and ionization state dependency of the diffusion coefficient have been independently studied by Girichidis et al. (2022) and Farber et al. (2018) respectively, who both showed a greater CR feedback efficiency in regulating star formation and driving winds. Improved CR propagation models are therefore crucial to improve our understanding of the role of CRs on galaxy evolution.

4.4 Dependency of the results with resolution

Finally, we briefly discuss how our results vary with resolution. In Fig 16, we show the evolution with time of the stellar mass formed (left panel) and the outflow rate at 10 kpc from the midplane of the disc (right planel). We compare low resolution runs, where the minimum cell width is 9 pc for G8 and 18 pc for G9 and G10 (dashed thin lines) to runs where the minimum cell width is 4.5 pc for G8 and 9 pc for the two other galaxies (solid lines). In the low resolution runs, the maximum cell width is 2.34 kpc, 4.68 kpc and 4.68 kpc and the stellar particle mass is 2.5×10^3 $M_\odot$, 2×10^4 $M_\odot$ and 2×10^4 $M_\odot$ by increasing order of galaxy mass. In the high resolution runs, the maximum cell width is 2.34 kpc for all the galaxies and the stellar particle mass is 310 $M_\odot$, 2.5×10^3 $M_\odot$, and 2.5×10^3 $M_\odot$ by increasing order of galaxy mass.

During the first 70 Myr, the runs with the higher resolution tend to

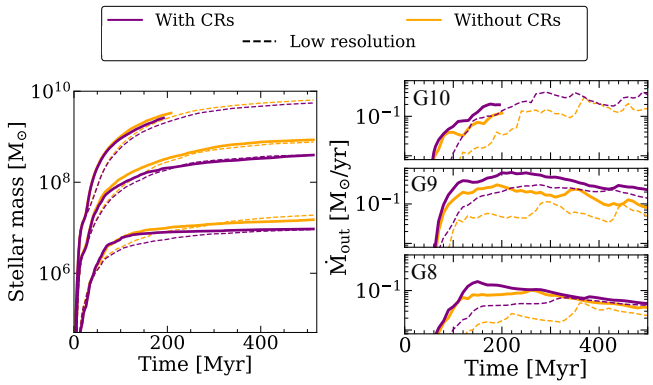

Figure 16. Stellar mass (left panel) and mass outflow rate at 10 kpc from the disc (right panels) as a function of time for G8, G9 and G10 from the lower to the upper panels. The orange curves correspond to the galaxies without cosmic ray feedback, and the purple to runs with CRs added. Solid lines represent the runs with a fine resolution of 9 pc for G9 and G10 and 4.5 pc for G8, while the dashed lines show the equivalent with a 18 pc maximum resolution for the two more massive galaxies and 9 pc for G8.

produce more stars, regardless of whether CRs are included or not. However, after the initial collapse of the disk and once star formation stabilises (by $t \sim 200$ Myr), the stellar masses are similar, with approximately equal final stellar masses regardless of resolution. Moreover, we find that the CR feedback efficiency in suppressing star formation and driving winds does not depend sensitively on the cell resolution. Regarding the right panel, we systematically measure stronger outflows at higher resolution. Gas reaches higher densities in runs with higher resolution, and this may lead to more efficient entrainment of gas into galactic winds. Yet we approximately measure the same increase of outflows when CR feedback is included, with the noticeable exception of G8. We further note that the mass outflow rate in G8 becomes similar in the last 150 Myr, for the low and high resolution runs. We also emphasise the fact that the temperature of these outflows follows the same trend regardless of the resolution (not shown in the paper), with runs with CRs being always dominated by warm and cold gas while runs without CR are almost entirely hotter than 10^5 K. Therefore, even though varying the resolution changes quantitatively some of our results, it does not impact the strength of CR feedback compared to the SN feedback alone (boosted or not). Changing the resolution does not either impact the effects of CRs in producing a colder CGM and impacting the escape of ionising radiation, and is unlikely to change the effects of varying the diffusion coefficient.

5 CONCLUSIONS

The aim of this study is to investigate the role of CRs in suppressing star formation in galaxies and driving outflows. For this purpose, we perform the first cosmic ray radiation-magnetohydrodynamics simulations of three gas-rich galaxies of different masses, using the RAMSES-RT code (Teyssier 2002; Rosdahl et al. 2013), merged with the magnetohydrodynamics implementation of Fromang et al. (2006) and modified to include anisotropic cosmic ray transport as described by Dubois & Commerçon (2016). By comparing our three galaxies with and without CRs, added to our fiducial SN and ionizing radiation feedback, we first investigate how the effects of CR feedback vary with galaxy mass. However, the uncertainty associated with CR transport (specifically the value of the CR diffusion coefficient) complicates determining these effects. For this reason, we investigate in more detail how our results change when varying the diffusion coefficient from 10^{27} to 3×10^{29} cm^2 s^{-1}, which are reasonable limits for the CR diffusion. We also study to what extent CRs provide the galaxy growth suppression required by cosmological simulations. We compare the efficiency of CRs in regulating star formation against the same calibrated model with enhanced SN strength employed by the SPHINX simulations of reionization (Rosdahl et al. 2018). This serves as a precursor of our future work reviewing this in cosmological simulations. In addition, this allows us to assess how CR feedback affects the escape of LyC radiation from galaxies, and hence, indirectly, the process of reionization. We summarise our main conclusions as follows.

- *Cosmic rays have an important effect on the ISM.* On ISM scales, the pressure from cosmic rays tends to smooth out density contrasts. This also tends to produce thicker gas disks than without CR feedback.
- *CR feedback efficiency in regulating star formation decreases with galaxy mass.* In our two dwarf galaxies, for which the gravitational potential is relatively weak, CRs can easily act locally. They make the regions where stars form and explode more diffuse, which reduces in turn the number and the mass of star-forming clumps. However, for galaxies so massive that even SN feedback starts being inefficient, as it is the case for G10, they have almost no effect at ISM scales.
- *At any galaxy mass, CRs drive stronger and colder outflows than thermal pressure from SNe and radiation alone.* Depending on the distance where the outflows are measured, CR feedback increases the mass loading factor by a factor of 2-10. With CRs, the outflows are much colder, predominantly between 10^4 K and 10^5 K, and we measure outflows colder than 10^4 K, completely absent in runs without CRs.
- *Low diffusion coefficients make CRs act locally, smoothing out density contrasts in the ISM and reducing star formation, but having negligible and even negative effects on outflow rates.* The regulation of star formation depends on the amount of CR energy trapped in the disc. With low diffusion coefficient, CRs remain confined longer, thus having more time to interact with the ISM gas and therefore decrease the star formation rate, but cannot drive strong outflows.
- *The mass outflow rate and temperature composition are sensitive to the diffusion coefficient.* The higher the diffusion coefficient, the greater the outflow rate, with a consistently higher fraction of hot gas. We find an inflexion value that depends on galaxy mass, beyond which the amount of cold outflows drops, and the total mass outflow rate stagnates. Although we do not capture it in our simulations, if the galaxies were to evolve for a longer time and in a cosmological context, the large increase in the mass-loading factor found for our lower-mass galaxies is likely to lead to a long-term suppression in star formation.
- *CR feedback does not provide a sufficient 'replacement' for artificially enhanced SN feedback model used in high-redshift cosmological simulations.* The strong SN model is especially more efficient than CRs to regulate star formation. In addition, the outflows driven by SN or CR feedback have very different temperatures. While the CR energy is linked to the ability of pushing more dense and cold gas from the ISM, the SN feedback, boosted or not, tends to push only hot and diffuse gas from the galaxies.
- *Replacing the strong SN feedback used in the* SPHINX *cosmological simulations of reionization by CR feedback reduces the escape fraction of LyC radiation significantly.*

Overall, we find CR feedback to notably impact star formation

in low-mass galaxies, and it alters the amount and the temperature of the outflowing gas. The quantification of these effects is however sensitive to the diffusion coefficient and, comparing to other works, to the details of initial conditions and sub-grid models. It is also important to consider the limitations of idealized non-cosmological simulations. While they provide the perfect laboratory to explore the secular effects of CR physics and their interplay with our sub-grid models, they model a highly unrealistic circum-galactic medium, which may impact the properties of the feedback-driven outflows. Besides, they are not evolved long enough to consistently capture the consequences of gas ejection, and overlook the effects of gas inflows. Cosmological simulations are required in order to consistently predict the consequences of CR-driven winds on long term galaxy evolution. In a follow-up paper, we will study CR feedback in cosmological zoom simulations using the same methods and physics employed here. We will then have a better picture of the efficiency of CRs in shaping high-redshift galaxies and the escape of ionizing photons, in order to determine how cosmic ray feedback may affect reionization.

ACKNOWLEDGEMENTS

The authors thank the anonymous referee for the constructive comments which improved the manuscript. We gratefully thank Dmitry Makarov for his careful reading of the paper and his comments, as well as Benoît Commerçon, Léo Michel-Dansac, Edouard Tollet and Gohar Dashyan for insightful discussions. We thank Taysun Kimm for making the methods for star formation and feedback available and for helping to set up the simulations. This work has been granted access to the HPC resources of TGCC under the allocation 2020-A00806955 made by GENCI. A consequent part of the runs were performed at the Common Computing Facility (CCF) of the LABEX Lyon Institute of Origins (ANR-10-LABX-0066). We also acknowledge support from the PSMN (Pôle Scientifique de Modélisation Numérique) of the ENS de Lyon for the computing resources.

Software: NUMPY (Van der Walt et al. 2011), MATPLOTLIB (Hunter 2007), RAMSES (Teyssier 2002), PYMSES

DATA AVAILABILITY

The data underlying this article will be shared on reasonable request to the corresponding author.

REFERENCES

Andersson E. P., Agertz O., Renaud F., 2020, MNRAS, 494, 3328
Aubert D., Pichon C., Colombi S., 2004, MNRAS, 352, 376
Axford W. I., Leer E., Skadron G., 1977, in International Cosmic Ray Conference. p. 132
Beck R., 2015, A&A, 578, A93
Bell A. R., 1978, MNRAS, 182, 147
Blandford R. D., Ostriker J. P., 1978, ApJ, 221, L29
Booth C. M., Agertz O., Kravtsov A. V., Gnedin N. Y., 2013, ApJ, 777, L16
Bordoloi R., et al., 2011, The Astrophysical Journal, 743, 10
Bouché N., Hohensee W., Vargas R., Kacprzak G. G., Martin C. L., Cooke J., Churchill C. W., 2012, MNRAS, 426, 801
Boulares A., Cox D. P., 1990, ApJ, 365, 544
Buck T., Pfrommer C., Pakmor R., Grand R. J. J., Springel V., 2020, MNRAS, 497, 1712
Bustard C., Zweibel E. G., 2021, ApJ, 913, 106
Butsky I. S., et al., 2021, arXiv e-prints, p. arXiv:2106.14889
Chan T. K., Kereš D., Hopkins P. F., Quataert E., Su K. Y., Hayward C. C., Faucher-Giguère C. A., 2019, MNRAS, 488, 3716
Commerçon B., Marcowith A., Dubois Y., 2019, A&A, 622, A143
Daddi E., et al., 2010, ApJ, 713, 686
Dashyan G., Dubois Y., 2020, A&A, 638, A123
Dekel A., Silk J., 1986, ApJ, 303, 39
Dermer C. D., Powale G., 2013, A&A, 553, A34
Diesing R., Caprioli D., 2018, Phys. Rev. Lett., 121, 091101
Dubois Y., Commerçon B., 2016, A&A, 585, A138
Dubois Y., Teyssier R., 2008, A&A, 477, 79
Dubois Y., Commerçon B., Marcowith A., Brahimi L., 2019, A&A, 631, A121
Emerick A., Bryan G. L., Mac Low M.-M., 2018, ApJ, 865, L22
Enßlin T. A., Pfrommer C., Springel V., Jubelgas M., 2007, A&A, 473, 41
Farber R., Ruszkowski M., Yang H. Y. K., Zweibel E. G., 2018, ApJ, 856, 112
Faucher-Giguère C.-A., 2018, MNRAS, 473, 3717
Federrath C., Klessen R. S., 2012, ApJ, 761, 156
Ferland G. J., Korista K. T., Verner D. A., Ferguson J. W., Kingdon J. B., Verner E. M., 1998, PASP, 110, 761
Fromang S., Hennebelle P., Teyssier R., 2006, A&A, 457, 371
Fujimoto Y., Chevance M., Haydon D. T., Krumholz M. R., Kruijssen J. M. D., 2019, MNRAS, 487, 1717
Gelli V., Salvadori S., Pallottini A., Ferrara A., 2020, MNRAS, 498, 4134
Genzel R., et al., 2015, ApJ, 800, 20
Girichidis P., Naab T., Hanasz M., Walch S., 2018, MNRAS, 479, 3042
Girichidis P., Pfrommer C., Pakmor R., Springel V., 2022, MNRAS, 510, 3917
Grudić M. Y., Hopkins P. F., Faucher-Giguère C.-A., Quataert E., Murray N., Kereš D., 2018, MNRAS, 475, 3511
Guo F., Oh S. P., 2008, MNRAS, 384, 251
Haardt F., Madau P., 2012, ApJ, 746, 125
Heckman T. M., Alexandroff R. M., Borthakur S., Overzier R., Leitherer C., 2015, ApJ, 809, 147
Hillas A. M., 2005, Journal of Physics G Nuclear Physics, 31, R95
Hopkins P. F., Quataert E., Murray N., 2011, MNRAS, 417, 950
Hopkins P. F., Kereš D., Oñorbe J., Faucher-Giguère C.-A., Quataert E., Murray N., Bullock J. S., 2014, MNRAS, 445, 581
Hopkins P. F., et al., 2020, MNRAS, 492, 3465
Hopkins P. F., Chan T. K., Ji S., Hummels C. B., Kereš D., Quataert E., Faucher-Giguère C.-A., 2021, MNRAS, 501, 3640
Hu C.-Y., 2019, MNRAS, 483, 3363
Hu C.-Y., Naab T., Glover S. C. O., Walch S., Clark P. C., 2017, MNRAS, 471, 2151
Hunter J. D., 2007, Computing in Science and Engineering, 9, 90
Jacob S., Pakmor R., Simpson C. M., Springel V., Pfrommer C., 2018, MNRAS, 475, 570
Jana R., Gupta S., Nath B. B., 2020, MNRAS, 497, 2623
Ji S., et al., 2020, MNRAS, 496, 4221
Jubelgas M., Springel V., Enßlin T., Pfrommer C., 2008, A&A, 481, 33
Kannan R., Vogelsberger M., Marinacci F., McKinnon R., Pakmor R., Springel V., 2019, MNRAS, 485, 117
Keller B. W., Kruijssen J. M. D., 2022, MNRAS, 512, 199
Kimm T., Cen R., 2014, ApJ, 788, 121
Kimm T., Cen R., Devriendt J., Dubois Y., Slyz A., 2015, MNRAS, 451, 2900
Kimm T., Katz H., Haehnelt M., Rosdahl J., Devriendt J., Slyz A., 2017, MNRAS, 466, 4826
Kroupa P., 2001, MNRAS, 322, 231
Krymskii G. F., 1977, Akademiia Nauk SSSR Doklady, 234, 1306
Ma X., Kasen D., Hopkins P. F., Faucher-Giguère C.-A., Quataert E., Kereš D., Murray N., 2015, MNRAS, 453, 960
Ma X., Hopkins P. F., Kasen D., Quataert E., Faucher-Giguère C.-A., Kereš D., Murray N., Strom A., 2016, MNRAS, 459, 3614
Mitchell P. D., Blaizot J., Devriendt J., Kimm T., Michel-Dansac L., Rosdahl J., Slyz A., 2018, MNRAS, 474, 4279
Miyoshi T., Kusano K., 2005, in AGU Fall Meeting Abstracts. pp SM51B–1295

Morlino G., Caprioli D., 2012, A&A, 538, A81
Navarro J. F., White S. D. M., 1993, MNRAS, 265, 271
Navarro J. F., Frenk C. S., White S. D. M., 1997, ApJ, 490, 493
Oppenheimer B. D., Davé R., Kereš D., Fardal M., Katz N., Kollmeier J. A., Weinberg D. H., 2010, MNRAS, 406, 2325
Pakmor R., Pfrommer C., Simpson C. M., Springel V., 2016, ApJ, 824, L30
Peters T., et al., 2017, MNRAS, 466, 3293
Pfrommer C., Pakmor R., Schaal K., Simpson C. M., Springel V., 2017, MNRAS, 465, 4500
Quataert E., Thompson T. A., Jiang Y.-F., 2022, MNRAS, 510, 1184
Rasera Y., Teyssier R., 2006, A&A, 445, 1
Rodríguez Montero F., Martin-Alvarez S., Sijacki D., Slyz A., Devriendt J., Dubois Y., 2022, MNRAS, 511, 1247
Rosdahl J., Teyssier R., 2015, MNRAS, 449, 4380
Rosdahl J., Blaizot J., Aubert D., Stranex T., Teyssier R., 2013, MNRAS, 436, 2188
Rosdahl J., Schaye J., Teyssier R., Agertz O., 2015, Monthly Notices of the Royal Astronomical Society, 451, 34
Rosdahl J., et al., 2018, MNRAS, 479, 994
Rosen A., Bregman J. N., 1995, ApJ, 440, 634
Ruszkowski M., Yang H. Y. K., Zweibel E., 2017, ApJ, 834, 208
Salem M., Bryan G. L., 2014, MNRAS, 437, 3312
Salem M., Bryan G. L., Corlies L., 2016, MNRAS, 456, 582
Schaye J., et al., 2015, MNRAS, 446, 521
Semenov V. A., Kravtsov A. V., Caprioli D., 2021, ApJ, 910, 126
Sharma P., Hammett G. W., 2007, Journal of Computational Physics, 227, 123
Smith M. C., Sijacki D., Shen S., 2019, MNRAS, 485, 3317
Smith M. C., Bryan G. L., Somerville R. S., Hu C.-Y., Teyssier R., Burkhart B., Hernquist L., 2021, MNRAS, 506, 3882
Springel V., Di Matteo T., Hernquist L., 2005, MNRAS, 361, 776
Stanway E. R., Eldridge J. J., 2018, MNRAS, 479, 75
Stanway E. R., Eldridge J. J., Becker G. D., 2016, MNRAS, 456, 485
Strong A. W., Moskalenko I. V., 1998, ApJ, 509, 212
Strong A. W., Moskalenko I. V., Ptuskin V. S., 2007, Annual Review of Nuclear and Particle Science, 57, 285
Strong A. W., Porter T. A., Digel S. W., Jóhannesson G., Martin P., Moskalenko I. V., Murphy E. J., Orlando E., 2010, ApJ, 722, L58
Tacconi L. J., et al., 2010, Nature, 463, 781
Tacconi L. J., et al., 2013, ApJ, 768, 74
Teyssier R., 2002, A&A, 385, 337
Teyssier R., Fromang S., Dormy E., 2006, Journal of Computational Physics, 218, 44
Trebitsch M., Blaizot J., Rosdahl J., Devriendt J., Slyz A., 2017, MNRAS, 470, 224
Trotta R., Jóhannesson G., Moskalenko I. V., Porter T. A., Ruiz de Austri R., Strong A. W., 2011, ApJ, 729, 106
Tweed D., Devriendt J., Blaizot J., Colombi S., Slyz A., 2009, A&A, 506, 647
van der Walt S., Colbert S. C., Varoquaux G., 2011, Computing in Science and Engineering, 13, 22
van Leer B., 1979, Journal of Computational Physics, 32, 101
Vogelsberger M., et al., 2014, MNRAS, 444, 1518
Vogelsberger M., Marinacci F., Torrey P., Puchwein E., 2020, Nature Reviews Physics, 2, 42
Werk J. K., Prochaska J. X., Thom C., Tumlinson J., Tripp T. M., O'Meara J. M., Peeples M. S., 2013, ApJS, 204, 17
Werk J. K., et al., 2016, ApJ, 833, 54
Wiener J., Pfrommer C., Oh S. P., 2017, MNRAS, 467, 906
Zweibel E. G., 2013, Physics of Plasmas, 20, 055501
Zweibel E. G., 2017, Physics of Plasmas, 24, 055402

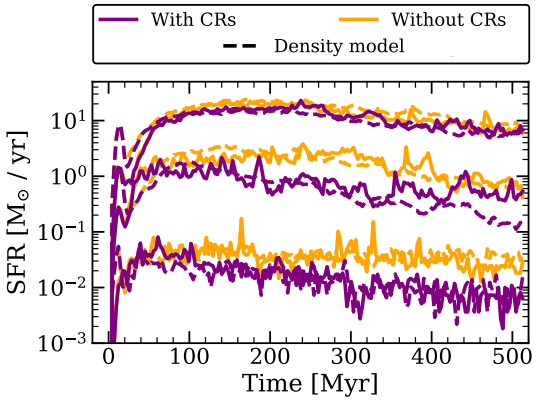

Figure A1. Star formation rate versus time for G8, G9 and G10 from bottom to top. Orange (purple) curves show runs without (with) CRs. Solid lines correspond to runs with the turbulent star formation model, while dashed are for the classical model based on a gas density threshold and a constant but small local star formation efficiency. The two SF models produce fairly similar star formation at any galaxy mass, though it tends to be more bursty with the turbulent model. The density SF model tends to slightly increase cosmic ray feedback efficiency, especially for G9.

APPENDIX A: DENSITY THRESHOLD VS MORE REALISTIC THERMO-TURBULENT STAR FORMATION MODELS

This paper aims to provide a continuity to the results presented by DD20. One of the main differences between their setup and the one adopted in this work is the star formation model, as described in Section 2.4. Because the SF model employed by DD20 is based on a density threshold criterion, we refer to this one as "density". In our fiducial runs, the formation of stars is based on the gravo-turbulent properties of the gas, taking inspiration from Federrath & Klessen (2012) work, hence the SF model is labelled "turbulent".

We investigate how sensitive our results are to the star formation model. Fig A1 show star formation rate versus time for our three galaxies, with (without) CRs in purple (orange). The solid lines show the same as in Fig. 3, that is to say galaxies run with the turbulent model, while the dashed lines show the counterparts with the density SF model. We find that the turbulent SF model is generally more bursty than the density model. Globally, the stellar mass formed with one model or another is almost the same, at any time and no matter the galaxy mass. The small differences, especially during the last 200 Myr for G9, suggest that CRs are more efficient to reduce the star formation with the density SF model.

Figure A2 shows the mass outflow rate as a function of time, measured at 10 kpc from the three galaxies. We apply the same colour code as for Fig A1 to distinguish between the inclusion of CRs or not and the star formation model. With the exception of G8, the same flux of outflowing gas is measured for both models after a few hundred Myr. Only G8 without CRs has considerably higher outflow rates with the turbulent SF model than with the model using a gas density threshold, and consequently shows a less significant contribution of CRs, as discussed in Section 4.

APPENDIX B: OUTFLOWS AT 2 KPC WITH DIFFERENT DIFFUSION COEFFICIENTS

Figure B1 is the equivalent of Fig. 11 for mass outflow rate measured at 2 kpc (instead of 10 kpc for the latter). We show the outflows for

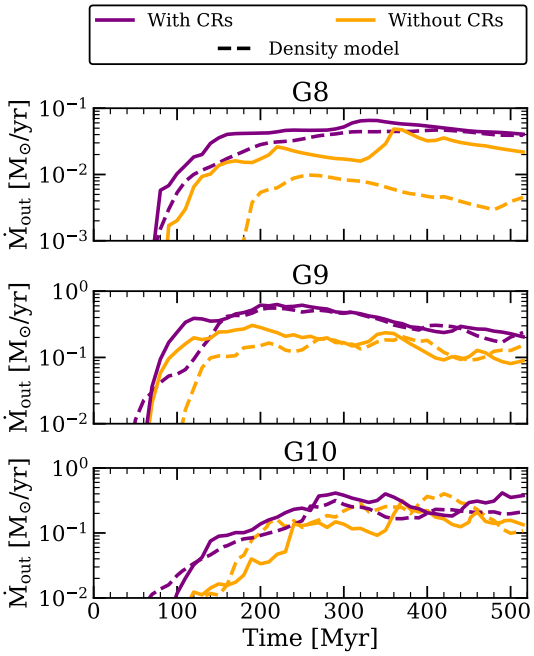

Figure A2. Mass outflow rate versus time measured at 10 kpc from the discs, by increasing order of galaxy mass from top to bottom. Orange (purple) curves show runs without (with) CRs. Solid lines correspond to runs with the turbulent star formation model, while dashed are for the classical density threshold model. The two SF models give similar results at any galaxy mass and regardless of the inclusion of CRs, except for a significantly enhanced amount of outflowing gas for G8 without CRs when we switch from the density to the turbulent SF model, as discussed in Section 4.

increasing galaxy mass from left to right as a function of the diffusion coefficient, at the exception of the leftmost symbols that represent runs without CR feedback. For each simulation we take the average of 31 snapshots (with 10 Myr intervals) between 200 and 500 Myr to compute the outflow rates, shown in black, blue, green and red for the total, cold, warm and hot outflowing gas respectively. Generally, the trends are similar at 2 kpc and at 10 kpc. We measure increasing hot outflow rate with higher diffusion coefficient, and warm and cold outflows that stagnate or even decrease above a given value of κ which differs with galaxy mass. While at 10 kpc, G10 has more outflows without CRs than with the lowest $\kappa = 10^{27}$ cm^2 s^{-1}, the total outflow rates are slightly higher with the small diffusion coefficient than without CRs at 2 kpc. This is also visible in Fig. 10, where using $\kappa = 10^{27}$ cm^2 s^{-1} produces a thick disc with dense gas close to the galaxy midplane, but remains inefficient to push the outflows further out as most of the CR energy is likely dissipated before escaping the galaxy. Besides, CRs diffusion is slower with lower diffusion coefficient, as visible in Fig. 8. The winds supported by CRs that have $\kappa = 10^{27}$ cm^2 s^{-1} are too slow to be equally measured at small and large distances from the galaxy, as they quickly fall back to the disc if they cannot escape its gravity rapidly enough.

This paper has been typeset from a TEX/LATEX file prepared by the author.

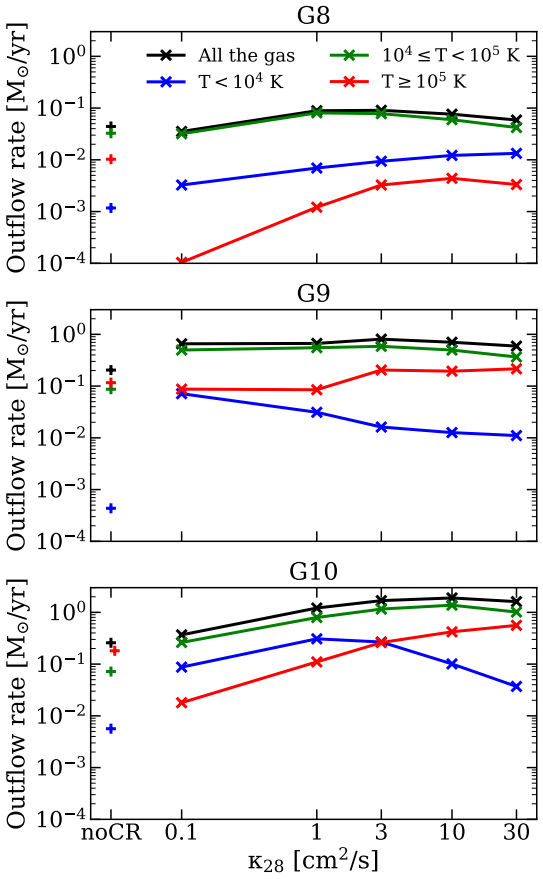

Figure B1. Gas outflow rate at 2 kpc from the galaxy midplane as a function of the diffusion coefficient, in order of increasing galaxy mass from left to right. For each galaxy, data are stacked between 200 and 500 Myr. We show the total amount of outflowing gas in black, the cold ($T < 10^4$ K) in blue, the warm ($10^4 \leq T < 10^5$ K) in green and the hot outflows ($T \geq 10^5$ K) in red . The leftmost symbols represent galaxies without CRs. Similarly to outflows measured at 10 kpc, the total rate of outflowing gas and especially its hot component are globally enhanced with higher values of κ. However, the rate of cool outflows stops increasing and even drops, at a diffusion coefficient limit which increases with galaxy mass.

3.3 The distinct effects of radiation, magnetic field and resolution

Before investigating deeper certain aspects of CR feedback, we further expand on several basic components included in the setup of the galaxies from the **CosmicShine** paper. We notably focus on the effects that radiation feedback and magnetic field have on star formation and on the launching of winds. We also come back on the discussion about resolution convergence to distinguish between the effects from spatial to stellar particle resolution.

3.3.1 Radiation feedback

Radiation feedback, mainly originating from stars and AGN, is thought to play an important role in galaxy evolution (see the introduction in **Section 1.2.2**). Due to the cost and the complexity of RHD simulations, radiation feedback is sometimes modelled with sub-grid recipes, which makes the investigation of the role of radiation dependent to the prescription adopted (e.g. Hopkins et al., 2012a). In order to more consistently study the effect of stellar radiation feedback at galactic scales, Rosdahl et al. (2015) was among the first to perform RHD simulations of galaxies at different masses (G8, G9 and G10) and distinguish the effects of photoionisation heating, direct pressure from ionising photons and indirect pressure from reprocessed IR photons. Their main conclusions was that photoionisation heating is the dominant process among the three listed, but that stellar radiation feedback reduces star formation less than SN feedback and does not contribute to drive outflows. However, conflicting results can be found in the literature, and no general agreement has yet been made on the effects of radiation feedback (Wise et al., 2012; Agertz & Kravtsov, 2015; Trujillo-Gomez et al., 2015; Emerick et al., 2018; Hopkins et al., 2020a). This may be partly due to limited resolution, that does not allow to capture scales at which (individual) stars form and evolve, which are the most relevant scales because this is where radiation is emitted. Consequences of radiation feedback may also be sensitive to the SN feedback recipe. As they note, Rosdahl et al. (2015) use a relatively weak SN feedback model, and it cannot be guaranteed that their results remain the same with a more efficient and realistic feedback prescription (see e.g. Smith et al., 2021). The simulations from the **CosmicShine** paper couple the state-of-the art mechanical feedback described in **Section 2.2.5** with photoionisation heating and radiation pressure. In order to investigate the interplay between this more realistic SN feedback recipe and stellar radiation, I performed one more simulation of the G9 galaxy without radiative transfer, and so without radiation feedback. On another side, Dashyan & Dubois (2020) studied the impact of CR feedback in the same galaxy, but without considering radiation feedback in their simulations. To our knowledge, radiation and cosmic ray feedback have never been coupled and studied together in RHD simulations of galaxies. Therefore, I also performed the G9 galaxy with CR feedback, but without radiation. We end up with 4 simulations of interest: without RT and CRs, with RT only (the fiducial G9_noCR), with CRs only, and with both combined (the fiducial G9_CR). They all include MHD and a mechanical feedback recipe for SN feedback. This set of 4 runs is available in two versions, that we call "fiducial" and "old". The fiducial version has a similar

setup as the SPHINX simulations, and is the one adopted in the **CosmicShine** paper with multiple SN explosions and a turbulent star formation model. The set with the older version of the models comes back to the less physically motivated setup from Rosdahl et al. (2015) and Dashyan & Dubois (2020), with single SN explosion and a star formation model based on a density criterion and a local star formation efficiency of 2% (and the same spatial resolution as Rosdahl et al. (2015), i.e. a maximum resolution of 18 pc). Therefore, this allows us to make the bridge between the previous studies of Rosdahl et al. (2015) and Dashyan & Dubois (2020) and conclude on the interplay between SN, radiation and CR feedback[2]. Apart from this section, all the runs presented in the thesis include radiative transfer and radiation feedback, as described in the **CosmicShine** paper.

We first investigate the interplay between the different feedback channels on star formation. Fig. 3.1 shows the stellar mass formed as a function of time in the G9 galaxy. Throughout this section, we show in orange and purple runs without and with CRs respectively, and in dotted and solid lines runs without and with RT. For the sake of comparison, we show the stellar mass when no feedback (no SN nor radiation) is included in grey for the set of runs with the fiducial models (Fig. 3.1a). With both sets of models, CR feedback alone (with SN but without radiation feedback) is more efficient than radiation to prevent star formation. However, the efficiency of radiation feedback varies with the SF and SN models adopted. In Fig. 3.1a, the addition of radiative feedback on top of SN and CR feedback only marginally decreases the stellar mass during the first $\sim$ 200 Myr. On the other hand, Fig. 3.1b shows a much greater effect from radiation, which reduces the total stellar mass formed by the end of the runtime by a factor of 1.7 when there are no CRs, and by a factor of 1.3 when there is CR feedback. The difference in radiation feedback efficiency is likely connected to the star formation model. The turbulent model leads to bursty and clumpy star formation, while the combination of a simple density threshold condition and a small local star formation efficiency produces a much smoother star formation, with stellar particles more broadly distributed than with the fiducial turbulent model. This is shown in Fig. 3.2a and Fig. 3.2c, that represent face-on maps of the stellar mass distribution in G9 without RT or CRs and with the two SF models. During the first Myr, stars emit radiation that reduces the gas density locally until the first SNe explode and blow away gas more significantly. Then, the feedback from SN is already so strong in clumps of stars that it takes over the effect that radiation may have. Conversely, if the stellar particle distribution is more extended, the effect of a single isolated SN explosion on star formation is least, and including the effects from radiation further dissipates gas and prevents star formation. This goes in line with the results from Rosdahl et al. (2015), who found a similar cumulative effect from adding radiation to SN feedback. With the old SN and SF models, adding more and more physics suppresses star formation to a greater extent, as the runs that include SN, radiation and CRs have the lowest final stellar mass.

[2]We remind that a comparison between switching from one star formation model to another, with multiple or single SN explosions, is already provided in the **CosmicShine** paper.

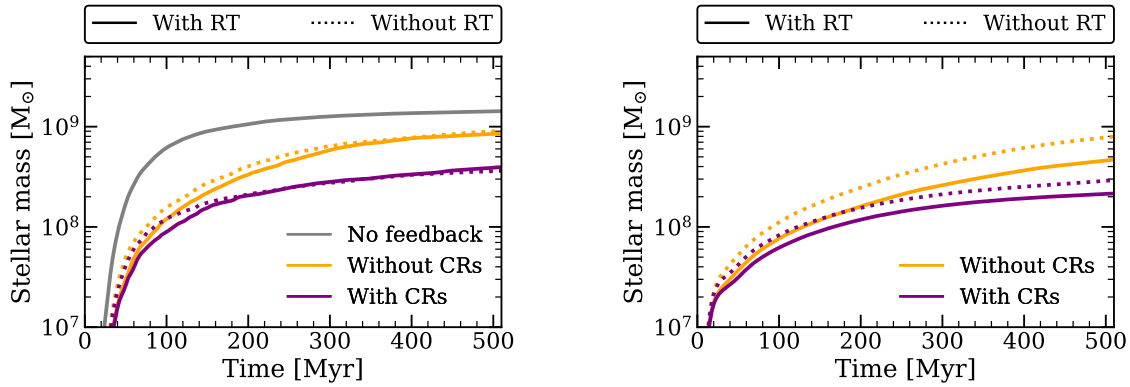

(a) Fiducial models *(b) Old models*

Figure 3.1: *Stellar mass formed in G9 as a function of time, with (without) CRs in purple (orange) and with (without) RT in solid (dotted) lines. In the left panel, we show the equivalent run without feedback in grey for reference. 3.1a: fiducial setup with turbulent star formation model and multiple SN explosions ; 3.1b: setup closer to the one adopted by Rosdahl et al. (2015) and Dashyan & Dubois (2020), with a simpler star formation model based on gas density and small constant star formation efficiency, and with a single SN event per stellar particle. In our setup with state-of-the art star formation and feedback models, radiation marginally reduces the total stellar mass and is much less efficient than CR feedback in suppressing star formation. Radiation feedback is more efficient when a smooth prescription for star formation is adopted.*

To have a more quantitative view of how the different feedback mechanisms impact gas around stars, Fig. 3.3 shows the median density of cells that host stellar particles as a function of their age. To avoid any transient effects, each bin of stellar age of 2 Myr shows the median gas density by stacking outputs between 200 and 500 Myr. When SNe explode, the energy they release disperses the gas locally, and density around stars decreases. As we explained previously, the effect from radiation differs depending on the burstiness of star formation. With the turbulent model, stars are spatially concentrated in clumps of several stellar particles (see Fig. 3.2a). Adding the early radiation feedback causes these individual clumps to be smaller, and consequently less concentrated than without RT. This is visible from the map of stellar mass in G9 with RT and the fiducial SF model shown in Fig. 3.2b. By reducing the early burst of star formation, radiation feedback smoothes the effects of SN feedback, which is less efficient to disrupt the star forming regions. This phenomenon acts as a positive feedback, by reducing the strength of SN and CR feedback. A similar result has been recently pointed out by Smith et al. (2021), who find that stellar radiation provides an early feedback that eventually reduces the disruptive power of SN feedback. Furthermore, this shows the importance of coupling radiation and CR feedback together to have accurate predictions on the role of CRs during galaxy evolution. As we see with the dotted purple line in Fig. 3.3a, CR feedback without RT is more efficient to reduce the gas density in stellar clumps. The interpretation of the role of radiation feedback is however completely different with the less physically motivated density star formation model. In this case, the stellar distribution is much smoother (as visible in Fig. 3.2), and the effects from additional physics are cumulative. We note that overall, the density at which a stellar particle forms is lower with the density SF model than with the fiducial

turbulent one. This is due to the coarser resolution in the former case, as cells have a size of 18 pc at best (instead of 9 pc in the fiducial set of runs). It also depends on the density threshold that allows stars to form, which is set here to 10 H cm^{-3}.

We also point out that gas density surprisingly starts to decrease when stellar particles are younger than 5 Myr, which is the precise time at which they explode as a single SN episode. Then, regardless of radiation, runs with CR feedback show a lower gas density after 5 Myr, before gas density around older stellar particles converges towards 10 H cm^{-3} again. This is the consequence of CR pressure that helps to expel more gas out of the star forming regions, before CR energy escapes and allows local gas to fall back.

Our results may still be sensitive to the mandatory use of sub-grid models, due to limited resolution that does not allow to model individual stars. Nonetheless, adopting physically motivated star formation and feedback models are our best way to correctly understand the roles of the different physical ingredients on star formation and galaxy growth. With our fiducial setup, we conclude that radiation and CRs both play an important role. While the latter suppresses star formation, radiation feedback prevents star formation locally, making the SN feedback less efficient which in turn globally enhances star formation.

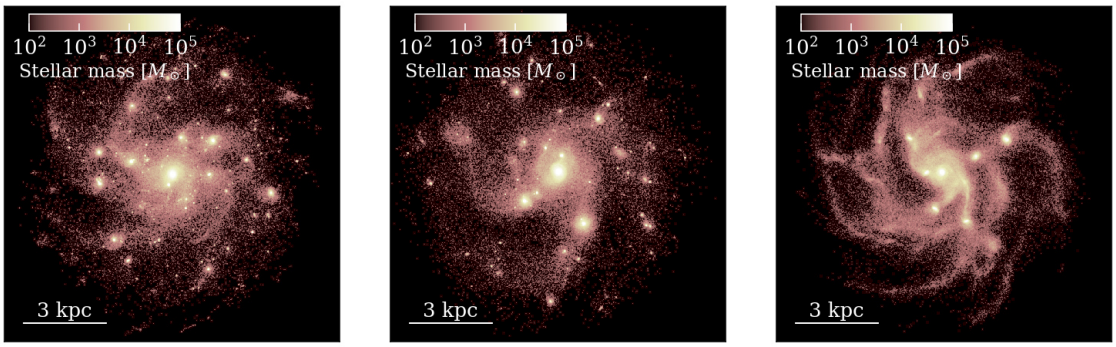

(a) Fiducial models *(b) Fiducial models with RT* *(c) Old models*

Figure 3.2: *Face-on maps of stellar mass at 350 Myr in G9 without CR feedback, and without RT except for the middle panel. 3.2a: the stellar distribution is clumpy when using the turbulent star formation model. 3.2b: when adding RT, the turbulent SF model leads to a less clumpy stellar distribution. 3.2c: adopting a SF model based on a constant and small star formation efficiency leads to a more broadly distributed star formation.*

Finally, we focus on the fiducial models to investigate the effects of SN, radiation and CR feedback on the outflows. From left to right, Fig. 3.4 shows the time evolution of the mass outflow rate for cold, warm and hot gas measured at a height of 10 kpc from the disc. As we already noticed, cosmic rays are needed to drive gas colder than 10^4 K at large distances from the galaxy. Without CRs, the outflows are dominated by gas hotter than 10^5 K. In both cases, radiation consistently but rather mildly reduces the fraction of cold and hot outflowing gas, and winds have a greater fraction of warm component. This is partly the consequence of photoionisation heating, which tends to heat neutral gas originally at $T \sim 10^4$ K, as explained in **Section 1.2.2**. In addition, because RT reduces the efficiency of SN explosions, the radiation feedback leads to slightly less hot gas.

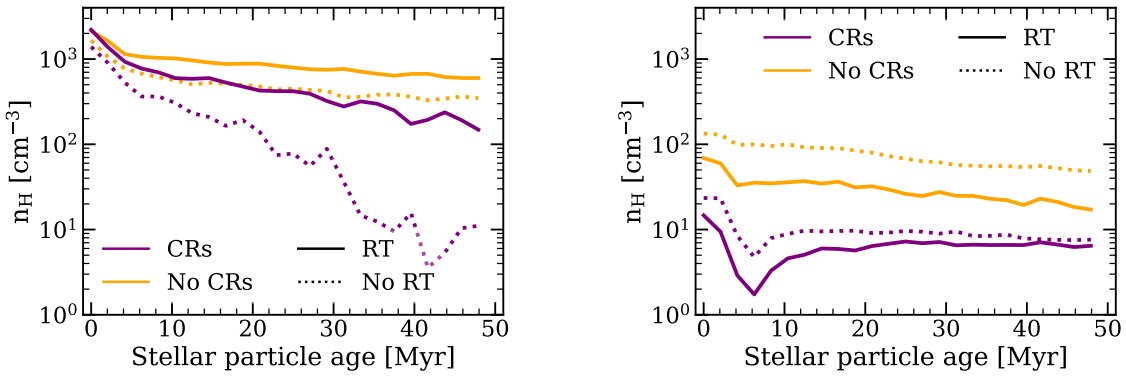

(a) Fiducial models *(b) Old models*

Figure 3.3: *Median gas density of cells hosting stellar particles as a function of their age in G9, binned every 2 Myr and with data stacked from 200 to 500 Myr. 3.3a: with the fiducial models, radiation reduces the efficiency of SN feedback, so that gas around stars is denser when RT is included. 3.3b: The old SF model leads to a more extended distribution of stellar particles, so that SN, radiation and CR feedback individually or together decreases density at which stars form and explode.*

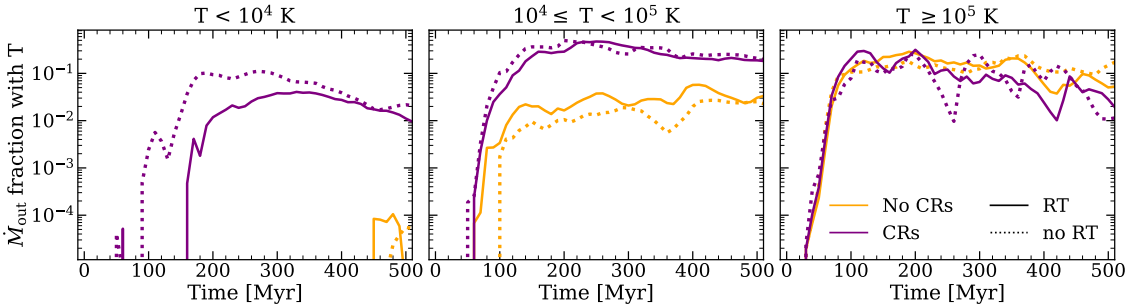

Figure 3.4: *Cold, warm and hot mass outflow rates as a function of time in G9, for outflows measured at 10 kpc from the disc. Due to photoionisation heating, the fraction of warm outflows in runs with radiation is higher, especially at the cost of cold outflows driven by CRs.*

3.3.2 Magnetic field

Theoretically, the magnetic field can play a role on ISM scales, when magnetic pressure is comparable to thermal pressure. As first pointed by Shu et al. (1987), the magnetic field can also help to stabilise GMC thanks to its pressure support, which scales with the strength of the magnetic field squared, i.e. B^2. However, the rare measurements we have of B in the GMC suggest that the magnetic field does not provide sufficient pressure support against gas accretion, given the potential well of the GMC (Crutcher et al., 1999; Bourke et al., 2001). Whether the magnetic field can regulate star formation or not hence remains a topic of investigation. For these reasons, it is interesting to know if magnetic field has a specific effect on galaxy growth.

Therefore, I performed an additional set of galaxies with a hydrodynamical solver instead of an MHD one, without the magnetic field but otherwise with the same setup as the noCR runs from the **CosmicShine** paper. We remind that the galaxies

performed with MHD have a magnetic field strength of 1 μG, as commonly observed in galaxies (Fletcher et al., 2011; Han, 2017; Akahori et al., 2018). In Fig. 3.5, we show the gas outflow rate at 10 kpc from the midplane of the disc as a function of time for runs with and without magnetic field (and without CRs in both cases). Similarly, we show the time evolution of the SFR in Fig. 3.6. The blue curves correspond to galaxies without magnetic field, i.e. using only the radiation-hydro solver. The orange curves show their counterparts with a toroidal magnetic field, and otherwise all the same settings. At any galaxy mass, these two sets of plots reveal a very marginal effect of the magnetic field on star formation, and a stochastic effect in the launching of outflows. G8, which has the shallowest gravitational potential, is more sensitive to bursts of star formation and occasionally reveals higher outflow rate with MHD. Nevertheless, we do not expect the magnetic field to directly strongly impact the CGM, as winds are only weakly magnetised.

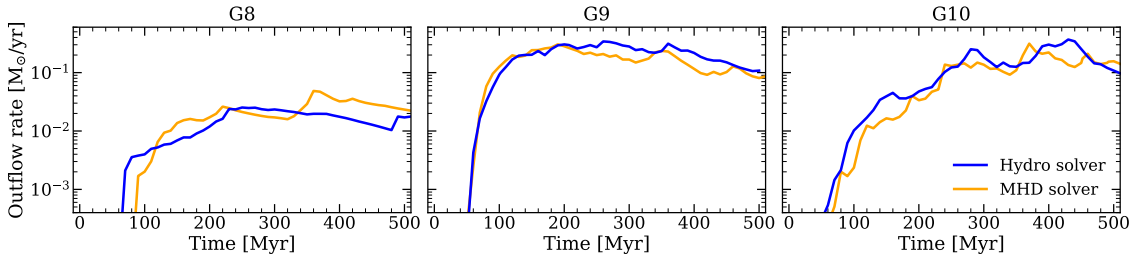

Figure 3.5: *Mass outflow rate measured at 10 kpc from the discs versus time for the three disc galaxies. The blue curves correspond to runs where no magnetic field is included, using a hydro solver. The orange curves show runs seeded with a toroidal magnetic field evolved with our MHD solver. Adding the magnetic field leads to small variations in the outflow rate.*

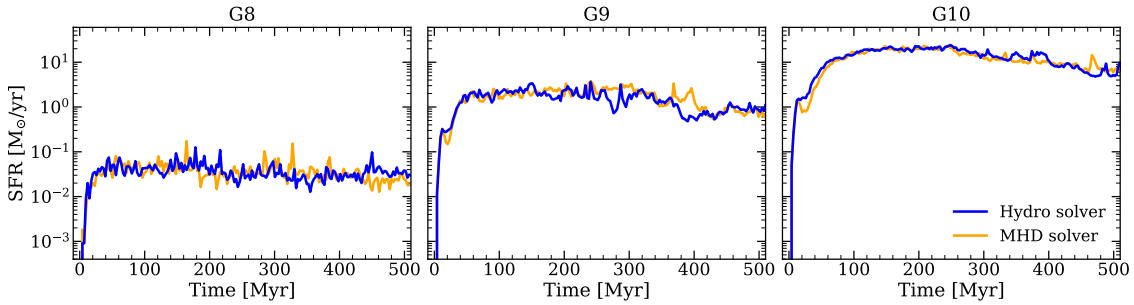

Figure 3.6: *Star formation rate as a function of time for the three galaxies. The blue curves correspond to runs without magnetic field, using a hydro solver. The orange curves show runs seeded with a toroidal magnetic field evolved with an MHD solver. The SFR is barely impacted by the addition of the magnetic field.*

While the magnetic field has a marginal effect at any galaxy mass in our simulations, it does not build up the same way. In Fig. 3.7, we show volume weighted mean thermal and magnetic pressure (Fig. 3.7a) and the mean magnetic field strength (Fig. 3.7b) in cylinders of ISM of 4 kpc height. We remind that magnetic pressure is $P_{\rm mag} = B^2/8\pi$ (in CGS units), where B is the magnetic field strength (in Gauss

units). The strength of magnetic pressure follows the galaxy mass, even though magnetic pressure is less significant than thermal pressure at any galaxy mass. Massive galaxies have a deeper potential well, which allows stronger gas compression, and therefore stronger amplification of the magnetic field through adiabatic compression (Dubois & Teyssier, 2010; Pakmor & Springel, 2013). As magnetic pressure scales with the magnetic field strength, G10 reaches higher magnetic pressure than G9 which also has a higher $P_{\rm mag}$ than G8. Even if magnetic pressure equals thermal pressure in G10, it is not sufficient to impact the SFR in such a massive galaxy where SN feedback is already inefficient to regulate star formation. Besides, we note that the total volume-weighted magnetic pressure, not shown here, is between 1 and 2 orders of magnitude below the thermal pressure for all galaxies. Therefore, it is not surprising that a magnetic field of this strength does not affect our galaxies, as already shown in other studies (e.g. Su et al., 2017; Martin-Alvarez et al., 2020).

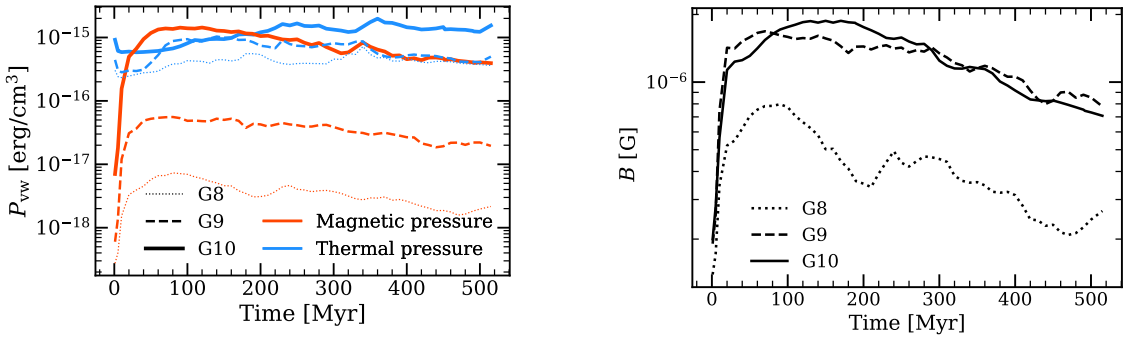

Figure 3.7: *Properties of the magnetic field in arbitrary cylinders of ISM gas of 4 kpc height. 3.7a:Volume-weighted mean thermal (in blue) and magnetic (in red) pressure as a function of time. 3.7b: Time evolution of the mean magnetic field strength. G8, G9 and G10 are shown with thin dotted, dashed and thick solid lines respectively. Magnetic pressure is well below thermal pressure for G8 and G9. G10, which has a deeper potential well, can amplify stronger magnetic field and therefore has a magnetic pressure comparable to the thermal one in the ISM.*

Initially, our three galaxies that include MHD are seeded with a toroidal topology and a magnetic field strength of 1 μG, as commonly observed in galaxies (Fletcher et al., 2011; Han, 2017; Akahori et al., 2018). We now investigate the consequences of changing the initial strength B_0 of the magnetic field, comparing our fiducial G9 with $B_0 = 1$ μG to equivalent runs with $B_0 = 0.1$ μG and $B_0 = 10$ μG, which are in the lower and upper limits of acceptable values (e.g. Wezgowiec et al., 2022). The three galaxies include SN and radiation feedback, but we keep omitting CRs to infer the effect of the magnetic field by itself. We first show in Fig. 3.8a the evolution with time of the mean magnetic field for the different initial strengths, measured in a cylinder of 4 kpc in height and of 89 kpc in radius (which corresponds to the virial radius of G9). After the first 20 Myr, the initial galactic gas collapse amplifies B until it saturates to approximately B_0 in the cases of the weaker initial magnetic field. In the run with $B_0 = 10$ μG, magnetic energy progressively dissipates, and reaches a final value of 2 μG. On larger timescales, we can extrapolate that runs with the larger seed fields will finally converge to a similar magnetic field strength of 1 μG

(Pakmor & Springel, 2013). Fig. 3.8b additionally shows the radial profile of the magnetic field strength, measured at 250 Myr. While the amplitude of the magnetic field is roughly flat below 5 kpc for the three simulations, it suddenly drops when reaching the CGM, which is barely magnetised. We note that initially, the CGM is almost empty of gas and is not pervaded by a magnetic field until magnetised winds escape the galaxies, which explains the very weakly magnetised CGM we measure.

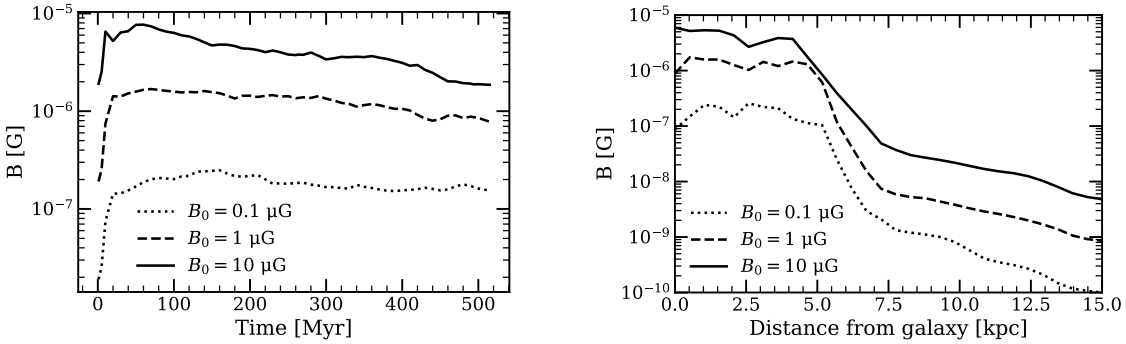

(a) *(b)*

Figure 3.8: *3.8a: Amplitude of the magnetic field as a function of time in a cylinder of ISM of 4 kpc height. 3.8b: Amplitude of the magnetic field as a function of distance from the galaxy, measured at 250 Myr in spherical radial profiles. The curves correspond to G9 with $B_0 = 0.1$, 1 and 10 μG in dotted, dashed and solid lines respectively. Seeding the magnetic field with a greater initial strength leads to stronger magnetic field over time and across distances. The magnetic field significantly drops beyond $\sim$ 5 kpc for the three simulations.*

In order to have a visual inspection of how the G9 galaxy is impacted by different magnetic field strengths, Fig. 3.9 shows face-on maps of the hydrogen column density and the magnetic pressure with increasing B_0 from left to right. As B is stronger with higher B_0, magnetic pressure is consequently more important in the run with $B_0 = 10$ μG. Thanks to this additional pressure support, the gas distribution in the disc becomes smoother and less clumpy. The largest magnetic field hence has the largest dynamical effect on gas, by reducing the density contrast. Therefore, we expect the magnetic field to have an important effect both on the bulk and turbulent motion of the gas (Birnboim et al., 2018), and especially on star formation. The sites of star formation are molecular clouds, which consist in very dense and cold gas. Because they have a low thermal pressure, the beta plasma, which is the ratio of thermal to magnetic pressure $\beta = P/P_{\rm mag}$, is expected to be < 1. We investigate this with Fig. 3.10, which represents density temperature phase diagrams of G9 at 350 Myr, when $B_0 = 10$ μG. To get rid of the very diffuse gas in the CGM of the galaxy, set by the initial conditions, we select only gas contained in a cylinder of 4 kpc in height around the mid-plane of the galaxy. In Fig. 3.10a, the colorbar shows the value of β in each bin of the 2D histogram, and reveals that the magnetic pressure effectively dominates in cold and dense regions. However, when the phase diagram is weighted by the mass of the gas in Fig. 3.10b, it appears that only a small fraction of the ISM is significantly subject to the magnetic pressure. Besides, runs with lower B_0 shows that thermal pressure dominates at any temperature and density, as they naturally have lower magnetic pressure. Regardless of the initial strength of the

magnetic field, thermal pressure provides by far the dominant contribution for the majority of the galactic gas.

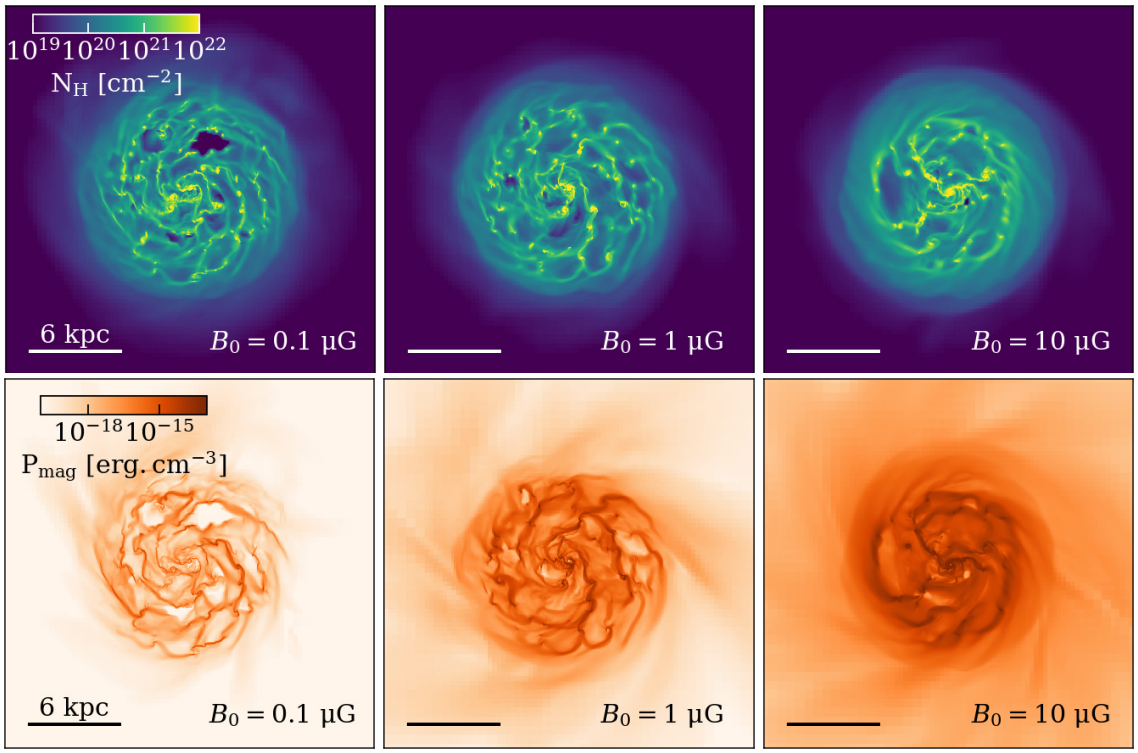

Figure 3.9: *Face-on maps of hydrogen column density (top panels) and magnetic pressure (bottom panels) of G9 at 350 Myr, with increasing B_0 from left to right. With higher initial magnetic field strength, the magnetic field in the disc is stronger, which smooths the inner gas distribution.*

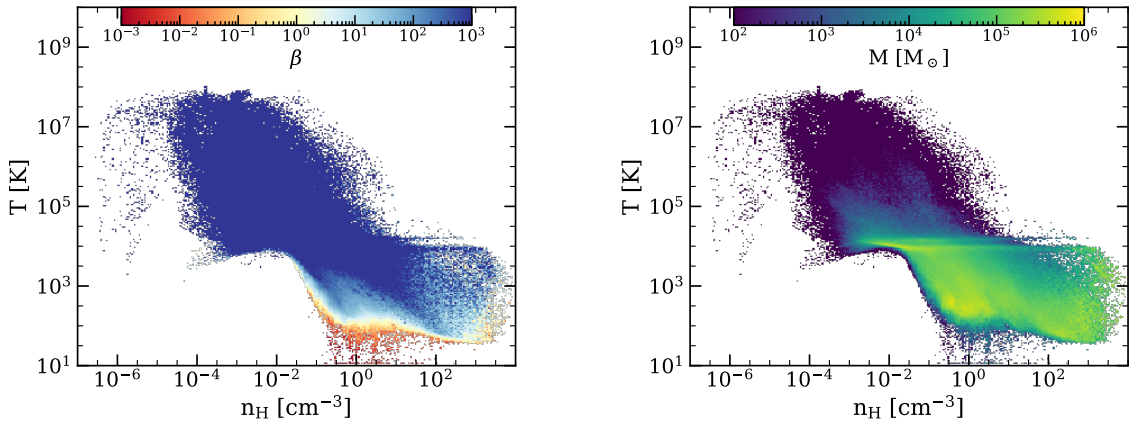

(a) ***(b)***

Figure 3.10: *Density temperature phase diagrams weighted by β (3.10a) and gas mass (3.10b) for G9, with $B_0 = 10$ μG, at 350 Myr. Magnetic pressure dominates over thermal pressure only in a small mass fraction of cold and dense gas.*

We can further quantify how the magnetic field acts on gas density with Fig. 3.11, focusing on gas in a cylinder of ISM of 4 kpc in height. For 3 different times, the

plots depict the hydrogen density probability distribution function (PDF) weighted by the mass in each density bin. We add in blue the results from the run without magnetic field discussed previously in the beginning on the section. During the first 50 Myr, the magnetic field amplifies before reaching its maximum value. In the case where $B_0 = 10$ μG, the magnetic pressure has significantly built up to narrow the density PDF, and there is less gas at high density than in the other runs. This is the consequence of the magnetic pressure support, that prevents gas from reaching high densities. Because magnetic pressure is so efficient during the early stages of the galaxy, it reduces gas density where it resides and leads to larger mass outflow rates in the first two 200 Myr. This is shown in Fig. 3.12, which shows the mass outflow rate measured at 10 kpc from the disc plane as a function of time. Mass outflow rates vary by up to a factor of three with both time and magnetic field strength. The mass outflow rate is higher for stronger magnetic field between 100 and 200 Myr, becomes similar in the three runs for the following 100 Myr, and are finally lower in the $B_0 = 10$ μG run. This follows the behaviour we noticed in Fig. 3.8, where we note that the build up of the magnetic field becomes lower with time in the $B_0 = 10$ μG run. With time, the hydrogen density PDF from the different runs finally converge, and the effect from magnetic pressure remains only marginally visible. With higher initial magnetic field strength, gas denser than 10 H cm^{-3} is somewhat more smoothed compared to when no magnetic field is evolved.

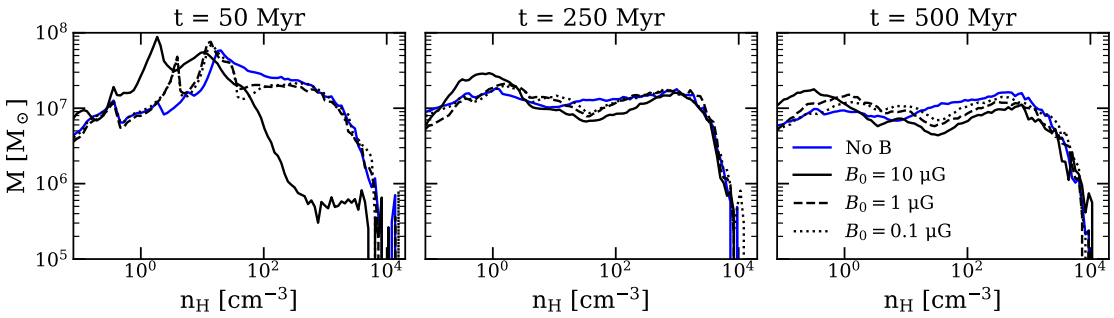

Figure 3.11: *PDF of hydrogen gas density at 50, 250 and 500 Myr from left to right, showing the total mass in each bin. We show runs without magnetic field in blue, and runs with $B_0 = 0.1$, 1 and 10 μG in dotted, dashed and solid black lines. When the B_0 is the highest, it initially significantly decreases the mass of gas denser than 10^2 H cm^{-3}. After $\sim$ 50 Myr, magnetic pressure only remains efficient to marginally reduce the fraction of gas at densities above 10 H cm^{-3}, in a similar way regardless of B_0.*

We finally show how different magnetic field strengths affect star formation in G9 with Fig. 3.13. The two runs with the smallest seed fields have very similar star formation rates, and their stellar mass content is consequently the same at any time. However, when $B_0 = 10$ μG, star formation is significantly delayed during the first 100 Myr. This goes in line with the previous results we discussed. When the initial magnetic field strength is high enough, the pressure that builds up provides an additional support against gas collapse. This reduces density contrasts in the ISM (Figures 3.9 and 3.11), slowing down star formation (Krumholz & Federrath, 2019). In the absence of any further magnetic field amplification, this effect vanishes as magnetic pressure dilutes. As a result, the total stellar mass formed after 200 Myr becomes independent of the initial magnetic field strength. Therefore, we do not

expect substantial differences between our simulations from varying the magnetic field seed, except during the first evolutionary times during which the magnetic field is amplified.

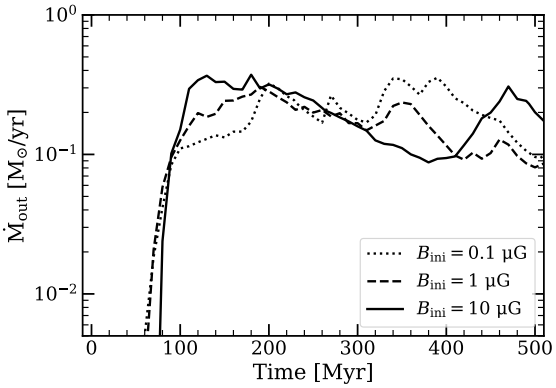

Figure 3.12: *Mass outflow rate measured at 10 kpc from the disc plane as a function of time, when varying the initial magnetic field strength from $B_0 = 0.1$, 1 and 10 μG (in dotted, dashed and solid lines respectively). The strong magnetic field initially leads to strong outflows before the mass outflow rate decreases with time.*

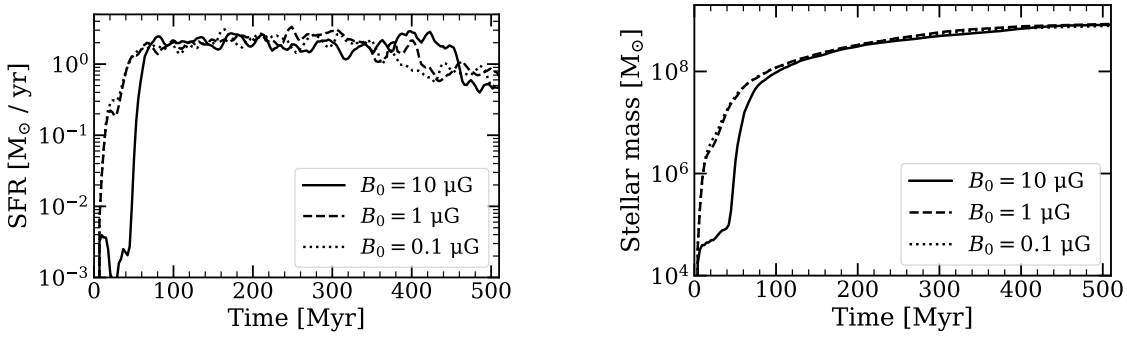

(a) ***(b)***

Figure 3.13: *Effect of varying the initial magnetic field strength from $B_0 = 0.1$, 1 and 10 μG (in dotted, dashed and solid lines respectively) on star formation. 3.13a: SFR as a function of time, averaged over 10 Myr ; 3.13b: Stellar mass formed as a function of time. The strong magnetic field suppresses the initial SFR, but the total stellar mass formed by the end of the runtime of 500 Myr is similar regardless of B_0.*

3.3.3 Impact of stellar particle mass resolution

In the **CosmicShine** paper, there is a discussion about the convergence of the results with resolution. Because G8 has a shallow gravitational potential, we showed that this galaxy is most sensitive to changes in resolution. With or without CRs, the stellar mass of G8 takes approximately 200 Myr to converge in runs with maximum cell width of 4.5 and 9 pc. Also, the ability of CRs to drive outflows slightly decreases in the higher resolution runs. However, this is balanced by the fact that CR-driven outflows share a similar temperature decomposition at any resolution. In any case, we could wonder if this is the consequence of changing the cell width or from changing

the stellar particle masses. In the **CosmicShine** paper, the minimum stellar particle mass m_0 is 310 and 2500 $M_\odot$ with a maximum resolution is 4.5 and 9 pc respectively, so both cell and particle resolution are changed at the same time. In the following, we set the spatial resolution to 9 pc in G8, and only change the mass resolution m_0 from 950 to 7600 $M_\odot$.

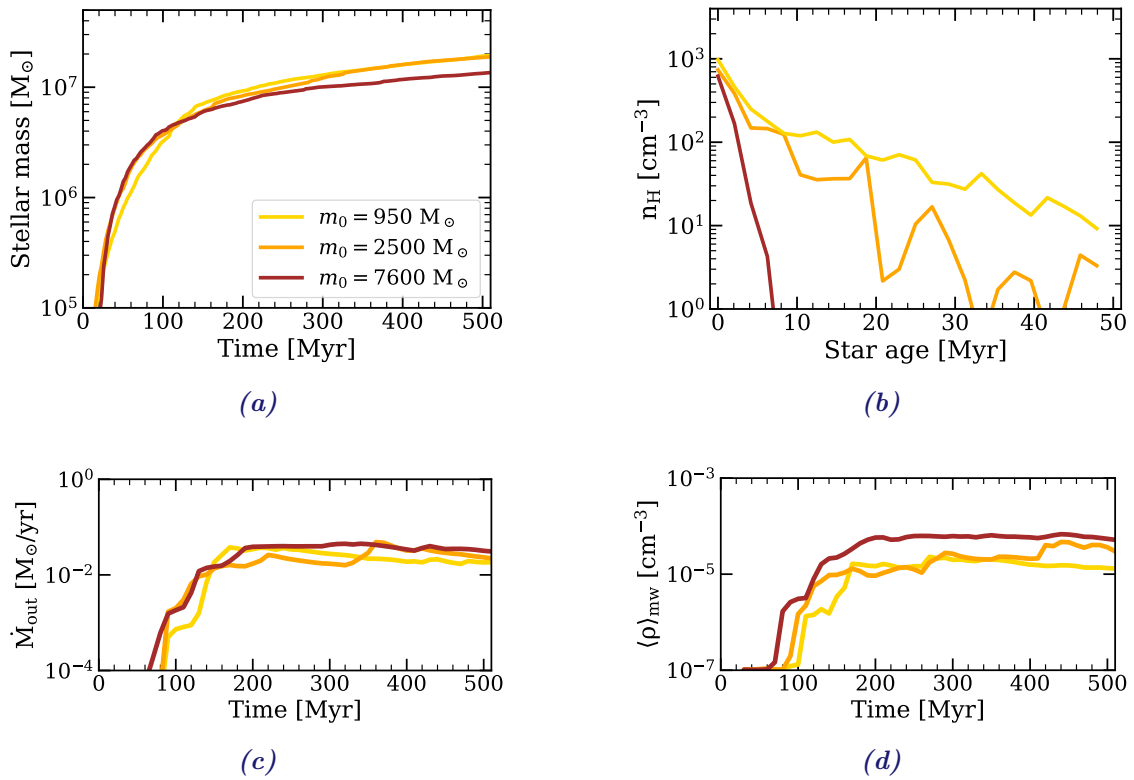

Figure 3.14: *Effect of the stellar particle mass resolution in G8, keeping a fixed maximum cell resolution of 9 pc. In the four panels, the minimum initial masses of the stellar particles are 950, 2500 (fiducial) and 7600* $M_\odot$ *and are shown in yellow, orange and brown respectively. We show, clockwise: 3.14a: stellar mass formed as a function of time ; 3.14b: median density of cells hosting stars as a function of the stellar particle age, binned every 2 Myr ; 3.14c: mass outflow rate measured across a plane 10 kpc above the disc as a function of time ; 3.14d: mass-weighted average density of the outflowing gas (measured at 10 kpc from the disc) versus time. When the stellar particles are more massive, SN explosions generate denser outflow. Results with* $m_0 \leq 2500$ $M_\odot$ *are reasonably well converged.*

Fig. 3.14 shows the consequences of varying m_0 on star formation and outflows. For this purpose, Fig. 3.14a and Fig. 3.14c directly show the time evolution of the stellar mass formed and of the outflow rate measured at 10 kpc from the galaxy. Overall, they both show little difference between the runs with $m_0 = 950$ $M_\odot$ (in yellow) and $m_0 = 2500$ $M_\odot$ (in orange, our fiducial setup). However, when stellar particles have a minimum mass of $m_0 = 7600$ $M_\odot$, the total stellar mass by the end of the 500 Myr runtime is 1.4 times lower than for the two other runs, and mass outflow rates are slightly higher at any time. To explain this behaviour, we show in Fig. 3.14b a histogram of the density of cells that host stellar particles as a function of their age. Just as in the **CosmicShine** paper, the stellar particles age is binned every 2 Myr, and the lines represent the median density of gas in

each bin for outputs stacked between 200 and 500 Myr. Regardless of m_0, stars form approximately at the same density (age between 0 and 3 Myr). However, more massive stellar particles lead to more SN energy released, which disperses gas more easily from sites of star formation than with low-mass stellar particles, that explode fewer times. As a result, gas density around stars is increasingly diminished for increasing m_0. This is also visible in Fig. 3.14d, which shows how the mass-weighted average density of outflowing gas, measured at 10 kpc away from the galaxy, evolves with time. By definition, increasing m_0 increases the clustering of star formation, leading to the same burstiness effect that the one discussed in the context of early feedback in previous sections. Consequently, the galaxy with the highest m_0 has a decreasing SFR and ends up with the smallest total stellar mass.

Eventually, regarding the small variations in stellar mass and outflow rate with different initial stellar particle masses, we can conclude that the results from the convergence study in the **CosmicShine** paper are the consequence of varying the maximum cell width rather than changing the initial mass of the stars, because the changes in those quantities are much larger when the cell resolution is also varied. In the end, stellar mass and outflow rate converge reasonably well unless spatial and particle resolutions are degraded too much.

3.4 Sensitivity of cosmic ray feedback to the initial gas fraction

In the **CosmicShine** paper, the galaxies studied all have a relatively high gas fraction similar to high-redshift galaxies, with gas that initially contributes to $\sim 50\%$ of the baryonic mass in G8 and G9 and to $\sim 30\%$ in G10. In this section, we want to investigate whether CR feedback acts similarly with lower gas fraction. We focus exclusively on G10, which has approximately the mass of the Milky-Way but remains far from being representative of it, especially because it has a much higher gas fraction in its disk. Indeed, by fitting observations from HI line surveys to models of hydrogen distribution in the Milky-Way, our galaxy is expected to have a gas fraction of $\sim 10\%$ (Kalberla et al., 2007; Kalberla & Kerp, 2009). For this reason, we compare our fiducial G10, with a gas fraction $f_{\rm gas} = 30\%$, to a counterpart galaxy with $f_{\rm gas} = 10\%$. For this purpose, we perform an additional set of runs with this lower gas fraction, by changing the initial conditions used to evolve the galaxy. The setup for G10 remains otherwise unchanged, and we run this rough Milky-Way analogue with and without CRs, as well as without any feedback at all (meaning no SN explosions, no radiation and no CRs).

We first visually inspect the effect of CR feedback on gas and star distribution with Fig. 3.15. The maps are face-on views of the hydrogen column density, plotted on top of the stellar mass with $f_{\rm gas} = 30\%$ in the left, and with $f_{\rm gas} = 10\%$ on the right. In the fiducial gas-rich galaxy, the bulk of the stellar mass is located in dense clumps of gas, at distances up to ~ 10 kpc from the center. Conversely, the distribution of stars is much less extended when $f_{\rm gas} = 10\%$, and both stars and dense gas remain confined towards the center of the galaxy.

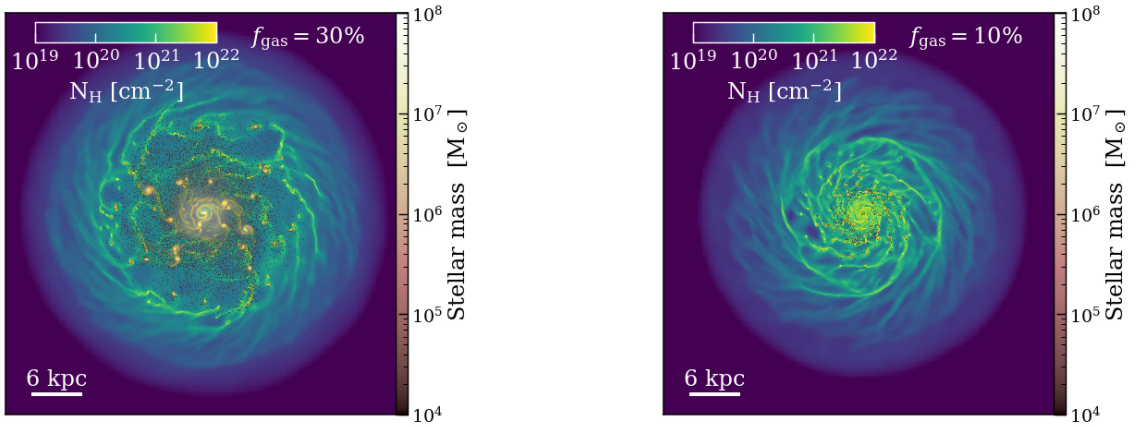

(a) *(b)*

Figure 3.15: *Face-on maps of G10 with CRs at 500 Myr with $f_{gas} = 30\%$ in the left panel (3.15a) and $f_{gas} = 10\%$ in the right panel (3.15b). The maps have a size of 48 kpc and show hydrogen column density with stellar mass overlaid. G10 with $f_{gas} = 30\%$ reveals massive clumps of stars and dense gas in the galaxy, while the gas-poor counterpart has a more centrally localised star formation and gas concentration.*

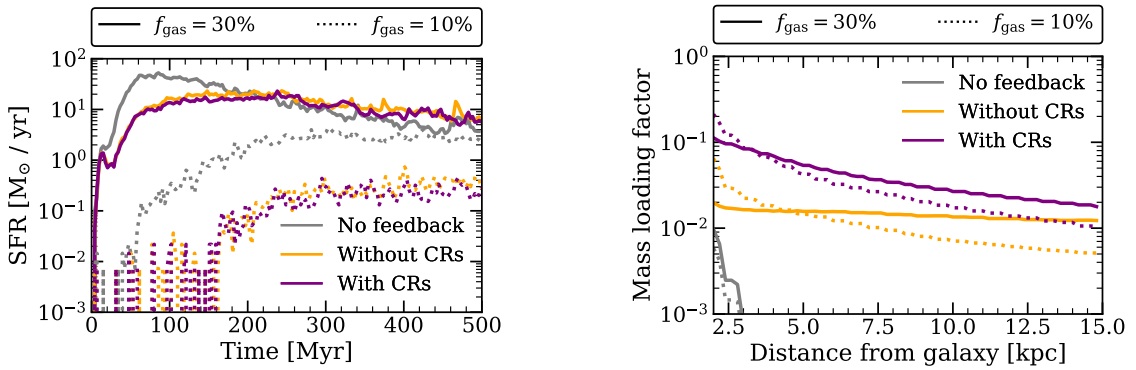

(a) *(b)*

Figure 3.16: *Effect of CR and SN feedback in G10 with different gas fractions $f_{gas} = 30\%$ (fiducial runs, in solid lines) and $f_{gas} = 10\%$ (in dotted lines). We show runs without any feedback in grey, with SN and radiation feedback in orange and with CRs added in purple. 3.16a: SFR as a function of time ; 3.16b: Mass loading factor for outflowing gas crossing planes at different distances from the disc, from data stacked between 200 and 500 Myr. Without feedback, the SFR is much higher (at least initially) and almost no gas is outflowing. For both gas fractions, CR feedback has the same efficiency in reducing star formation and driving stronger winds. SN feedback is much more efficient in suppressing star formation when $f_{gas} = 10\%$, with G10 ending up with star formation rates 50 times lower than when $f_{gas} = 30\%$.*

We quantify the efficiency of CR feedback in suppressing star formation and driving winds in Fig. 3.16. We show with solid lines G10 from the fiducial setup with $f_{gas} = 30\%$, and the gas-poor counterpart with $f_{gas} = 10\%$ with dotted lines, as we will for the other plots from this section. We add the results from galaxies without any feedback in grey. Regardless of the gas fraction, Fig. 3.16a shows that the star formation rate is similarly regulated by CRs, by a marginal factor ~ 1.2.

However, turning on SN feedback has a greater effect in suppressing star formation in the gas-poor case. When $f_{\rm gas} = 30\%$, runs without feedback initially have between 5 and 8 times higher SFR, before reaching similar values as in the case with feedback, once most of the gas has been converted into stars. On the other hand, when $f_{\rm gas} = 10\%$, runs that include SN feedback consistently have 10 times lower SFR. The galaxies have less gas and less dense than in the case where $f_{\rm gas} = 30\%$, so it is easier for the SNe to heat and disperse the gas, which prevents star formation. In all cases, feedback is needed to drive winds away from the galaxy. This is shown in Fig. 3.16b, where mass loading factors (mass outflow rate normalised by the SFR, averaged over the last 50 Myr) are plotted as a function of their distance from the disc. When feedback is included, gas is more efficiently driven out of the ISM, and reaches larger distances, with mass loading factors orders of magnitude larger than in runs without feedback. Besides, CR feedback similarly leads to greater mass loading factors in galaxies with different gas fractions even if, overall, they help to maintain the outflows at larger distances in the galaxies that have the highest $f_{\rm gas}$.

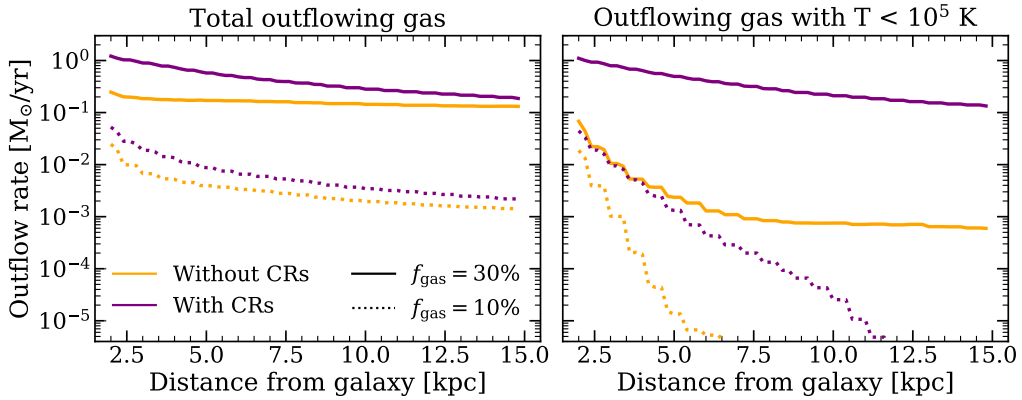

Figure 3.17: *Mass outflow rate of gas in cells crossing planes at different distances from the disc, from outputs stacked between 200 and 500 Myr. Runs with a fiducial gas fraction of 30% are depicted in solid lines, while dotted lines represent the equivalent galaxies with an initial gas fraction of 10%. From left to right, we show outflows without temperature distinction and colder than* 10^5 K. *Regardless of the initial gas fraction in G10, CRs lead to higher outflow rates and cooler outflows. The mass outflow rate at any temperature is however much lower in the runs that have 10% initial gas fraction, as a consequence of lower SFR.*

To better evaluate the effects of CRs on driving winds in our different G10 runs, Fig. 3.17 shows the mass outflow rate as a function of distance from the disc, for all gas and cool gas ($T < 10^5$ K) from left to right. Globally, CRs have the same effect in moderately enhancing the total outflow rate in the gas-poor and the gas-rich G10, especially at small distances from the disc. But it is especially visible that G10 with a low gas fraction has much lower outflow rate than its gas-rich counterpart. The G10 runs roughly all have the same gravitational potential, as gas has a negligible contribution compared to dark matter. However, the gas-poor G10 runs have lower SFR, and consequently fewer SN episodes. While it is enough to efficiently suppress star formation due to more localised events, it is also responsible for powering less winds, and mass outflow rates decrease more rapidly with distance than in the galaxy with $f_{\rm gas} = 30\%$. This particularly impacts the cool outflows, whose amount

decreases sharply with distance in G10 with $f_{\rm gas} = 10\%$. Nevertheless, CR feedback contributes to expel more cold outflowing gas than in runs without CRs. Again, fewer SN explosions leads to less CR energy than in the gas-rich galaxy, and CRs have a harder time to maintain the dense cold winds in the CGM due to their limited pressure support. We show in Fig. 3.18 the pressure exerted by cosmic rays in G10 with different $f_{\rm gas}$, which reveals that CR pressure distribution is more extended in the gas-rich G10, while almost no CR pressure is measured beyond ~ 6 kpc in the gas-poor galaxy.

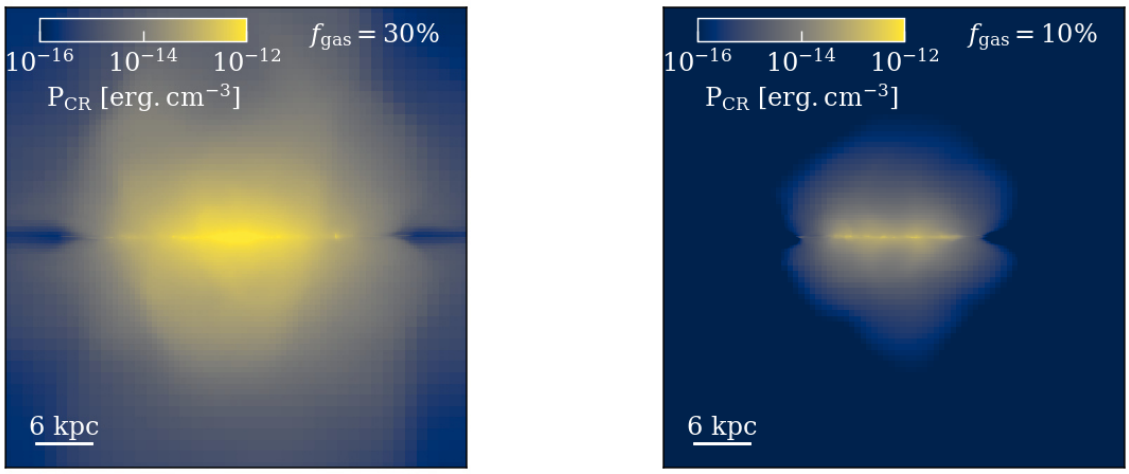

(a) *(b)*

Figure 3.18: *Edge-on maps of cosmic ray pressure in G10 at 500 Myr, with $f_{\rm gas} = 30\%$ in the left panel (3.18a) and $f_{\rm gas} = 10\%$ in the right panel (3.18b). CR pressure is much lower in the low gas-fraction case and remains confined closer to the galaxy disc than when $f_{\rm gas} = 30\%$.*

Finally, and for the sake of the comparison, we can analyse some of the properties we measure in light of observations. Measurements from the Milky-Way report SFR between 0.6 and 4 $M_\odot$/yr (e.g. Diehl et al., 2006; Robitaille & Whitney, 2010; Chomiuk & Povich, 2011; Licquia & Newman, 2015). This is in the upper limit of our Milky-Way analogue, as G10 with a gas fraction of 10% has an averaged SFR between 200 and 500 Myr of 0.2 $M_\odot$/yr, regardless of the inclusion of CR feedback. Conversely, the averaged SFR when G10 has a gas fraction of 30% is $\gtrsim 10$ $M_\odot$/yr. This last case remains however in good agreement with results from nearby highly star forming and massive high-redshift ($1.2 \leq z \leq 2.2$) galaxies (Kennicutt, 1998; Tacconi et al., 2013). Continuing on our broad comparison, we globally find low mass loading factor values compared to values of a few that are estimated for local and massively star forming galaxies at $2 \leq z \leq 3$ (as e.g. in Martin, 1999; Sato et al., 2009; Steidel et al., 2010; Coil et al., 2011). This reveals the weakness of our feedback in such massive galaxy. To reach mass loading factors of order unity, we would need to combine both a boosted SN feedback and CRs, which we show in **Section 3.5**. We stress nonetheless that the aim of this section is to analyse the effect of CR feedback with varying galaxy properties, namely gas fraction that impacts in turn star formation, rather than reproducing realistic simulated Milky-Way or high-redshift starburst galaxies. In particular, environmental effects, that

arise from a cosmological context, would be mandatory to produce a reliable Milky-Way like simulation.

3.5 The strength of CR feedback

To test the robustness of my previous results, I investigate in **Section 3.5.1** how the effect of CR feedback varies when CRs are coupled to a stronger SN feedback, such as the one adopted in the SPHINX simulations. In addition, parameters that describe CR energetics and diffusivity are barely constrained, while decisive to interpret the role of CR feedback. In **Section 3.5.2**, I study the impact of a stronger CR feedback, in which 4 times more CR energy is injected at each SN explosion.

3.5.1 Sensitivity of CR feedback to the SN feedback strength

Galaxy simulations can significantly differ, in particular due to the implementation of star formation and feedback models. Feedback models, and especially SN feedback models, are often calibrated to overcome the overcooling problem, which may be due to e.g. a lack of physics, oversimplified physics, lack of resolution, or over-mixing of gas. This complicates the study of CR feedback, which may be sensitive to the strength of the other feedback processes. In particular, the quantitative effect of CR feedback can differ significantly from one study to another. For example, Hopkins et al. (2018) find that CR feedback is inefficient to regulate star formation in low-mass galaxies, and only plays a role in reducing star formation and launching winds in galaxies whose halo mass is above $10^{11}\,M_\odot$, while I find opposite trends with halo mass. Among other reasons, this may be the consequence of different feedback strength reducing or enhancing that of CR feedback. In order to determine how CR feedback is affected by the strength of the SN feedback in our galaxies, this section compares the effects of CRs when using our fiducial SN feedback, with a SN rate of $1\,\mathrm{SN}/100\,M_\odot$, to the SN feedback used in the SPHINX simulations, for which the SN rate is $4\,\mathrm{SNe}/100\,M_\odot$. We already studied how CR feedback compares with this 4-fold boosted SN feedback in the Section 3.4 of the **CosmicShine** paper. The aim is now to add CRs in top of this already strong feedback, and determine if the same conclusions about CR feedback still hold under this extreme configuration.

As we did in the **CosmicShine** paper to visually inspect our simulations, Fig. 3.19 and Fig. 3.20 show hydrogen column density and temperature maps in runs without and with CRs, when using the fiducial (the two leftmost columns labelled "noCR" and "CR") and the boosted (the two rightmost columns labelled "SNboost" and "SNboost+CRs") SN feedback recipes. We remind that with the boosted SN feedback, there are 4 SN explosions per $100\,M_\odot$ of stars formed. Because there is 10% of the energy released going into CR energy (both with the fiducial and with the boosted SN feedback), this means that a CR energy of $4 \times 10^{40}\,\mathrm{erg}$ is injected each $100\,M_\odot$ formed, which is four times more than in the CR runs.

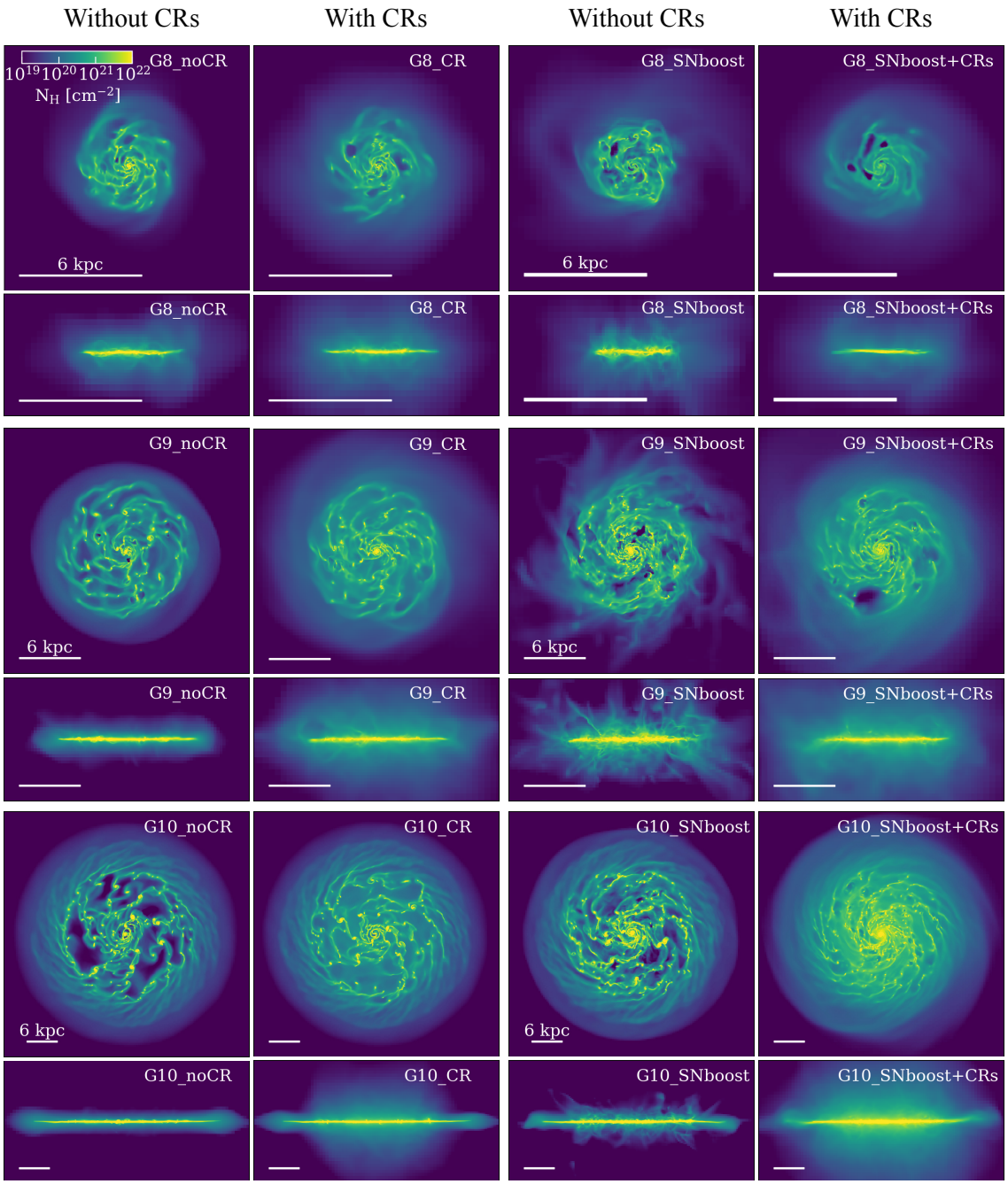

Figure 3.19: *Maps of the three discs at 500 Myr in order of increasing mass from top to bottom. We show 12, 24 and 48 kpc maps of face-on and edge-on hydrogen column density for each run, respectively. From left to right, the runs have fiducial SN feedback without and with CRs, and a four times boosted SN feedback without and with CRs. Regardless of the strength of the SN feedback, CRs smooth the gas distribution at any galaxy mass, and lead to a thicker disc, especially for the two most massive galaxies.*

Switching from a modest to a strong SN feedback (without CR feedback in both cases) tends to disrupt the galaxies. This is especially visible in the density maps of the lower-mass galaxies. The gaseous structures in the disc of G8 are less distinguishable than in the counterparts with a weaker SN feedback. The strong SN model in G9_SNboost leads to a more efficient expulsion of gas remaining in the vicinity of

the disc. Besides, the edge-on temperature maps reveal that runs with the boosted SN rate suffer from more violent winds, either with cold gas reaching larger distances or hot gas pervading the content of the CGM, depending on the galaxy mass and the presence of CRs. Transient features can be noticed in G9_SNboost+CRs and G10_SNboost+CRs, that both have hot bubbles of low-pressurised gas originating from the explosive SN feedback. Nevertheless, CRs qualitatively have the same effect on the galaxies, regardless of the strength of the SN feedback. The face-on maps of hydrogen column density exhibit a smoother gas distribution for all the galaxies that have CR feedback, and the edge-on views show that they are all globally thicker and surrounded by gas denser than when CRs are not included. At any galaxy mass, the CGM contains much more cold gas, supported by CR pressure, than when CRs are absent. Quantitatively however, the exact content of the CGM varies both with the SN feedback strength and the presence of CR feedback.

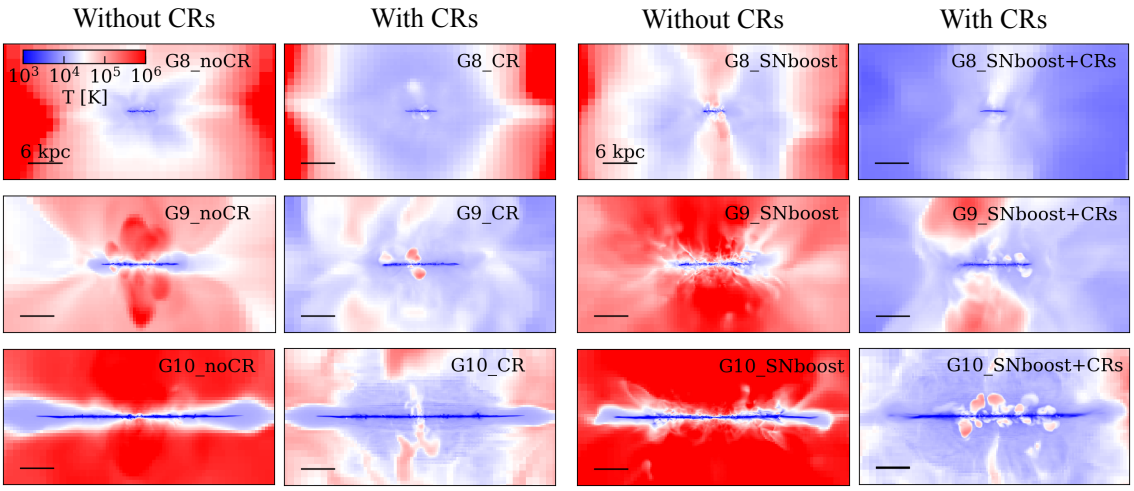

Figure 3.20: *Mass-weighted 48 kpc-wide slices of the three discs at 500 Myr, in order of increasing galaxy mass from top to bottom. For each galaxy and from left to right, we show edge-on temperature maps for runs with a fiducial SN feedback without and with CRs, and with a four times boosted SN feedback without and with CRs. The CGM of the galaxies is colder when CRs are included. When the SN feedback is stronger, the CGM of the two most massive galaxies tends to be hotter, with hot bubbles of outflowing gas.*

We quantitatively investigate the differences between the simulations in Fig. 3.21, for increasing galaxy mass from left to right. From top to bottom, we show the time evolution of the stellar mass formed, the SFR, the total mass outflow rate, and the fraction of outflowing gas colder than 10^5 K (that we refer to as cool outflows). The effect of CRs on star formation in the sets of four simulations is particularly interesting. With the fiducial SN feedback, CRs somewhat mildly suppress star formation by a factor two in the dwarf galaxies G8 and G9, with a decreasing efficiency with increasing galaxy mass. The trend is totally different when CRs are combined to a strong SN feedback. With the latter, the SFR in G8 quickly drops around zero after a couple of hundreds of Myr. Then, adding CRs does not have the same impact as in the unboosted case, even if they still marginally reduce furthermore the total stellar mass formed. In G9, the boosted SN feedback almost suppresses star formation as drastically as in G8, and adding CRs leads to the

same factor 2 reduction of the total stellar mass. However, the results in G10 are dramatically different. Star formation is barely impacted with either CRs or the boosted SN feedback, but combining both radically suppresses SFR by a factor of between 3 and 5. At 500 Myr, this leads to a total stellar mass more than four times lower than in G10_noCR, which is the strongest effect from CRs on star formation measured in our simulations. Additionally, this changes our previous conclusion about the fact that CR feedback regulates star formation more efficiently in low mass galaxies. Combined with a strong SN feedback, CRs better regulate the growth of our most massive galaxy. This is closer to the findings of Hopkins et al. (2020b) who find that CR feedback only suppresses star formation in high-mass halos. The inefficiency of CR feedback in their low-mass galaxies may be attributed to the strength of their SN feedback, which already significantly suppresses star formation, in combination with their diffusion coefficient 30 times higher than the one I adopt, which causes most CR energy to escape before acting on the ISM. Therefore, this shows the complexity of accurately predicting the role of CR feedback on galaxy evolution, which is sensitive to numerical modelling.

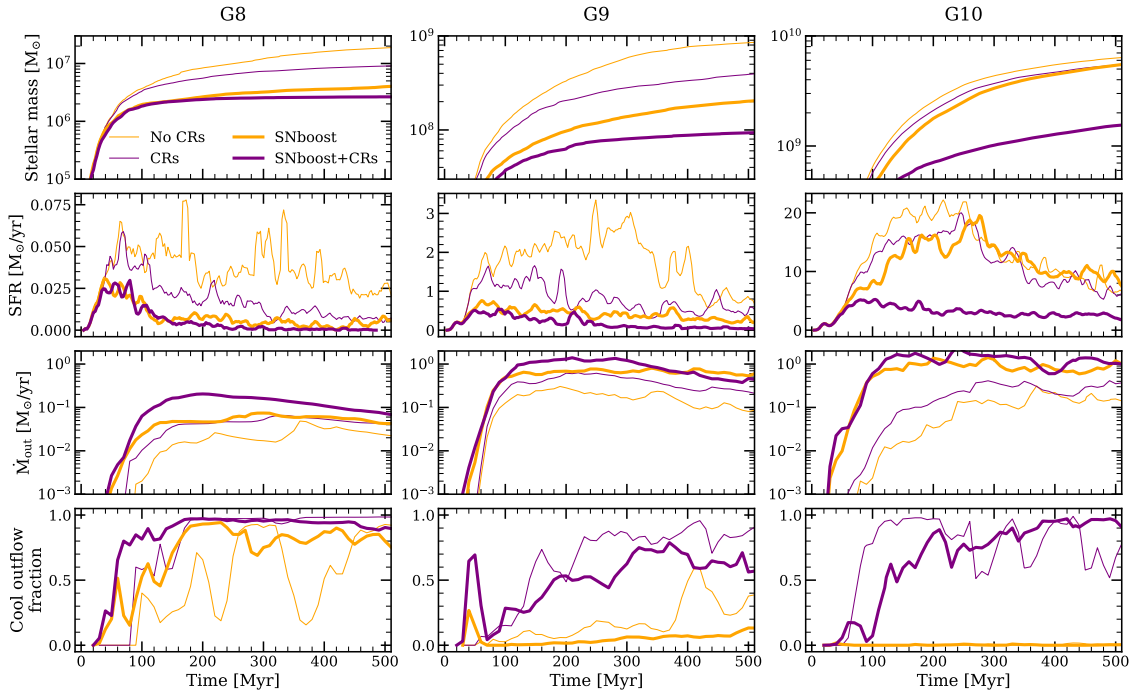

Figure 3.21: *From top to bottom: evolution with time of stellar mass, star formation rate, mass outflow rate measured at 10 kpc and fraction of cool outflowing gas with temperature below* 10^5 *K. We show runs without CRs in orange, with CRs in purple, and distinguish the fiducial and the strong SN feedback with thin and thick lines respectively. Combining a boosted SN feedback and CRs leads to stronger star formation suppression and the strongest winds, whose temperature composition remains similar to that of runs with weaker CRs and a weaker SN feedback.*

Regardless of the strength of the SN feedback, CRs help to drive more winds at a distance of 10 kpc from the galaxies, dominated by gas colder than 10^5 K. While CR feedback generally increase a lot the fraction of cold gas in the outflows, both G9 and G10 have a smaller fraction of cool outflows when the SN feedback is

the strongest. This is due to the efficiency of the boosted SN feedback in expelling large amounts of gas, predominantly hot and diffuse. Including CRs provides an additional and non thermal pressure support that enables denser and colder gas to be driven out of the galaxy, in a slightly less proportion when the SN feedback is boosted.

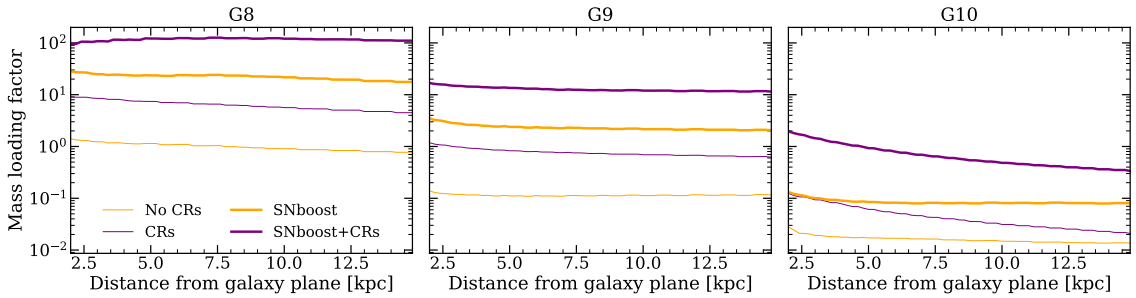

Figure 3.22: *Mass loading factor as a function of distance from the disc, with data stacked from 200 to 500 Myr, and for increasing galaxy mass from left to right. The mass loading factors are similarly increased when including CRs, regardless of the strength of the SN feedback. For G10, CRs combined to the boosted SN feedback are even more efficient to drive galactic winds.*

In order to better appreciate the ability of CRs to participate in launching winds, Fig. 3.22 focuses on mass loading factors, as a function of the distance from the disc. Galaxy mass increases from left to right, and data are stacked from 200 to 500 Myr. For G8 and G9, CRs increase the mass loading factors by a similar factor at any distance from the galaxies (up to 15 kpc). This result is independent of the strength of the SN feedback. Regardless of the feedback strength, the efficiency of CRs in driving winds decreases with distance in G10, with approximately the same slopes for G10_CR and G10_SNboost+CRs. However, due to the greatly suppressed star formation by CRs in G10_SNboost+CRs, the mass loading factor is initially one order of magnitude above that of the equivalent run without CRs. For this reason, the efficiency of CRs to drive winds at large distances is enhanced in the run for which the SN feedback is boosted.

3.5.2 Sensitivity of CR feedback to its energy injection

Essentially, two main parameters govern CR feedback. One of them is the diffusion coefficient κ, which rules the transport of CRs out of their injection sites, and therefore affects their ability to act on small or large scales. The role of κ on CR feedback has been studied in section 3.3 of the **CosmicShine** paper. The other parameter is the amount of CR energy injected by SNe $f_{\rm ecr}$, usually taken to be 0.1, so that 10% of the energy released by SNe goes into the acceleration of CRs. This canonical value of $f_{\rm ecr} = 0.1$ is typically adopted in numerical simulations of CR feedback in galaxies, and mainly relies on observation of local SNRs (Hillas, 2005; Strong et al., 2010; Morlino & Caprioli, 2012; Dermer & Powale, 2013; H. E. S. S. Collaboration et al., 2018). However, $f_{\rm ecr}$ is a poorly constrained quantity, and most studies diverge and find values ranging from 0.1 to beyond 0.4 (Kang & Jones, 2006; Ellison et al., 2010; Helder et al., 2013). This may translate the fact that SN explosions occur in places

where CRs have already been injected by previous SN events, so that this previous generation of CRs is further accelerated, at a rate higher than 10% (Caprioli & Spitkovsky, 2014; Caprioli et al., 2018). To account for this re-acceleration process, Jubelgas et al. (2008); Salem et al. (2016); Butsky & Quinn (2018); Semenov et al. (2021) use $f_{\rm ecr}$ from 0.1 up to 0.4 in their galaxy simulations. To justify which fraction of the SN kinetic energy must be channelled into CRs, one of the most commonly invoked argument is that a SN acceleration efficiency of 10% is sufficient to explain the gamma luminosity of the Milky-Way and the CR energy density inferred from our galaxy (Hillas, 2005; Boulares & Cox, 1990). However, gamma-ray observations of the starburst galaxies M82 and NGC 253 suggest CR energy densities up to two orders of magnitude above that of the Milky-Way (VERITAS Collaboration et al., 2009; Paglione & Abrahams, 2012; Yoast-Hull et al., 2013). In this section, we investigate how CR feedback is affected in our three different mass galaxies when switching from $f_{\rm ecr} = 0.1$ to $f_{\rm ecr} = 0.4$, which is probably conservatively at the upper end of 'allowed' CR energy injections. We also compare this additional case, that we label CRboost, to the other runs used to test the variability of CR feedback in our simulations, in order to better determine what can be expected from CRs with different modelling. In particular, for each $100\,{\rm M}_\odot$ of stellar particles formed, the CRboost and the SNboost+CRs feedback both inject the same CR energy, via either one or four SN explosions respectively.

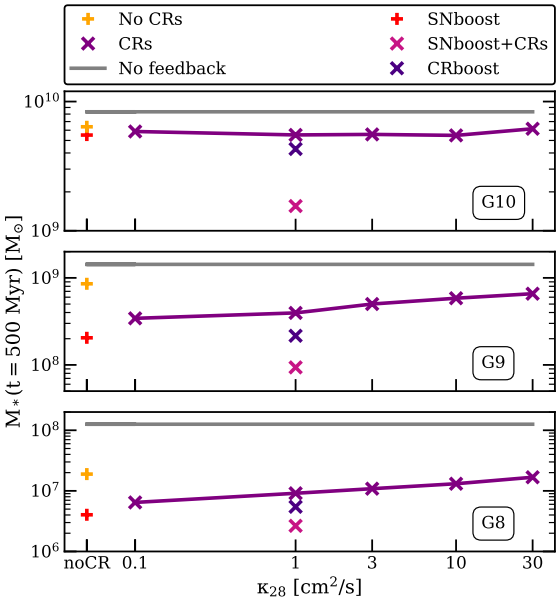

Figure 3.23: *Stellar mass formed after 500 Myr for decreasing galaxy mass from top to bottom and increasing diffusion coefficient from left to right. The leftmost orange and red plus markers correspond to runs without CRs and with a fiducial and boosted SN feedback, respectively. Light purple crosses stand for runs with CRs and boosted SN feedback, and dark purple correspond to the simulations that have a SN energy injection into CRs of 40%. We show counterpart runs without feedback (no SN, no radiation, no CRs) in grey lines. The injection of more CR energy reduces star formation at any galaxy mass, and is more efficient than only boosting the SN feedback in G10.*

Fig. 3.23 shows the total stellar mass formed in 500 Myr, for increasing galaxy mass from bottom to top, and gathering the results from various simulations. The

stellar mass is plotted as a function of the diffusion coefficient κ_{28}, expressed in units of $10^{28}\,\mathrm{cm^2\,s^{-1}}$. Grey lines show runs without feedback (no SN, no RT and no CRs) as a reference, and the coloured crosses show runs with different feedback (see the legend). We keep the same colour code throughout the section. Switching from $f_{\rm ecr} = 0.1$ to $f_{\rm ecr} = 0.4$ leads to a reduction of the stellar mass by a factor of 1.7, 1.8 and 1.3 respectively for G8, G9 and G10. While this is a mild effect, boosting the injection of CR energy is almost as efficient as boosting the SN energy for G8, and as or even more efficient for G9 and G10. In the **CosmicShine** paper, we use runs with a strong SN feedback (the red points) as references to assess the efficiency of CR feedback, because this is the model that allows the high-redshift SPHINX simulations to sufficiently regulate galaxy growth, in order to reproduce high-redshift luminosity functions. Therefore, Fig. 3.23 tells us that a similar star formation regulation may be manageable using the upper range of acceptable energy injection values for CRs instead of calibrating SN feedback. This would need to be tested in cosmological simulations (as I do in the next chapter), since results in isolated disks do not necessarily translate very well to a cosmological context. If we compare simulations with CRs and a fiducial SN feedback model, it appears that at any galaxy mass, injecting more CR energy reduces more efficiently star formation than confining a lower amount of CR energy for longer with a low diffusion coefficient. Finally, we note that combining a boosted SN feedback with CRs leads to the strongest star formation regulation.

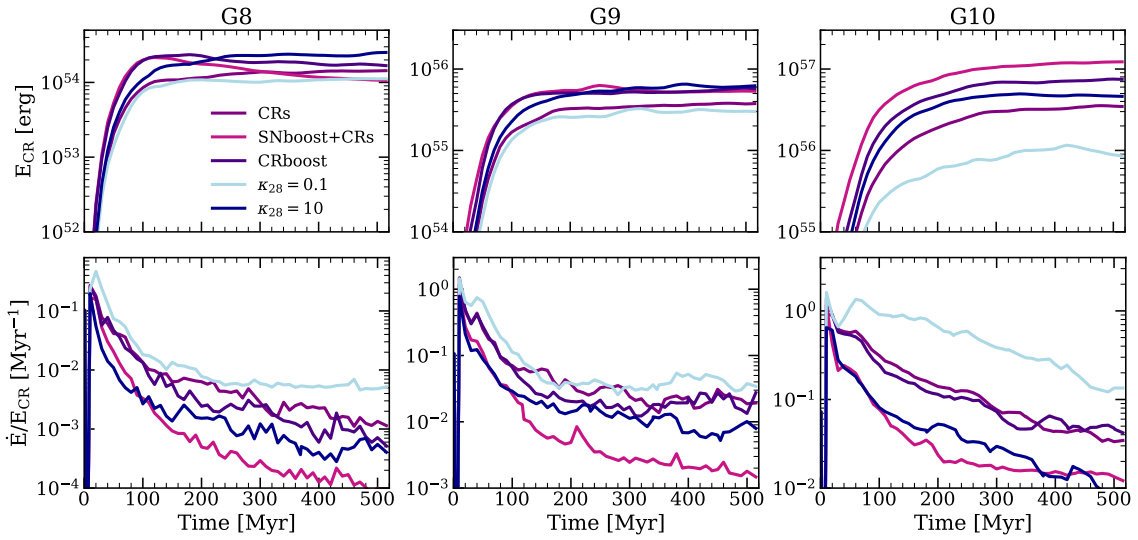

Figure 3.24: *Time evolution of the total CR energy (top panels) and hadronic and Coulomb loss rate (bottom panels). We show increasing galaxy mass from left to right (see the text for the explanation of the colour code). Slow diffusivity leads to more energy losses, which results in the lowest total CR energies. Without changing the diffusion coefficient, increasing the CR energy injection leads to similar loss rates, and consequently and enhanced CR energy budget. When the SN feedback is boosted, the sites of CR injection is so disrupted that the energy loss rate is least, which helps to maintain more CR energy.*

The different efficiencies of CR feedback measured are the consequences of the total CR energy available, the residence time of CRs in the ISM and the ability of SN feedback to disrupt the ISM, on top of which the effect of CRs accumulates. To

illustrate this, Fig. 3.24 shows the time evolution of the total CR energy (top panels) and loss rate (bottom panels), for increasing galaxy mass from left to right. The CR energy loss rate corresponds to the hadronic and Coulomb cooling rate, which scales linearly with gas density (see respectively Equation 2.25 and Equation 2.24). The CR energy and loss rate are measured in the whole box as a way to determine, at a given time, what is the amount of CR energy previously injected and still able to act on the CGM gas. The fact that some CRs exit the box boundaries does not impact the value of CR energy losses, as CR losses occur on dense gas such as in the ISM of the galaxies. The CRs runs with an injection efficiency $f_{\rm ecr} = 0.1$ and a diffusion coefficient $\kappa = 10^{28}\,{\rm cm^2\,s^{-1}}$ are shown in purple, light and dark blue correspond to the equivalent runs with $\kappa = 10^{27}\,{\rm cm^2\,s^{-1}}$ and $\kappa = 10^{29}\,{\rm cm^2\,s^{-1}}$, and light and dark purple represent the SNboost+CRs and CRboost runs, respectively. With a low diffusion coefficient, CRs populate more than with a higher κ the dense star-forming regions from where they originate, and where hadronic and Coulomb interactions happens more frequently. As a result, CRs that diffuse slowly suffer from the highest energy losses, and have the lowest total energy. Nonetheless, their longer confinement time in the ISM enables them to suppress the SFR more efficiently than CRs diffusing faster, as stated in the **CosmicShine** paper. Due to the same confinement time consideration, CRs that have the same diffusion coefficient but a different energy injection suffer from comparable loss rates, comparing CRs to CRboost runs. Simulations with $f_{\rm ecr} = 0.4$ accumulate more CR energy in the ISM, which has been shown to further reduce star formation, and which consequently reduces the number of SN explosions and the future injection of CR energy. For this reason, the total CR energy when switching from $f_{\rm ecr} = 0.1$ to $f_{\rm ecr} = 0.4$ is globally greater by a factor 2 instead of 4. Naively, we could also expect that enabling four times more SN explosions would lead to a similar CR energy budget than boosting the injection of CR energy by a factor four. Again, different SF regulation from one model to another leads to different total CR energies. With the boosted SN prescription, each SN explosion provides a net CR energy per stellar particle 4 times greater than in the fiducial model counterpart. This is however balanced by the decreased SFR, leading to less SN explosions in total. Consequently, there is not 4 times more CR energy in total with the boosted SN model than with the fiducial one with 4 times more CR energy injection per SN event. In any case, boosting the SN rate is more disruptive for the ISM, carving diffuse regions where CRs experience slower energy losses, which helps to maintain CR energy.

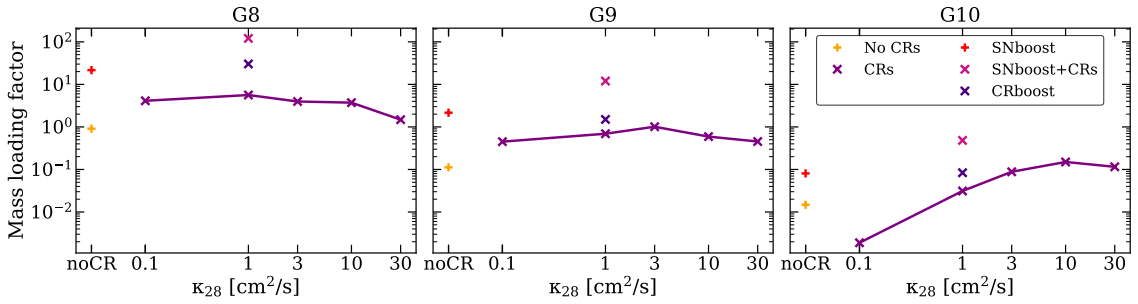

Figure 3.25: *Mass loading factor as a function of the diffusion coefficient, measured at 10 kpc from the disc and with data stacked from 200 to 500 Myr. We show increasing galaxy mass from left to right. The two leftmost data points correspond to simulations without CRs. Mass loading factors are greater when injecting 40% CR energy per SN event, but remain smaller than when boosting the SN feedback and injecting 10% of the SN energy into CRs.*

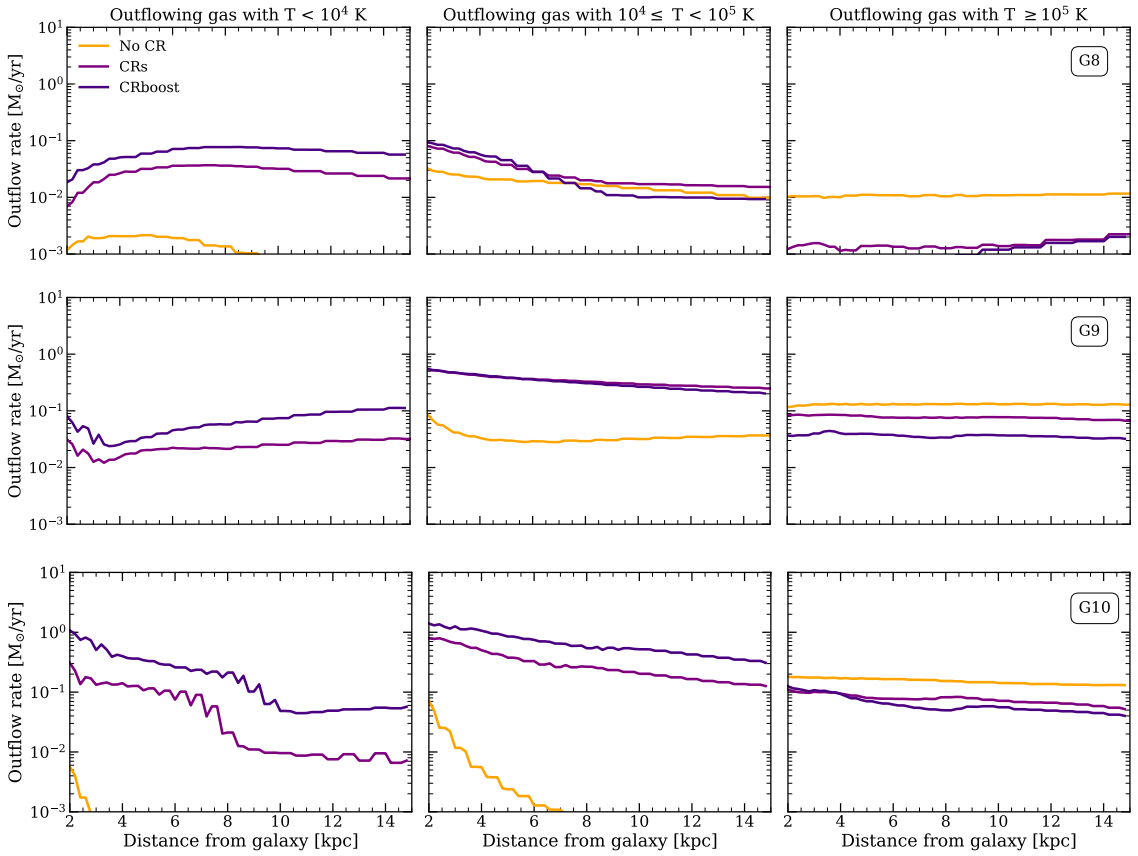

Figure 3.26: *Mass outflow rate as a function of distance for increasing galaxy mass from top to bottom. Data are stacked from 200 to 500 Myr, and the outflow rates are decomposed into cold, warm and hot outflows from left to right, as indicated in the titles of the columns. Globally, injecting 4 times more CR energy leads to more cold and warm outflows, and less hot outflows.*

The different aspects we mentioned regarding CR energy result in different efficiencies to drive galactic winds. Fig. 3.25 shows mass loading factor at 10 kpc from the galaxies, as a function of the diffusion coefficient, and with data stacked from

200 to 500 Myr. Again, the two leftmost points refer to simulations without CRs, and galaxy mass increases from left to right. Injecting 40% of the SN energy into CRs instead of 10% consistently leads to greater mass loading factors. This is the natural result of the enhanced CR pressure, which helps to eject more winds into the CGM. Besides, as for star formation regulation, it appears that boosting the CR energy produces similar mass loading factors as boosting the rate of SN events, except for G9 for which the latter is twice more efficient than the former. Nonetheless, this shows that calibrating CR physics within the realm of acceptable values, both in terms of energy injection and diffusion coefficient, can reproduce similar effects on star formation and mass outflow rate as when empirically tweaking the SN feedback. In order to test the limit of this statement, cosmological simulations are needed to let galaxies evolve across cosmic time, as we do in **Chapter 4**. This allows to check if gas accretion and galaxy mergers change the impact of CR feedback, and to assess the legitimacy of our model for CR physics, by looking for instance at the compatibility of our results with gamma-ray luminosity, as a constraint for CR propagation.

We finally focus on the temperature composition of the outflows when $f_{\rm ecr} = 0$ (no CRs, in orange), $f_{\rm ecr} = 0.1$ (the fiducial CRs runs, in purple) and $f_{\rm ecr} = 0.4$ (CRboost, in dark purple). Fig. 3.26 shows the mass outflow rate as a function of distance from the disc, for data stacked between 200 and 500 Myr. We show increasing galaxy mass from top to bottom, and cold, warm and hot outflows from left to right, defined as gas colder than 10^4 K, with $10^4 \leq T < 10^5$ K and hotter than 10^5 K. At any galaxy mass, increasing the CR energy injection by a factor 4 leads to colder outflows. The increased CR pressure gradient participates in driving dense and cold winds in a greater proportion up to larger distances, as there is more CR energy available in the galaxy to power galactic scales outflows. Conversely, less hot outflows are measured than when $f_{\rm ecr} = 0.1$. This may come from the lower thermal energy available, as 60% of the kinetic energy released by the SNe are in the thermal pool when $f_{\rm ecr} = 0.4$ instead of 90% when $f_{\rm ecr} = 0.1$. While hot winds are preferentially diffuse and low-pressurised gas driven by SN feedback, the mass outflow rate of hot gas consequently decreases with increasing CR energy injection.

3.6 Cosmic ray streaming transport and heating

Models of CR propagation usually assume that diffusion originates from external magnetic turbulence (the extrinsic turbulence model) or from self-generated streaming instabilities (self-confinement model, Zweibel, 2013). In some simulations, and in particular in the RAMSES code, the origin of CR diffusion is not distinguished. CRs diffuse with a constant diffusion coefficient, and can additionally stream along the magnetic field down their own pressure gradient. In this case, diffusion and streaming are solved in RAMSES as a variable effective diffusion modulated by the Alfvén speed of the plasma, as we explain in **Section 2.3.2**. A part of the CR energy is transferred to gas as a heating process to mimic their energy loss when they generate the self-induced Alfvén waves. Both aspects lead to what is called streaming transport and streaming heating. Neither of them are included in the simulations presented so far. This is due to the additional computational cost of considering streaming, as explained in **Section 2.3**. Furthermore, our choice of

neglecting streaming is motivated by Dashyan & Dubois (2020) who showed that "classical" diffusion, referring to CR scattering, is more efficient than streaming to drive galactic winds. However, while they study the distinct effects of CR advection, streaming and diffusion, the three processes are not coupled together: they either couple advection with diffusion, or advection with streaming. In this section, we investigate the impact of streaming when coupled to our fiducial G9_CR, for which diffusion occurs at a constant diffusion coefficient of $10^{28}\,\mathrm{cm^2\,s^{-1}}$. To determine the effect of adding streaming transport and streaming heating, one run includes only the latter component with advection and diffusion (referred to as Str_heat), and another one couple both of them (denoted Str $\times1$) with advection and CR diffusion. Besides, the Alfvén waves generated though the streaming instability process are subject to damping mechanisms, such as ion-neutral, non-linear Laudau and turbulence damping (e.g. Kulsrud & Pearce, 1969; Kulsrud, 2005; Lazarian, 2016; Armillotta et al., 2021). Depending on the damping strength (Wiener et al., 2013), this causes the CR streaming velocity to exceed the Alfvén speed by a factor of a few. To account for this phenomenon, we adopt the same approach as Ruszkowski et al. (2017) and Dashyan & Dubois (2020), for which the streaming velocity is boosted by a factor 4. As explained by Ruszkowski et al. (2017), in the case of turbulent damping, the Alfvén waves excited by CRs are dissipated via collisions with turbulent-driven MHD waves that propagate in the opposite direction, which translates into a boost of the streaming velocity by a factor of ~ 4.3. We therefore perform one more galaxy simulation with advection, diffusion, streaming transport and heating, with the streaming velocity being 4 times that of the Alfvén waves (the run is labelled Str $\times4$). This last simulation has been performed down to 250 Myr of evolution instead of 500 Myr for the other ones. Because the streaming velocity is boosted, the effective streaming diffusion coefficient is higher, which increases the number of iterative steps needed for the implicit solver to converge and consequently the runtime of the simulation. We stress that the aim is not to determine which among diffusion and streaming dominates CR transport (this is unanswered yet), but rather to check that including the streaming propagation mode does not significantly change the results presented in the **CosmicShine** paper.

We first investigate the effect of streaming heating and diffusion on star formation with Fig. 3.27, which shows the time evolution of the stellar mass formed in G9. We show our runs in different colors, as indicated by the legend. Regardless of CR transport, the stellar mass formed from one run to another evolves similarly apart from marginal fluctuations. After 500 Myr, twice less stars are formed in the simulations that include CRs. This is the consequence of CR diffusion, which determines the time during which CR energy resides in the ISM and acts on star formation. If we consider a magnetic field strength of 1 μG and a gas density of 100 $\mathrm{H\,cm^{-3}}$, the Alfvén velocity is of the order of a few $\mathrm{km\,s^{-1}}$, while diffusion velocity with $\kappa = 10^{28}\,\mathrm{cm^2\,s^{-1}}$ is around a few hundreds $\mathrm{km\,s^{-1}}$ at ISM scales. Therefore, CR transport is dominated by diffusion, which happens on timescales shorter than advection and streaming (see also Fig. 8 from the **CosmicShine** paper). For this reason, the effect of CRs on star formation in our simulations is predominantly determined by the constant diffusion coefficient value chosen. For the Str $\times4$ run, we note a small enhancement of the stellar mass after 200 Myr compared to the other runs with CRs. This effect may be due to the stochasticity of star formation,

or shows that when streaming velocity becomes high enough, it reduces the ability of CRs to suppress star formation, just as increasing the CR diffusion coefficient does.

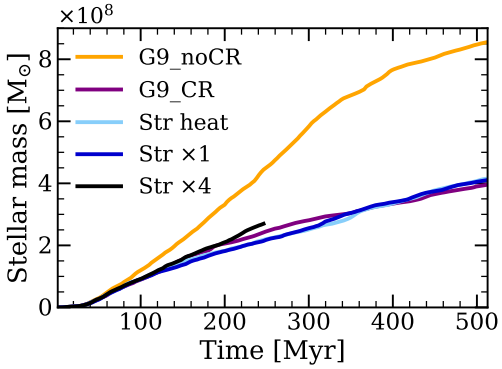

Figure 3.27: *Stellar mass formed as a function of time. We show respectively in orange, purple, lightblue, blue and black runs without CR (G9_noCR), with CR anisotropic diffusion (G9_CR), with streaming heating (Str heat), with streaming transport (Str ×1) and with a 4 times boosted streaming velocity (Str ×4). All the simulations with CRs form less stars than in the counterpart run without CRs. This is valid regardless of the CR transport, which shows that star formation regulation by CRs is dominated by "classical" diffusion, included in all our simulations with CRs.*

Cosmic ray streaming is mostly regarded for its impact on galactic winds. We show mass outflow rates as a function of time (measured at 10 kpc from the disc plane) in Fig. 3.28. The leftmost panel shows the total mass outflow rate, the middle panel focuses on outflows colder than 10^5 K, and the rightmost panel shows the mass outflow rate for gas hotter than 10^5 K. Again, the results roughly converge no matter whether streaming is included or not. In all the simulations with CRs, we measure mass outflow rates at least twice larger than in G9_noCR. Only a noticeable difference arises: runs that include streaming heating have slightly less cold outflows, and correspondingly have a greater fraction of their winds hotter than 10^5 K than G9_CR. A similar result is measured for instance by Butsky & Quinn (2018), although using a different code and a different setup. Streaming heating is proportional to the Alfvén speed and to the gradient of CR pressure, which is especially strong in the galactic winds it helps to lift (as shown in Fig. 10 from the **CosmicShine** paper). Therefore, streaming heating in galactic outflows slightly heats the gas, by converting from CR to thermal pressure. It is nonetheless intricate to quantitatively assess the effect CR streaming has in our idealised simulations, where the CGM is initially homogeneous, hot and diffuse. CR streaming heating may have a more significant effect in a cosmological context where outflows would be driven in a more realistic CGM.

Interestingly, conclusions regarding the effects of streaming on launching winds can drastically differ from one study to another. Butsky & Quinn (2018) and Holguin et al. (2019) respectively find lower integrated mass loading factor for runs with advection and streaming than runs with advection and diffusion and runs with only CR advection. Holguin et al. (2019) additionally show that accounting for realistic streaming instability suppression, with a turbulent damping rate that depends on the properties of the gas, significantly reduces the instantaneous mass loading

factor. Conversely, Ruszkowski et al. (2017) find the complete opposite trend in simulations of Milky-Way size starburst galaxy. They measure no significant wind with diffusion alone, and higher mass loading factor without diffusion but when boosting the streaming velocity from a constant value relative to the Alfvén velocity. In their case, higher streaming velocities lead to more efficient wind driving, with the limitation than if driven too fast from the galaxy, they may consist in more diffuse gas. They measure larger mass outflow rates but higher SFR with increasing streaming velocity, as CRs escape the disc faster and remove their pressure support from star-forming regions. On the other hand, Dashyan & Dubois (2020) and Wiener et al. (2017) measure weaker galactic winds with streaming alone than with diffusion. Dashyan & Dubois (2020) invoke the low Alfvén velocity, even boosted by a factor 4, compared to the speed of the winds, which renders CR streaming dynamically irrelevant to drive significant outflows. Wiener et al. (2017) explain that the phenomenon of weaker winds with CR streaming comes from the fact that this process drains CR energy, which is eventually radiated away and therefore unable to participate to drive winds.

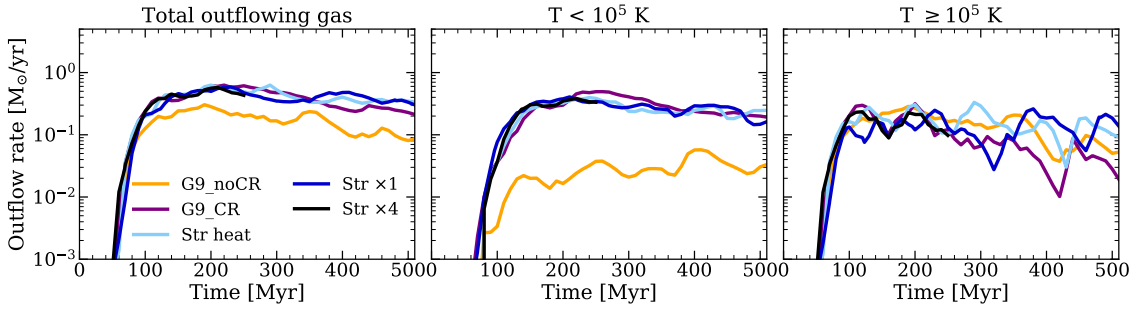

Figure 3.28: *Mass outflow rate as a function of time, measured at 10 kpc from the disc plane. We show respectively in orange, purple, lightblue, blue and black runs without CR (G9_noCR), with CR anisotropic diffusion(G9_CR), with added streaming heating (Str heat), with streaming transport (Str times1) and with a 4 times boosted streaming velocity (Str ×4). From left to right, the outflows are measured for all the gas, for gas colder than* 10^5 *K and for gas hotter than* 10^5 *K. Regardless of CR transport, the total mass outflow rate is at least a factor two larger with than without CRs. Runs that further include streaming heating have marginally less cool outflows and respectively drive hotter winds than G9_CR.*

We further investigate the reason why including CR streaming does not change the total mass outflow rate in Fig. 3.29. We first focus on the time evolution of the total CR energy, shown in Fig. 3.29a. At any time, the total energy of cosmic rays in the whole simulation box is roughly the same for all the runs that include CRs. This is the consequence of a balance between the CR energy injection and losses through adiabatic expansion and hadronic and Coulomb interactions for all, and streaming heating for the runs Str heat, Str ×1 and Str ×4. As shown in Fig. 3.27, the runs with CRs have similar star formation with time, which results in a similar number of SN events and consequently the same injection of CR energy regardless of the CR transport included. Therefore, this also shows that the CR energy losses are roughly the same, despite streaming heating. While in the absence of "classical" diffusion, runs with CR streaming would have their CR energy density trapped in

the dense regions of the galaxies where losses are significant (Dashyan & Dubois, 2020), we measure very similar total CR energy across time. Consequently, CRs provide a similar pressure support to drive winds in all our runs.

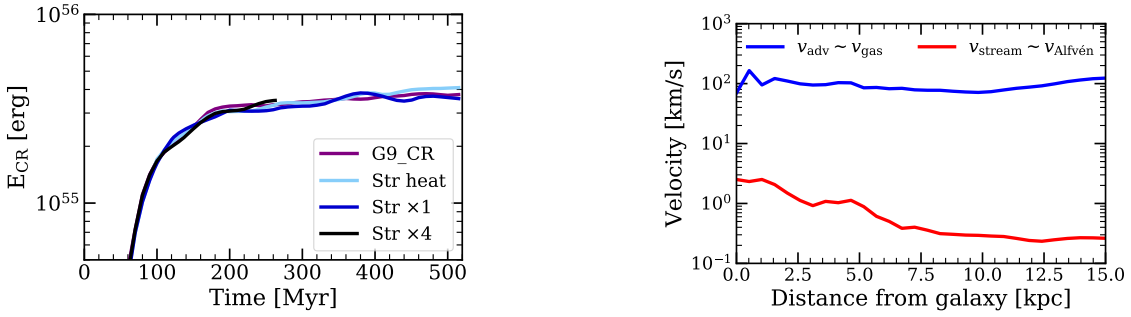

(a) *(b)*

Figure 3.29: *3.29a: Total CR energy as a function of time for G9 with anisotropic diffusion (in purple) + streaming heating (in lightblue) + streaming transport at the Alfvén speed (in blue) or 4 times faster (in black). The CR energy within the simulation box is approximately the same for all the runs. 3.29b: Typical averaged velocities as a function of distance from the disc plane for the Str ×1 run, at 250 Myr. We show in blue the gas velocity, equivalent to the CR advection speed, and the streaming velocity in red, equivalent to the Alfvén velocity. As the Alfvén speed in the CGM is so low compared to gas velocity, streaming transport cannot have any significant effect on the mass outflow rate.*

Fig. 3.29b compares the gas and the streaming mean velocities (in blue and red respectively) as a function of distance in the run Str ×1, at 250 Myr. We note that we show average values, which does not reflect the lower velocities that can be measured for gas in the ISM in the absence of SN explosion. At any distance from the galaxy, the Alfvén speed is lower than the gas velocity, which means that CR streaming is slower than advection. This still holds when boosting the streaming velocity by a factor of a few. CR streaming depends on the Alfvén velocity, which is proportional to the magnetic field strength over the square root of the gas density. Therefore, for streaming to significantly contribute to CR dynamics, it would be needed to reach higher magnetic field values, in order to lead to a faster streaming velocity. In the ISM, this would be mandatory to balance the high gas density. Besides, the magnetic field barely pervades the CGM (see also Fig. 3.8b), and even though the gas density is much lower, the Alfvén velocity remains more than 100 times lower than the speed of feedback-driven winds. Consequently, CR transport in the CGM is dominated by advection, which occurs at gas velocity.

All in all, the role of CR streaming in our simulations is somehow weakened by the other CR transport processes, namely diffusion and advection, that respectively dominate CR propagation at ISM and CGM scales. In order for streaming transport to additionally supply the acceleration of galactic winds, we would need the Alfvén velocity to be of the same order as gas velocity. In any case, the effect of streaming on the launching of CR winds is not settled, and may be furthermore sensitive to sub-grid feedback, resolution and ISM physics.

3.7 Summary

By means of idealised simulations of disc galaxies of different masses, this chapter investigates the effect of CR feedback on galaxy evolution, when coupled to RMHD, radiation and SN feedback. I find that CR feedback helps to disperse gas from the star-forming sites and smooths density contrast in the ISM. This prevents radiation to escape, and reduces star formation with a decreasing efficiency at increasing galaxy mass. In the three galaxies, CRs also help to drive stronger and colder winds. Quantitatively, these results vary with the CR diffusion coefficient and the CR energy injection efficiency. With a high diffusion coefficient, CRs escape quickly from their injection sites. They have less time to act on the ISM, which reduces their impact on star formation, but conversely maintains more CR energy to drive large outflow rates. For a similar reason, if more CR energy is injected at each SN explosions, star formation is more significantly suppressed and more winds are ejected up to larger distances. These results about CR feedback are robust to both cell and stellar particle mass resolution changes, and are qualitatively the same for different star formation and SN feedback models. This is not the case for radiation feedback, which is less efficient to prevent star formation when the stellar distribution is clumpy, as it reduces the efficiency of SN feedback. I find that the magnetic field, the initial gas fraction and CR streaming do not play any significant role in the simulated galaxies. Finally, in these idealised galaxies that have high gas fraction like high-redshift galaxies, I show that CR feedback reduces the escape fraction of LyC radiation. This study helps to understand the effect and the limit of CR feedback in an idealised context, in regulating galaxy growth and in impacting the escape of ionising photons. Therefore, it sets the baseline to investigate the impact of CRs during the early Universe and on reionisation in the next chapter.

CHAPTER 4

Cosmic rays during the Epoch of Reionisation

In this chapter, I analyse the effects of cosmic ray feedback during the Epoch of Reionisation. I first remind the purposes and motivations of this study in **Section 4.1**. I describe the setup of the cosmological simulations performed and the RASCAS code used to measure the escape fraction of LyC radiation in **Section 4.2**. Then, the results are organised in two sections. In **Section 4.3**, I study two halos from SPHINX20 re-simulated with the zoom-in technique, without SN feedback calibration and with and without CRs, which provides a follow-up to the results from the previous chapter. I finally investigate the effects of CR feedback on the reionisation process by comparing two calibrated SPHINX5 simulations with and without CRs in **Section 4.4**.

4.1 Motivations

The results presented in **Chapter 3** confirm that CR feedback regulates star formation and contributes to remove dense gas out of the ISM, which thickens the galaxy discs and enriches the CGM. In addition to these results qualitatively noted in previous studies from the literature (e.g. Jubelgas et al., 2008; Pakmor et al., 2016; Butsky & Quinn, 2018; Girichidis et al., 2018), I showed that CR feedback in idealised disc galaxies reduces the escape of hydrogen ionising radiation (LyC), which we expect to have consequences on the reionisation process. In order to understand the impact of CR feedback on galaxies and reionisation during the EoR, it is needed to perform cosmological simulations, coupling CR-MHD and RHD to evolve the ionisation state of the Universe through cosmic time. For this purpose, I use the SPHINX simulations presented in **Section 2.4**, that match observational constraints at high-redshift regarding both star formation and the reionisation of the Universe thanks to a strong and calibrated SN feedback. The aim is now to reduce the strength of SN feedback to render it closer to the expectations from stellar population models adding CR feedback instead, and study how galaxy growth and reionisation are affected by this.

Firstly, this chapter provides a follow-up to the results of **Chapter 3**. The galaxies studied in the previous chapter are embedded in DM halos of 10^{10}, 10^{11} and $10^{12}\,\mathrm{M}_{\odot}$, which would be relatively massive objects during the EoR and require simulation volumes large enough to let them emerge before $z = 5$, which is typically where we stop our cosmological simulations. Indeed, the evolution of the initial DM density field up to massive halos is determined by the possibility of merging numerous small structures, which is limited by the amount of DM mass contained in the simulation box and hence by its volume size. Using the zoom-in technique (see **Section 2.1.1**) to avoid the numerical cost of simulating thousands of resolved

galaxies in a large volume, I target two halos with masses of $\sim 10^{10}$ and $10^{11}\,\mathrm{M}_\odot$ and run them with and without CRs down to $z = 5$. These two halos, which have virial masses similar to those hosting G8 and G9, are studied in **Section 4.3**.

The second part of the chapter is dedicated to the reionisation of the Universe. In order to study the process of reionisation globally, it is needed to form enough galaxies in a given simulation volume, and look at their impact on the state of the IGM. This implies to perform cosmological simulations in which galaxies are equally resolved over the whole volume, which provides a much greater statistical sample of galaxies than the zoom-in technique. I combine this requirement and the numerical cost of CR-RMHD simulations by focusing on small SPHINX5 volumes (i.e. with a width of 5 co-moving Mpc). In **Section 4.4**, I compare two SPHINX5 simulations: one with the fiducial SPHINX setup using strong SN feedback, and a counterpart run with CRs and SNe calibrated to regulate star formation with a similar efficiency. Because these two simulations produce similar amounts of LyC photons, we can better investigate the effects of CRs on the reionisation of the Universe and more specifically on the escape of hydrogen ionising photons at different galaxy masses.

Before showing the results from the aforementioned simulations, I now describe their initial conditions and setup, and present the RASCAS code used to measure the escape fraction of LyC photons and determine the UV magnitudes of the simulated galaxies.

4.2 Simulations and methods

4.2.1 Description of the simulations

Initial conditions

The starting point for simulations of any kind is a set of initial conditions (ICs). In particular, the ICs for cosmological simulations consist in seeding DM fluctuations following a Gaussian distribution, to resemble the state of the Universe as inferred from the CMB. For the simulations studied in this chapter, the ICs are generated with the MUSIC code[1], which stands for MUlti-Scale-Initial-Conditions and was developed by Hahn & Abel (2011). Given a set of cosmological parameters, MUSIC generates a white noise of random values sampled from a Gaussian distribution. Using a Fast Fourier Transform algorithm, the code then ensures that their amplitude follows the power spectrum determined by the cosmological model specified by the user. For zoom-in simulations, MUSIC can further refine the white noise for a targeted nested subdomain compared to the rest of the simulation volume. The code eventually generate files readable by RAMSES containing lists of initial velocities and positions for DM particles and gas velocity and density fields.

The SPHINX simulations follow a ΛCDM Universe, and adopt the following cosmological parameters: the total matter density is $\Omega_\mathrm{m} = 0.3175$, the cosmological constant density is $\Omega_\Lambda = 0.6825$, the baryon density is $\Omega_\mathrm{b} = 0.049$ and the Hubble constant is $H_0 = 67.11\,\mathrm{km\,s^{-1}\,Mpc^{-1}}$ (so that $h = H_0/100\,\mathrm{km\,s^{-1}\,Mpc^{-1}} = 0.6711$).

[1] https://www-n.oca.eu/ohahn/MUSIC/

The power spectrum used to generate the ICs with MUSIC is normalised by[2] $\sigma_8 = 0.83$ and the power law index of the density perturbation spectrum is $n_{\rm spec} = 0.962$. These cosmological parameters are chosen from the Planck 2013 results (Planck Collaboration et al., 2014) and are the same for all the SPHINX volumes. They also all have a hydrogen mass fraction $X = 0.76$, a helium mass fraction $Y = 0.24$, and assume an initial homogeneous metal gas fraction $Z_{\rm ini} = 3.2 \times 10^{-4}\,{\rm Z}_\odot$ (where the Solar metal mass fraction ${\rm Z}_\odot = 0.02$) in order to form the first stars at $z = 15$ despite the lack of primordial molecular hydrogen cooling in the simulations (which is in reality what allows primordial gas almost only comprised of hydrogen and helium to cool and collapse to form the first stars).

In this chapter, we focus on target regions from SPHINX20, and on fully resolved SPHINX5 simulations. SPHINX20 and SPHINX5 are simulation volumes of 20 cMpc and 5 cMpc in width respectively. They have the same minimum and maximum cell widths, which are respectively 19.5 ckpc and 76.3 cpc. At $z = 5$, this corresponds to minimum and maximum cell widths of 3.3 kpc and 12.7 pc, that are smaller at higher redshift as the refinement levels are fixed throughout the simulation. In my SPHINX5 simulations, there are 256^3 DM particles whose mass is set to $2.5 \times 10^5\,{\rm M}_\odot$, and the minimum mass of the stellar particles is $1000\,{\rm M}_\odot$. In the fiducial SPHINX20 simulation, the 1024^3 DM particles also have a mass of $2.5 \times 10^5\,{\rm M}_\odot$ but the minimum mass of the stellar particles is set to $380\,{\rm M}_\odot$, and I use the same properties for the zoom-in halos which are described below.

Initial conditions of the zoom simulations

My first step to study the effect of CR feedback on galaxies in a cosmological context has been to make use of the zoom-in technique to re-simulate two fairly isolated halos from SPHINX20 without the boosted SN feedback but with and without CRs. To identify the halos, I use the ADAPTAHOP algorithm in the most massive submaxima mode (Aubert et al., 2004; Tweed et al., 2009). Following the notation used by Aubert et al. (2004, in Appendix B), we adopt $N_{\rm SPH} = 32$, $N_{\rm HOP} = 16$, $\rho_{\rm TH} = 80$ and $f_{\rm Poisson} = 4$. Then, we define a halo as a region in which the virial theorem is satisfied and where the density is 200 times the critical value ($\rho_{\rm crit} = 3H_0^2/8\pi G$). The halo must contain at least 20 DM particles, and its densest part corresponds to its centre (see also Rosdahl et al., 2018).

The first of the two halos targeted has a virial mass $M_{\rm vir} = 1.5 \times 10^{10}\,{\rm M}_\odot$ and a virial radius $R_{\rm vir} = 13\,{\rm kpc}$ at $z = 5$. The second halo is almost ten times more massive at the same redshift, with $M_{\rm vir} = 9 \times 10^{10}\,{\rm M}_\odot$ and $R_{\rm vir} = 23\,{\rm kpc}$ (see also Table 4.1 below). We will refer to them as Zoom1 and Zoom2 respectively, by increasing order of mass. To get the ICs of these two objects, the first step consists in performing a DM only simulation with the same configuration as the original SPHINX20 with MUSIC. This allows to identify the regions to be zoomed-in, and get the list of DM particles they contain. In the next stage, MUSIC will be given the corresponding list of DM particles to identify the region that is to be refined, unlike the rest of the box which remains at a coarser resolution. The transition between the zoom region and the outside is done progressively: the box

[2]The normalisation of the power spectrum is written σ_8 because it measures the amplitude of the power spectrum on scales of $8\,{\rm Mpc\,h^{-1}}$.

has a coarse refinement level $\ell = 8$, a "stamp" region before the targeted area is at level $\ell = 9$, and the region of interest has the same minimum and maximum refinement levels as the fiducial SPHINX20 simulation, that is to say $\ell = 10$ and $\ell = 18$ respectively. The mass distribution inside the target halos is refined to reach a DM particle mass of $2.5 \times 10^5\,\mathrm{M}_\odot$, while DM particles have a mass eight times higher in the stamp region and 64 times higher everywhere outside the zoom region. To avoid any contamination of the halo with lower mass DM particles from the rest of the simulation volume, the region to be refined has a size twice that of the virial radius of the targeted halo. I specifically verify with pure-DM runs that there is no contamination by higher mass DM particles. This procedure is repeated for each target, in order to have individual ICs for the Zoom1 and Zoom2 simulations.

General setup

The code, physics, and methods for the cosmological simulations presented in this chapter are globally the same as those stated in the **CosmicShine** paper, and details about the SPHINX simulations are provided by Rosdahl et al. (2018). I use RAMSES-RT to perform RMHD simulations with and without CRs, in which the equations are solved as explained in **Section 2.2** and **Section 2.3.2**. Each simulation is evolved down to $z = 5$, and outputs are equispaced in time by 10 Myr for the SPHINX5 volumes and 20 Myr for the zoom simulations.

To initialise the magnetic field, we define a uniform grid at a coarser level than the simulation (128^3 cells for the potential vector grid instead of 256^3 coarse cells for the simulation grid), and assign to each of its cell interface a random magnetic potential component value, so that we have a random Gaussian vector potential field over the uniform grid. The magnetic field components are then built from the curl of the magnetic potential vector and reconstructed in order to match the simulation grid, which ensures that the magnetic field is divergence free by construction. We eventually normalise the 6 magnetic field components of each cell to get comoving Gauss units, and normalise the strength of the initial magnetic field B_0 at a scale of 1 cMpc to $B_0 = 10^{-12}\,\mathrm{G}$ (Shaw & Lewis, 2012; Planck Collaboration et al., 2016).

I use the same turbulent SF model and mechanical SN feedback as in the fiducial SPHINX simulations, respectively described in **Section 2.2.6** and **Section 2.2.7**. The minimum stellar particle mass is set to $400\,\mathrm{M}_\odot$ for the zooms (as in SPHINX20) and to $1000\,\mathrm{M}_\odot$ for the SPHINX5 simulations (as in the fiducial SPHINX5 and SPHINX10 from Rosdahl et al., 2018). Each SN explosion releases an energy of $10^{51}\,\mathrm{erg}$. The fraction of mass recycled into SN ejecta is of 20% and 7.5% of this mass is recycled back into the ISM as elements heavier than hydrogen and helium, which means that the metal yield is of 0.075. The SN rate is $1\ \mathrm{SN}/100\,\mathrm{M}_\odot$ (as derived from a Kroupa IMF) for the zoom simulations and the non calibrated SPHINX5 volumes, $2\ \mathrm{SN}/100\,\mathrm{M}_\odot$ for the CR calibrated SPHINX5 simulation and $4\ \mathrm{SN}/100\,\mathrm{M}_\odot$ for the analogue of the fiducial SPHINX5 simulation.

I use the same prescription for radiation as in the fiducial SPHINX20 simulation (Rosdahl et al., 2022), that is to say that radiation is split into two photon groups which correspond to hydrogen and helium ionising photons. The group of photons that can ionise HeII is skipped for memory purposes, as it avoids to track four more RT variables. The radiation injected by stars follows the same SED as SPHINX20 and the idealised galaxies from the previous chapter which is version 2.2.1 of the

Binary Population And Spectral Synthesis model (BPASS; Stanway et al., 2016 ; Stanway & Eldridge, 2018).

Finally, CR feedback is modelled by including CR anisotropic diffusion and radiative losses. CR streaming transport and heating are neglected. I adopt a diffusion coefficient $\kappa = 10^{28}\,\mathrm{cm^2\,s^{-1}}$. The fraction of SN energy injected into CRs in the CR calibrated SPHINX5 simulation is $f_{\rm ecr} = 0.2$, while we keep $f_{\rm ecr} = 0.1$ for the zoom simulations.

4.2.2 Escape fractions with the RASCAS code

The radiative transfer method implemented in RAMSES allows to know the ionisation state of the gas, and models the effects of radiation on gas. However, individual photons and their direction of propagation are not tracked, and it is not directly possible to determine where and when the radiation emitted by a stellar particle is absorbed. In the context of the reionisation process, we want to measure accurately the escape fraction of LyC photons, which cannot be directly done from the RAMSES-RT outputs because of the variable speed of light. As we do not know exactly the travel-time of all photons from their sources, we cannot determine the delay time from emission in the galaxy to the IGM. For this purpose, I use the public code RASCAS, which stands for RAdiative SCattering in Astrophysical Simulations and which is described by Michel-Dansac et al. (2020). RASCAS is a 3D post-processing RT code which allows to propagate photons such as LyC photons on an adaptive mesh, but does not model radiation feedback like RAMSES-RT. To track the possible interactions of the photons with gas and dust, the idea is to cast a large number of rays that model photons of a given frequency, and to integrate the optical depth of these photons to infer the probability of absorption and/or scattering of the photons along their journey away from the source which emitted them. For this purpose, RASCAS retrieves from the RAMSES-RT output the properties of the medium through which the photons are propagated, such as the ionisation state, density and velocity of gas. The code also needs to know information about the stellar particles and their continuum emission to propagate LyC photons in a way consistent with what has been done previously in the RHD simulation.

In this chapter, I mainly use the RASCAS code to compute, for each halo, the escape fraction of LyC photons. When it is not mentioned, the escape fraction refers to the number of rays that reach the virial radius of a halo compared to the total number of rays emitted within this halo. For each snapshot, the halos are first identified with the halo finder algorithm described previously. Then, the simulation volume is decomposed by RASCAS into domains that have the positions and sizes of the halos. The gas cells composing each halo are also sent to RASCAS. The code is then used to post-process the emission and the propagation of LyC photons through each domain. Photon packets are cast isotropically from stellar particles with a probability proportional to their LyC luminosity. The photon packets are then propagated following a Monte-Carlo procedure described by Michel-Dansac et al. (2020). We consider that the LyC photons propagate until they are absorbed by neutral hydrogen or helium, which occurs with a probability that depends on the optical depth, that is to say on the cross section of interaction between neutral hydrogen and LyC photons and on the column density of neutral hydrogen along

the line of sight. For this calculation, the effect of dust is neglected, as it has been found to be negligible on the escape fraction of ionising radiation during the EoR by Rosdahl et al. (2018); Mauerhofer et al. (2021).

To recover the escape fraction associated to one halo, the number of LyC photons that reach the boundary of the halo without being absorbed is compared to the total number of LyC photons emitted by all the stellar particles of the halo, derived from the SED used as a function of the age and metallicity of each stellar particle. The global escape fraction at one given snapshot is measured as the intrinsic LyC luminosity-weighted escape fraction averaged among all the stellar particles.

To compare the luminosities of the galaxies formed in the SPHINX simulations to observations, I also use RASCAS to compute the magnitude of each halo at 1500 $\mathring{A}$, otherwise known as the UV luminosity. In this case, the same procedure described to compute the escape fraction of LyC is used, but we now take into account the effect of dust. The UV photons can be absorbed and scattered by dust grains with a probability scaling with the dust albedo $A = 0.38$, following Li & Draine (2001). Dust grains are not directly modelled with RAMSES nor RASCAS. Instead, RASCAS models the dust absorption in each cell depending on its metallicity and on the dust cross-section per atom of hydrogen. The latter is normalised to the extinction curve of the Small Magellanic Cloud following Laursen et al. (2009) and Smith et al. (2019a), as it is more appropriate for low-mass high-redshift galaxies that have young stellar populations. Following this prescription gives us the intrinsic 1500 $\mathring{A}$ luminosity $L_{\mathrm{int},1500}$ and the escape fraction of the corresponding photons, which are the photons that have not been absorbed by dust. The product of these two quantities gives the attenuated UV luminosity L_{1500}, which is eventually converted into the magnitude M_{1500} following the formula derived by Oke & Gunn (1983):

$$M_{AB} = 51.595 - 2.5 \log \left(\frac{L_{1500}}{\mathrm{erg\,s^{-1}\,Hz}} \right) \tag{4.1}$$

4.3 Cosmic ray feedback in cosmological zoom-in halos

This section aims at showing how CR feedback impacts galaxies in a cosmological context, unlike the previous chapter which focuses on idealised disc galaxies. Most specifically, this section relies on two halos targeted in the fiducial SPHINX20 and re-simulated with the zoom-in technique, referred to as Zoom1 and Zoom2 or equivalently Halo 1 and Halo 2 by order of increasing halo mass. Throughout the chapter, the equivalent halos from SPHINX20 are modelled with the "Strong SNe", which corresponds to the calibrated SN feedback boosted by a factor of four that I do not include in my zoom simulations, to better focus on the effect of CRs alone. We summarise in Table 4.1 the differences between the properties of the fiducial halos from SPHINX20 and of the zooms with and without CRs, at $z = 5$. At $z = 5$, Halo 1 has a virial mass $M_{\mathrm{vir}} = 1.5 \times 10^{10}\,\mathrm{M}_{\odot}$ and a virial radius $R_{\mathrm{vir}} = 13\,\mathrm{kpc}$, and for Halo 2 $M_{\mathrm{vir}} = 9 \times 10^{10}\,\mathrm{M}_{\odot}$ and $R_{\mathrm{vir}} = 23\,\mathrm{kpc}$. We remind that for the zoom simulations with CRs, the fraction of SN energy injected into CR energy is $f_{\mathrm{ecr}} = 0.1$ and the diffusion coefficient is $\kappa = 10^{28}\,\mathrm{cm^2\,s^{-1}}$.

Simulation	M_* ($M_\odot$)	MHD	CRs	# / 100 $M_\odot$
SPHINX20 Halo 1	2.6×10^8	✗	✗	4
Zoom1_noCR	1.6×10^9	✓	✗	1
Zoom1_CR	6.2×10^8	✓	✓	1
SPHINX20 Halo 2	4.5×10^9	✗	✗	4
Zoom2_noCR	1.3×10^{10}	✓	✗	1
Zoom2_CR	9.8×10^9	✓	✓	1

Table 4.1: *Properties of the two halos studied in this section, from the* SPHINX*20 simulation and from the zoom simulations without and with CR feedback for each of them. From left to right: simulation name, M_*: stellar mass at $z = 5$, use of an MHD solver (if not, a hydro solver is used instead), inclusion of CR feedback, # / 100* $M_\odot$*: rate of SN explosions per 100* $M_\odot$ *formed.*

4.3.1 Effect of CR feedback on star formation through cosmic time

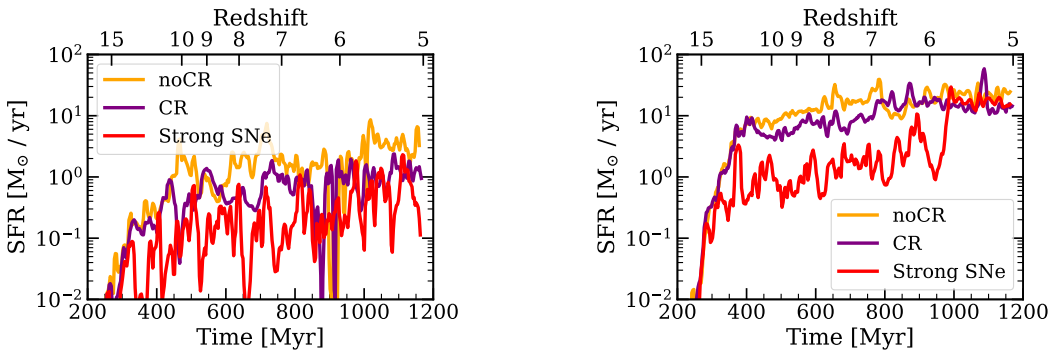

(a) *Halo 1* ***(b)*** *Halo 2*

Figure 4.1: *Time evolution of the SFR averaged over 10 Myr for Halo 1 (4.1a) and Halo 2 (4.1b). We show in red the fiducial halos from the* SPHINX*20 simulation which includes a strong SN feedback (Strong SNe), and in orange and purple the zoom-in halos without and with CRs and without the strong SN feedback (noCR and CR), respectively. At any halo mass, CRs are less efficient than the strong SN feedback but reduce the SFR compared to the noCR runs. The efficiency of CR feedback decreases with halo mass, as it has a stronger effect in Zoom1 than in Zoom2.*

We first show how CR feedback impacts the star formation within our two halos in Figures 4.1 and 4.2. The figures show the time evolution of the SFR in Halo 1 and Halo2 and of the stellar mass formed in Halo 1 and Halo 2, respectively. All along this section, we use red colors for the SPHINX20 simulations, labelled Strong SNe, and orange and purple respectively for the zooms without and with CRs (labelled noCR and CR), and without the boosted SN feedback from SPHINX20. Qualitatively, we observe the same trend for the two halos targeted. The SFR in the noCR runs are the highest at almost all times, as shown in Figures 4.1a and 4.1b. When we add CR feedback, the SFR is reduced, but to a lesser extent than when using a strong

SN feedback. As a consequence, the stellar mass at $z = 5$ is respectively 2.4 and 2.2 times higher with CRs than with the SPHINX calibrated SN feedback (Figures 4.2a and 4.2b), which means that with our choice of CR physics, CR feedback is unable to sufficiently regulate galaxy growth at high redshift in these two halos. Moreover, as we found in the **CosmicShine** paper, CR feedback becomes less efficient at increasing galaxy mass. For Halo 1 and Halo 2, they respectively suppress star formation by a factor of 2.6 and 1.3 compared to the noCR runs. This decreasing efficiency with galaxy mass is also measured with the boosted SN feedback. Beyond $z = 6$ for Halo 2, the SFR in the simulation with the Strong SNe rises and becomes similar to that of the two other runs. This is in agreement with what has been shown by Mitchell et al. (2018), who find that the calibrated SN feedback used in SPHINX becomes progressively inefficient to regulate star formation at lower redshift, when the galaxies and their DM halos are more massive.

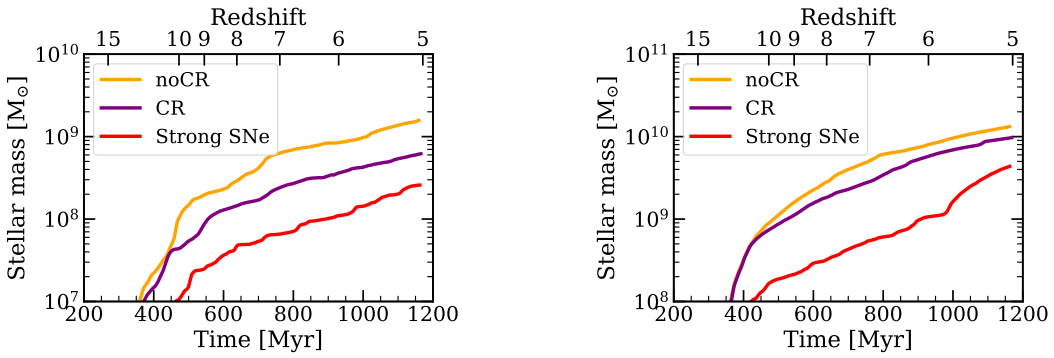

(a) Halo 1 *(b) Halo 2*

Figure 4.2: *Time evolution of the stellar mass formed for Halo 1 (4.2a) and Halo 2 (4.2b). The color-coding is the same as in Fig. 4.1. At any halo mass, CRs are less efficient than the strong SN feedback and the stellar mass at $z = 5$ with CRs is 2.4 and 2.2 times higher than with the Strong SNe model in Halo 1 and Halo 2 respectively. Compared to the noCR case, they lead to a stellar mass reduced by a factor 2.6 and 1.3 for Halo 1 and Halo 2 at $z = 5$. This is completely in step with the results from the idealised galaxies, i.e. CR feedback is increasingly efficient in regulating star formation at decreasing halo mass.*

4.3.2 The impact of CRs on the galactic gas distribution

To qualitatively see how the different sources of feedback impact the gas properties in our two halos, Fig. 4.3 shows maps of their hydrogen column density at $z = 5$, for increasing halo mass from top to bottom, for the fiducial halo from SPHINX20 and the zooms without and with CRs from left to right. We similarly show mass-weighted temperature projections of the halos in Fig. 4.4. The width of the maps corresponds to twice the virial radius of the halos, so that they show the gas distribution within one $R_{\rm vir}$. In the two fiducial halos from SPHINX20, the strong SN model is so explosive that it disrupts the CGM gas, which shows a filamentary structure. The CGM of the two halos is also composed of diffuse regions, and mainly consists in gas hotter than 10^5 K. This strong SN feedback is also efficient at ISM scales to heat the gas in the central galaxies, while there is slightly more cold gas with the weaker standard SN feedback. Conversely, the CGM of the two halos is much colder

with CR feedback, in which there are only traces of gas hotter than 10^5 K. The gas distribution is also much smoother, and we distinguish less cavities of diffuse gas and less filamentary structures than in the runs without CRs.

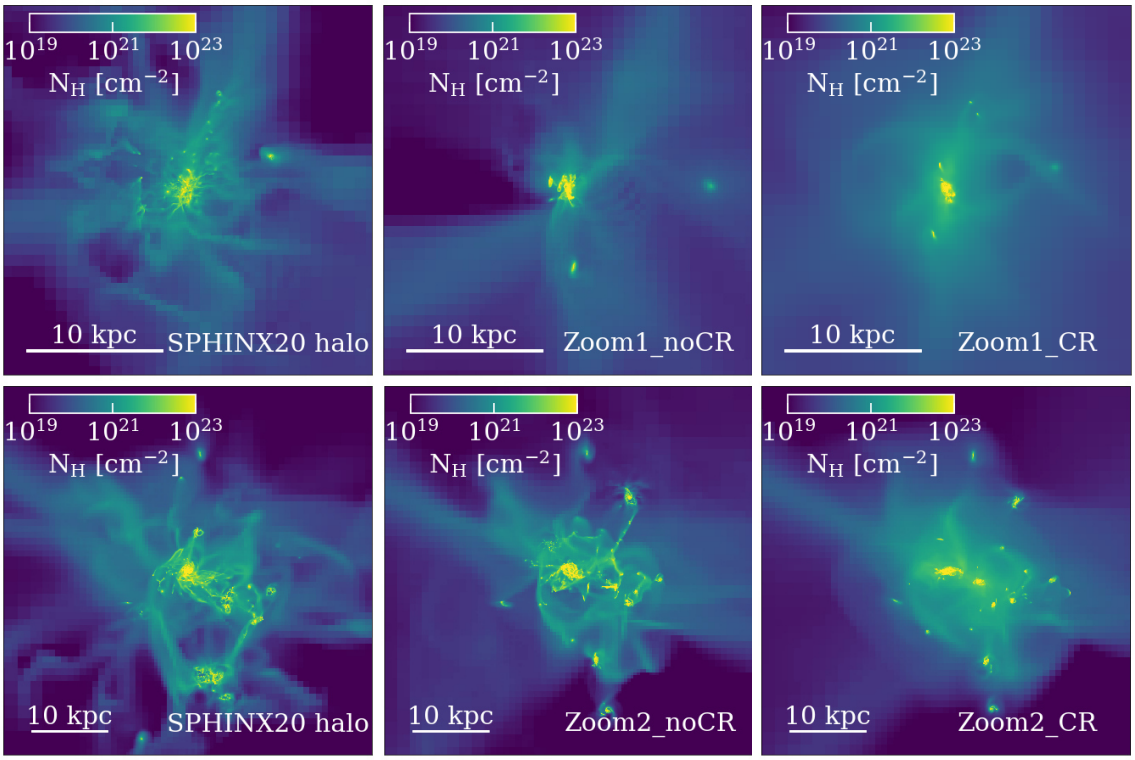

Figure 4.3: *Hydrogen column density maps for Halo 1 (top panels) and Halo 2 (bottom panels) at $z = 5$. From left to right, we show the fiducial halo from* SPHINX*20, and the zoom simulations without and with CRs. CR feedback leads to a smooth gas distribution, while the Strong SNe model from* SPHINX*20 disrupts the galaxies whose CGM is more fragmented.*

Overall, these maps are in qualitative agreement with what we observed in the idealised disc galaxies from the previous chapter. The idealised galaxies have an unrealistic initial CGM that may alter the effect of CR feedback, but these zoom-in cosmological simulations similarly show that CR pressure helps to eject and maintain a relatively dense and cold CGM, smoothing the gas distribution at any halo mass. The distribution of CR pressure is shown in Figures 4.5a and 4.5b for Halo 1 and Halo 2. By comparing these maps with that of the hydrogen column density, we clearly see that CR pressure follows the gas distribution which is pushed out of the central galaxies as CRs propagate out of their ISM. CR pressure reaches lower values in Halo 1 than in Halo 2, due to a lower SFR, which implies less SN explosions and so less CR energy injection. However, because the gravitational potential of Halo 1 is shallower than that of Halo 2, CR pressure reaches more easily the edges of the halo.

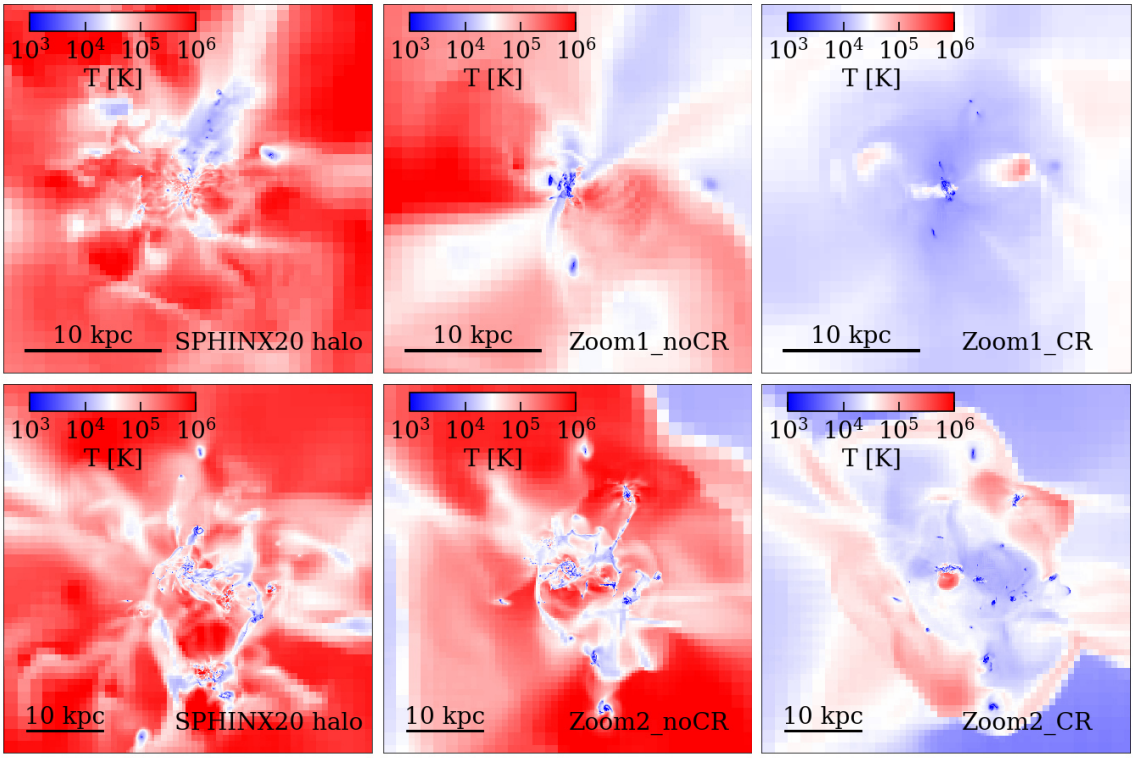

Figure 4.4: *Mass-weighted temperature projections for Halo 1 (top panels) and Halo 2 (bottom panels) at $z = 5$. From left to right, we show the fiducial halo from* SPHINX*20, and the zoom simulations without and with CRs. The CGM of the galaxies is much colder with CR feedback, and conversely almost composed of hot gas with the strong SN model.*

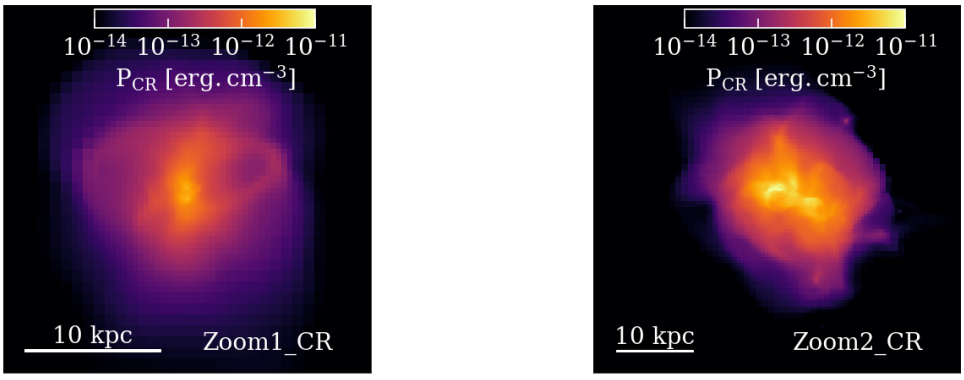

(a) ***(b)***

Figure 4.5: *Projection maps of cosmic ray pressure at $z = 5$ for Zoom1 (4.5a) and Zoom2 (4.5b). The CR pressure reaches larger values in Zoom2 in which the number of SNe that inject CR energy is higher, following the SFR. CR pressure however propagates more easily up to the edges of the halo in Zoom1 which has a shallower gravitational potential than the DM halo from Zoom2.*

4.3.3 Escape of ionising radiation with CR feedback

One of the results from the **CosmicShine** paper that we want to confirm in a cosmological context is that CR feedback prevents the escape of LyC photons, by

providing a denser and smoother gas distribution in which radiation is likely to be absorbed. The escape of ionising photons over time varies depending on how feedback enables or prevents radiation to escape, and is especially sensitive to SN explosions (Ma et al., 2015; Trebitsch et al., 2017; Rosdahl et al., 2018). During an episode of star formation, LyC photons are emitted by the youngest stars. Progressively, stars explode as SNe, and the explosions locally disrupt the ISM and clear the way for flashes of LyC radiation to escape. Along their journey to the IGM, the LyC photons have a probability to be absorbed by the neutral gas, either in the galaxy or in its CGM. This probability scales with the neutral hydrogen optical depth, which itself depends on the column density of neutral hydrogen. Therefore, because CR pressure helps to push dense gas out of the ISM, it fills the low-density bubbles of gas originating from the SN explosions with neutral hydrogen, ready to absorb LyC radiation. In addition, the energy released by the SN explosions temporarily prevents the formation of stars. As long as there are no new stars, the production of LyC photons practically stops, on a scale of a few Myrs. For these reasons, the escape fraction of radiation has been found to roughly follow the burstiness of the SFR, but with a lag of a few Myrs corresponding to the time it takes for the most massive stars to start exploding as SNe, and thus to be highly regulated by feedback (Trebitsch et al., 2017).

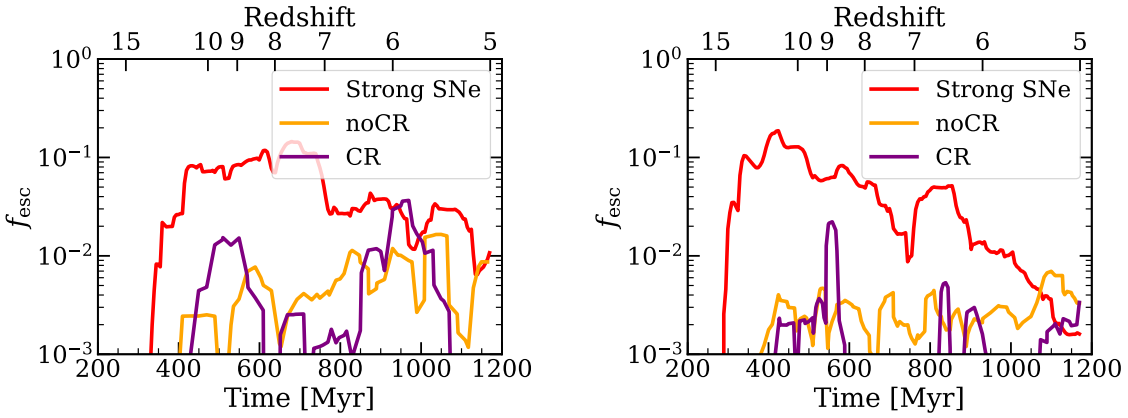

(a) Halo 1 *(b) Halo 2*

Figure 4.6: *Time evolution of the escape fraction of LyC photons, averaged over 100 Myr. We show the results for the fiducial halos from* SPHINX*20 in red, and from the zooms without and with CRs in orange and purple, for Halo 1 (4.6a) and Halo 2 (4.6b). For the two halos, CR feedback leads overall to lower escape fraction of LyC photons than in the noCR runs.*

To check how the propagation of the LyC photons through the ISM and CGM is impacted by CR feedback in our two targeted halos, Figures 4.6a and 4.6b show the escape fraction of LyC photons as a function of time for Halo 1 and Halo 2, respectively. The escape fractions are derived at the virial radius of the halos, using the RASCAS code and following the methodology described in **Section 4.2.2**. As we explained, the escape fraction of radiation is quite bursty (following the SFR), so we show the $f_{\rm esc}$ averaged over 100 Myr for clarity. For the two halos, the strong SN model leads to much higher escape fractions than with the non boosted SN feedback, that are further reduced with CR feedback. We also note that the escape fractions

are globally lower for the more massive halo. These two results are the consequence of SN feedback being less efficient to disrupt the ISM and let radiation escape at increasing galaxy mass. CR feedback helps to eject dense gas and smooths the inner gas distribution close to the SN explosion sites, which reduces the central densities. However, this does not boost the escape fractions like the strong SN feedback, but conversely leads to overall lower $f_{\rm esc}$.

To better compare the results from the three setups, we measure the luminosity-weighted escape fractions $\langle f_{\rm esc}\rangle_{\rm lw}$, averaged between $z = 15$ and $z = 5$. For Halo 1, the values with a strong SNe, without CRs and with CRs are respectively $\langle f_{\rm esc}\rangle_{\rm lw} =$ 0.027, 0.004 and 0.004. In the same order for Halo 2, $\langle f_{\rm esc}\rangle_{\rm lw} = 0.008$, 0.003 and 0.002. There is almost a factor 7 lower escape fractions with the weak standard SN feedback than with their boosted calibrated one, which is a difference 1.5 times larger than what Rosdahl et al. (2018) measured globally in a SPHINX5 simulation (in which halos are less massive). In the halos with and without CRs, $\langle f_{\rm esc}\rangle_{\rm lw}$ are almost the same. While CRs act on the ISM, they do not lead to higher escape fractions unlike what stellar feedback is expected to do. This shows that CR feedback does not help radiation to escape, if not prevent it. As CR feedback is expected to be increasingly efficient with decreasing galaxy mass, it would be interesting to repeat the same analysis for less massive galaxies. In all cases, the escape fractions measured in these two massive halos are extremely low compared to what is expected from models of reionisation by the most massive high-redshift galaxies. For instance, Naidu et al. (2020) measure 50% escape fraction of LyC for $z = 2$ massive Lyman alpha emitters. However, galaxies with such high escape fractions are rare (e.g. Izotov et al., 2016), and the majority of observations measure escape fractions lower than $\sim 5\%$ (Siana et al., 2010; Rutkowski et al., 2017; Grazian et al., 2017), which is more comparable to what we measure in our two halos.

To determine the contribution of a galaxy to the reionisation process, it is not only needed to know what fraction of ionising radiation escape but also what is the luminosity emitted. The product of these two quantities gives the escaping LyC luminosity $\mathcal{L}_{\rm esc}$, which is shown as a function of time in Figures 4.7a and 4.7b for Halo 1 and Halo 2 respectively. Because the strong SN model leads the highest escape fractions, it also produces the largest $\mathcal{L}_{\rm esc}$ for the two halos of our sample. We note that the difference in escaping LyC luminosity between boosted and unboosted SN feedback is less than that of the escape fraction, because the SFR and hence the LyC luminosity with the Strong SNe model is up to one order of magnitude lower than in the noCR runs, which mitigates the increase of $\mathcal{L}_{\rm esc}$. Similarly, the zooms with CR feedback have lower LyC luminosity than the noCR runs, which, added to low escape fractions, produces the lowest $\mathcal{L}_{\rm esc}$. All in all, Fig. 4.7 hints that CR feedback may lead to escaping LyC luminosity too low to let reionisation happens, if we consider the Strong SNe model as the reference to be compared with. This prediction however holds for two specific halos, rather massive and isolated, while reionisation is a global process which may be fed by lower mass halos. In the next section, we compare the reionisation history with and without CRs in SPHINX5 simulations in which hundreds of star-forming galaxies are resolved, and from which we predict the escape of LyC radiation.

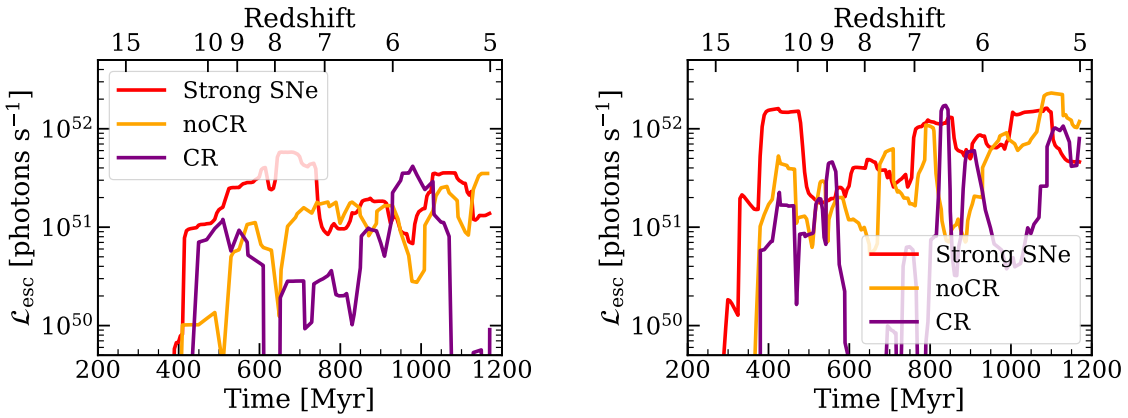

(a) Halo 1 *(b) Halo 2*

Figure 4.7: *Escaping LyC luminosity as a function of time for Halo 1 (4.7a) and Halo 2 (4.7b), averaged over 100 Myr. Red, orange and purple colors correspond to runs with the strong SN model, without CRs and with CRs respectively. For the two halos, the Strong SNe produce higher escaping luminosity than the non boosted SN feedback. With CRs, the escaping ionising luminosity is the lowest, mostly as a consequence of reduced SFR compared to the noCR zooms.*

4.4 Impact of cosmic ray feedback on the reionisation of the Universe

We now want to determine how and to what extent CR feedback impacts the reionisation of the Universe. For this purpose, I performed RMHD simulations of SPHINX5 volumes, one with the calibrated strong SN feedback which has been shown to produce a realistic reionisation history (Rosdahl et al., 2018), and another one which includes CR feedback. This CR-RMHD cosmological simulation is the first of its kind, as previous studies of CR feedback in a cosmological context rely on small samples of zoom-in galaxies only. As we explained previously, the contribution of a galaxy to the reionisation process depends both on its intrinsic LyC luminosity and on the escape of these LyC photons. In order to better appreciate the effect of CRs on the reionisation of the IGM, we have to ensure that the intrinsic LyC luminosity is the same in the two simulations, which means that they globally need to regulate star formation similarly. From the study of the idealised galaxy in **Chapter 3**, we know that considering 40% injection of CR energy by SNe can efficiently reduce star formation, and that combining a strong SN feedback with CRs strongly suppresses star formation in the G8, G9 and G10 galaxies. For the SPHINX5 simulation which includes CRs, I choose an intermediate calibration of SN and CR feedback. The number of SN explosions per $100\,M_\odot$ of stars formed is set to 2, which reduces the tension with the expectations from a Kroupa IMF by a factor of two compared to the fiducial SPHINX5 without CRs which has $4\,\mathrm{SN}/100\,M_\odot$. In addition, the fraction of SN energy which goes into CRs is set to $f_{\mathrm{ecr}} = 0.2$, which is above the canonical $f_{\mathrm{ecr}} = 0.1$ but still on the realm of acceptable values (Kang & Jones, 2006; Ellison et al., 2010; Helder et al., 2013). By analogy with the label Strong SNe for the fiducial SPHINX5 simulation, we refer to this calibrated CR feedback as Strong CRs.

Throughout this chapter, the results for these two runs are shown in red and light purple respectively for the Strong SNe and the Strong CRs models.

We first show the mass-distribution of halos in the two simulations at $z = 5$ in Fig. 4.8, which illustrates the number of star forming halos per bin of virial mass. Following Rosdahl et al. (2018), we ignore sub-halos and consider only the halos more massive than 300 DM particles, that is to say halos sufficiently resolved and with $M_{\rm vir} \geq 7 \times 10^7\,{\rm M}_\odot$. The two simulations roughly have the same number of halos, which is 791 for the Strong SNe run and 802 for the Strong CRs one. This is perfectly expected, since the baryonic processes included are not expected to have significant effects on DM halo masses. The virial mass of their most massive halo is $\simeq 2.5 \times 10^{10}\,{\rm M}_\odot$ at $z = 5$. We note that the simulation with CRs has one halo with $M_{\rm vir} = 10^{10}\,{\rm M}_\odot$ which does not appear in the histogram of the simulation without CRs. In the latter, the equivalent halo is flagged as a sub-halo by the halo finder algorithm, which is a numerical limitation of our definition of halos based on the distribution of DM overdensities[3].

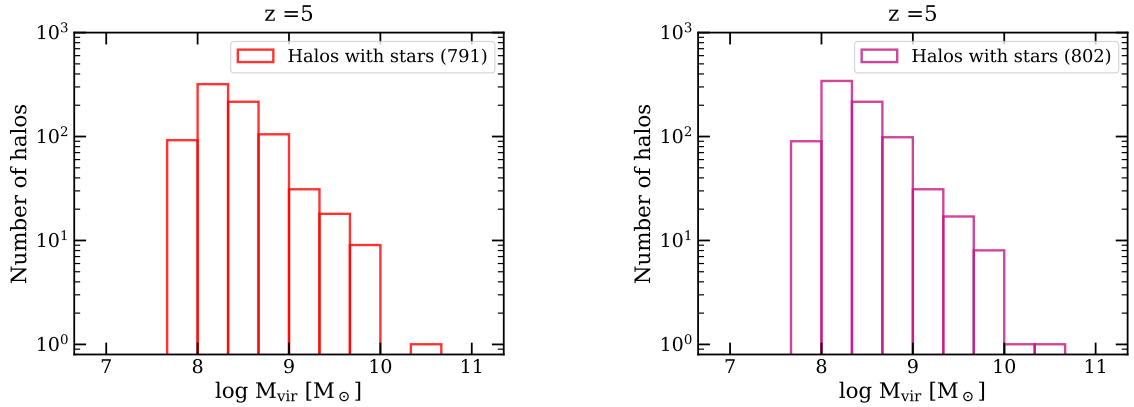

(a) Strong SNe *(b) Strong CRs*

Figure 4.8: *Number of halos at $z = 5$ binned by virial mass for the* SPHINX*5 simulations with the Strong SNe (4.8a) and the Strong CRs (4.8b) models. We select only halos that have more than 300 DM particles and in which stars form. There are 791 halos with the Strong SNe model and 802 with the Strong CRs. For the latter, there is one halo with $M_{\rm vir} \simeq 10^{10}\,{\rm M}_\odot$ which does not appear in the SN calibrated simulation, in which the equivalent halo is considered as a sub-halo by the halo finder algorithm.*

4.4.1 Regulation of star formation and UV luminosity

In order to illustrate how star formation is regulated in our two simulations, Fig. 4.9 shows the stellar mass to halo mass relation at $z = 5$, which corresponds to the averaged stellar mass enclosed in halos from a virial mass bin. We additionally show the 1σ standard deviation with shaded area, which is larger at lower halo mass due to an increasing number of objects with different stellar masses. At any halo mass, the average stellar masses in the two simulations are very similar, and stellar masses with the Strong CRs model are slightly lower for halos with $M_{\rm vir} \lesssim 10^9\,{\rm M}_\odot$

[3]In a future study, I will check the variability of the results presented in the following when changing the definition of main halo, by including subhalos that do not belong to the virial radius of any host halo.

than without CRs. At $z = 5$, the total stellar mass formed in the SPHINX5 runs is $2.2 \times 10^9\,M_\odot$ without CRs and $2 \times 10^9\,M_\odot$ with CRs, so they differ by less than 10%. Our calibrated CR feedback is slightly more efficient to regulate star formation in low mass galaxies than the boosted SN feedback, although the total energy released by the SN explosions is much higher with the Strong SNe model. While the Strong SNe model injects a thermal energy of 4×10^{51} erg each $100\,M_\odot$ of stars formed, the Strong CRs model injects a thermal energy of 1.6×10^{51} erg and a CR energy of 4×10^{50} erg. Therefore, Fig. 4.9 shows that CR feedback can have a similar effect on star formation as artificially boosting the SN feedback, and that CRs may have a significant role in regulating galaxy growth during the EoR. To better assess the strength of our two feedback models, Fig. 4.9 also shows observational estimates of the SMHM relation for local dwarf galaxies from Read et al. (2017) with black triangles, and observational constraints at $z = 5$ and $z = 5.6$ from Behroozi et al. (2019) and Stefanon et al. (2021) with dark and light shaded regions respectively. Although the SMHM relations are similar for our two simulations, their extrapolation is slightly above the observational constraints at $z \simeq 5$ from Behroozi et al. (2019) and Stefanon et al. (2021). Even if the SMHM relations from our simulations have roughly the same slope as observational estimates, this may show that our feedback models remain too weak to sufficiently regulate star formation at high redshift. This is however mitigated by uncertainties when inferring the observed SMHM, especially at high redshift. Compared to the local observations of low-mass galaxies from Read et al. (2017), the SMHM relations from our simulations are in broad agreement for intermediate mass halos, and above the observational estimates for halo masses around $10^{10}\,M_\odot$.

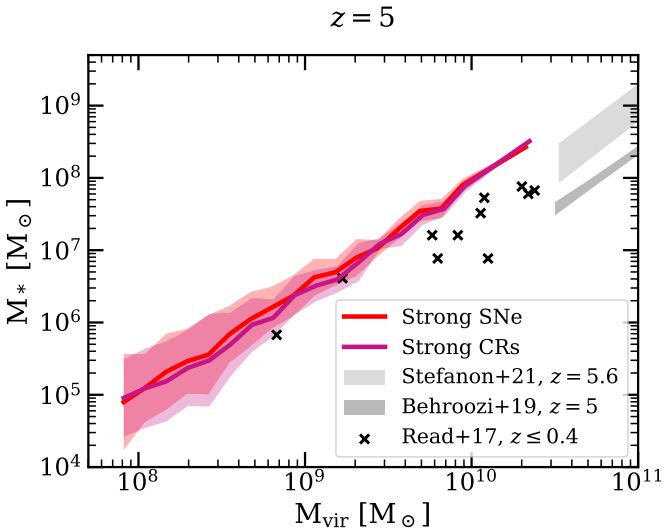

Figure 4.9: *Stellar mass to halo mass relation in the* SPHINX5 *simulations with and without CRs (in purple and red) at $z = 5$. The curves show the averaged stellar mass per bin of halo virial mass, and the colored shaded regions represent the standard deviation. We also show observational constraints from Read et al. (2017) at $0.2 \leq z \leq 0.4$ with black crosses, from Behroozi et al. (2019) at $z = 5$ with a dark grey shaded area and from Stefanon et al. (2021) at $z = 5.6$ with a light grey shaded region. At any halo mass, the stellar mass is roughly the same in the two simulations, but tends to be higher than the observational constraints.*

Another way to estimate the efficiency of feedback in regulating star formation is to look at the galaxy UV luminosity function, shown in Fig. 4.10 at redshift between 5 and 10 from the upper left to the bottom right panels. Unlike stellar mass which has to be inferred from SED model fitting[4], UV luminosity is a direct observable, which traces light emission from young and massive stars. Therefore, the UV luminosity of a galaxy correlates with its stellar mass content, and is a useful tool to probe the effect of feedback. To derive the UV luminosity of my simulated galaxies, I use the RASCAS code and the procedure explained at the end of **Section 4.2.2**. The resulting UV magnitude M_{1500}, which takes into account dust absorption, is obtained following Equation 4.1. The UV luminosity function thereby depicts the number of galaxies in a given bin of M_{1500}, normalised by the simulation volume and by the size of the observed sample of galaxies for simulation and observation data respectively. The observed UV luminosity functions shown at different redshifts are taken from Finkelstein et al. (2015); Bouwens et al. (2015, 2017); Livermore et al. (2017); Atek et al. (2018); Ishigaki et al. (2018); Oesch et al. (2018). Observations are limited by the sensitivity of the instruments, and can hardly probe the low-luminosity end of the UV luminosity function. High-redshift observations also rely on lensing magnification, and are generally all from the same 5 or 6 lensed fields. Conversely, the volume of our SPHINX5 simulations is too small to contain massive and bright galaxies, and we do not measure magnitude brighter than -18. Overall, the two SPHINX5 simulations with and without CRs have similar UV luminosity functions at any time, and are in good agreement with the observations. At $z = 8$ and $z = 10$, there are more bright galaxies in the simulation with CRs than without. This is not an effect of dust extinction (which reduces the luminosity of bright galaxies at $z \lesssim 7$, but it is not shown here) but rather shows that CR feedback is slightly less efficient to reduce star formation than the Strong SNe model at early times. This may also simply be a stochastic effect, as the luminous end of the curve typically contains very few galaxies or even one. In any case, the agreement between observations and the two SPHINX5 simulations indicates a realistic emission of UV radiation in our simulated galaxies. This result, combined with the previous one from Fig. 4.9, shows that our model of CR feedback produces galaxies whose stellar mass and UV luminosity reasonably matches observational estimates.

[4]Observed stellar masses are derived from SED model fitting, which associates a stellar mass to galaxies emitting a specific luminosity. For simulated galaxies, this is the opposite: the stellar mass is known, and the luminosity has to be reconstructed from a SED model.

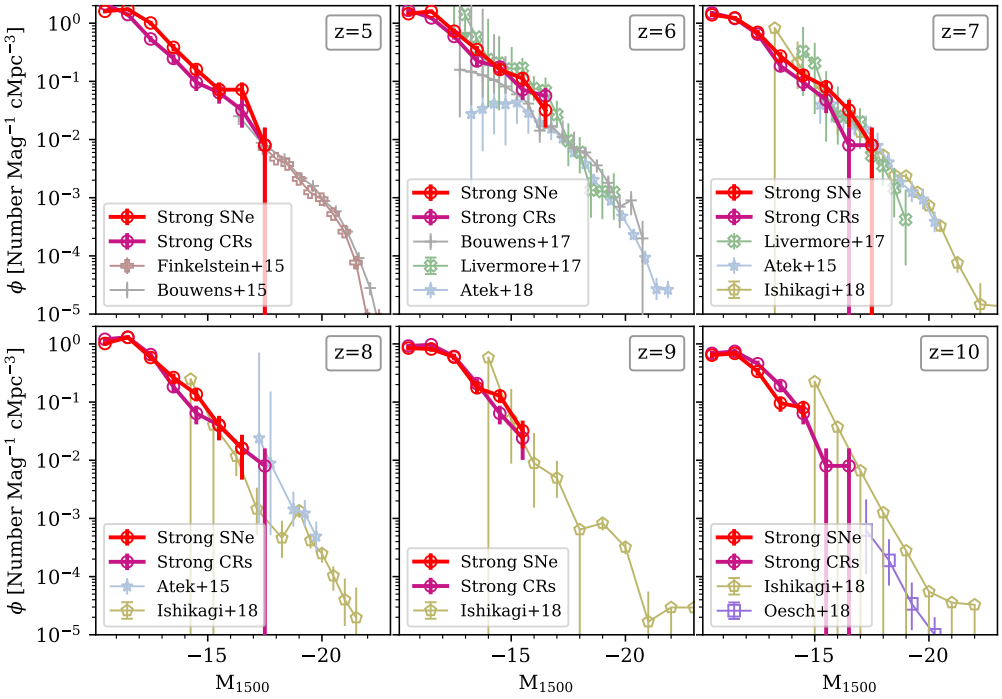

Figure 4.10: *UV luminosity function in the* SPHINX*5 simulations with and without CRs (in purple and red), with Poissonian error-bars. From the top left to the bottom right panel, we show increasing redshift from 5 to 10. The references of the observations shown in each panel are written in the legend. At any time, the UV luminosity functions with and without CRs are very similar and in good agreement with the observational constraints.*

4.4.2 Global impact of CR feedback on the reionisation

Now that we established that our two SPHINX5 simulations similarly regulate star formation and therefore the intrinsic production of LyC photons, we want to determine how CRs impact LyC escape fractions and the reionisation of the Universe. Fig. 4.11 shows the volume-weighted fraction of neutral gas in the whole simulation volume as a function of time, comparing the Strong SNe (in red) and the Strong CRs (in purple) feedback to black data points corresponding to observational estimates from Fan et al. (2006); Schroeder et al. (2013); McGreer et al. (2015); Ouchi et al. (2018); Inoue et al. (2018); Bañados et al. (2018); Davies et al. (2019); Mason et al. (2018, 2019); Greig & Mesinger (2017); Greig et al. (2019). As found previously by Rosdahl et al. (2018) with a similar SED, the SPHINX simulation with the boosted SN feedback is in good agreement with the observational estimates, i.e. it produces a realistic reionisation history. After $z = 6$, the fraction of neutral hydrogen is extremely low ($Q_{\rm HII} \simeq 10^{-4}$ at $z = 5$) and the whole simulation volume can be considered as ionised. However, the picture becomes completely different with CR feedback. From between $z = 10$ and $z = 9$ and beyond, the fraction of neutral gas in the simulation with the Strong CRs model starts to diverge with that of the fiducial SPHINX run and remains much higher at any time. As a consequence, the reionisation history in our simulation with CRs is delayed, and the neutral gas fraction is well above the observational estimates, especially between $z = 6$ and $z = 5$. At $z = 5$, almost half of the simulation volume is still not ionised. This is in strong

disagreement with our actual models of reionisation, and even with late-reionisation models (e.g. Keating et al., 2020; Nasir & D'Aloisio, 2020). Nonetheless, the delayed reionisation with CRs conforms with what I suspected based on my previous studies of CR feedback in idealised and zoom simulations, where CR feedback hampers the escape of ionising photons. Therefore, the impact of CRs on the reionisation of the Universe is predominantly determined by the way CR feedback affects the escape fraction of LyC photons.

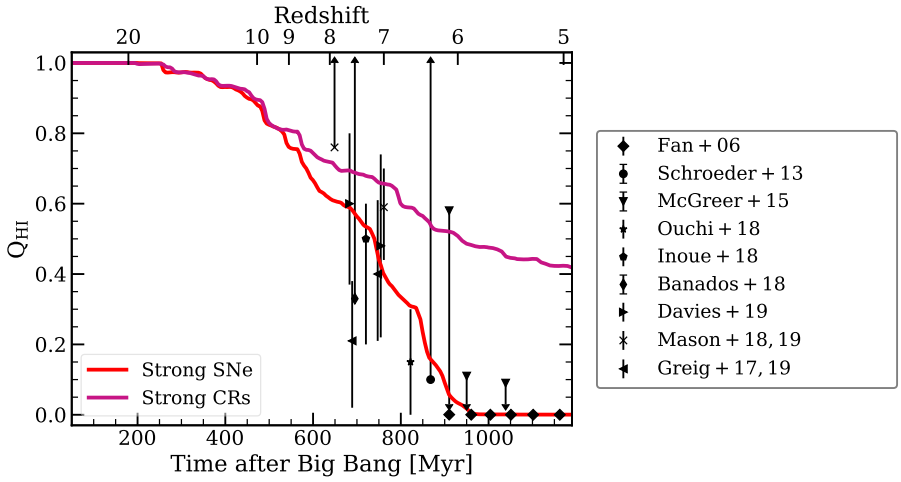

Figure 4.11: *Time evolution of the volume-filling fraction of neutral gas with (in purple) and without (in red) CRs. We additionally show with black data points observational estimates from studies indicated in the legend. The reionisation history is drastically delayed with CRs, and the simulation volume is still composed of 42% of neutral hydrogen at $z = 5$. With the Strong SNe model, the simulation volume is largely ionised by $z = 5$, which is in much better agreement with the observational estimates.*

We illustrate the previous statement in Fig. 4.12a, which shows how the global luminosity-weighted escape fraction of LyC photons averaged over 100 Myr evolves with time in the two simulations. At any time, and especially after $z \simeq 9$, the escape fractions of LyC photons are lower with CRs than with the strong SN feedback. The values between differ by up to a factor of five with a difference which tends to increase with time. The decrease of escape fraction with time is steeper in the simulation with CR feedback, which eventually slows down the reionisation process. In Fig. 4.12b, we show the volumic LyC luminosity emitted (in thin dashed lines) and the escaping LyC luminosity per volume $\mathcal{L}_{\mathrm{LyC,\ esc}}$ (in thick solid lines) as a function of time, also averaged over 100 Myr. This demonstrates that while the number of LyC photons intrinsically emitted is roughly the same in the two simulations, the amount of LyC photons effectively ionising the IGM is lower with CR feedback, due to the reduced escape fractions.

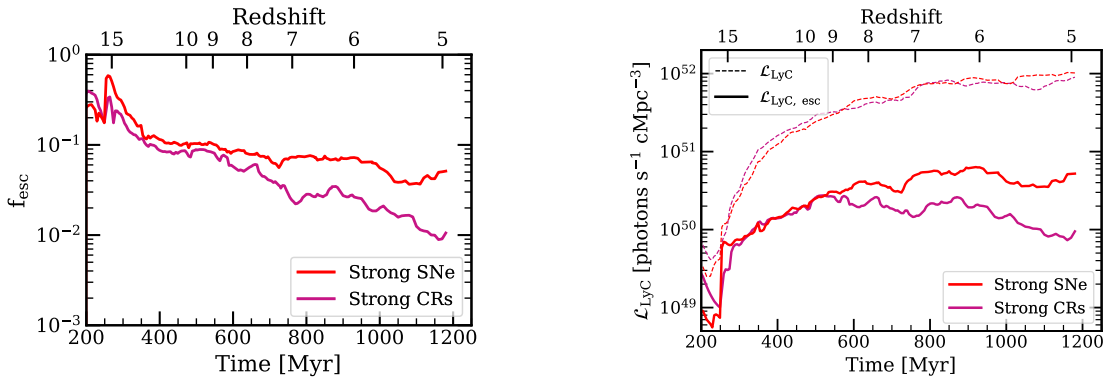

(a) *(b)*

Figure 4.12: *4.12a: Evolution with time of the global luminosity-weighted escape fraction of LyC photons f_{esc} with (purple) and without (red) CRs. 4.12b: Time evolution of the intrinsic LyC luminosity per volume $\mathcal{L}_{LyC,}$ (thin dashed lines) and of the escaping LyC luminosity per volume $\mathcal{L}_{LyC,\ esc}$ (thick solid lines), defined as the product of $\mathcal{L}_{LyC,}$ with f_{esc}. The f_{esc}, $\mathcal{L}_{LyC,}$ and $\mathcal{L}_{LyC,\ esc}$ are luminosity-weighted mean properties over the last 100 Myr, to smooth their bursty fluctuations with time. With CRs, the escape fraction of ionising radiation is reduced. As a consequence, even if the intrinsic LyC luminosities with the Strong SNe model and with CRs are similar, the escaping LyC luminosity is reduced by a factor of between two and five with CRs after $z \simeq 8$.*

4.4.3 Effect of CR feedback on the escape of LyC photons with halo mass

While CR feedback globally lowers the escape fraction of ionising radiation, it remains to be determined if they have this effect at any halo mass, or for a specific category of galaxies whose escaping LyC luminosity dominates the reionisation budget. In Fig. 4.13, we show the intrinsic LyC luminosity per volume as a function of virial mass, in 6 bins between $\log(M_{vir}) = 7.5$ and 10.5. To increase the statistics and smooth any transient effects, we stack data from approximately 60 snapshots between $z = 15$ and $z = 7$ in Fig. 4.13a and from 100 snapshots between $z = 7$ and $z = 5$ in Fig. 4.13b. We summarise the number of halos, the total intrinsic LyC luminosity per volume and the mean luminosity-weighted escape fraction in each bin for each simulation in Table 4.2 and Table 4.3, for data stacked between $z = 15$ and $z = 7$ and between $z = 7$ and $z = 5$ respectively. On average, Fig. 4.13 shows that the intrinsic luminosity emitted by the halos at different masses is similar in the simulations with and without CRs. This goes in line with Figures 4.9 and 4.10 previously described, where we showed that our two simulations are calibrated to produce similar star formation rate and UV luminosity, and we confirm here that this holds for different halo masses. We can however note a small difference between the two runs. The intrinsic LyC luminosity with CR feedback is slightly lower than with the strong SN model for $8.5 \leq \log(M_{vir}) \leq 9$.

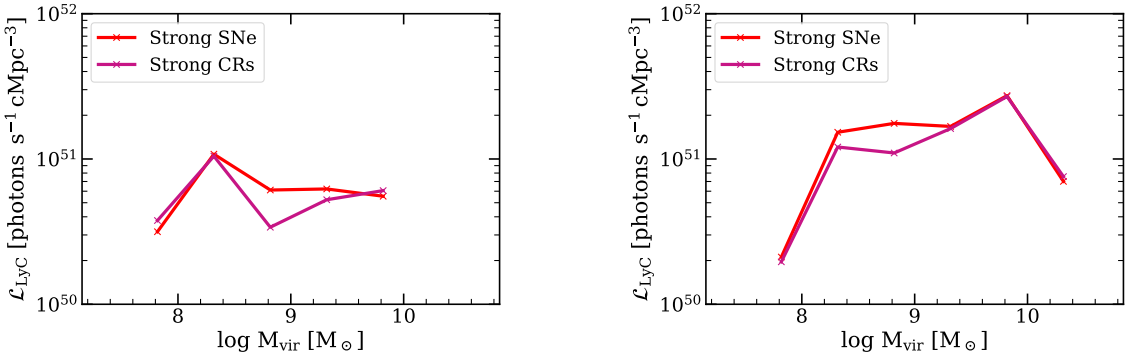

(a) *(b)*

Figure 4.13: *LyC luminosity per bin of virial mass in simulation with (purple) and without (red) CRs, for data stacked between $z = 15$ and $z = 7$ (4.13a) and between $z = 7$ and $z = 5$ (4.13b). Globally, the intrinsic LyC luminosity is roughly the same with and without CRs at any halo mass.*

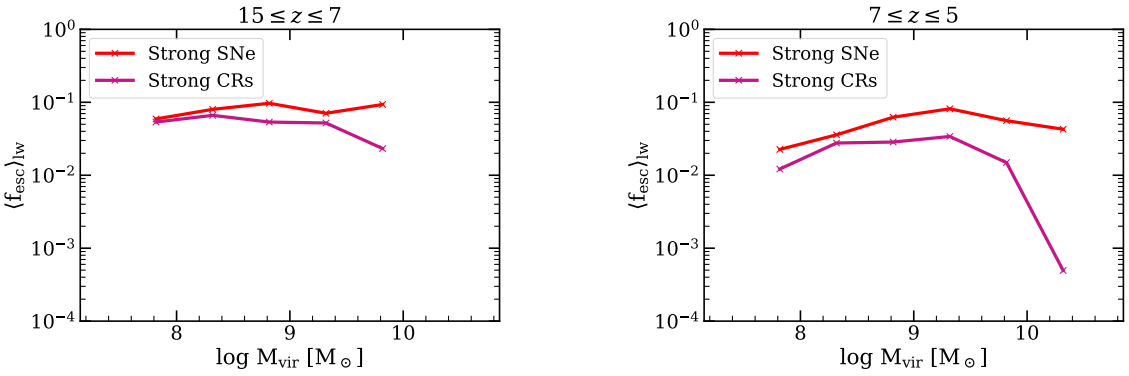

(a) *(b)*

Figure 4.14: *Luminosity-weighted escape fraction per bin of virial mass in simulation with (purple) and without (red) CRs, for data stacked between $z = 15$ and $z = 7$ (4.13a) and between $z = 7$ and $z = 5$ (4.13b). On average, the escape fractions are always smaller with CRs, especially for the most massive halos.*

Again, the difference of reionisation history in our two simulations must be explained by radiation escaping differently depending on the feedback. In Figures 4.14a and 4.14b, we show the luminosity-weighted mean escape fraction as a function of virial mass (with the same binning as previously) for data stacked between $z = 15$ and $z = 7$ and $z = 7$ and $z = 5$, respectively. For both $15 \leq z \leq 7$ and $7 \leq z \leq 5$, $f_{\rm esc}$ does not vary much with mass with the Strong SNe model, while it decreases with halo mass with CR feedback, especially at $7 \leq z \leq 5$. We should note that the very last bin at $\log(M_{\rm vir}) \geq 10$ may not be representative of the effect of CR feedback on "massive" halos, as we are focusing on the same halo between $z = 5.3$ and $z = 5$ only. At earlier times, this halo is counted in the previous mass bin(s), where the reduction of $f_{\rm esc}$ with CR feedback is not as dramatic. Excluding this most massive bin, CR feedback reduces the escape fraction of LyC photons compared to the Strong SNe by a factor of between 0.8 and 1.9 at $15 \leq z \leq 7$, and of between 1.3 and 3.5 at $7 \leq z \leq 5$. Interestingly, I find that CR feedback is increas-

ingly efficient to reduce star formation at decreasing galaxy mass, but conversely reduces more significantly the fraction of escaping photons in massive galaxies, as also measured in **Section 4.3**. This behaviour can be explained as follows. When feedback is efficient enough to disrupt the ISM and prevent star formation, it also provides the condition for radiation to easily escape from the galaxy. This is especially what SN and CR feedback do in low mass galaxies. In more massive galaxies, CR feedback becomes progressively inefficient to suppress star formation, but the CR pressure gradient which builds up still acts on the ISM gas. In particular, the time needed for CRs to diffuse out of the ISM increases with galaxy mass, during which CR feedback somehow reduces the benefit of SN explosions in clearing the way for radiation to escape, which increasingly impedes the escape of LyC photons.

	Property	$\log(M_{\rm vir})$					
		7.5 - 8	8 - 8.5	8.5 - 9	9 - 9.5	9.5 - 10	10 - 10.5
S. SNe	Number	7711	15415	3030	553	120	0
	$\mathcal{L}_{\rm LyC}$	3.2×10^{50}	1.1×10^{51}	6.1×10^{50}	6.2×10^{50}	5.5×10^{50}	
	$\langle f_{\rm esc} \rangle_{\rm lw}$	0.059	0.080	0.097	0.071	0.093	
S. CRs	Number	7248	14472	2712	543	113	0
	$\mathcal{L}_{\rm LyC}$	3.8×10^{50}	1.0×10^{51}	3.4×10^{50}	5.2×10^{50}	6.1×10^{50}	
	$\langle f_{\rm esc} \rangle_{\rm lw}$	0.054	0.066	0.054	0.052	0.023	

Table 4.2: *Summary of the stacked number of halos, total intrinsic LyC luminosity $\mathcal{L}_{\rm LyC}$ per volume and mean escape fraction $\langle f_{\rm esc} \rangle$ (from top to bottom) per bin of the log of the virial mass $\log(M_{\rm vir})$, with increasing mass from left to right and with data stacked from $z = 15$ to $z = 7$. The three first rows of results correspond to the simulation with the Strong SNe model (written S. SNe for short) and the next three lines show the equivalent results in the simulation with the Strong CRs feedback (written S. CRs for short).*

	Property	$\log(M_{\rm vir})$					
		7.5 - 8	8 - 8.5	8.5 - 9	9 - 9.5	9.5 - 10	10 - 10.5
S. SNe	Number	6091	23080	7288	1645	608	32
	$\mathcal{L}_{\rm LyC}$	2.1×10^{50}	1.5×10^{51}	1.8×10^{51}	1.7×10^{51}	2.7×10^{51}	7.0×10^{50}
	$\langle f_{\rm esc} \rangle_{\rm lw}$	0.023	0.036	0.062	0.081	0.056	0.043
S. CRs	Number	6949	25953	7828	1840	659	31
	$\mathcal{L}_{\rm LyC}$	1.9×10^{50}	1.2×10^{51}	1.1×10^{51}	1.7×10^{51}	2.7×10^{51}	7.6×10^{50}
	$\langle f_{\rm esc} \rangle_{\rm lw}$	0.012	0.028	0.029	0.034	0.015	0.0005

Table 4.3: *Same as Table 4.2 for data stacked between $z = 7$ and $z = 5$.*

To determine which halos have the dominant contribution to the reionisation process across time, Fig. 4.15a shows the total escaping LyC luminosity $\mathcal{L}_{\rm LyC,\ esc}$ between $z = 15$ and $z = 5$, in the same bins of halo mass as for the previous plots. This allows to assess the mass regimes that provide the bulk of escaping LyC photons. With the Strong SNe feedback, halos for which $8 \leq \log(M_{\rm vir}) \leq 10$ provide the highest and fairly unvarying total $\mathcal{L}_{\rm LyC,\ esc}$. Halos less massive than $10^8\,{\rm M}_\odot$, as well as the most massive halo, have 7 times lower total $\mathcal{L}_{\rm LyC,\ esc}$. With CR feedback, the bulk of LyC photons is also provided by halos with $8 \leq \log(M_{\rm vir}) \leq 10$, but with a most important contribution from the halo mass between 10^8 and $10^{8.5}\,{\rm M}_\odot$.

Regardless of CR feedback, the two lowest mass bins have a similar $\mathcal{L}_{\mathrm{LyC,\ esc}}$, just as they have similar f_{esc}. However, halos more massive than $10^{8.5}\,\mathrm{M}_{\odot}$ have escaping LyC luminosity between 3.2 and 70 lower with CR feedback than without. To determine more precisely the range of masses that contribute the most to the reionisation of the IGM, Fig. 4.15b shows as a function of virial mass the cumulative escaping LyC luminosity between $z = 15$ and $z = 5$ normalised by the total intrinsic LyC luminosity emitted during this redshift. We enclose in shaded area the lower and upper mass limits for which halos contribute respectively to 25% and 75% of the reionisation budget during $z = 15$ and $z = 5$. These limits are slightly shifted towards the lower masses with CR feedback, as a result of decreasing escape fraction and total $\mathcal{L}_{\mathrm{LyC,\ esc}}$ with halo mass. With the Strong SNe feedback, halos dominating the reionisation process have $8.4 \leq \log(M_{\mathrm{vir}}) \leq 9.5$, which changes to halos with $8.2 \leq \log(M_{\mathrm{vir}}) \leq 9.3$ with CRs. These intervals of masses correspond to 26 and 46% of the whole sample of halos between $z = 15$ and $z = 5$ for the simulations without and with CRs, respectively. However, we have to note that in the small SPHINX5 volumes, the sample of galaxies is biased and restricted to low mass objects, and that we do no resolve halo with masses below $7.5 \times 10^{7}\,\mathrm{M}_{\odot}$. To overcome this issue and study the robustness of my results, I started to perform equivalent SPHINX10 simulations. These new simulations, 8 times larger in volume, will be the basis for a paper presenting those results, with much better statistics and a wider halo mass range.

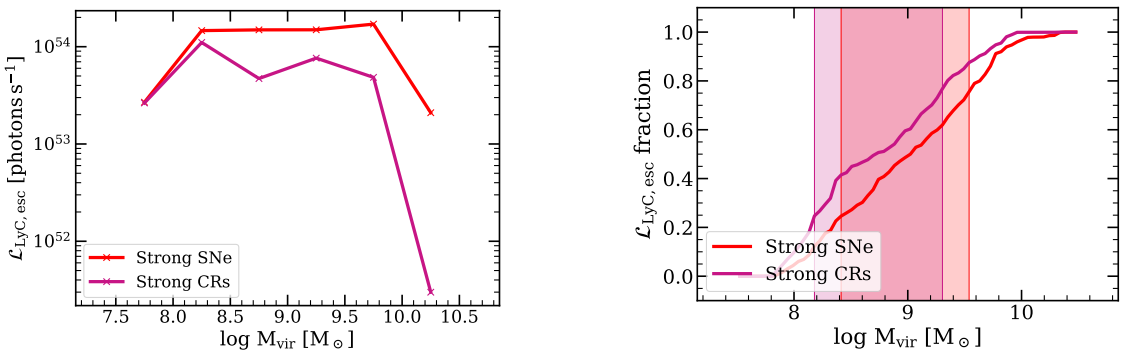

(a) *(b)*

Figure 4.15: *Total escaping LyC luminosity (4.15a) and cumulative fraction of escaping LyC photons (4.15a) per bin of virial mass in simulation with (purple) and without (red) CRs, for data stacked between $z = 15$ and $z = 5$. The shaded areas show the lower and upper masses for which halos respectively contribute to 25% and 75% of the total escaping LyC photon budget between $z = 15$ and $z = 5$. Lower mass halos contribute to the reionisation with CR feedback, and their total escaping LyC radiation is least than in the simulation with the Strong SNe feedback.*

We just discussed the finding that the escape fraction of ionising photons is reduced with CR feedback, but this does not tell us at which length scales CR feedback causes radiation to be increasingly absorbed, as the values of escape fractions shown so far are derived at the virial radius of the halos. In order to determine if CR feedback prevents the escape of radiation in the ISM of the galaxies or farther away, I also compute the f_{esc} of LyC photons at arbitrary distances of 0.1 kpc and 1 kpc from the stellar particles. The distance of 0.1 kpc is within the ISM of galaxies in

most halos (and larger than the resolution of my simulations), and I choose 1 kpc as an intermediate distance approaching the galaxy CGM. The resulting luminosity-weighted mean $\langle f_{\rm esc}\rangle_{\rm lw}$ at 0.1 kpc, 1 kpc and $R_{\rm vir}$ as a function of halo mass is shown in Fig. 4.16a. To better visualise the variation of values between two distances, Fig. 4.16b shows the ratio of $\langle f_{\rm esc}\rangle_{\rm lw}$ at 0, 0.1 and 1 kpc and $\langle f_{\rm esc}\rangle_{\rm lw}$ at 0.1, 1 kpc and $R_{\rm vir}$, respectively. As for Fig. 4.14b, we apply the same mass binning (the number of halos per bin is the same as written in Table 4.3), and show the mean values per bin from data stacked between $z = 7$ and $z = 5$.

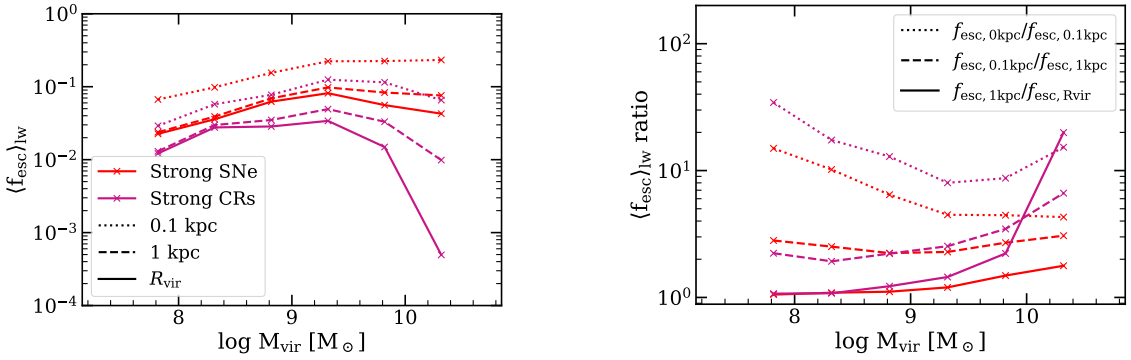

(a) *(b)*

Figure 4.16: *Luminosity-weighted mean escape fraction per bin of virial mass in simulations with the Strong SNe (in red) and the Strong CRs (in purple) models. 4.16a: Dotted, dashed and solid lines respectively show $f_{\rm esc}$ at 0.1 kpc, 1 kpc and at the virial radius of the halos. 4.16b: ratio of $\langle f_{\rm esc}\rangle_{\rm lw}$ at 0, 0.1 and 1 kpc and $\langle f_{\rm esc}\rangle_{\rm lw}$ at 0.1, 1 kpc and $R_{\rm vir}$, respectively in dotted, dashed and solid lines. With CR feedback, the escape fractions at a given distance are always below that measured in the counterpart simulation without CRs, and the difference increases at higher halo mass. In both cases and except for the most massive bin, radiation is mainly absorbed before 0.1 kpc.*

Naturally, the escape fractions decrease with distance, because the probability for a LyC photon to be absorbed increases with the amount of matter it goes through. At 0.1 kpc from the stellar particles, between 77 and 93% of the LyC photons are absorbed with the Strong SNe feedback, and this increases to between 88 and 97% with CRs (dotted lines in Fig. 4.16a). This means that even so close to the stellar particles that emitted them, LyC photons escape in a lower proportion with CR feedback than without. This may be also attributed to the more efficient SN feedback in the Strong SNe model, which makes it easier for photons to escape the 0.1 kpc limit. More precisely, approximately twice less LyC photons escape this 0.1 kpc limit with CRs than without, and this goes up to a factor three for the most massive halo. If we go further out, at 1 kpc and beyond, the escape fractions are similarly reduced in the two simulations (at the exception of the most massive halos). Therefore, the difference in escape fractions between the two simulations for the lower mass halos are determined by the absorption of LyC photons in the first 0.1 kpc. For halos more massive than $10^{9.5}\,M_\odot$, the escape fractions are reduced by a factor of 3.5 and 6.6 between 0.1 and 1 kpc with CRs (dashed purple line in Fig. 4.16b), and by a factor of 2.2 and 20 beyond 1 kpc (solid purple line in Fig. 4.16b). In these most massive halos, CR feedback prevents the escape of ionising photons both at ISM and CGM scales. To summarise, in the fiducial SPHINX5 simulation, LyC are absorbed

rather locally in the ISM of galaxies at any halo mass, which has previously been found by e.g. Trebitsch et al. (2017). With CR feedback, LyC photons are also preferentially absorbed in the vicinity of the stars, but an important amount of LyC photons are also absorbed in the CGM of the most massive halos, which is likely to be the consequence of the dense CR-driven winds in the CGM.

4.5 Summary

The aim of this chapter is to probe the effect of CR feedback during the Epoch of Reionisation in a cosmological context. For this purpose, I perform zoom-in simulations of two massive halos from the SPHINX20 simulation, and a set of SPHINX5 simulations with and without CRs. Repeating a similar analysis as the one done in the **CosmicShine** paper globally leads to the same conclusion: CR feedback helps to reduce star formation, smooths the galaxy gas distribution and produces a CGM much colder than SN feedback does. However, canonical injection of CR energy and SN rate does not sufficiently regulate galaxy growth at high-redshift. In order to produce realistic SMHM relations and UV luminosity functions, I strengthen CR feedback by injecting 20% of the SN energy into CRs, and by adopting a SN rate of $2\,\mathrm{SNe}/100\,\mathrm{M}_\odot$. This calibration reduces the tension with the expectations from a Kroupa IMF compared to the four-fold boost used in the fiducial SPHINX simulations. It also encloses a number of uncertainties, such as the precise amount of CR energy and its transport in high-redshift galaxies, the lack of other complementary feedback processes and the limitations of sub-grid models to translate the complexity of physical processes acting at unresolved scales. With this parametrisation, CR feedback suppresses star formation in a similar way as the strongly boosted SN feedback. CR feedback therefore likely plays a role in the regulation of galaxy growth during the Epoch of Reionisation, even if quantifying precisely this effect depends on the accuracy of our feedback models. However, CR feedback also leads to an unrealistically delayed and incomplete reionisation of the SPHINX5 volume. At any halo mass, CR feedback reduces the escape fraction of LyC photons in the close vicinity of the stars, and also in the CGM of the most massive halos of my sample.

CHAPTER 5
Conclusions and future prospects

5.1 Summary of the thesis and conclusions

From the Epoch of Reionisation (EoR) until the present time, galaxies form and evolve via a multitude of complex physics. In this thesis, I investigate the role of cosmic ray (CR) feedback on galaxy evolution, and on reionisation. For this purpose, I use the RAMSES-RT code (Teyssier, 2002; Rosdahl et al., 2013) to perform the first idealised and cosmological CR radiation-magnetohydrodynamics (CR-RMHD) simulations of galaxies, coupling supernovae (SN), radiation and CR feedback.

In the first part of my thesis, I study the effect of CR feedback on three idealised galaxy discs of different masses. The main results of this study were published in the journal MNRAS (Farcy et al., 2022). At any galaxy mass, the CR energy injected as a result of SN explosions smooths out density contrasts in the interstellar medium (ISM), which has the effect of thickening galaxy discs. This also contributes to reduce the number and the mass of star-forming clumps, suppressing star formation with an increasing efficiency with decreasing galaxy mass. In addition, CR pressure helps to drive stronger and colder winds than thermal pressure from SNe and radiation alone, which is likely to contribute to the metal enrichment observed in the circum-galactic medium (CGM) of galaxies via absorption in quasar sightlines. I also find that CR feedback suppresses the escape of Lyman Continuum (LyC) radiation. In order to determine the mechanisms of CR feedback, I dissect the effects of distinct physics and parameters in my models, such as magnetic field, gas fraction, CR streaming, and radiation feedback. I also test the robustness of my results with numerical limitations like cell and particle mass resolution, and star formation and SN feedback modelling. With this analysis, I show that the aforementioned effects of CR feedback are qualitatively the same, insensitive to these model details.

These results are however sensitive to the efficiency of CR energy injection $f_{\rm ecr}$ and to the diffusion coefficient κ, governing respectively the amount of CR energy in the ISM and their timescale for escape. In my idealised galaxies, I show that the nature and efficiency of CR feedback is quite sensitive to those two parameters. When SNe inject a larger fraction of their energy into CRs, CR pressure increasingly suppresses star formation and enhances the mass outflow rate. If CRs quickly diffuse out of their injection sites, with a high κ, they have less time to act on the ISM and hence on star formation. However, they suffer from less energy losses and provide a greater pressure support to outflowing gas. While neither parameter is well constrained, $f_{\rm ecr}$ and κ determine the ability of CRs to regulate star formation and drive winds, to a greater extent than the other physical and numerical ingredients tested.

Using the same physics as in my idealised simulations, I test my conclusions in a more realistic cosmological context, by re-simulating two relatively massive halos from a large SPHINX simulation with the zoom-in technique, and focusing at

high-redshift. In agreement with my results from the idealised galaxies, I find that CR feedback reduces star formation more efficiently in the less massive halo, and provides a cool CGM for both galaxies.

One of the main goals of this thesis was to determine if CRs play a role in the reionisation of the Universe by affecting the escape of ionising radiation from galaxies. However, the process of reionisation is not captured in my idealised and zoom simulations, which makes it hard to predict how CR feedback impacts the reionisation of the Universe. To overcome this issue, I perform non-zoom CR-RMHD cosmological simulations with small SPHINX volumes of 5 cMpc in width. This provides a sample of hundreds of resolved low-mass galaxies in which to study the effects of CR feedback and its impact on the escape fraction of LyC radiation. These simulations, one with a calibrated strong SN feedback and the other with similarly calibrated CR feedback, reasonably match observational estimates of the SMHM relation and high-redshift UV luminosity functions. However, the simulated Universe in which CRs are included has a strongly delayed and incomplete reionisation, in strong disagreement with observational estimates of the reionisation history. This is due to CR feedback suppressing the escape of LyC radiation in the vicinity of stars, and also in the CGM of the most massive galaxies of my sample.

5.2 Perspectives

I finally present some future works that will help to complete the study initiated in this thesis.

Cosmic rays and the EoR

The results presented in **Chapter 4** point toward an incompatibility between CR feedback and reionisation models. Naively, this may come from either too low LyC luminosity, or too inefficient escape of LyC photons. As the UV luminosity functions at high redshift in my simulation with CRs are in fair agreement with observations, we may be tempted to consider the reduction of escape fraction as the discriminant factor. While I find that CR feedback is too suppressive for the escape of ionising radiation, CRs are present in the real Universe, which did reionise successfully around a billion years after the Big Bang. Therefore, one possible explanation for having too low escape fractions with CRs in my simulation is that my calibrated CR feedback model is not representative of the behaviour of the CR population in the young Universe. Only a few observations in our very local Universe exist to constrain the amount and escape time of CR energy within star-forming galaxies, and I showed in **Chapter 3** how the injection of CR energy and the CR diffusion coefficient change the effects of CR feedback. In work in progress, I am currently investigating whether reducing the injection of CR energy and varying the diffusion coefficient impacts the effect of CR feedback on the reionisation of additional SPHINX5 volumes, while still maintaining its ability to suppress star formation.

In the continuity of **Chapter 4**, the next step to study how CR feedback impacts the reionisation of the Universe is to perform an 8 times larger simulation volume, i.e. a SPHINX simulation of 10 cMpc in width. For this ongoing project, I have been granted 7.5 million CPU hours on national supercomputers. This will

provide a much better statistical sample of galaxies and extend the halo mass range, as massive galaxies are relatively absent in my SPHINX5 simulations. I plan to repeat a similar analysis as done in **Chapter 4**, i.e. investigate how CR feedback regulates galaxy growth, how it impacts the escape of LyC radiation with time and with halo mass, and compare the reionisation history of equivalent simulations with and without CRs in volumes of 5 and 10 cMpc in width. This will be the basis of my next paper on CR feedback and reionisation.

Towards a better modelling of CR feedback

CRs have an important role in galaxy evolution. Their effects range from delaying star formation, especially in low mass galaxies, to launching cold outflows that change the composition of the CGM. However, as stated previously and shown in **Chapter 3**, CR feedback is predominantly determined by the efficiency of CR energy injection, and by the diffusion coefficient. In my study, the values of these two parameters are constant and, even if chosen to be in the realm of acceptable values, likely to be an oversimplification of reality. Recently, efforts have been made to account for a better modelling of CR transport in simulations of galaxies, with a diffusion coefficient varying with local plasma properties (Farber et al., 2018; Semenov et al., 2018; Hopkins et al., 2021c). A new implementation of CR transport model has also been developed by Girichidis et al. (2022), which resolves the CR energy spectrum from $\sim$ MeV to TeV, and models the diffusion coefficient and energy losses depending on the energy of the CR population. With these more realistic approaches, it would be particularly interesting to study if and how CR feedback differently impacts the escape of ionising radiation and the reionisation process.

Supernovae, AGN and cosmic rays

In the context of reionisation, two main candidates are thought to produce the bulk of the LyC photons, which are star-forming galaxies (e.g. Finkelstein et al., 2015; Eldridge et al., 2017; Shivaei et al., 2018) and Active Galactic Nucleus (AGN) (e.g. Grazian et al., 2018). In this thesis, I exclusively focused on the former. Even if some studies tend to show that the contribution of AGN to reionisation is negligible (e.g. Jiang et al., 2022), this remains a debated topic (e.g. Grazian et al., 2018). Nonetheless, AGN feedback may play a role in galaxy growth during the Epoch of Reionisiation. In particular, CRs can also be indirectly injected by AGN, with an efficiency scaling with the black hole mass accretion rate, and Wellons et al. (2022) recently show that CRs injected by supermassive black holes may have an important contribution on galaxy evolution. In addition, injecting CR energy both via SNe and AGN may have important consequences both on galaxy and black hole growth. Therefore, one promising avenue is to explore the interplay between SN, AGN and CR feedback. While these three feedback mechanisms differently regulate galaxy evolution and the escape of ionising photons, their coupling may produce different effect. Biernacki & Teyssier (2018) already show that the non linear coupling of SN and AGN feedback can power massive outflows in the CGM of high-redshift galaxies, to a greater extent than when they are individually considered. CR feedback may even accentuate this effect, and it is highly intriguing to know how combining all of

these physical processes impacts the reionisation of the Universe.

APPENDIX A
Cosmic rays in the literature

Because this thesis is dedicated to the study of CR feedback, it naturally includes sections about CR astrophysics (acceleration, propagation, observational probes) as well as numerical implementations and results from CRs in galaxy simulations. The aim of this appendix is to gather the references and results that are mentioned throughout the manuscript and to complete them with papers and reviews that have been useful for my own understanding of CRs. The list of references and their description are obviously not intended to be exhaustive, and are provided in the hope of being useful to anyone interested.

A.1 CR feedback in galaxy simulations

A plethora of studies investigated the effect of CRs on galaxy evolution. They all originate from different setups and astrophysical codes, target various objects, and have diverse goals. I try to give an overview of their results, focusing on the most recent ones and on those that studied the effects of CRs on star formation and CR-driven winds. The papers are listed chronologically. For each of them, I provide the reference of the study, its title, and some additional information such as the type of numerical experiment, the code used to perform it, the physical resolution reached or any extra information thought to be relevant. A short summary of their findings is listed by topic, according to the following color code to be more easily spotted:

- ★ Star formation
- ★ Gas properties
- ★ Outflows
- ★ Diffusion coefficient

I also provide the references of the codes used to perform the different simulations in the studies listed below:

- ART: AMR, Kravtsov et al. (1997)
- FLASH: AMR, Fryxell et al. (2000)
- RAMSES: AMR, Teyssier (2002)
- GADGET: SPH, Springel et al. (2001); Springel (2005)
- AREPO: moving-mesh finite volume, Springel (2010a)
- ENZO: AMR, Bryan et al. (2014)
- GIZMO: mesh-free finite mass finite volume, Hopkins (2015)
- CHANGA: SPH, Menon et al. (2015)

Jubelgas et al. (2008): Cosmic ray feedback in hydrodynamical simulations of galaxy formation
Idealised and cosmological zoom simulations - GADGET - efficiency of SN energy injection into CRs of 0.1 and 0.3

- $\kappa = 3 \times 10^{27}\ \mathrm{cm^2\,s^{-1}} \times (T/10^4\ \mathrm{K})^{1/6} \times (\rho/10^6\ \mathrm{M_\odot\,kpc^{-3}})^{-1/2}$
- SF significantly reduced for idealised and high-redshift low-mass galaxies, with SF reduction stronger for the faint-end of the luminosity function
- Greater SF suppression with higher energy injection by SNe
- Gas density projection maps show that galaxies of any mass have a thicker disc when CRs are added

Booth et al. (2013): Simulations of disk galaxies with cosmic ray driven galactic winds

Idealised simulations of a Milky-Way size galaxy and the Small Magellanic Cloud - RAMSES - $\sim$ 40 pc resolution

- $\kappa = 3 \times 10^{27}\ \mathrm{cm^2\,s^{-1}}$
- CRs are more efficient to reduce the SFR for the simulation of the Small Magellanic Cloud, less massive than the Milky-Way size galaxy
- Mass loading factors are similar for the Milky-Way like galaxy with and without CRs, but are one order of magnitude enhanced for the Small Magellanic Cloud when CRs are included

Salem & Bryan (2014): Cosmic ray driven outflows in global galaxy disc models

Idealised simulations - ENZO - $\sim$ 60 pc resolution

- $\kappa = 10^{27} - 10^{29}\ \mathrm{cm^2\,s^{-1}}$
- Runs with low diffusion coefficient are more efficient to suppress star formation.
- Winds are more rarefied in simulations with high κ

Pakmor et al. (2016): Galactic winds driven by isotropic and anisotropic cosmic ray diffusion in disk galaxies

Idealised simulations - AREPO

- $\kappa = 10^{28}\ \mathrm{cm^2\,s^{-1}}$
- CR anisotropic diffusion is more efficient to suppress star formation than the simpler isotropic CR transport
- Both isotropic and anisotropic diffusion lead to the formation of strong bipolar outflows

Salem et al. (2016): Role of cosmic rays in the circumgalactic medium

Cosmological zoom simulations - ENZO - $\sim$ 400 pc resolution - efficiency of SN energy injection into CRs of 0.3

- $\kappa = 3 \times 10^{27} - 3 \times 10^{28}\ \mathrm{cm^2\,s^{-1}}$
- CRs lead to a metal-enriched CGM that better match with observational data, with more diffuse cold gas
- Gamma-ray luminosity better match with observations when $\kappa = 3 \times 10^{28}\ \mathrm{cm^2\,s^{-1}}$, and too high for lower diffusion coefficient values

Pfrommer et al. (2017): Simulating cosmic ray physics on a moving mesh

Idealised and cosmological zoom simulations - AREPO

- $\kappa = 3 \times 10^{28}\ \mathrm{cm^2\,s^{-1}}$
- The reduction of SFR by CRs is stronger for low-mass galaxies

Wiener et al. (2017): Cosmic ray-driven galactic winds: streaming or diffusion?
Idealised simulations - GADGET - mean particle spacing of ~ 60 pc
- $\kappa = 3 \times 10^{28}$ cm^2 s^{-1}
- Classical diffusion is more efficient than streaming to reduce SFR. CRs that would propagate through advection only would be even more efficient to suppress star formation. Approximately the same SFR suppression from CRs in their two galaxies of different masses
- Diffusion leads to 10 times more mass loss rates than streaming

Butsky & Quinn (2018): The role of cosmic ray transport in shaping the simulated circumgalactic medium
Idealised simulations of a Milky-Way mass galaxy- ENZO - efficiency of SN energy injection into CRs of 0.1 and 0.3 - simulations evolved for 14 Gyr
- $\kappa = 10^{28} - 3 \times 10^{28}$ cm^2 s^{-1}
- All CR transport models tested have lower SFR than the run without CRs, and anisotropic diffusion is more efficient than streaming and isotropic diffusion to regulate star formation
- Isotropic or anisotropic diffusion and streaming all produce strong metal-enriched outflows
- Isotropic diffusion leads to a warm spatially uniform CGM, anisotropic diffusion creates a reservoir of cold gas up to large distances from the galaxy, and streaming allows a multiphase medium in agreement with a number of ionic species column density measurements

Farber et al. (2018): Impact of cosmic ray transport on galactic winds
Slab of ISM - FLASH - ~ 30 pc resolution
- Model that decouples CRs in the cold neutral ISM, to have $\kappa = 10^{29}$ cm^2 s^{-1} when $T < 10^4$ K, and $\kappa = 3 \times 10^{27}$ cm^2 s^{-1} when $T \geq 10^4$ K
- CRs are the most efficient to suppress SF when they are only advected, and are less efficient with their diffusion decoupling model
- Diffusion, without the decoupling model, is the most efficient process for CRs to drive the greatest mass outflow rates up to distances of 5 kpc. Advection alone is inefficient

Girichidis et al. (2018): Cooler and smoother - the impact of cosmic rays on the phase structure of galactic outflows
Stratified box of ISM - FLASH - ~ 4 pc resolution - constant SFR
- $\kappa = 10^{27} - 10^{29}$ cm^2 s^{-1}
- CR-driven outflows are slower, denser, smoother and colder than SN-driven winds, and the mass loading factor is higher with $\kappa = 10^{28}$ cm^2 s^{-1} than with $\kappa = 3 \times 10^{28}$ cm^2 s^{-1}

Jacob et al. (2018): The dependence of cosmic ray driven galactic winds on halo mass
Idealised simulations of galaxies at different masses - AREPO
- $\kappa = 3 \times 10^{27} - 10^{29}$ cm^2 s^{-1}
- CRs are more efficient at reducing SF in low-mass galaxies

- Mass loading factors are the smallest when $\kappa = 10^{29}$ cm^2 s^{-1}, at any galaxy mass. The mass outflow rates are actually the greatest with increasing diffusion coefficient (except the most extreme value) at increasing galaxy mass

Chan et al. (2019): Cosmic ray feedback in the FIRE simulations: constraining cosmic ray propagation with GeV gamma ray emission
Cosmological zoom simulations - GIZMO - FIRE-2 simulations
- $\kappa = 3 \times 10^{27} - 3 \times 10^{29}$ cm^2 s^{-1}
- The SF efficiency is the lowest when CRs are trapped in the disk, for low diffusion coefficients
- The best match with the gamma-ray luminosity - FIR relation is achieved when $\kappa = 3 \times 10^{29}$ cm^2 s^{-1}

Buck et al. (2020): The effects of cosmic rays on the formation of Milky Way-like galaxies in a cosmological context
Cosmological zoom simulations - AREPO - galaxies from the AURIGA project
- $\kappa = 10^{28}$ cm^2 s^{-1}
- Star formation only varies marginally with different CR transport (advection, iso/anisotropic diffusion, Alfvén-wave cooling, no CRs)
- Models with advection and diffusion exhibit smoother and colder CGM than the Alfvén-wave model or runs without CRs
- Only models with Alfvén-wave cooling can reproduce observations of gamma-ray emission from hadronic interactions

Dashyan & Dubois (2020): Cosmic ray feedback from supernovae in dwarf galaxies
Idealised simulations - RAMSES - 9 pc resolution
- $\kappa = 3 \times 10^{27} - 10^{29}$ cm^2 s^{-1}
- SFR suppressed by a factor 2 for their two dwarf galaxies
- Advection alone reduces more drastically star formation, as no diffusion implies that CRs remain trapped in the disc where they lose energy
- There are up to two order of magnitudes more outflows when $\kappa = 10^{29}$ cm^2 s^{-1} than when there is no CRs. CR streaming alone is inefficient to drive winds

Hopkins et al. (2020b): But what about... cosmic rays, magnetic fields, conduction, & viscosity in galaxy formation
Cosmological zoom simulations - GIZMO - FIRE-2 simulations
- $\kappa = 3 \times 10^{29}$ cm^2 s^{-1}
- CRs are rather inefficient to alter star formation in dwarf galaxy, but conversely can suppress SF by a factor from 2 to 4 in massive galaxies
- CR support helps to maintain cool and dense gas in the CGM

Ji et al. (2020): Properties of the circumgalactic medium in cosmic ray-dominated galaxy halos
Cosmological zoom simulations - GIZMO - FIRE-2 simulations
- $\kappa = 3 \times 10^{29}$ cm^2 s^{-1}
- CRs produce a colder and more realistic CGM when their pressure dominate the galaxy halos, which is especially the case at low redshift and for massive galaxies

Hopkins et al. (2021b): Cosmic-ray driven outflows to Mpc scales from L_* galaxies
Cosmological zoom simulations - GIZMO - FIRE-2 simulations

- $\kappa = 3 \times 10^{29}$ cm^2 s^{-1}
- CR pressure continuously pushes gas in the CGM and up to large distances from the galaxies. Outflows are preferentially biconical, volume-filling, cool and slower than in runs without CRs, but mainly for massive galaxies at low-redshift

Butsky et al. (2021): The impact of cosmic rays on the kinematics of the circum-galactic medium
Cosmological zoom simulations - CHANGA

- $\kappa = 10^{29}$ cm^2 s^{-1}
- The CR pressure that dominates leads to a cooler CGM in the inner 50 kpc of their Milky-Way like galaxies
- The synthetic spectral lines from runs with CRs better reproduce the ion column densities measurements from absorption-line data

Semenov et al. (2021): Cosmic-Ray diffusion suppression in star-forming regions inhibits clump formation in gas-rich galaxies
Idealised simulations of different gas fractions - ART - 40 pc resolution - efficiency of SN energy injection into CRs of 0.2

- $\kappa = 10^{28}$ cm^2 s^{-1}. In the CR diffusion suppression model, $\kappa = 10^{25} - 5 \times 10^{25}$ cm^2 s^{-1} in cells for which the youngest stellar particle age is < 40 Myr (the limit before it explodes as a SN) and where gas density > 1 cm^{-3} and temperature $< 10^5$ K
- The SFR is significantly reduced in runs with CRs, especially with their CR diffusion suppression model
- The suppression of CR diffusivity in star-forming regions eliminates high-density clumps and reduces the maximal densities reached in the disk more than in runs with a constant diffusion coefficient and even more than in runs without CRs.

Girichidis et al. (2022): Spectrally resolved cosmic rays: II-momentum-dependent cosmic ray diffusion drives powerful galactic winds
Idealised simulations - AREPO

- Spectrally resolved CR distribution, so bins of CRs from 0.1 GeV to 300 GeV with individual diffusion coefficient, energy loss processes and adiabatic index per momentum bin
- Their spectrally resolved model of CRs leads to a greater SF suppression than the grey approximation. Runs with CRs but with advection transport only have less effect on the SFR than with those with a constant diffusion or with their spectral diffusion model
- With their model, outflows become filamentary and are launched earlier and not only from the center of the galaxy. The mass outflow rates is not specifically changed, but rather the outflow morphology, dominated by the pressure exerted by the most energetic CRs

A.2 Reviews about CRs

In case it may be of use, I also list some reviews related to CRs and summarise briefly their focus. The main sections of the reviews (as found in the documents) are written in italic. Low-energy CRs refer to CRs with energies $E \lesssim$ GeV, and unless mentioned, CRs are supposed to have $E \geq$ GeV.

A.2.1 Low-energy CRs

Padovani et al. (2020): Impact of low-energy cosmic rays on star formation
- *CR observations and observables*
- *overview of CR transport and interactions in the ISM*
- *galactic CRs in molecular clouds and in circumstellar discs*
- *locally accelerated CRs, low-energy CRs at different galactic scales*

Specifically describes CR ionisation and impact on molecular clouds, on the ISM and on its chemistry.

Gabici (2022): Low energy cosmic rays
- *what are CRs*
- *difficulties in the direct observations of the local interstellar spectrum of low energy CRs*
- *indirect measurements of the remote interstellar spectrum of low energy CRs: gamma-ray and radio observations*
- *integral constraints on the remote intensity of low energy cosmic rays: the CR ionisation rate*
- *the transport of CRs in and around molecular clouds*
- *open questions*

Emphasis on observational signatures and CR induced astrochemistry.

A.2.2 CRs from an observational point of view

Helder et al. (2012): Observational signatures of particle acceleration in supernova remnants
- *observational diagnostics*
- *Balmer dominated shocks*
- *increased compression ratio*
- *molecular ion diagnostics of CR acceleration sources*
- *particle acceleration in the galactic central regions*
- *alternatives for SN remnants being main sources for galactic CRs*

Probes and consequences of the acceleration of CRs by SN remnants.

Grenier et al. (2015): The nine lives of CRs in galaxies
- *advances from direct measurements*
- *advances in CR propagation*
- *CR wanderers in the Milky-Way*
- *CR/ISM interaction processes*
- *CR stimuli on the ISM*

- *CR tracers of the ISM*
- *CR in starburst environments*
- *a few more words*

Review of the state-of-the art CR observations, propagation and composition in 2015 and before.

Morlino (2017): High energy CRs from supernovae
- *the acceleration mechanism*
- *DSA in the non linear regime*
- *Escaping from the sources*
- *the journey to the Earth*
- *observational evidence*

Acceleration of CRs from SN remnants with the DSA theory.

Amato & Blasi (2018): CR transport in the galaxy: a review
- *a summary of standard predictions*
- *self-excited Alfvén waves and their damping*
- *galactic CR transport in self-generated waves*
- *propagation in the vicinity of sources*
- *CR induced galactic winds*
- *secondary particles and antiparticles*

Propagation of CRs outside of their acceleration sites and comparison of recent theoretical developments with observations.

Urošević et al. (2019): Particle acceleration in interstellar shocks
- *Fermi acceleration*
- *Observational signatures of particle acceleration in ISM: a quick overview*

Fermi processes for CR acceleration.

Bykov et al. (2020): High-Energy particles and radiation in star-forming regions
- *overview of the sources of high-energy particles and radiation associated with star-forming regions*
- *models of particle acceleration by large-scale magnetohydrodynamic turbulence with multiple shocks in star-forming regions*
- *CR propagation near their sources*
- *the specific features of cosmic rays accelerated in young massive stellar clusters the observational persepectives*

CRs acceleration and radiation observational signatures in young massive star clusters.

A.2.3 Effect of CRs on galactic winds

Zweibel (2017): The basis for CR feedback: written on the wind
- *selected properties of the galactic magnetic field and CRs*
- *kinetic theory*
- *from Fokker- Planck to fluid*

- *applications: gravitationally stratified gas in galaxies, galactic winds*
Theory for CR driven winds and coupling to the thermal plasma

Recchia (2021): CR driven galactic winds
- *galactic winds*
- *CRs in a nutshell*
- *CR driven winds: CR transport and hydrodynamics*
- *Stationaty CR driven winds in the Milky-Way*
Formation, evolution and hydrodynamics of winds powered by CRs

A.2.4 CRs and CR feedback in simulations

Strong et al. (2007): CR propagation and interactions in the galaxy
- *CR propagation: theory*
- *confrontation of theory with data*
Propagation equations for CRs in numerical and analytical models, from in particular the GALPROP code.

Marcowith et al. (2020): Multi-scale simulations of particle acceleration in astrophysical systems
- *astrophysical and physical contexts*
- *solving kinetic problems*
- *small and meso-scale numerical particle acceleration studies*
- *macro-scale numerical particle acceleration studies*
Up-to-date status of the numerical techniques that exist to study CRs with a kinetic approach.

Hanasz et al. (2021): Simulations of CR propagation
- *early models*
- *phenomenological models*
- *self-consistent models*
- *numerical details*
- *astrophysical applications*
Overview of the numerical approaches for CR transport and models, from phenomenological codes to galaxy simulations, and their results about CR feedback.

APPENDIX B
List and runtime of the simulations

The work presented in this thesis relies on a number of simulations, idealised, zoomed-in, or fully resolved cosmological ones. In case it could of any utility for the reader, I gathered some of the main properties of the idealised simulations in this appendix, as well as their computational time cost. It should be noted that all of the galaxy simulations have been performed with a specific version of RAMSES which gathers the CR implementation from Dubois & Commerçon (2016), the turbulent star formation prescription from Federrath & Klessen (2012) and described by Kimm et al. (2017), and the mechanical SN feedback model of Kimm & Cen (2014); Kimm et al. (2015). This is the same version of the code used to perform the SPHINX suite of simulations, dedicated to the study of the EoR, hence labelled RAMSES_EOR. In between, Joakim Rosdahl developed a more convenient version of RAMSES, merging all the modules aforementioned to avoid the need of using patches and specific branches of RAMSES_EOR. Because this new RAMSES comes from and is used by people at CRAL (Centre de Recherche Astrophysique de Lyon), we refer to it as RAMSES_CRAL. The take home message is that the CPU times listed below hold for a certain setup but with a unique code (RAMSES_EOR), and they could differ with other versions of RAMSES. In particular, I do not include the plethora of test runs that I performed with RAMSES_CRAL to ensure that no significant errors arise from the merging of all the physical modules used, and to check that results were similar to those obtained with RAMSES_EOR. Finally, the simulations have been run on different machines, from the local Common Computing Facilities of the LABEX Lyon Institute of Origins, the regional Pôle Scientifique de Modélisation Numérique of the ENS de Lyon, to the national HPC resources of TGCC under two allocations granted by GENCI. Again the CPU times are an indicative information that does not take into account the variability of efficiency from one machine to another.

The tables are constructed as follows. The first column, labelled "SF" for star formation, specifies if stars form following a density criterion and a global star formation efficiency of 2% ("density") or if star formation is rather described with a local star formation efficiency, based on the gravo-turbulent properties of the gas following the implementation described by Kimm et al. (2017) ("turbulent"). The two next columns are dedicated to the modelling of SN explosions. We first provide the number of SN explosions per stellar particle (# / M_*) which is either 0 (no SN feedback), 1 or N (multiple SN explosions). The strength of SN feedback is indicated via the number of SN per 100 $M_\odot$ formed (# / 100 $M_\odot$). The rate of SN is set via the SN progenitor mass, in order to have the same SN energy released than expected from a Kroupa IMF if # / 100 $M_\odot = 1$. Again, 0 means that there is no SN feedback, and 4 corresponds to the four-fold boost used in the fiducial SPHINX simulations. The next set of two columns indicates if a MHD solver is used ("No" meaning that a hydrodynamical solver is used instead) and what is the initial strength of the magnetic field. The next three columns are then dedicated to CR feedback, first with the SN energy injection fraction (1 would mean that 100% of the SN energy

is converted into CR energy), then with the CR diffusion coefficient κ_{28} in units of 10^{28} cm^2 s^{-1}. We inform of the inclusion of streaming CR transport, "Yes" meaning the inclusion of both streaming diffusion and heating, "No" meaning none of them, "Heating" standing for the inclusion of streaming heating only. The notation "x4" means that the streaming velocity is 4 times that of the Alfvén velocity, in order to artificially account for the damping of the Alfvén waves that is thought to boost the streaming velocity (Ruszkowski et al., 2017). In the next column, runs when RT is "Yes" include radiation feedback through photoionisation heating and radiation pressure, track hydrogen and helium ionisation states, and include non equilibrium chemistry. We specify the maximum spatial resolution (smaller cell width) as well as the minimum initial stellar particle mass. Eventually, we note the "astrophysical" time during which the galaxy has been evolved and the "real" time needed to reach this point. To take into account the fact that a different number of CPUs has been used from one run to another, the "real" time is given in units of CPU-hours, which represents the number of hours needed with 1 CPU to evolve the galaxy during the time written in the left column.

Table B.1, Table B.2 and Table B.3 provide all of these information for the G8, G9 and G10 galaxies. They include all the runs from the **CosmicShine** paper, as well as those presented in **Chapter 3**.

SF	SN		MHD		CRs			RT	Best resolution		Time	
	# / M_*	# / 100 $M_\odot$	Solver	$B_{\rm ini}$ [μG]	$f_{\rm ecr}$	κ_{28}	Streaming		cell [pc]	M_* [$M_\odot$]	Run [Myr]	Real [CPU-h]
Density	N	1	Yes	1	0	0	No	Yes	9	2000	515	7020
Density	N	1	Yes	1	0.1	1	No	Yes	9	2000	515	8730
Turbulent	0	0	No	0	0	0	No	No	9	2500	515	1660
Turbulent	N	1	No	0	0	0	No	Yes	9	2500	515	5620
Turbulent	N	1	Yes	1	0	0	No	Yes	4.5	310	515	8940
Turbulent	N	1	Yes	1	0	0	No	Yes	9	950	515	5560
Turbulent	N	1	Yes	1	0	0	No	Yes	9	2500	515	7960
Turbulent	N	1	Yes	1	0	0	No	Yes	9	7600	515	5275
Turbulent	N	4	Yes	1	0	0	No	Yes	9	2500	515	5910
Turbulent	N	1	Yes	1	0.1	0.1	No	Yes	9	2500	515	6260
Turbulent	N	1	Yes	1	0.1	1	No	Yes	4.5	310	515	12200
Turbulent	N	1	Yes	1	0.1	1	No	Yes	9	2500	515	9610
Turbulent	N	1	Yes	1	0.4	1	No	Yes	9	2500	515	7130
Turbulent	N	4	Yes	1	0.1	1	No	Yes	9	2500	515	6740
Turbulent	N	1	Yes	1	0.1	3	No	Yes	9	2500	515	8710
Turbulent	N	1	Yes	1	0.1	10	No	Yes	9	2500	515	12400
Turbulent	N	1	Yes	1	0.1	30	No	Yes	9	2500	515	25400

Table B.1: *List of runs for the G8 galaxy. See the text for the description of the columns.*

SF	SN		MHD		CRs			RT	Best resolution		Time	
	# / M_*	# / 100 $M_\odot$	Solver	$B_{\rm ini}$ [μG]	$f_{\rm ecr}$	κ_{28}	Streaming		cell [pc]	M_* [$M_\odot$]	Run [Myr]	Real [CPU-h]
Density	N	1	Yes	1	0	0	No	Yes	9	2000	515	32470
Density	1	1	Yes	1	0	0	No	Yes	9	2000	515	39790
Density	1	1	Yes	1	0	0	No	No	18	2000	515	2700
Density	1	1	Yes	1	0	0	No	Yes	18	2000	515	5210
Density	N	1	Yes	1	0.1	1	No	Yes	9	2000	515	45070
Density	1	1	Yes	1	0.1	1	No	Yes	18	2000	515	16490
Density	1	1	Yes	1	0.1	1	No	Yes	18	2000	515	19140
Turbulent	0	0	No	0	0	0	No	No	9	2500	515	9540
Turbulent	N	1	No	0	0	0	No	Yes	9	2500	515	37570
Turbulent	N	1	Yes	1	0	0	No	No	9	2500	515	26450
Turbulent	N	1	Yes	1	0	0	No	Yes	9	2500	515	32960
Turbulent	1	1	Yes	1	0	0	No	Yes	9	2500	515	42180
Turbulent	N	1	Yes	0.1	0	0	No	Yes	9	2500	515	37440
Turbulent	N	1	Yes	10	0	0	No	Yes	9	2500	515	19170
Turbulent	N	1	Yes	1	0	0	No	Yes	18	20000	515	15790
Turbulent	N	4	Yes	1	0	0	No	Yes	9	2500	515	51790
Turbulent	N	1	Yes	1	0.1	0.1	No	Yes	9	2500	515	49170
Turbulent	N	1	Yes	1	0.1	1	No	No	9	2500	515	39670
Turbulent	N	1	Yes	1	0.1	1	No	Yes	9	2500	515	46720
Turbulent	N	1	Yes	1	0.1	1	Heating	Yes	9	2500	515	48550
Turbulent	N	1	Yes	1	0.1	1	Yes	Yes	9	2500	515	327640
Turbulent	N	1	Yes	1	0.1	1	Yes, x4	Yes	9	2500	250	157000
Turbulent	N	1	Yes	1	0.1	1	No	Yes	18	20000	515	18360
Turbulent	N	1	Yes	1	0.4	1	No	Yes	9	2500	515	45160
Turbulent	N	4	Yes	1	0.1	1	No	Yes	9	2500	515	52170
Turbulent	N	1	Yes	1	0.1	3	No	Yes	9	2500	515	62840
Turbulent	N	1	Yes	1	0.1	10	No	Yes	9	2500	515	101640
Turbulent	N	1	Yes	1	0.1	30	No	Yes	9	2500	515	228670

Table B.2: *List of runs for the G9 galaxy. See the text for the description of the columns.*

SF	SN		MHD		CRs			RT	Best resolution		Time	
	# / M_*	# / 100 $M_\odot$	Solver	$B_{\rm ini}$ [μG]	$f_{\rm ecr}$	κ_{28}	Streaming		cell [pc]	M_* [$M_\odot$]	Run [Myr]	Real [CPU-h]
Density	N	1	Yes	1	0	0	No	Yes	9	2000	204	59350
Density	N	1	Yes	1	0.1	1	No	Yes	9	2000	127	52460
Density	N	1	Yes	1	0	0	No	Yes	18	16000	515	98040
Density	N	1	Yes	1	0.1	1	No	Yes	18	16000	515	102800
Turbulent	0	0	No	0	0	0	No	No	18	20000	515	36740
$f_{\rm gas} = 10\%$								No				14490
Turbulent	N	1	No	0	0	0	No	Yes	18	20000	515	82210
Turbulent	N	1	Yes	1	0	0	No	Yes	9	2500	212	74250
Turbulent	N	1	Yes	1	0	0	No	Yes	18	20000	515	96320
$f_{\rm gas} = 10\%$								No				31810
Turbulent	N	4	Yes	1	0	0	No	Yes	18	20000	515	140900
Turbulent	N	1	Yes	1	0.1	0.1	No	Yes	18	20000	515	89210
Turbulent	N	1	Yes	1	0.1	1	No	Yes	9	2500	195	107610
Turbulent	N	1	Yes	1	0.1	1	No	Yes	18	20000	515	107700
$f_{\rm gas} = 10\%$								No				39310
Turbulent	N	1	Yes	1	0.4	1	No	Yes	18	20000	515	125340
Turbulent	N	4	Yes	1	0.1	1	No	Yes	18	20000	515	173020
Turbulent	N	1	Yes	1	0.1	3	No	Yes	18	20000	515	91080
Turbulent	N	1	Yes	1	0.1	10	No	Yes	18	20000	515	140590
Turbulent	N	1	Yes	1	0.1	30	No	Yes	18	20000	515	308490

Table B.3: *List of runs for the G10 galaxy. See the text for the description of the columns.*

Bibliography

Abel T., Anninos P., Zhang Y., Norman M. L., 1997, *Modeling primordial gas in numerical cosmology*, New A, 2, 181

Abraham R. G., 1999, *Quantifying Morphological Evolution from Low to High Redshifts*, Ap&SS, 269, 323

Abraham J., et al., 2004, *Properties and performance of the prototype instrument for the Pierre Auger Observatory*, Nuclear Instruments and Methods in Physics Research A, 523, 50

Ackermann M., et al., 2013, *Detection of the Characteristic Pion-Decay Signature in Supernova Remnants*, Science, 339, 807

Agertz O., Kravtsov A. V., 2015, *On the Interplay between Star Formation and Feedback in Galaxy Formation Simulations*, apJ, 804, 18

Agertz O., et al., 2007, *Fundamental differences between SPH and grid methods*, MNRAS, 380, 963

Aharonian F., et al., 2006, *The H.E.S.S. Survey of the Inner Galaxy in Very High Energy Gamma Rays*, apJ, 636, 777

Ahn H. S., et al., 2008, *Measurements of cosmic-ray secondary nuclei at high energies with the first flight of the CREAM balloon-borne experiment*, Astroparticle Physics, 30, 133

Akahori T., et al., 2018, *Cosmic magnetism in centimeter- and meter-wavelength radio astronomy*, PASJ, 70, R2

Alfvén H., 1942, *Existence of Electromagnetic-Hydrodynamic Waves*, Nature, 150, 405

Ali S. S., Bharadwaj S., Chengalur J. N., 2008, *Foregrounds for redshifted 21-cm studies of reionization: Giant Meter Wave Radio Telescope 153-MHz observations*, MNRAS, 385, 2166

Alpher R. A., Bethe H., Gamow G., 1948, *The Origin of Chemical Elements*, Physical Review, 73, 803

Amato E., Blasi P., 2018, *Cosmic ray transport in the Galaxy: A review*, Advances in Space Research, 62, 2731

Angulo R. E., Springel V., White S. D. M., Jenkins A., Baugh C. M., Frenk C. S., 2012, *Scaling relations for galaxy clusters in the Millennium-XXL simulation*, MNRAS, 426, 2046

Antoni T., et al., 2003, *The cosmic-ray experiment KASCADE*, Nuclear Instruments and Methods in Physics Research A, 513, 490

Armillotta L., Ostriker E. C., Jiang Y.-F., 2021, *Cosmic-Ray Transport in Simulations of Star-forming Galactic Disks*, apJ, 922, 11

Armillotta L., Ostriker E. C., Jiang Y.-F., 2022, *Cosmic-Ray Transport in Varying Galactic Environments*, arXiv e-prints, p. arXiv:2203.11949

Atek H., et al., 2015, *New Constraints on the Faint End of the UV Luminosity Function at z ~7-8 Using the Gravitational Lensing of the Hubble Frontier Fields Cluster A2744*, apJ, 800, 18

Atek H., Richard J., Kneib J.-P., Schaerer D., 2018, *The extreme faint end of the UV luminosity function at $z \sim 6$ through gravitational telescopes: a comprehensive assessment of strong lensing uncertainties*, MNRAS, 479, 5184

Attia O., Teyssier R., Katz H., Kimm T., Martin-Alvarez S., Ocvirk P., Rosdahl J., 2021, *Cosmological magnetogenesis: the Biermann battery during the Epoch of reionization*, MNRAS, 504, 2346

Atwood W. B., et al., 2009, *The Large Area Telescope on the Fermi Gamma-Ray Space Telescope Mission*, apJ, 697, 1071

Aubert D., Pichon C., Colombi S., 2004, *The origin and implications of dark matter anisotropic cosmic infall on $\sim L_*$ haloes*, MNRAS, 352, 376

Auger P., Ehrenfest P., Maze R., Daudin J., Fréon R. A., 1939, *Extensive Cosmic-Ray Showers*, Reviews of Modern Physics, 11, 288

Axford W. I., Leer E., Skadron G., 1977, in International Cosmic Ray Conference. p. 132

Axford W. I., Leer E., McKenzie J. F., 1982, *The structure of cosmic ray shocks*, A&A, 111, 317

Bañados E., et al., 2018, *An 800-million-solar-mass black hole in a significantly neutral Universe at a redshift of 7.5*, Nature, 553, 473

Baade W., Zwicky F., 1934, *Remarks on Super-Novae and Cosmic Rays*, Physical Review, 46, 76

Barkana R., Loeb A., 2001, *In the beginning: the first sources of light and the reionization of the universe*, Phys. Rep., 349, 125

Barnett R., Warren S. J., Becker G. D., Mortlock D. J., Hewett P. C., McMahon R. G., Simpson C., Venemans B. P., 2017, *Observations of the Lyman series forest towards the redshift 7.1 quasar ULAS J1120+0641*, A&A, 601, A16

Bassett R., Ryan-Weber E. V., Cooke J., Meštrić U., Kakiichi K., Prichard L., Rafelski M., 2021, *IGM transmission bias for $z \geq 2.9$ Lyman continuum detected galaxies*, MNRAS, 502, 108

Becker G. D., Bolton J. S., 2013, *New measurements of the ionizing ultraviolet background over $2 < z < 5$ and implications for hydrogen reionization*, MNRAS, 436, 1023

Becker R. H., et al., 2001, *Evidence for Reionization at z˜6: Detection of a Gunn-Peterson Trough in a z=6.28 Quasar*, AJ, 122, 2850

Becker G. D., Bolton J. S., Madau P., Pettini M., Ryan-Weber E. V., Venemans B. P., 2015, *Evidence of patchy hydrogen reionization from an extreme Lyα trough below redshift six*, MNRAS, 447, 3402

Behroozi P. S., Wechsler R. H., Conroy C., 2013, *The Average Star Formation Histories of Galaxies in Dark Matter Halos from z = 0-8*, apJ, 770, 57

Behroozi P., Wechsler R. H., Hearin A. P., Conroy C., 2019, *UNIVERSEMACHINE: The correlation between galaxy growth and dark matter halo assembly from z = 0-10*, MNRAS, 488, 3143

Bell A. R., 1978, *The acceleration of cosmic rays in shock fronts - I.*, MNRAS, 182, 147

Bennett C. L., et al., 2003a, *First-Year Wilkinson Microwave Anisotropy Probe (WMAP) Observations: Preliminary Maps and Basic Results*, ApJS, 148, 1

Bennett C. L., et al., 2003b, *First-Year Wilkinson Microwave Anisotropy Probe (WMAP) Observations: Foreground Emission*, ApJS, 148, 97

Bennett C. L., et al., 2013, *Nine-year Wilkinson Microwave Anisotropy Probe (WMAP) Observations: Final Maps and Results*, ApJS, 208, 20

Benson A. J., Lacey C. G., Baugh C. M., Cole S., Frenk C. S., 2002, *The effects of photoionization on galaxy formation - I. Model and results at z=0*, MNRAS, 333, 156

Berger M. J., Oliger J., 1984, *Adaptive Mesh Refinement for Hyperbolic Partial Differential Equations*, Journal of Computational Physics, 53, 484

Bertschinger E., 2001, *Multiscale Gaussian Random Fields and Their Application to Cosmological Simulations*, ApJS, 137, 1

Bian F., Fan X., 2020, *Lyman continuum escape fraction in Ly α emitters at z ≈ 3.1*, MNRAS, 493, L65

Biernacki P., Teyssier R., 2018, *The combined effect of AGN and supernovae feedback in launching massive molecular outflows in high-redshift galaxies*, MNRAS, 475, 5688

Bigiel F., Leroy A., Walter F., Brinks E., de Blok W. J. G., Madore B., Thornley M. D., 2008, *The Star Formation Law in Nearby Galaxies on Sub-Kpc Scales*, AJ, 136, 2846

Binney J., 1978, *On the rotation of elliptical galaxies.*, MNRAS, 183, 501

Birnboim Y., Dekel A., 2003, *Virial shocks in galactic haloes?*, MNRAS, 345, 349

Birnboim Y., Federrath C., Krumholz M., 2018, *Compression of turbulent magnetized gas in giant molecular clouds*, MNRAS, 473, 2144

Blandford R. D., Ostriker J. P., 1978, *Particle acceleration by astrophysical shocks.*, ApJ, 221, L29

Blasi P., Amato E., 2012, *Diffusive propagation of cosmic rays from supernova remnants in the Galaxy. I: spectrum and chemical composition*, J. Cosmology Astropart. Phys., 2012, 010

Blondin J. M., Wright E. B., Borkowski K. J., Reynolds S. P., 1998, *Transition to the Radiative Phase in Supernova Remnants*, apJ, 500, 342

Blümer J., Engel R., Hörandel J. R., 2009, *Cosmic rays from the knee to the highest energies*, Progress in Particle and Nuclear Physics, 63, 293

Bolton J. S., Haehnelt M. G., 2007, *The observed ionization rate of the intergalactic medium and the ionizing emissivity at $z \geq 5$: evidence for a photon-starved and extended epoch of reionization*, MNRAS, 382, 325

Booth C. M., Agertz O., Kravtsov A. V., Gnedin N. Y., 2013, *Simulations of Disk Galaxies with Cosmic Ray Driven Galactic Winds*, ApJ, 777, L16

Bosman S. E. I., Fan X., Jiang L., Reed S., Matsuoka Y., Becker G., Haehnelt M., 2018, *New constraints on Lyman-α opacity with a sample of 62 quasars at $z > 5.7$*, MNRAS, 479, 1055

Boulares A., Cox D. P., 1990, *Galactic Hydrostatic Equilibrium with Magnetic Tension and Cosmic-Ray Diffusion*, apJ, 365, 544

Bourke T. L., Myers P. C., Robinson G., Hyland A. R., 2001, *New OH Zeeman Measurements of Magnetic Field Strengths in Molecular Clouds*, apJ, 554, 916

Bouwens R. J., et al., 2015, *UV Luminosity Functions at Redshifts $z \sim 4$ to $z \sim 10$: 10,000 Galaxies from HST Legacy Fields*, apJ, 803, 34

Bouwens R. J., Oesch P. A., Illingworth G. D., Ellis R. S., Stefanon M., 2017, *The $z \sim 6$ Luminosity Function Fainter than -15 mag from the Hubble Frontier Fields: The Impact of Magnification Uncertainties*, apJ, 843, 129

Brackbill J. U., Barnes D. C., 1980, *The Effect of Nonzero $\nabla \cdot B$ on the numerical solution of the magnetohydrodynamic equations*, Journal of Computational Physics, 35, 426

Branch D., Nomoto K., Filippenko A. V., 1991, *The supernova-progenitor connection.*, Comments on Astrophysics, 15, 221

Braspenning J., Schaye J., Borrow J., Schaller M., 2022, *Sensitivity of non-radiative cloud-wind interactions to the hydrodynamics solver*, arXiv e-prints, p. arXiv:2203.13915

Brush S. G., 1992, *How Cosmology Became a Science*, Scientific American, 267, 62

Bruzual G., Charlot S., 2003, *Stellar population synthesis at the resolution of 2003*, MNRAS, 344, 1000

Bryan G. L., et al., 2014, *ENZO: An Adaptive Mesh Refinement Code for Astrophysics*, ApJS, 211, 19

Buck T., Pfrommer C., Pakmor R., Grand R. J. J., Springel V., 2020, *The effects of cosmic rays on the formation of Milky Way-mass galaxies in a cosmological context*, MNRAS, 497, 1712

Bullock J. S., Boylan-Kolchin M., 2017, *Small-Scale Challenges to the ΛCDM Paradigm*, ARA&A, 55, 343

Butsky I. S., Quinn T. R., 2018, *The Role of Cosmic-ray Transport in Shaping the Simulated Circumgalactic Medium*, apJ, 868, 108

Butsky I. S., et al., 2021, *The Impact of Cosmic Rays on the Kinematics of the Circumgalactic Medium*, arXiv e-prints, p. arXiv:2106.14889

Bykov A. M., Marcowith A., Amato E., Kalyashova M. E., Kruijssen J. M. D., Waxman E., 2020, *High-Energy Particles and Radiation in Star-Forming Regions*, Space Sci. Rev., 216, 42

Caprioli D., Spitkovsky A., 2014, *Simulations of Ion Acceleration at Non-relativistic Shocks. I. Acceleration Efficiency*, apJ, 783, 91

Caprioli D., Zhang H., Spitkovsky A., 2018, *Diffusive shock re-acceleration*, Journal of Plasma Physics, 84, 715840301

Capriotti E. R., Kozminski J. F., 2001, *Relative Effects of Ionizing Radiation and Winds from O-Type Stars on the Structure and Dynamics of H II Regions*, PASP, 113, 677

Carroll S. M., 2001, *The Cosmological Constant*, Living Reviews in Relativity, 4, 1

Casey C. M., Narayanan D., Cooray A., 2014, *Dusty star-forming galaxies at high redshift*, Phys. Rep., 541, 45

Castellina A., 2017, *Ground-based cosmic ray experiments: A review*, Nuovo Cimento C Geophysics Space Physics C, 40, 143

Cen R., Ostriker J. P., 1992, *Galaxy Formation and Physical Bias*, ApJ, 399, L113

Chabrier G., 2003, *Galactic Stellar and Substellar Initial Mass Function*, PASP, 115, 763

Chaikin E., Schaye J., Schaller M., Bahé Y. M., Nobels F. S. J., Ploeckinger S., 2022, *The importance of the way in which supernova energy is distributed around young stellar populations in simulations of galaxies*, arXiv e-prints, p. arXiv:2203.07134

Chan T. K., Kereš D., Hopkins P. F., Quataert E., Su K. Y., Hayward C. C., Faucher-Giguère C. A., 2019, *Cosmic ray feedback in the FIRE simulations: constraining cosmic ray propagation with GeV γ-ray emission*, MNRAS, 488, 3716

Cherenkov Telescope Array Consortium et al., 2019, *Science with the Cherenkov Telescope Array*. World Scientific Publishing Co. Pte. Ltd., doi:10.1142/10986

Chevalier R. A., 1977, *The interaction of supernovae with the interstellar medium.*, ARA&A, 15, 175

Cho J., Lazarian A., 2003, *Compressible magnetohydrodynamic turbulence: mode coupling, scaling relations, anisotropy, viscosity-damped regime and astrophysical implications*, MNRAS, 345, 325

Chomiuk L., Povich M. S., 2011, *Toward a Unification of Star Formation Rate Determinations in the Milky Way and Other Galaxies*, AJ, 142, 197

Cicone C., et al., 2015, *Very extended cold gas, star formation and outflows in the halo of a bright quasar at $z > 6$*, A&A, 574, A14

Ciotti L., Ostriker J. P., 2001, *Cooling Flows and Quasars. II. Detailed Models of Feedback-modulated Accretion Flows*, apJ, 551, 131

Clay J., van Alphen P. M., Hooft C. G. T., 1934, *Results of the Dutch Cosmic Ray Expedition 1933: II. The magnetic latitude effect of cosmic rays a magnetic longitude effect*, Physica, 1, 829

Coil A. L., Weiner B. J., Holz D. E., Cooper M. C., Yan R., Aird J., 2011, *Outflowing Galactic Winds in Post-starburst and Active Galactic Nucleus Host Galaxies at $0.2 < z < 0.8$*, apJ, 743, 46

Commerçon B., Teyssier R., Audit E., Hennebelle P., Chabrier G., 2011, *Radiation hydrodynamics with adaptive mesh refinement and application to prestellar core collapse. I. Methods*, A&A, 529, A35

Cooper A. P., Parry O. H., Lowing B., Cole S., Frenk C., 2015, *Formation of in situ stellar haloes in Milky Way-mass galaxies*, MNRAS, 454, 3185

Costa T., Rosdahl J., Sijacki D., Haehnelt M. G., 2018, *Quenching star formation with quasar outflows launched by trapped IR radiation*, MNRAS, 479, 2079

Croton D. J., et al., 2006, *The many lives of active galactic nuclei: cooling flows, black holes and the luminosities and colours of galaxies*, MNRAS, 365, 11

Crutcher R. M., Roberts D. A., Troland T. H., Goss W. M., 1999, *The Magnetic Field of the NGC 2024 Molecular Cloud*, apJ, 515, 275

De Haro J., Elizalde E., 2022, *Some topics in Cosmology – Clearly explained by means of simple examples –*, arXiv e-prints, p. arXiv:2201.06097

Dale J. E., Bonnell I. A., 2008, *The effect of stellar winds on the formation of a protocluster*, MNRAS, 391, 2

Dale J. E., Ngoumou J., Ercolano B., Bonnell I. A., 2013, *Massive stars in massive clusters - IV. Disruption of clouds by momentum-driven winds*, MNRAS, 436, 3430

Dale J. E., Ngoumou J., Ercolano B., Bonnell I. A., 2014, *Before the first supernova: combined effects of H II regions and winds on molecular clouds*, MNRAS, 442, 694

Dalla Vecchia C., Schaye J., 2008, *Simulating galactic outflows with kinetic supernova feedback*, MNRAS, 387, 1431

Dalla Vecchia C., Schaye J., 2012, *Simulating galactic outflows with thermal supernova feedback*, MNRAS, 426, 140

Dashyan G., Dubois Y., 2020, *Cosmic ray feedback from supernovae in dwarf galaxies*, A&A, 638, A123

Dashyan G., Silk J., Mamon G. A., Dubois Y., Hartwig T., 2018, *AGN feedback in dwarf galaxies?*, MNRAS, 473, 5698

Davies R. L., et al., 2019, *Kiloparsec Scale Properties of Star Formation Driven Outflows at $z \sim 2.3$ in the SINS/zC-SINF AO Survey*, apJ, 873, 122

Dawoodbhoy T., et al., 2018, *Suppression of star formation in low-mass galaxies caused by the reionization of their local neighbourhood*, MNRAS, 480, 1740

De Lucia G., Blaizot J., 2007, *The hierarchical formation of the brightest cluster galaxies*, MNRAS, 375, 2

Dekel A., Silk J., 1986, *The Origin of Dwarf Galaxies, Cold Dark Matter, and Biased Galaxy Formation*, apJ, 303, 39

Van der Vorst H. A., 1992, *Bi-CGSTAB: A Fast and Smoothly Converging Variant of Bi-CG for the Solution of Nonsymmetric Linear Systems*, SIAM Journal on Scientific and Statistical Computing, 13, 631

Dermer C. D., 1986, *Secondary production of neutral pi-mesons and the diffuse galactic gamma radiation*, A&A, 157, 223

Dermer C. D., Powale G., 2013, *Gamma rays from cosmic rays in supernova remnants*, A&A, 553, A34

Di Cintio A., Brook C. B., Macciò A. V., Stinson G. S., Knebe A., Dutton A. A., Wadsley J., 2014, *The dependence of dark matter profiles on the stellar-to-halo mass ratio: a prediction for cusps versus cores*, MNRAS, 437, 415

Di Matteo T., Perna R., Abel T., Rees M. J., 2002, *Radio Foregrounds for the 21 Centimeter Tomography of the Neutral Intergalactic Medium at High Redshifts*, apJ, 564, 576

Diehl R., et al., 2006, *Radioactive ^{26}Al from massive stars in the Galaxy*, Nature, 439, 45

Drury L. O., Voelk J. H., 1981, *Hydromagnetic shock structure in the presence of cosmic rays*, apJ, 248, 344

Dubois Y., Commerçon B., 2016, *An implicit scheme for solving the anisotropic diffusion of heat and cosmic rays in the RAMSES code*, A&A, 585, A138

Dubois Y., Teyssier R., 2008, *On the onset of galactic winds in quiescent star forming galaxies*, A&A, 477, 79

Dubois Y., Teyssier R., 2010, *Magnetised winds in dwarf galaxies*, A&A, 523, A72

Dubois Y., et al., 2014, *Dancing in the dark: galactic properties trace spin swings along the cosmic web*, MNRAS, 444, 1453

Dubois Y., Peirani S., Pichon C., Devriendt J., Gavazzi R., Welker C., Volonteri M., 2016, *The HORIZON-AGN simulation: morphological diversity of galaxies promoted by AGN feedback*, MNRAS, 463, 3948

Dubois Y., Commerçon B., Marcowith A., Brahimi L., 2019, *Shock-accelerated cosmic rays and streaming instability in the adaptive mesh refinement code Ramses*, A&A, 631, A121

Eilers A.-C., Davies F. B., Hennawi J. F., 2018, *The Opacity of the Intergalactic Medium Measured along Quasar Sightlines at $z \sim 6$*, apJ, 864, 53

Einstein A., 1916, *Die Grundlage der allgemeinen Relativitätstheorie*, Annalen der Physik, 354, 769

Eldridge J. J., Stanway E. R., Xiao L., McClelland L. A. S., Taylor G., Ng M., Greis S. M. L., Bray J. C., 2017, *Binary Population and Spectral Synthesis Version 2.1: Construction, Observational Verification, and New Results*, PASA, 34, e058

Ellison D. C., Patnaude D. J., Slane P., Raymond J., 2010, *Efficient Cosmic Ray Acceleration, Hydrodynamics, and Self-Consistent Thermal X-Ray Emission Applied to Supernova Remnant RX J1713.7-3946*, apJ, 712, 287

Emerick A., Bryan G. L., Mac Low M.-M., 2018, *Stellar Radiation Is Critical for Regulating Star Formation and Driving Outflows in Low-mass Dwarf Galaxies*, ApJ, 865, L22

Enßlin T. A., Pfrommer C., Springel V., Jubelgas M., 2007, *Cosmic ray physics in calculations of cosmological structure formation*, A&A, 473, 41

Evans C. R., Hawley J. F., 1988, *Simulation of Magnetohydrodynamic Flows: A Constrained Transport Model*, apJ, 332, 659

Evoli C., Yan H., 2014, *Cosmic Ray Propagation in Galactic Turbulence*, apJ, 782, 36

Fabian A. C., 2012, *Observational Evidence of Active Galactic Nuclei Feedback*, ARA&A, 50, 455

Fan X., et al., 2006, *Constraining the Evolution of the Ionizing Background and the Epoch of Reionization with z~6 Quasars. II. A Sample of 19 Quasars*, AJ, 132, 117

Farber R., Ruszkowski M., Yang H. Y. K., Zweibel E. G., 2018, *Impact of Cosmic-Ray Transport on Galactic Winds*, apJ, 856, 112

Farcy M., Rosdahl J., Dubois Y., Blaizot J., Martin-Alvarez S., 2022, *Radiation-magnetohydrodynamics simulations of cosmic ray feedback in disc galaxies*, MNRAS, 513, 5000

Federrath C., Klessen R. S., 2012, *The Star Formation Rate of Turbulent Magnetized Clouds: Comparing Theory, Simulations, and Observations*, apJ, 761, 156

Feix M. R., Bertrand P., 2005, *A Universal Model: The Vlasov Equation*, Transport Theory and Statistical Physics, 34, 7

Fensch J., et al., 2017, *High-redshift major mergers weakly enhance star formation*, MNRAS, 465, 1934

Ferland G. J., Korista K. T., Verner D. A., Ferguson J. W., Kingdon J. B., Verner E. M., 1998, *CLOUDY 90: Numerical Simulation of Plasmas and Their Spectra*, PASP, 110, 761

Fermi E., 1949, *On the Origin of the Cosmic Radiation*, Physical Review, 75, 1169

Finkelstein S. L., et al., 2015, *The Evolution of the Galaxy Rest-frame Ultraviolet Luminosity Function over the First Two Billion Years*, apJ, 810, 71

Finkelstein S. L., et al., 2019, *Conditions for Reionizing the Universe with a Low Galaxy Ionizing Photon Escape Fraction*, apJ, 879, 36

Fletcher A., Beck R., Shukurov A., Berkhuijsen E. M., Horellou C., 2011, *Magnetic fields and spiral arms in the galaxy M51*, MNRAS, 412, 2396

Flores R. A., Primack J. R., 1994, *Observational and Theoretical Constraints on Singular Dark Matter Halos*, ApJ, 427, L1

Friedmann A., 1922, *Über die Krümmung des Raumes*, Zeitschrift fur Physik, 10, 377

Fromang S., Hennebelle P., Teyssier R., 2006, *A high order Godunov scheme with constrained transport and adaptive mesh refinement for astrophysical magnetohydrodynamics*, A&A, 457, 371

Froning C. S., Green J. C., 2009, *The cosmic origins spectrograph: capabilities and prelaunch performance*, Ap&SS, 320, 181

Fryxell B., et al., 2000, *FLASH: An Adaptive Mesh Hydrodynamics Code for Modeling Astrophysical Thermonuclear Flashes*, ApJS, 131, 273

Furlong M., et al., 2015, *Evolution of galaxy stellar masses and star formation rates in the EAGLE simulations*, MNRAS, 450, 4486

Gabici S., 2022, *Low energy cosmic rays*, arXiv e-prints, p. arXiv:2203.14620

Gabor J. M., Bournaud F., 2014, *Active galactic nuclei-driven outflows without immediate quenching in simulations of high-redshift disc galaxies*, MNRAS, 441, 1615

Gabrielpillai A., Somerville R. S., Genel S., Rodriguez-Gomez V., Pandya V., Yung L. Y. A., Hernquist L., 2021, *Galaxy Formation in the Santa Cruz semi-analytic model compared with IllustrisTNG – I. Galaxy scaling relations, dispersions, and residuals at z=0*, arXiv e-prints, p. arXiv:2111.03077

Gaches B. A. L., Offner S. S. R., Bisbas T. G., 2019a, *The Astrochemical Impact of Cosmic Rays in Protoclusters. I. Molecular Cloud Chemistry*, apJ, 878, 105

Gaches B. A. L., Offner S. S. R., Bisbas T. G., 2019b, *The Astrochemical Impact of Cosmic Rays in Protoclusters. II. CI-to-H_2 and CO-to-H_2 Conversion Factors*, apJ, 883, 190

Gaggero D., Maccione L., Grasso D., Di Bernardo G., Evoli C., 2014, *PAMELA and AMS-02 e^+ and e^- spectra are reproduced by three-dimensional cosmic-ray modeling*, Phys. Rev. D, 89, 083007

Gaisser T. K., Stanev T., 2006, *High-energy cosmic rays*, Nucl. Phys. A, 777, 98

Gaisser T. K., Stanev T., Tilav S., 2013, *Cosmic ray energy spectrum from measurements of air showers*, Frontiers of Physics, 8, 748

Gao L., Yoshida N., Abel T., Frenk C. S., Jenkins A., Springel V., 2007, *The first generation of stars in the Λ cold dark matter cosmology*, MNRAS, 378, 449

Gardner J. P., et al., 2006, *The James Webb Space Telescope*, Space Sci. Rev., 123, 485

Garel T., Blaizot J., Rosdahl J., Michel-Dansac L., Haehnelt M. G., Katz H., Kimm T., Verhamme A., 2021, *Ly α as a tracer of cosmic reionization in the SPHINX radiation-hydrodynamics cosmological simulation*, MNRAS, 504, 1902

Ghosh A., Prasad J., Bharadwaj S., Ali S. S., Chengalur J. N., 2012, *Characterizing foreground for redshifted 21 cm radiation: 150 MHz Giant Metrewave Radio Telescope observations*, MNRAS, 426, 3295

Gingold R. A., Monaghan J. J., 1977, *Smoothed particle hydrodynamics: theory and application to non-spherical stars.*, MNRAS, 181, 375

Ginzburg V. L., Syrovatskii S. I., 1964, *The Origin of Cosmic Rays*. New York: Macmillan

Girichidis P., Naab T., Hanasz M., Walch S., 2018, *Cooler and smoother - the impact of cosmic rays on the phase structure of galactic outflows*, MNRAS, 479, 3042

Girichidis P., Pfrommer C., Pakmor R., Springel V., 2022, *Spectrally resolved cosmic rays - II. Momentum-dependent cosmic ray diffusion drives powerful galactic winds*, MNRAS, 510, 3917

Gnat O., Sternberg A., 2007, *Time-dependent Ionization in Radiatively Cooling Gas*, ApJS, 168, 213

Gnedin N. Y., Abel T., 2001, *Multi-dimensional cosmological radiative transfer with a Variable Eddington Tensor formalism*, New A, 6, 437

Gonnet P., Schaller M., Theuns T., Chalk A. B. G., 2013, *SWIFT: Fast algorithms for multi-resolution SPH on multi-core architectures*, arXiv e-prints, p. arXiv:1309.3783

González-Alfonso E., et al., 2013, *Excited OH^+, H_2O^+, and H_3O^+ in NGC 4418 and Arp 220*, A&A, 550, A25

González-Alfonso E., et al., 2018, *Outflowing OH^+ in Markarian 231: The Ionization Rate of the Molecular Gas*, apJ, 857, 66

Goto T., Utsumi Y., Walsh J. R., Hattori T., Miyazaki S., Yamauchi C., 2012, *Spectroscopy of the spatially extended Lyα emission around a quasar at z= 6.4*, MNRAS, 421, L77

Grand R. J. J., et al., 2017, *The Auriga Project: the properties and formation mechanisms of disc galaxies across cosmic time*, MNRAS, 467, 179

Grazian A., et al., 2017, *Lyman continuum escape fraction of faint galaxies at z 3.3 in the CANDELS/GOODS-North, EGS, and COSMOS fields with LBC*, A&A, 602, A18

Grazian A., et al., 2018, *The contribution of faint AGNs to the ionizing background at z=4*, A&A, 613, A44

Green J. C., et al., 2012, *The Cosmic Origins Spectrograph*, apJ, 744, 60

Greig B., Mesinger A., 2017, *Simultaneously constraining the astrophysics of reionization and the epoch of heating with 21CMMC*, MNRAS, 472, 2651

Greig B., Mesinger A., Bañados E., 2019, *Constraints on reionization from the z = 7.5 QSO ULASJ1342+0928*, MNRAS, 484, 5094

Greisen K., 1966, *End to the Cosmic-Ray Spectrum?*, Phys. Rev. Lett., 16, 748

Grenier I. A., Black J. H., Strong A. W., 2015, *The Nine Lives of Cosmic Rays in Galaxies*, ARA&A, 53, 199

Gunn J. E., Peterson B. A., 1965, *On the Density of Neutral Hydrogen in Intergalactic Space.*, apJ, 142, 1633

Guo F., Oh S. P., 2008, *Feedback heating by cosmic rays in clusters of galaxies*, MNRAS, 384, 251

H. E. S. S. Collaboration et al., 2018, *Detailed spectral and morphological analysis of the shell type supernova remnant RCW 86*, A&A, 612, A4

Hahn O., Abel T., 2011, *Multi-scale initial conditions for cosmological simulations*, MNRAS, 415, 2101

Han J. L., 2017, *Observing Interstellar and Intergalactic Magnetic Fields*, ARA&A, 55, 111

Han J. L., Qiao G. J., 1994, *The magnetic field in the disk of our Galaxy*, A&A, 288, 759

Hanasz M., Lesch H., Naab T., Gawryszczak A., Kowalik K., Wóltański D., 2013, *Cosmic Rays Can Drive Strong Outflows from Gas-rich High-redshift Disk Galaxies*, ApJ, 777, L38

Hanasz M., Strong A. W., Girichidis P., 2021, *Simulations of cosmic ray propagation*, Living Reviews in Computational Astrophysics, 7, 2

Harikane Y., et al., 2018, *GOLDRUSH. II. Clustering of galaxies at $z \sim 4$-6 revealed with the half-million dropouts over the 100 deg^2 area corresponding to 1 Gpc^3*, PASJ, 70, S11

Heckman T. M., Lehnert M. D., Strickland D. K., Armus L., 2000, *Absorption-Line Probes of Gas and Dust in Galactic Superwinds*, ApJS, 129, 493

Helder E. A., Vink J., Bykov A. M., Ohira Y., Raymond J. C., Terrier R., 2012, *Observational Signatures of Particle Acceleration in Supernova Remnants*, Space Sci. Rev., 173, 369

Helder E. A., Vink J., Bamba A., Bleeker J. A. M., Burrows D. N., Ghavamian P., Yamazaki R., 2013, *Proper motions of Hα filaments in the supernova remnant RCW 86*, MNRAS, 435, 910

Hess V. F., 1912, *Über Beobachtungen der durchdringenden Strahlung bei sieben Freiballonfahrten*, Physikalische Zeitschrift, 13, 1084

Hillas A. M., 1984, *The Origin of Ultra-High-Energy Cosmic Rays*, ARA&A, 22, 425

Hillas A. M., 2005, *TOPICAL REVIEW: Can diffusive shock acceleration in supernova remnants account for high-energy galactic cosmic rays?*, Journal of Physics G Nuclear Physics, 31, R95

Hinshaw G., et al., 2013, *Nine-year Wilkinson Microwave Anisotropy Probe (WMAP) Observations: Cosmological Parameter Results*, ApJS, 208, 19

Hockney R. W., Eastwood J. W., 1981, *Computer Simulation Using Particles*. New York: McGraw-Hill

Hogan C. J., Rees M. J., 1979, *Spectral appearance of non-uniform gas at high z.*, MNRAS, 188, 791

Holdship J., et al., 2022, *Energizing Star Formation: The Cosmic Ray Ionization Rate in NGC 253 Derived From ALCHEMI Measurements of H_3O^+ and SO*, arXiv e-prints, p. arXiv:2204.03668

Holguin F., Ruszkowski M., Lazarian A., Farber R., Yang H. Y. K., 2019, *Role of cosmic-ray streaming and turbulent damping in driving galactic winds*, MNRAS, 490, 1271

Hopkins P. F., 2015, *A new class of accurate, mesh-free hydrodynamic simulation methods*, MNRAS, 450, 53

Hopkins P. F., Quataert E., Murray N., 2011, *Self-regulated star formation in galaxies via momentum input from massive stars*, MNRAS, 417, 950

Hopkins P. F., Quataert E., Murray N., 2012a, *The structure of the interstellar medium of star-forming galaxies*, MNRAS, 421, 3488

Hopkins P. F., Quataert E., Murray N., 2012b, *Stellar feedback in galaxies and the origin of galaxy-scale winds*, MNRAS, 421, 3522

Hopkins P. F., Kereš D., Oñorbe J., Faucher-Giguère C.-A., Quataert E., Murray N., Bullock J. S., 2014, *Galaxies on FIRE (Feedback In Realistic Environments): stellar feedback explains cosmologically inefficient star formation*, MNRAS, 445, 581

Hopkins P. F., et al., 2018, *FIRE-2 simulations: physics versus numerics in galaxy formation*, MNRAS, 480, 800

Hopkins P. F., Grudić M. Y., Wetzel A., Kereš D., Faucher-Giguère C.-A., Ma X., Murray N., Butcher N., 2020a, *Radiative stellar feedback in galaxy formation: Methods and physics*, MNRAS, 491, 3702

Hopkins P. F., et al., 2020b, *But what about...: cosmic rays, magnetic fields, conduction, and viscosity in galaxy formation*, MNRAS, 492, 3465

Hopkins P. F., Squire J., Butsky I. S., Ji S., 2021a, *Standard Self-Confinement and Extrinsic Turbulence Models for Cosmic Ray Transport are Fundamentally Incompatible with Observations*, arXiv e-prints, p. arXiv:2112.02153

Hopkins P. F., Chan T. K., Ji S., Hummels C. B., Kereš D., Quataert E., Faucher-Giguère C.-A., 2021b, *Cosmic ray driven outflows to Mpc scales from L_* galaxies*, MNRAS, 501, 3640

Hopkins P. F., Chan T. K., Squire J., Quataert E., Ji S., Kereš D., Faucher-Giguère C.-A., 2021c, *Effects of different cosmic ray transport models on galaxy formation*, MNRAS, 501, 3663

Hubble E. P., 1926, *Extragalactic nebulae.*, apJ, 64, 321

Hubble E., 1929, *A Relation between Distance and Radial Velocity among Extra-Galactic Nebulae*, Proceedings of the National Academy of Science, 15, 168

Hutter A., Dayal P., Legrand L., Gottlöber S., Yepes G., 2021, *Astraeus - III. The environment and physical properties of reionization sources*, MNRAS, 506, 215

Iben I. J., Tutukov A. V., 1984, *Supernovae of type I as end products of the evolution of binaries with components of moderate initial mass.*, ApJS, 54, 335

Iliev I. T., Mellema G., Ahn K., Shapiro P. R., Mao Y., Pen U.-L., 2014, *Simulating cosmic reionization: how large a volume is large enough?*, MNRAS, 439, 725

Inoue A. K., Iwata I., 2008, *A Monte Carlo simulation of the intergalactic absorption and the detectability of the Lyman continuum from distant galaxies*, MNRAS, 387, 1681

Inoue A. K., et al., 2018, *SILVERRUSH. VI. A simulation of Lyα emitters in the reionization epoch and a comparison with Subaru Hyper Suprime-Cam survey early data*, PASJ, 70, 55

Ipavich F. M., 1975, *Galactic winds driven by cosmic rays.*, apJ, 196, 107

Ishigaki M., Kawamata R., Ouchi M., Oguri M., Shimasaku K., Ono Y., 2018, *Full-data Results of Hubble Frontier Fields: UV Luminosity Functions at $z \sim$ 6-10 and a Consistent Picture of Cosmic Reionization*, apJ, 854, 73

Izotov Y. I., Schaerer D., Thuan T. X., Worseck G., Guseva N. G., Orlitová I., Verhamme A., 2016, *Detection of high Lyman continuum leakage from four low-redshift compact star-forming galaxies*, MNRAS, 461, 3683

Jacob S., Pakmor R., Simpson C. M., Springel V., Pfrommer C., 2018, *The dependence of cosmic ray-driven galactic winds on halo mass*, MNRAS, 475, 570

Jacobs H., Mertsch P., Phan V. H. M., 2021, *Self-confinement of low-energy cosmic rays around supernova remnants*, arXiv e-prints, p. arXiv:2112.09708

Jana R., Gupta S., Nath B. B., 2020, *Role of cosmic rays in the early stages of galactic outflows*, MNRAS, 497, 2623

Jelić V., et al., 2008, *Foreground simulations for the LOFAR-epoch of reionization experiment*, MNRAS, 389, 1319

Ji S., et al., 2020, *Properties of the circumgalactic medium in cosmic ray-dominated galaxy haloes*, MNRAS, 496, 4221

Jiang L., et al., 2022, *Definitive upper bound on the negligible contribution of quasars to cosmic reionization*, Nature Astronomy

Jokipii J. R., 1966, *Cosmic-Ray Propagation. I. Charged Particles in a Random Magnetic Field*, apJ, 146, 480

Jones T. W., Kang H., 2005, *An efficient numerical scheme for simulating particle acceleration in evolving cosmic-ray modified shocks*, Astroparticle Physics, 24, 75

Jubelgas M., Springel V., Enßlin T., Pfrommer C., 2008, *Cosmic ray feedback in hydrodynamical simulations of galaxy formation*, A&A, 481, 33

Kakiichi K., et al., 2018, *The role of galaxies and AGN in reionizing the IGM - I. Keck spectroscopy of $5 < z < 7$ galaxies in the QSO field J1148+5251*, MNRAS, 479, 43

Kalberla P. M. W., Kerp J., 2009, *The Hi Distribution of the Milky Way*, ARA&A, 47, 27

Kalberla P. M. W., Dedes L., Kerp J., Haud U., 2007, *Dark matter in the Milky Way. II. The HI gas distribution as a tracer of the gravitational potential*, A&A, 469, 511

Kang H., Jones T. W., 2006, *Numerical studies of diffusive shock acceleration at spherical shocks*, Astroparticle Physics, 25, 246

Kannan R., Vogelsberger M., Marinacci F., McKinnon R., Pakmor R., Springel V., 2019, *AREPO-RT: radiation hydrodynamics on a moving mesh*, MNRAS, 485, 117

Katz N., 1992, *Dissipational Galaxy Formation. II. Effects of Star Formation*, apJ, 391, 502

Katz N., Weinberg D. H., Hernquist L., 1996, *Cosmological Simulations with TreeSPH*, ApJS, 105, 19

Katz H., Kimm T., Sijacki D., Haehnelt M. G., 2017, *Interpreting ALMA observations of the ISM during the epoch of reionization*, MNRAS, 468, 4831

Katz H., et al., 2020, *How to quench a dwarf galaxy: The impact of inhomogeneous reionization on dwarf galaxies and cosmic filaments*, MNRAS, 494, 2200

Katz H., et al., 2021, *Introducing SPHINX-MHD: the impact of primordial magnetic fields on the first galaxies, reionization, and the global 21-cm signal*, MNRAS, 507, 1254

Katz H., et al., 2022, *The nature of high [O III]$_{88\mu m}$/[C II]$_{158\mu m}$ galaxies in the epoch of reionization: Low carbon abundance and a top-heavy IMF?*, MNRAS, 510, 5603

Kawamata R., Ishigaki M., Shimasaku K., Oguri M., Ouchi M., Tanigawa S., 2018, *Size-Luminosity Relations and UV Luminosity Functions at z = 6-9 Simultaneously Derived from the Complete Hubble Frontier Fields Data*, apJ, 855, 4

Keating L. C., Kulkarni G., Haehnelt M. G., Chardin J., Aubert D., 2020, *Constraining the second half of reionization with the Ly β forest*, MNRAS, 497, 906

Kennicutt Robert C. J., 1998, *Star Formation in Galaxies Along the Hubble Sequence*, ARA&A, 36, 189

Kennicutt R. C., Evans N. J., 2012, *Star Formation in the Milky Way and Nearby Galaxies*, ARA&A, 50, 531

Kereš D., Katz N., Weinberg D. H., Davé R., 2005, *How do galaxies get their gas?*, MNRAS, 363, 2

Kim C.-G., Ostriker E. C., 2015, *Momentum Injection by Supernovae in the Interstellar Medium*, apJ, 802, 99

Kim J.-h., et al., 2014, *The AGORA High-resolution Galaxy Simulations Comparison Project*, ApJS, 210, 14

Kim J.-h., et al., 2016, *The AGORA High-resolution Galaxy Simulations Comparison Project. II. Isolated Disk Test*, apJ, 833, 202

Kimm T., Cen R., 2014, *Escape Fraction of Ionizing Photons during Reionization: Effects due to Supernova Feedback and Runaway OB Stars*, apJ, 788, 121

Kimm T., Cen R., Devriendt J., Dubois Y., Slyz A., 2015, *Towards simulating star formation in turbulent high-z galaxies with mechanical supernova feedback*, MNRAS, 451, 2900

Kimm T., Katz H., Haehnelt M., Rosdahl J., Devriendt J., Slyz A., 2017, *Feedback-regulated star formation and escape of LyC photons from mini-haloes during reionization*, MNRAS, 466, 4826

King A., Pounds K., 2015, *Powerful Outflows and Feedback from Active Galactic Nuclei*, ARA&A, 53, 115

Kissmann R., 2014, *PICARD: A novel code for the Galactic Cosmic Ray propagation problem*, Astroparticle Physics, 55, 37

Knebe A., et al., 2015, *nIFTy cosmology: comparison of galaxy formation models*, MNRAS, 451, 4029

Komatsu E., et al., 2011, *Seven-year Wilkinson Microwave Anisotropy Probe (WMAP) Observations: Cosmological Interpretation*, ApJS, 192, 18

Koopmans L., et al., 2015, in Advancing Astrophysics with the Square Kilometre Array (AASKA14). p. 1 (arXiv:1505.07568), doi:10.22323/1.215.0001

Kormendy J., Kennicutt Robert C. J., 2004, *Secular Evolution and the Formation of Pseudobulges in Disk Galaxies*, ARA&A, 42, 603

Kounine A., 2012, *The Alpha Magnetic Spectrometer on the International Space Station*, International Journal of Modern Physics E, 21, 1230005

Kravtsov A. V., Klypin A. A., Khokhlov A. M., 1997, *Adaptive Refinement Tree: A New High-Resolution N-Body Code for Cosmological Simulations*, ApJS, 111, 73

Kravtsov A. V., Berlind A. A., Wechsler R. H., Klypin A. A., Gottlöber S., Allgood B., Primack J. R., 2004, *The Dark Side of the Halo Occupation Distribution*, apJ, 609, 35

Kroupa P., 2001, *On the variation of the initial mass function*, MNRAS, 322, 231

Krumholz M. R., Federrath C., 2019, *The Role of Magnetic Fields in Setting the Star Formation Rate and the Initial Mass Function*, Frontiers in Astronomy and Space Sciences, 6, 7

Krumholz M. R., Tan J. C., 2007, *Slow Star Formation in Dense Gas: Evidence and Implications*, apJ, 654, 304

Krymskii G. F., 1977, *A regular mechanism for the acceleration of charged particles on the front of a shock wave*, Akademiia Nauk SSSR Doklady, 234, 1306

Kudritzki R.-P., Puls J., 2000, *Winds from Hot Stars*, ARA&A, 38, 613

Kulkarni G., Keating L. C., Haehnelt M. G., Bosman S. E. I., Puchwein E., Chardin J., Aubert D., 2019, *Large Ly α opacity fluctuations and low CMB τ in models of late reionization with large islands of neutral hydrogen extending to z ¡ 5.5*, MNRAS, 485, L24

Kulsrud R. M., 2005, *Plasma physics for astrophysics*. Princeton University Press

Kulsrud R., Pearce W. P., 1969, *The Effect of Wave-Particle Interactions on the Propagation of Cosmic Rays*, apJ, 156, 445

Kusakabe H., et al., 2020, *The MUSE Hubble Ultra Deep Field Survey. XIV. Evolution of the Lyα emitter fraction from z = 3 to z = 6*, A&A, 638, A12

Lapi A., Danese L., 2015, *Cold or warm? Constraining dark matter with primeval galaxies and cosmic reionization after Planck*, J. Cosmology Astropart. Phys., 2015, 003

Larson R. B., 2005, *Thermal physics, cloud geometry and the stellar initial mass function*, MNRAS, 359, 211

Larson R. B., Tinsley B. M., Caldwell C. N., 1980, *The evolution of disk galaxies and the origin of S0 galaxies*, apJ, 237, 692

Larson D., et al., 2011, *Seven-year Wilkinson Microwave Anisotropy Probe (WMAP) Observations: Power Spectra and WMAP-derived Parameters*, ApJS, 192, 16

Laursen P., Sommer-Larsen J., Andersen A. C., 2009, *Lyα Radiative Transfer with Dust: Escape Fractions from Simulated High-Redshift Galaxies*, apJ, 704, 1640

Lazarian A., 2016, *Damping of Alfvén Waves by Turbulence and Its Consequences: From Cosmic-ray Streaming to Launching Winds*, apJ, 833, 131

Lemaître G., 1927, *Un Univers homogène de masse constante et de rayon croissant rendant compte de la vitesse radiale des nébuleuses extra-galactiques*, Annales de la Société Scientifique de Bruxelles, 47, 49

Levermore C. D., 1984, *Relating Eddington factors to flux limiters.*, J. Quant. Spec. Radiat. Transf., 31, 149

Li A., Draine B. T., 2001, *Infrared Emission from Interstellar Dust. II. The Diffuse Interstellar Medium*, apJ, 554, 778

Licquia T. C., Newman J. A., 2015, *Improved Estimates of the Milky Way's Stellar Mass and Star Formation Rate from Hierarchical Bayesian Meta-Analysis*, apJ, 806, 96

Livermore R. C., Finkelstein S. L., Lotz J. M., 2017, *Directly Observing the Galaxies Likely Responsible for Reionization*, apJ, 835, 113

Lucy L. B., 1977, *A numerical approach to the testing of the fission hypothesis.*, AJ, 82, 1013

Ma X., Kasen D., Hopkins P. F., Faucher-Giguère C.-A., Quataert E., Kereš D., Murray N., 2015, *The difficulty of getting high escape fractions of ionizing photons from high-redshift galaxies: a view from the FIRE cosmological simulations*, MNRAS, 453, 960

Ma X., et al., 2018, *Simulating galaxies in the reionization era with FIRE-2: galaxy scaling relations, stellar mass functions, and luminosity functions*, MNRAS, 478, 1694

Madau P., Dickinson M., 2014, *Cosmic Star-Formation History*, ARA&A, 52, 415

Madau P., Haardt F., 2015, *Cosmic Reionization after Planck: Could Quasars Do It All?*, ApJ, 813, L8

Madau P., Meiksin A., Rees M. J., 1997, *21 Centimeter Tomography of the Intergalactic Medium at High Redshift*, apJ, 475, 429

Madau P., Haardt F., Rees M. J., 1999, *Radiative Transfer in a Clumpy Universe. III. The Nature of Cosmological Ionizing Sources*, apJ, 514, 648

Maraston C., 2005, *Evolutionary population synthesis: models, analysis of the ingredients and application to high-z galaxies*, MNRAS, 362, 799

Marcowith A., Ferrand G., Grech M., Meliani Z., Plotnikov I., Walder R., 2020, *Multi-scale simulations of particle acceleration in astrophysical systems*, Living Reviews in Computational Astrophysics, 6, 1

Martin C. L., 1999, *Properties of Galactic Outflows: Measurements of the Feedback from Star Formation*, apJ, 513, 156

Martin-Alvarez S., Slyz A., Devriendt J., Gómez-Guijarro C., 2020, *How primordial magnetic fields shrink galaxies*, MNRAS, 495, 4475

Martin D. C., et al., 2007, *The UV-Optical Galaxy Color-Magnitude Diagram. III. Constraints on Evolution from the Blue to the Red Sequence*, ApJS, 173, 342

Mason C. A., Treu T., Dijkstra M., Mesinger A., Trenti M., Pentericci L., de Barros S., Vanzella E., 2018, *The Universe Is Reionizing at $z \sim 7$: Bayesian Inference of the IGM Neutral Fraction Using Lyα Emission from Galaxies*, apJ, 856, 2

Mason C. A., et al., 2019, *Inferences on the timeline of reionization at $z \sim 8$ from the KMOS Lens-Amplified Spectroscopic Survey*, MNRAS, 485, 3947

Mauerhofer V., Verhamme A., Blaizot J., Garel T., Kimm T., Michel-Dansac L., Rosdahl J., 2021, *UV absorption lines and their potential for tracing the Lyman continuum escape fraction*, A&A, 646, A80

Maurin D., 2020, *USINE: Semi-analytical models for Galactic cosmic-ray propagation*, Computer Physics Communications, 247, 106942

McGreer I. D., Mesinger A., D'Odorico V., 2015, *Model-independent evidence in favour of an end to reionization by $z \approx 6$*, MNRAS, 447, 499

McKee C. F., 1974, *X-Ray Emission from an Inward-Propagating Shock in Young Supernova Remnants*, apJ, 188, 335

Meiksin A. A., 2009, *The physics of the intergalactic medium*, Reviews of Modern Physics, 81, 1405

Mellema G., Koopmans L., Shukla H., Datta K. K., Mesinger A., Majumdar S., 2015, in Advancing Astrophysics with the Square Kilometre Array (AASKA14). p. 10 (arXiv:1501.04203)

Menon H., Wesolowski L., Zheng G., Jetley P., Kale L., Quinn T., Governato F., 2015, *Adaptive techniques for clustered N-body cosmological simulations*, Computational Astrophysics and Cosmology, 2, 1

Meštrić U., et al., 2020, *Outside the Lyman-break box: detecting Lyman continuum emitters at 3.5 ¡ z ¡ 5.1 with CLAUDS*, MNRAS, 494, 4986

Micelotta E. R., Matsuura M., Sarangi A., 2018, *Dust in Supernovae and Supernova Remnants II: Processing and Survival*, Space Sci. Rev., 214, 53

Michel-Dansac L., Blaizot J., Garel T., Verhamme A., Kimm T., Trebitsch M., 2020, *RASCAS: RAdiation SCattering in Astrophysical Simulations*, A&A, 635, A154

Mignone A., Zanni C., Tzeferacos P., van Straalen B., Colella P., Bodo G., 2012, *The PLUTO Code for Adaptive Mesh Computations in Astrophysical Fluid Dynamics*, ApJS, 198, 7

Mihalas D., Mihalas B. W., 1984, *Foundations of radiation hydrodynamics*. Oxford University Press

Millikan R. A., 1925, *High Frequency Rays of Cosmic Origin*, Nature, 116, 823

Miniati F., 2001, *COSMOCR: A numerical code for cosmic ray studies in computational cosmology*, Computer Physics Communications, 141, 17

Mitchell P. D., Blaizot J., Devriendt J., imm2017imm T., Michel-Dansac L., Rosdahl J., Slyz A., 2018, *Gas flows in the circumgalactic medium around simulated high-redshift galaxies*, MNRAS, 474, 4279

Mo H., van den Bosch F. C., White S., 2010, *Galaxy Formation and Evolution*. Cambridge

Moore B., 1994, *Evidence against dissipation-less dark matter from observations of galaxy haloes*, Nature, 370, 629

Morgan W. W., Keenan P. C., Kellman E., 1943, *An atlas of stellar spectra, with an outline of spectral classification*. Astrophysical Monographs, The University of Chicago Press

Morlino G., 2017, in Alsabti A. W., Murdin P., eds, , Handbook of Supernovae. Springer International, p. 1711, doi:10.1007/978-3-319-21846-5_11

Morlino G., Caprioli D., 2012, *Strong evidence for hadron acceleration in Tycho's supernova remnant*, A&A, 538, A81

Mukherjee D., Bicknell G. V., Wagner A. Y., Sutherland R. S., Silk J., 2018, *Relativistic jet feedback - III. Feedback on gas discs*, MNRAS, 479, 5544

Murray N., Quataert E., Thompson T. A., 2005, *On the Maximum Luminosity of Galaxies and Their Central Black Holes: Feedback from Momentum-driven Winds*, apJ, 618, 569

Murray N., Quataert E., Thompson T. A., 2010, *The Disruption of Giant Molecular Clouds by Radiation Pressure & the Efficiency of Star Formation in Galaxies*, apJ, 709, 191

Naab T., Ostriker J. P., 2017, *Theoretical Challenges in Galaxy Formation*, ARA&A, 55, 59

Naidu R. P., Tacchella S., Mason C. A., Bose S., Oesch P. A., Conroy C., 2020, *Rapid Reionization by the Oligarchs: The Case for Massive, UV-bright, Star-forming Galaxies with High Escape Fractions*, apJ, 892, 109

Nasir F., D'Aloisio A., 2020, *Observing the tail of reionization: neutral islands in the z = 5.5 Lyman-α forest*, MNRAS, 494, 3080

Nestor D. B., Shapley A. E., Kornei K. A., Steidel C. C., Siana B., 2013, *A Refined Estimate of the Ionizing Emissivity from Galaxies at z ~= 3: Spectroscopic Follow-up in the SSA22a Field*, apJ, 765, 47

Oesch P. A., Bouwens R. J., Illingworth G. D., Labbé I., Stefanon M., 2018, *The Dearth of z ∼ 10 Galaxies in All HST Legacy Fields—The Rapid Evolution of the Galaxy Population in the First 500 Myr*, apJ, 855, 105

Oke J. B., Gunn J. E., 1983, *Secondary standard stars for absolute spectrophotometry.*, apJ, 266, 713

Ouchi M., et al., 2018, *Systematic Identification of LAEs for Visible Exploration and Reionization Research Using Subaru HSC (SILVERRUSH). I. Program strategy and clustering properties of ∼2000 Lyα emitters at z = 6-7 over the 0.3-0.5 Gpc^2 survey area*, PASJ, 70, S13

Paardekooper J.-P., Khochfar S., Dalla Vecchia C., 2015, *The First Billion Years project: the escape fraction of ionizing photons in the epoch of reionization*, MNRAS, 451, 2544

Padoan P., Nordlund Å., 2011, *The Star Formation Rate of Supersonic Magnetohydrodynamic Turbulence*, apJ, 730, 40

Padovani M., Ivlev A. V., Galli D., Caselli P., 2018, *Cosmic-ray ionisation in circumstellar discs*, A&A, 614, A111

Padovani M., et al., 2020, *Impact of Low-Energy Cosmic Rays on Star Formation*, Space Sci. Rev., 216, 29

Pagano L., Delouis J. M., Mottet S., Puget J. L., Vibert L., 2020, *Reionization optical depth determination from Planck HFI data with ten percent accuracy*, A&A, 635, A99

Paglione T. A. D., Abrahams R. D., 2012, *Properties of nearby Starburst Galaxies Based on their Diffuse Gamma-Ray Emission*, apJ, 755, 106

Pakmor R., Springel V., 2013, *Simulations of magnetic fields in isolated disc galaxies*, MNRAS, 432, 176

Pakmor R., Kromer M., Röpke F. K., Sim S. A., Ruiter A. J., Hillebrandt W., 2010, *Sub-luminous type Ia supernovae from the mergers of equal-mass white dwarfs with mass ~0.9M_{solar}*, Nature, 463, 61

Pakmor R., Kromer M., Taubenberger S., Sim S. A., Röpke F. K., Hillebrandt W., 2012, *Normal Type Ia Supernovae from Violent Mergers of White Dwarf Binaries*, ApJ, 747, L10

Pakmor R., Pfrommer C., Simpson C. M., Springel V., 2016, *Galactic Winds Driven by Isotropic and Anisotropic Cosmic-Ray Diffusion in Disk Galaxies*, ApJ, 824, L30

Parker E. N., 1965, *The passage of energetic charged particles through interplanetary space*, Planet. Space Sci., 13, 9

Peebles P. J. E., Schramm D. N., Turner E. L., Kron R. G., 1994, *The Evolution of the Universe*, Scientific American, 271, 52

Pentericci L., et al., 2011, *Spectroscopic Confirmation of z ~7 Lyman Break Galaxies: Probing the Earliest Galaxies and the Epoch of Reionization*, apJ, 743, 132

Perlmutter S., et al., 1999, *Measurements of Ω and Λ from 42 High-Redshift Supernovae*, apJ, 517, 565

Pfrommer C., Pakmor R., Schaal K., Simpson C. M., Springel V., 2017, *Simulating cosmic ray physics on a moving mesh*, MNRAS, 465, 4500

Planck Collaboration et al., 2014, *Planck 2013 results. I. Overview of products and scientific results*, A&A, 571, A1

Planck Collaboration et al., 2016, *Planck 2015 results. XIX. Constraints on primordial magnetic fields*, A&A, 594, A19

Planck Collaboration et al., 2020, *Planck 2018 results. VI. Cosmological parameters*, A&A, 641, A6

Potgieter M. S., 2013, *Solar Modulation of Cosmic Rays*, Living Reviews in Solar Physics, 10, 3

Press W. H., Schechter P., 1974, *Formation of Galaxies and Clusters of Galaxies by Self-Similar Gravitational Condensation*, apJ, 187, 425

Puls J., et al., 1996, *O-star mass-loss and wind momentum rates in the Galaxy and the Magellanic Clouds Observations and theoretical predictions.*, A&A, 305, 171

Putze A., Maurin D., Donato F., 2011, *p, He, and C to Fe cosmic-ray primary fluxes in diffusion models. Source and transport signatures on fluxes and ratios*, A&A, 526, A101

Rasera Y., Teyssier R., 2006, *The history of the baryon budget. Cosmic logistics in a hierarchical universe*, A&A, 445, 1

Rauch M., 1998, *The Lyman Alpha Forest in the Spectra of QSOs*, ARA&A, 36, 267

Razoumov A. O., Sommer-Larsen J., 2006, *Escape of Ionizing Radiation from Star-forming Regions in Young Galaxies*, ApJ, 651, L89

Read J. I., Iorio G., Agertz O., Fraternali F., 2017, *The stellar mass-halo mass relation of isolated field dwarfs: a critical test of ΛCDM at the edge of galaxy formation*, MNRAS, 467, 2019

Recchia S., 2021, *Cosmic ray driven galactic winds*, arXiv e-prints, p. arXiv:2101.02052

Reynoso E. M., Walsh A. J., 2015, *Radio spectral characteristics of the supernova remnant Puppis A and nearby sources*, MNRAS, 451, 3044

Richard J., Kneib J.-P., Ebeling H., Stark D. P., Egami E., Fiedler A. K., 2011, *Discovery of a possibly old galaxy at z= 6.027, multiply imaged by the massive cluster Abell 383*, MNRAS, 414, L31

Riess A. G., et al., 1998, *Observational Evidence from Supernovae for an Accelerating Universe and a Cosmological Constant*, AJ, 116, 1009

Roberts-Borsani G. W., Saintonge A., Masters K. L., Stark D. V., 2020, *Outflows in star-forming galaxies: Stacking analyses of resolved winds and the relation to their hosts' properties*, MNRAS, 493, 3081

Robertson B. E., et al., 2013, *New Constraints on Cosmic Reionization from the 2012 Hubble Ultra Deep Field Campaign*, apJ, 768, 71

Robitaille T. P., Whitney B. A., 2010, *The Present-Day Star Formation Rate of the Milky Way Determined from Spitzer-Detected Young Stellar Objects*, ApJ, 710, L11

Roca-Fàbrega S., et al., 2021, *The AGORA High-resolution Galaxy Simulations Comparison Project. III. Cosmological Zoom-in Simulation of a Milky Way-mass Halo*, apJ, 917, 64

Rodriguez-Gomez V., et al., 2016, *The stellar mass assembly of galaxies in the Illustris simulation: growth by mergers and the spatial distribution of accreted stars*, MNRAS, 458, 2371

Romanello M., Menci N., Castellano M., 2021, *The Epoch of Reionization in Warm Dark Matter Scenarios*, Universe, 7, 365

Rosdahl J., Teyssier R., 2015, *A scheme for radiation pressure and photon diffusion with the M1 closure in RAMSES-RT*, MNRAS, 449, 4380

Rosdahl J., Blaizot J., Aubert D., Stranex T., Teyssier R., 2013, *RAMSES-RT: radiation hydrodynamics in the cosmological context*, MNRAS, 436, 2188

Rosdahl J., Schaye J., Teyssier R., Agertz O., 2015, *Galaxies that shine: radiation-hydrodynamical simulations of disc galaxies*, MNRAS, 451, 34

Rosdahl J., Schaye J., Dubois Y., Kimm T., Teyssier R., 2017, *Snap, crackle, pop: sub-grid supernova feedback in AMR simulations of disc galaxies*, MNRAS, 466, 11

Rosdahl J., et al., 2018, *The SPHINX cosmological simulations of the first billion years: the impact of binary stars on reionization*, MNRAS, 479, 994

Rosdahl J., et al., 2022, *LyC escape from SPHINX galaxies in the Epoch of Reionization*, arXiv e-prints, p. arXiv:2207.03232

Rosen A., Bregman J. N., 1995, *Global Models of the Interstellar Medium in Disk Galaxies*, apJ, 440, 634

Ruszkowski M., Yang H. Y. K., Zweibel E., 2017, *Global Simulations of Galactic Winds Including Cosmic-ray Streaming*, apJ, 834, 208

Rutkowski M. J., et al., 2017, *The Lyman Continuum Escape Fraction of Emission Line-selected $z \sim 2.5$ Galaxies Is Less Than 15%*, ApJ, 841, L27

Sai H., et al., 2022, *Observations of the very young Type Ia Supernova 2019np with early-excess emission*, MNRAS, 514, 3541

Salem M., Bryan G. L., 2014, *Cosmic ray driven outflows in global galaxy disc models*, MNRAS, 437, 3312

Salem M., Bryan G. L., Corlies L., 2016, *Role of cosmic rays in the circumgalactic medium*, MNRAS, 456, 582

Salpeter E. E., 1955, *The Luminosity Function and Stellar Evolution.*, apJ, 121, 161

Sato T., Martin C. L., Noeske K. G., Koo D. C., Lotz J. M., 2009, *AEGIS: The Nature of the Host Galaxies of Low-Ionization Outflows at z ¡ 0.6*, apJ, 696, 214

Schaye J., et al., 2015, *The EAGLE project: simulating the evolution and assembly of galaxies and their environments*, MNRAS, 446, 521

Schenker M. A., Ellis R. S., Konidaris N. P., Stark D. P., 2014, *Line-emitting Galaxies beyond a Redshift of 7: An Improved Method for Estimating the Evolving Neutrality of the Intergalactic Medium*, apJ, 795, 20

Schlickeiser R., 2002, *Cosmic Ray Astrophysics*. Berlin: Springer

Schmidt M., 1959, *The Rate of Star Formation.*, apJ, 129, 243

Schroeder J., Mesinger A., Haiman Z., 2013, *Evidence of Gunn-Peterson damping wings in high-z quasar spectra: strengthening the case for incomplete reionization at $z \sim$ 6-7*, MNRAS, 428, 3058

Scott D., Rees M. J., 1990, *The 21-cm line at high redshift: a diagnostic for the origin of large scale structure*, MNRAS, 247, 510

Sedov L. I., 1959, *Similarity and Dimensional Methods in Mechanics*. CRC Press, 10th Edition

Semenov V. A., Kravtsov A. V., Gnedin N. Y., 2018, *How Galaxies Form Stars: The Connection between Local and Global Star Formation in Galaxy Simulations*, apJ, 861, 4

Semenov V. A., Kravtsov A. V., Caprioli D., 2021, *Cosmic-Ray Diffusion Suppression in Star-forming Regions Inhibits Clump Formation in Gas-rich Galaxies*, apJ, 910, 126

Shapley A. E., Steidel C. C., Pettini M., Adelberger K. L., 2003, *Rest-Frame Ultraviolet Spectra of z~3 Lyman Break Galaxies*, apJ, 588, 65

Sharma P., Hammett G. W., 2007, *Preserving monotonicity in anisotropic diffusion*, Journal of Computational Physics, 227, 123

Sharma P., Colella P., Martin D. F., 2009, *Numerical Implementation of Streaming Down the Gradient: Application to Fluid Modeling of Cosmic Rays and Saturated Conduction*, arXiv e-prints, p. arXiv:0909.5426

Shaw J. R., Lewis A., 2012, *Constraining primordial magnetism*, Phys. Rev. D, 86, 043510

Shaw A. K., Bharadwaj S., Mondal R., 2019, *The impact of non-Gaussianity on the error covariance for observations of the Epoch of Reionization 21-cm power spectrum*, MNRAS, 487, 4951

Shivaei I., et al., 2018, *The MOSDEF Survey: Direct Observational Constraints on the Ionizing Photon Production Efficiency, ξ_{ion}, at $z \sim 2$*, apJ, 855, 42

Shu F. H., Adams F. C., Lizano S., 1987, *Star formation in molecular clouds: observation and theory.*, ARA&A, 25, 23

Siana B., et al., 2010, *A Deep Hubble Space Telescope Search for Escaping Lyman Continuum Flux at z ~1.3: Evidence for an Evolving Ionizing Emissivity*, apJ, 723, 241

Silk J., Rees M. J., 1998, *Quasars and galaxy formation*, A&A, 331, L1

Smith A., Ma X., Bromm V., Finkelstein S. L., Hopkins P. F., Faucher-Giguère C.-A., Kereš D., 2019a, *The physics of Lyman α escape from high-redshift galaxies*, MNRAS, 484, 39

Smith M. C., Sijacki D., Shen S., 2019b, *Cosmological simulations of dwarfs: the need for ISM physics beyond SN feedback alone*, MNRAS, 485, 3317

Smith M. C., Bryan G. L., Somerville R. S., Hu C.-Y., Teyssier R., Burkhart B., Hernquist L., 2021, *Efficient early stellar feedback can suppress galactic outflows by reducing supernova clustering*, MNRAS, 506, 3882

Smoot G., et al., 1990, *COBE Differential Microwave Radiometers: Instrument Design and Implementation*, apJ, 360, 685

Smoot G. F., et al., 1992, *Structure in the COBE Differential Microwave Radiometer First-Year Maps*, ApJ, 396, L1

Sobacchi E., Mesinger A., 2015, *The clustering of Lyman α emitters at $z \approx 7$: implications for reionization and host halo masses*, MNRAS, 453, 1843

Somerville R. S., Davé R., 2015, *Physical Models of Galaxy Formation in a Cosmological Framework*, ARA&A, 53, 51

Sotillo-Ramos D., et al., 2021, *Galaxy and mass assembly (GAMA): The environmental impact on SFR and metallicity in galaxy groups*, MNRAS, 508, 1817

Spergel D. N., et al., 2003, *First-Year Wilkinson Microwave Anisotropy Probe (WMAP) Observations: Determination of Cosmological Parameters*, ApJS, 148, 175

Springel V., 2005, *The cosmological simulation code GADGET-2*, MNRAS, 364, 1105

Springel V., 2010a, *Smoothed Particle Hydrodynamics in Astrophysics*, ARA&A, 48, 391

Springel V., 2010b, *E pur si muove: Galilean-invariant cosmological hydrodynamical simulations on a moving mesh*, MNRAS, 401, 791

Springel V., Yoshida N., White S. D. M., 2001, *GADGET: a code for collisionless and gasdynamical cosmological simulations*, New A, 6, 79

Springel V., Di Matteo T., Hernquist L., 2005, *Modelling feedback from stars and black holes in galaxy mergers*, MNRAS, 361, 776

Stanway E. R., Eldridge J. J., 2018, *Re-evaluating old stellar populations*, MNRAS, 479, 75

Stanway E. R., Bunker A. J., McMahon R. G., 2003, *Lyman break galaxies and the star formation rate of the Universe at z~6*, MNRAS, 342, 439

Stanway E. R., Eldridge J. J., Becker G. D., 2016, *Stellar population effects on the inferred photon density at reionization*, MNRAS, 456, 485

Stefanon M., Bouwens R. J., Labbé I., Illingworth G. D., Gonzalez V., Oesch P. A., 2021, *Galaxy Stellar Mass Functions from z 10 to z 6 using the Deepest Spitzer/Infrared Array Camera Data: No Significant Evolution in the Stellar-to-halo Mass Ratio of Galaxies in the First Gigayear of Cosmic Time*, apJ, 922, 29

Steidel C. C., Erb D. K., Shapley A. E., Pettini M., Reddy N., Bogosavljević M., Rudie G. C., Rakic O., 2010, *The Structure and Kinematics of the Circumgalactic Medium from Far-ultraviolet Spectra of z ~= 2-3 Galaxies*, apJ, 717, 289

Steidel C. C., Bogosavljević M., Shapley A. E., Reddy N. A., Rudie G. C., Pettini M., Trainor R. F., Strom A. L., 2018, *The Keck Lyman Continuum Spectroscopic Survey (KLCS): The Emergent Ionizing Spectrum of Galaxies at $z \sim 3$*, apJ, 869, 123

Stinson G., Seth A., Katz N., Wadsley J., Governato F., Quinn T., 2006, *Star formation and feedback in smoothed particle hydrodynamic simulations - I. Isolated galaxies*, MNRAS, 373, 1074

Strömgren B., 1939, *The Physical State of Interstellar Hydrogen.*, apJ, 89, 526

Strong A. W., Moskalenko I. V., 1998, *Propagation of Cosmic-Ray Nucleons in the Galaxy*, apJ, 509, 212

Strong A. W., Moskalenko I. V., Ptuskin V. S., 2007, *Cosmic-Ray Propagation and Interactions in the Galaxy*, Annual Review of Nuclear and Particle Science, 57, 285

Strong A. W., Porter T. A., Digel S. W., Jóhannesson G., Martin P., Moskalenko I. V., Murphy E. J., Orlando E., 2010, *Global Cosmic-ray-related Luminosity and Energy Budget of the Milky Way*, ApJ, 722, L58

Su K. Y., Hopkins P. F., Hayward C. C., Faucher-Giguère C. A., Kereš D., Ma X., Robles V. H., 2017, *Feedback first: The surprisingly weak effects of magnetic fields, viscosity, conduction and metal diffusion on sub-L* galaxy formation*, MNRAS, 471, 144

Swordy S. P., 2001, *The Energy Spectra and Anisotropies of Cosmic Rays*, Space Sci. Rev., 99, 85

Tacconi L. J., et al., 2013, *Phibss: Molecular Gas Content and Scaling Relations in z ~1-3 Massive, Main-sequence Star-forming Galaxies*, apJ, 768, 74

Taylor G., 1950, *The Formation of a Blast Wave by a Very Intense Explosion. I. Theoretical Discussion*, Proceedings of the Royal Society of London Series A, 201, 159

Tegmark M., Silk J., Rees M. J., Blanchard A., Abel T., Palla F., 1997, *How Small Were the First Cosmological Objects?*, apJ, 474, 1

Teyssier R., 2002, *Cosmological hydrodynamics with adaptive mesh refinement. A new high resolution code called RAMSES*, A&A, 385, 337

Teyssier R., 2015, *Grid-Based Hydrodynamics in Astrophysical Fluid Flows*, ARA&A, 53, 325

Teyssier R., Fromang S., Dormy E., 2006, *Kinematic dynamos using constrained transport with high order Godunov schemes and adaptive mesh refinement*, Journal of Computational Physics, 218, 44

Teyssier R., Pontzen A., Dubois Y., Read J. I., 2013, *Cusp-core transformations in dwarf galaxies: observational predictions*, MNRAS, 429, 3068

Thomas T., Pfrommer C., Enßlin T., 2020, *Probing Cosmic-Ray Transport with Radio Synchrotron Harps in the Galactic Center*, ApJ, 890, L18

Thomas T., Pfrommer C., Pakmor R., 2022, *Cosmic ray-driven galactic winds: transport modes of cosmic rays and Alfvén-wave dark regions*, arXiv e-prints, p. arXiv:2203.12029

Thompson T. A., Fabian A. C., Quataert E., Murray N., 2015, *Dynamics of dusty radiation-pressure-driven shells and clouds: fast outflows from galaxies, star clusters, massive stars, and AGN*, MNRAS, 449, 147

Thornton K., Gaudlitz M., Janka H. T., Steinmetz M., 1998, *Energy Input and Mass Redistribution by Supernovae in the Interstellar Medium*, apJ, 500, 95

Toro E., 1997, *Riemann Solvers and Numerical Methods for Fluid Dynamics: A Practical Introduction*. Springer, `https://books.google.fr/books?id=6QFAAQAAIAAJ`

Torrey P., Vogelsberger M., Genel S., Sijacki D., Springel V., Hernquist L., 2014, *A model for cosmological simulations of galaxy formation physics: multi-epoch validation*, MNRAS, 438, 1985

Trebitsch M., Blaizot J., Rosdahl J., Devriendt J., Slyz A., 2017, *Fluctuating feedback-regulated escape fraction of ionizing radiation in low-mass, high-redshift galaxies*, MNRAS, 470, 224

Trebitsch M., Hutter A., Dayal P., Gottlöber S., Legrand L., Yepes G., 2022, *Astraeus VI: Hierarchical assembly of AGN and their large-scale effect during the Epoch of Reionization*, arXiv e-prints, p. arXiv:2202.02337

Trotta R., Jóhannesson G., Moskalenko I. V., Porter T. A., Ruiz de Austri R., Strong A. W., 2011, *Constraints on Cosmic-ray Propagation Models from A Global Bayesian Analysis*, apJ, 729, 106

Trujillo-Gomez S., Klypin A., Colín P., Ceverino D., Arraki K. S., Primack J., 2015, *Low-mass galaxy assembly in simulations: regulation of early star formation by radiation from massive stars*, MNRAS, 446, 1140

Tsujimoto T., Nomoto K., Yoshii Y., Hashimoto M., Yanagida S., Thielemann F. K., 1995, *Relative frequencies of Type Ia and Type II supernovae in the chemical evolution of the Galaxy, LMC and SMC*, MNRAS, 277, 945

Tumlinson J., Peeples M. S., Werk J. K., 2017, *The Circumgalactic Medium*, ARA&A, 55, 389

Tweed D., Devriendt J., Blaizot J., Colombi S., Slyz A., 2009, *Building merger trees from cosmological N-body simulations. Towards improving galaxy formation models using subhaloes*, A&A, 506, 647

Urošević D., Arbutina B., Onić D., 2019, *Particle acceleration in interstellar shocks*, Ap&SS, 364, 185

Van der Tak F. F. S., Weiß A., Liu L., Güsten R., 2016, *The ionization rates of galactic nuclei and disks from Herschel/HIFI observations of water and its associated ions*, A&A, 593, A43

VERITAS Collaboration et al., 2009, *A connection between star formation activity and cosmic rays in the starburst galaxy M82*, Nature, 462, 770

Venturi G., et al., 2021, *MAGNUM survey: Compact jets causing large turmoil in galaxies. Enhanced line widths perpendicular to radio jets as tracers of jet-ISM interaction*, A&A, 648, A17

Vogelsberger M., et al., 2014, *Introducing the Illustris Project: simulating the coevolution of dark and visible matter in the Universe*, MNRAS, 444, 1518

Vogelsberger M., Marinacci F., Torrey P., Puchwein E., 2020, *Cosmological simulations of galaxy formation*, Nature Reviews Physics, 2, 42

Wadsley J. W., Keller B. W., Quinn T. R., 2017, *Gasoline2: a modern smoothed particle hydrodynamics code*, MNRAS, 471, 2357

Walker M. G., Peñarrubia J., 2011, *A Method for Measuring (Slopes of) the Mass Profiles of Dwarf Spheroidal Galaxies*, apJ, 742, 20

Wang L., Dutton A. A., Stinson G. S., Macciò A. V., Penzo C., Kang X., Keller B. W., Wadsley J., 2015, *NIHAO project - I. Reproducing the inefficiency of galaxy formation across cosmic time with a large sample of cosmological hydrodynamical simulations*, MNRAS, 454, 83

Weaver R., McCray R., Castor J., Shapiro P., Moore R., 1977, *Interstellar bubbles. II. Structure and evolution.*, apJ, 218, 377

Webbink R. F., 1984, *Double white dwarfs as progenitors of R Coronae Borealis stars and type I supernovae.*, apJ, 277, 355

Wellons S., et al., 2022, *Exploring supermassive black hole physics and galaxy quenching across halo mass in FIRE cosmological zoom simulations*, arXiv e-prints, p. arXiv:2203.06201

Werk J. K., et al., 2014, *The COS-Halos Survey: Physical Conditions and Baryonic Mass in the Low-redshift Circumgalactic Medium*, apJ, 792, 8

Werk J. K., et al., 2016, *The COS-Halos Survey: Origins of the Highly Ionized Circumgalactic Medium of Star-Forming Galaxies*, apJ, 833, 54

Wetzel A. R., Hopkins P. F., Kim J.-h., Faucher-Giguère C.-A., Kereš D., Quataert E., 2016, *Reconciling Dwarf Galaxies with ΛCDM Cosmology: Simulating a Realistic Population of Satellites around a Milky Way-mass Galaxy*, ApJ, 827, L23

Wezgowiec M., Beck R., Hanasz M., Soida M., Ehle M., Dettmar R. J., Urbanik M., 2022, *Magnetic fields and hot gas in M101*, arXiv e-prints, p. arXiv:2206.10980

Whelan J., Iben Icko J., 1973, *Binaries and Supernovae of Type I*, apJ, 186, 1007

White S. D. M., Rees M. J., 1978, *Core condensation in heavy halos: a two-stage theory for galaxy formation and clustering.*, MNRAS, 183, 341

Wiener J., Oh S. P., Guo F., 2013, *Cosmic ray streaming in clusters of galaxies*, MNRAS, 434, 2209

Wiener J., Pfrommer C., Oh S. P., 2017, *Cosmic ray-driven galactic winds: streaming or diffusion?*, MNRAS, 467, 906

Wise J. H., Cen R., 2009, *Ionizing Photon Escape Fractions From High-Redshift Dwarf Galaxies*, apJ, 693, 984

Wise J. H., Abel T., Turk M. J., Norman M. L., Smith B. D., 2012, *The birth of a galaxy - II. The role of radiation pressure*, MNRAS, 427, 311

Wise J. H., Demchenko V. G., Halicek M. T., Norman M. L., Turk M. J., Abel T., Smith B. D., 2014, *The birth of a galaxy - III. Propelling reionization with the faintest galaxies*, MNRAS, 442, 2560

Wolfire M. G., Hollenbach D., McKee C. F., Tielens A. G. G. M., Bakes E. L. O., 1995, *The Neutral Atomic Phases of the Interstellar Medium*, apJ, 443, 152

Woltjer L., 1972, *Supernova Remnants*, ARA&A, 10, 129

Womble D. S., Sargent W. L. W., Lyons R. S., 1996, in Bremer M. N., Malcolm N., eds, Astrophysics and Space Science Library Vol. 206, Cold Gas at High Redshift. p. 249 (arXiv:astro-ph/9511035), doi:10.1007/978-94-009-1726-2_27

Woosley S. E., 1990, in Supernovae. pp 182–212

Yan H., Lazarian A., Petrosian V., 2008, *Particle Acceleration by Fast Modes in Solar Flares*, apJ, 684, 1461

Yang J., et al., 2020, *Pōniuā'ena: A Luminous z = 7.5 Quasar Hosting a 1.5 Billion Solar Mass Black Hole*, ApJ, 897, L14

Yoast-Hull T. M., Everett J. E., Gallagher J. S. I., Zweibel E. G., 2013, *Winds, Clumps, and Interacting Cosmic Rays in M82*, apJ, 768, 53

Yoo T., Kimm T., Rosdahl J., 2020, *On the origin of low escape fractions of ionizing radiation from massive star-forming galaxies at high redshift*, MNRAS, 499, 5175

Zaroubi S., 2013, in Wiklind T., Mobasher B., Bromm V., eds, Astrophysics and Space Science Library Vol. 396, The First Galaxies. p. 45 (arXiv:1206.0267), doi:10.1007/978-3-642-32362-1_2

Zatsepin G. T., Kuz'min V. A., 1966, *Upper Limit of the Spectrum of Cosmic Rays*, Soviet Journal of Experimental and Theoretical Physics Letters, 4, 78

Zhang J.-F., Li Z.-R., Xiang F.-Y., Lu J.-F., 2018, *Electron transport with re-acceleration and radiation in the jets of X-ray binaries*, MNRAS, 473, 3211

Zinger E., et al., 2020, *Ejective and preventative: the IllustrisTNG black hole feedback and its effects on the thermodynamics of the gas within and around galaxies*, MNRAS, 499, 768

Zweibel E. G., 2013, *The microphysics and macrophysics of cosmic rays*, Physics of Plasmas, 20, 055501

Zweibel E. G., 2017, *The basis for cosmic ray feedback: Written on the wind*, Physics of Plasmas, 24, 055402

Čerenkov P. A., 1937, *Visible Radiation Produced by Electrons Moving in a Medium with Velocities Exceeding that of Light*, Physical Review, 52, 378